Wolfgang Kuch Rudolf Schäfer Peter Fischer Franz Ulrich Hillebrecht

# Magnetic Microscopy of Layered Structures



### **Springer Series in Surface Sciences**

Volume 57

### **Series editors**

Gerhard Ertl, Berlin, Germany Hans Lüth, Aachen, Germany This series covers the whole spectrum of surface sciences, including structure and dynamics of clean and adsorbate-covered surfaces, thin films, basic surface effects, analytical methods and also the physics and chemistry of interfaces. Written by leading researchers in the field, the books are intended primarily for researchers in academia and industry and for graduate students.

More information about this series at http://www.springer.com/series/409

Wolfgang Kuch · Rudolf Schäfer Peter Fischer · Franz Ulrich Hillebrecht

# Magnetic Microscopy of Layered Structures



Wolfgang Kuch Institut für Experimentalphysik Freie Universität Berlin Berlin Germany

Rudolf Schäfer Leibniz Institute for Solid State and Materials Research Dresden Dresden Germany Peter Fischer Materials Sciences Division Lawrence Berkeley National Laboratory Berkeley, CA USA

Franz Ulrich Hillebrecht Institut für Festkörperforschung Forschungszentrum Jülich Jülich Germany

ISSN 0931-5195 ISBN 978-3-662-44531-0 DOI 10.1007/978-3-662-44532-7

ISBN 978-3-662-44532-7 (eBook)

Library of Congress Control Number: 2014947699

Springer Heidelberg New York Dordrecht London

### © Springer-Verlag Berlin Heidelberg 2015

This work is subject to copyright. All rights are reserved by the Publisher, whether the whole or part of the material is concerned, specifically the rights of translation, reprinting, reuse of illustrations, recitation, broadcasting, reproduction on microfilms or in any other physical way, and transmission or information storage and retrieval, electronic adaptation, computer software, or by similar or dissimilar methodology now known or hereafter developed. Exempted from this legal reservation are brief excerpts in connection with reviews or scholarly analysis or material supplied specifically for the purpose of being entered and executed on a computer system, for exclusive use by the purchaser of the work. Duplication of this publication or parts thereof is permitted only under the provisions of the Copyright Law of the Publisher's location, in its current version, and permission for use must always be obtained from Springer. Permissions for use may be obtained through RightsLink at the Copyright Clearance Center. Violations are liable to prosecution under the respective Copyright Law. The use of general descriptive names, registered names, trademarks, service marks, etc. in this publication does not imply, even in the absence of a specific statement, that such names are exempt from the relevant protective laws and regulations and therefore free for general use.

While the advice and information in this book are believed to be true and accurate at the date of publication, neither the authors nor the editors nor the publisher can accept any legal responsibility for any errors or omissions that may be made. The publisher makes no warranty, express or implied, with respect to the material contained herein.

Printed on acid-free paper

Springer is part of Springer Science+Business Media (www.springer.com)

### **Preface**

Scientific investigations to understand the fascinating behavior of thin magnetic films originating from fundamental quantum mechanical properties and particular spin coupling phenomena already started in the 1970s. The exploitation of magnetic films in technologies such as magnetic storage and sensor devices has received enormous boost with the discovery of the giant magnetoresistance effect in 1988. This discovery marks the beginning of the era of spintronics in which, beyond the charge used so far exclusively for conventional electronics, the spin of the electrons plays a dominating role. It also enabled to a large part the tremendous miniaturization of magnetic devices which became requisite for the plethora of magnetic applications, ranging from supercomputers to simulate, for example, climate changes to the zillions of entertainment gadgets allowing, for example, to watch almost anywhere high-quality movies.

In view of the ongoing race to increase the speed and, at the same time, decrease the energy demand for spin-based devices, unconventional spin textures, such as skyrmions, which require broken inversion symmetry such as naturally present in layered thin film systems, have recently attracted enormous attention, indicating that even after nearly 40 years thin film magnetism is still among the most vivid and controversial topics in magnetism.

The success of magnetic thin films particularly in the realm of nanomagnetism was based on major advances in three areas. The first is related to major technological progress in the synthesis of such systems. Thin-film fabrication capabilities have tremendously matured and are widely available, ranging from molecular beam epitaxy with atomic precision to sputter deposition techniques, which enable large-scale production of high quality thin film structures. Beyond the stacking of layered thin films, reaching out into superlattices, where the vertical coupling can be tailored to highest degree, the investigation and the use of effects of confinement and proximity, i.e., reflecting the lateral coupling phenomena, became possible due to advances in nanopatterning capabilities, such as electron-beam lithography, focused ion beam milling, or even the self-assembled rearrangement of structures.

The second is the significant progress in the theoretical description of the magnetic properties of thin films, heterostructures and nanostructures. State-of-the-art

vi Preface

density functional theory approaches, again harnessing the computing power of supercomputers, have helped not only to achieve a much deeper understanding, but have also increased the predictive power of theories to guide the experimentalist in the search for better materials. The prediction of a large spin polarization in an Fe/MgO layered system by Butler and Mahon is just one of those hallmarks.

Whereas the synthesis and the theory set the framework, it is the advances in characterization which have ultimately unveiled the properties of thin magnetic films and layered structures. There, an enormous progress has been made over the last two decades, triggered by the need to look deeper and more detailed into those systems, but also enabled by the advent of new instrumentation technologies harnessing the interaction of photons with magnetic thin film materials.

Writing a book on the capabilities of advanced magnetic imaging techniques for thin-film systems, where new developments and achievements are reported almost daily, is not an easy task, but we think worth the effort and hopefully appreciated by our communities. The focus of our book is on those imaging techniques that allow to "see" the magnetic domains or spin textures in different layers separately. The techniques which are laid out in this monograph rely on the interaction of photons with magnetic materials, both of optical photons and of soft X rays. We tried to collect the current state-of-the-art in imaging layered magnetic heterostructures, but also to present the interested reader an up-to-date overview of the research field based on sufficient background information to provide guidance on the choice of the technique that is inherently best suited to solve a certain problem.

In the course of writing the book we were saddened with the passing away of our dear colleague Ulrich Hillebrecht. He has made seminal contributions specifically to the imaging of layered structures containing antiferromagnetic materials, which undoubtedly constitutes an integral part of this endeavor. By adding Uli to the list of coauthors we want to honor him and his contributions posthumously.

Berlin Dresden Berkeley Wolfgang Kuch Rudolf Schäfer Peter Fischer

### Acknowledgments

We would like to express our thanks to those who have helped make this project possible. Highly appreciated are numerous email communications with the late Vladimir Kamberský (Prague) in which he helped to straighten out some aspects of magneto-optical diffraction analysis. He further added simplified models for a descriptive presentation of the magneto-optical Voigt and Gradient effects that are considered in the corresponding book chapters. Examples of scientific work presented in the book were obtained with the help of M. Aeschlimann, E. Anderson, D.A. Arena, C. Back, D. Bayer, D. Bedau, M. Bernien, M. Bonfim, D. Bürgler, M. Buess, J. Camarero, W. Chao, L. Chelaru, S.B. Choe, S. Czekaj, G. Denbeaux, H.A. Dürr, T. Eimueller A. Fontaine, K. Fukumoto, J. Gilles, M. Gottwald, T. Hauet, T. Haug, O. Hellwig, R. Hertel, L.J. Heyderman, R. Hollinger, M.-Y. Im, S. Imada, B. Kang, S.S. Kang, A.D. Kent, D.H. Kim, J. Kirschner, M. Kotsugi, F. Kronast, J. Kuneš, J. Kurde, G. Kurlyandskaya, F. Macia, S. Mangin, J. McCord, J. Miguel, F. Nolting, F. Offi, T. Okuno, T. Ono, Y. Pennec, F. Petroff, S. Pizzini, A. Puzic, J. Raabe, G. Reiss, F. Romanens, K. Rott, J. Sánchez-Barriga, S.C. Shin, H. Stoll, S. Suga, A. Svalov, B. van Waeyenberge, J. Vogel, J. Wang, P. Warnicke, D. Weiss, and L. Wenzel. The text was critically read by Dominik Markó. Jaroslav Hamrle introduced us in the "parallel Kerr vector method", and L. Lokamani helped with diffraction simulations on layer selective imaging. Thanks to all of them. Peter Fischer acknowledges support by the Director, Office of Science, Office of Basic Energy Sciences, Materials Sciences and Engineering Division, of the U.S. Department of Energy under Contract No. DE-AC02-05-CH11231 and the Leading Foreign Research Institute Recruitment Program (Grant No. 2012K1A4A3053565) through the National Research Foundation of Korea (NRF) funded by the Ministry of Education, Science and Technology (MEST).

Special thanks go to our families (Renate Schaefer, Petra Fischer, Claudia Padberg) for their patience and understanding.

### **Contents**

1	Intr	oductio	n		
	1.1	Layer	ed Magnetic Structures		
		1.1.1	Magnetoresistive Devices		
		1.1.2	Spintronics		
		1.1.3	Ferromagnetic-Antiferromagnetic Heterostructures		
		1.1.4	Need for Layer-Resolved Information		
		1.1.5	Need for Time Resolution		
	1.2				
		1.2.1	Interference-Based Approach		
		1.2.2	Electronic Properties-Based Approach		
2	Mag	neto-O	optical Effects		
	2.1		iew		
	2.2		al Basics of Conventional Effects		
		2.2.1			
		2.2.2	Polarized Light		
		2.2.3	Birefringence, Dichroism, and Optical Activity 36		
		2.2.4	The Compensator		
		2.2.5	Reflection and Transmission of Polarized Light 4		
	2.3	Electro	omagnetic Basics of Conventional Effects 49		
		2.3.1	The Dielectric Permittivity Tensor		
		2.3.2	Solutions		
	2.4	Farada	ay and Kerr Effect		
		2.4.1	Phenomenological Description		
		2.4.2	Geometry of the Rotation Effects 63		
		2.4.3	Kerr Contrast and Signal		
		2.4.4	Microscopic Origin of the Kerr Effect		
	2.5	Voigt	Effect		
	26	_	ant Effect 9		

x Contents

	2.7		agnetic Dichroism.	86
			-Ray Magnetic Linear Dichroism	86
			ircularly Polarized X-rays	91
		2.7.3 X	-Ray Magnetic Circular Dichroism	92
3	Dep		e Conventional Magneto-Optical Microscopy	97
	3.1	-	Optical Microscopy and Magnetometry	97
			'ide-Field Microscopy	98
			aser-Scanning Microscopy	103
			agneto-Optical Magnetometry and Ellipsometry	105
	3.2		nsitivity of Conventional Magneto-Optics	107
			xperimental Proof of Depth Sensitivity	108
		3.2.2 Th	neoretical Approaches to Depth Sensitivity	
			Magneto-Optics	109
			epth Sensitivity Function	115
			epth Sensitivity in Magnetic Films	119
		3.2.5 De	epth Sensitivity in Magnetic Multilayers	124
		3.2.6 Do	epth Selectivity in Magnetic Multilayers	127
	3.3	Depth-Sel	lective Kerr Microscopy	130
	3.4	Voigt- an	d Gradient Microscopy	137
		C		
4	Dep	th-Sensitiv	e Photoelectron Emission Microscopy	141
4	4.1	t <b>h-Sensitiv</b> Photoelec	tron Emission Microscopy	141
4	4.1 4.2	th-Sensitiv Photoelec Electron	tron Emission Microscopy	
4	4.1	th-Sensitiv Photoelec Electron ` Imaging I	tron Emission Microscopy	141 142
4	4.1 4.2	th-Sensitiv Photoelec Electron \ Imaging I Dichroisn	Arron Emission Microscopy	141
4	4.1 4.2	th-Sensitiv Photoelec Electron \ Imaging I Dichroisn	tron Emission Microscopy	141 142 150 151
4	4.1 4.2	th-Sensitiv Photoelec Electron I Imaging I Dichroism 4.3.1 Ni 4.3.2 Co	Arron Emission Microscopy	141 142 150 151 153
4	4.1 4.2	th-Sensitiv Photoelec Electron I Imaging I Dichroism 4.3.1 Ni 4.3.2 Co	Arron Emission Microscopy	141 142 150 151 153 161
4	4.1 4.2	th-Sensitiv Photoelec Electron I Imaging I Dichroisn 4.3.1 No. 4.3.2 Co. 4.3.3 No. 4.3.4 No.	Arron Emission Microscopy	141 142 150 151 153
4	4.1 4.2	th-Sensitiv Photoelec Electron I Imaging I Dichroisn 4.3.1 No. 4.3.2 Co. 4.3.3 No. 4.3.4 No.	tron Emission Microscopy	141 142 150 151 153 161
4	4.1 4.2	th-Sensitiv Photoelec Electron Maging I Dichroism 4.3.1 No 4.3.2 Co 4.3.3 No 4.3.4 No 4.3.5 No 4.3.5 No	tron Emission Microscopy  Yield Detection of Absorption from Buried Layers  Ferromagnetic Materials by X-ray Magnetic Circular  i	141 142 150 151 153 161 163
4	4.1 4.2 4.3	th-Sensitiv Photoelectectron of Imaging I Dichroism 4.3.1 No. 4.3.2 Co. 4.3.3 No. 4.3.4 No. 4.3.5 No. Imaging I Linear Dichrosers	tron Emission Microscopy  Yield Detection of Absorption from Buried Layers  Ferromagnetic Materials by X-ray Magnetic Circular  i	141 142 150 151 153 161 163
4	4.1 4.2 4.3	th-Sensitiv Photoelectectron of Imaging I Dichroism 4.3.1 No. 4.3.2 Co. 4.3.3 No. 4.3.4 No. 4.3.5 No. Imaging I Linear Dichrosers	Artiforn Emission Microscopy  Yield Detection of Absorption from Buried Layers  Ferromagnetic Materials by X-ray Magnetic Circular  i	141 142 150 151 153 161 163 166
4	4.1 4.2 4.3	th-Sensitiv Photoelec Electron Imaging I Dichroism 4.3.1 Ni 4.3.2 Co 4.3.3 Ni 4.3.4 Ni 4.3.5 Ni Imaging A Linear Di 4.4.1 M	tron Emission Microscopy  Yield Detection of Absorption from Buried Layers  Ferromagnetic Materials by X-ray Magnetic Circular  i	141 142 150 151 153 161 163 166
4	4.1 4.2 4.3	th-Sensitiv Photoelec Electron Imaging I Dichroisn 4.3.1 Ni 4.3.2 Cc 4.3.3 Ni 4.3.4 Ni 4.3.5 Ni Imaging A Linear Di 4.4.1 M La	Artron Emission Microscopy  Yield Detection of Absorption from Buried Layers  Ferromagnetic Materials by X-ray Magnetic Circular  In	141 142 150 151 153 161 163 166
4	4.1 4.2 4.3	th-Sensitiv Photoelec Electron \( \) Imaging I Dichroisn 4.3.1 No 4.3.2 Co 4.3.3 No 4.3.4 No 4.3.5 No Imaging A Linear Di 4.4.1 M La 4.4.2 Ex	Artron Emission Microscopy  Yield Detection of Absorption from Buried Layers  Ferromagnetic Materials by X-ray Magnetic Circular  In	141 142 150 151 153 161 163 166 169 170
4	4.1 4.2 4.3	th-Sensitiv Photoelec Electron Imaging I Dichroism 4.3.1 Ni 4.3.2 Co 4.3.3 Ni 4.3.4 Ni 4.3.5 Ni Imaging A Linear Di 4.4.1 M La 4.4.2 Ex	Artiferromagnetic Materials by X-ray Magnetic Circular in	141 142 150 151 153 161 163 166 169
4	4.1 4.2 4.3	th-Sensitiv Photoelectectron of Imaging I Dichroism 4.3.1 Ni 4.3.2 Co 4.3.3 Ni 4.3.4 Ni 4.3.5 Ni Imaging A Linear Di 4.4.1 M La 4.4.2 Ex an 4.4.3 Co	Artiforn Emission Microscopy  Yield Detection of Absorption from Buried Layers  Ferromagnetic Materials by X-ray Magnetic Circular  i  iFe/Cu/Co Trilayers  o/Cu/Ni Trilayers  iFe/Al <sub>2</sub> O <sub>3</sub> /Co Trilayers  iFe/Co Trilayers  i/Fe/Co Trilayers  Antiferromagnetic Materials by X-ray Magnetic chroism  fagnetic Linear Dichroism as Contrast Mechanism for ayer-Resolved Magnetic Imaging Using PEEM  acknange Coupling at the Interface of NiO  and a Ferromagnetic Metal	141 142 150 151 153 161 163 166 169 170
4	4.1 4.2 4.3	th-Sensitiv Photoelectectron of Imaging I Dichroism 4.3.1 No. 4.3.2 Co. 4.3.3 No. 4.3.4 No. 4.3.5 No. Imaging A Linear Dichectectron of Linear Dichect	Artiferromagnetic Materials by X-ray Magnetic Circular in	141 142 150 151 153 161 163 166 169 170

Contents xi

5	Mag	netic Transmission Soft X-Ray Microscopy	89
	5.1	Introduction	89
	5.2	Absorption of X Rays in Transmission Experiments 1	90
	5.3	Basic Elements in Magnetic Transmission Soft	
		X-Ray Microscopy	97
			97
		5.3.2 Experimental Set-Up	99
		5.3.3 Sample Properties	202
		5.3.4 Sensitivity to Thin Layers	203
	5.4	Imaging Layered Magnetic Microstructures	204
		5.4.1 Elemental Specificity	204
		5.4.2 Magnetization Reversal Processes	
		in Nanostructured Elements	205
		5.4.3 Domain Structures in Multilayered Systems 2	210
	5.5	Time and Layer-Resolved Magnetic Imaging by M-TXM 2	216
	5.6	Future Perspectives	220
Re	feren	res	221
Ind	lev	2	41

## Chapter 1 Introduction

### 1.1 Layered Magnetic Structures

Not many fields in modern solid state physics have had such a dramatic impact on science and technology as thin film magnetism. More than 40 years ago, the coupling phenomena in multilayers were already predicted and described [1]. Ever since, a lot of effort has been dedicated on understanding the properties of magnetic films with thicknesses down to the few atom limit [2, 3]. The deposition of such films on top of supporting substrates bears the possibility to stabilize new materials by influencing their structure [4-8] and to study in detail the interaction between structural and magnetic properties [9, 10]. The latter were quite often found to deviate substantially from the properties known from the corresponding bulk magnetic materials. Finite size effects and the different coordination and environment of the atoms at the film's interfaces lead to deviating thermodynamic behavior [11–14], different spin [15–17] and orbital [18–21] magnetic moments, and different magnetic anisotropy energies [22–26]. More recently, novel ways to control spins, via pure spin currents, take into account non-collinear spin arrangements [27, 28], which are often amplified due to spin-orbit-driven interactions at such interfaces. Spin-orbit-driven interactions in layered systems of ferromagnetic and high-Z materials allow for an efficient electric current-induced domain wall motion [29]. Understanding the entanglement of the magnetic, electronic, and structural properties had, and still has, the attraction of finding ways to tailor magnetic properties in thin films by influencing parameters such as stress, strain, and electronic hybridization by the choice of the film and neighboring materials with respect to chemical composition and thickness.

### 1.1.1 Magnetoresistive Devices

Soon the focus in magnetic thin film research shifted from the investigation of single magnetic films to hybrid structures involving multilayered stacks of two or more magnetic layers, separated by non-magnetic spacer layers [30, 31]. The discovery of antiparallel coupling [32] and oscillatory interlayer coupling [33] in such multilayered systems paved the way for the controlled manipulation of the relative

1

2 1 Introduction

magnetization direction of different ferromagnetic layers. Ignited by the discovery of giant magnetoresistance (GMR) in magnetic multilayers at the end of the eighties [34, 35], and the realization of its giant potential for applications [36, 37], systematic investigations of the effect were launched [33, 38, 39]. They were accompanied by fundamental studies of the magnetic properties of multilayered structures [40–42], which are important if one wants to provide suitable operating conditions for devices based on giant magnetoresistance. It took less than a decade from discovery to commercial exploitation of the effect. At the end of 1997 the first hard disk drives equipped with a read head of the new technology were sold to the customer. Nowadays, essentially the entire hard disk head production has been switched to multilayered magneto-resistive devices.

Figure 1.1 sketches the principle of such magnetic read head sensors, and some of the developments and visions that followed. Panel (a) presents a schematics of a current-in-plane GMR sensor, as it was used in hard disk read heads for a while. The electric conductivity of a stack of at least two ferromagnetic (FM) layers that are separated by non-magnetic but electrically conductive spacer layers can change significantly if the magnetization directions of the two magnetic layers are aligned more parallel or more antiparallel to each other. Technically, one of the magnetic layers is usually designed as a hard magnetic layer, which is only little affected by usual external magnetic fields, while the other layer, called the soft magnetic layer, is made to respond easily on changes in the applied magnetic field. The giant size of the effect allowed to detect small changes in magnetic stray fields from the hard disk as small deviations in the magnetic alignment of the soft layer, which in turn enabled disk manufacturers to decrease the amount of stray field above the disk needed to detect a single bit of information, and correspondingly to decrease its size. This has led to a change in the annual growth rate of storage density of magnetic hard disks, which before 1997 followed a rapid annual increase of 60 %, and since then has sped up to increase by an astonishing 100 % each year for a while.

A related effect, the tunnel magnetoresistance (TMR), is sketched in Fig. 1.1b. Although discovered before the GMR effect [43], it experienced a renaissance in the nineties, when it was discussed with respect to possible applications in magnetic data storage [44, 45]. The effect relies on the spin-polarized tunneling of electrons between two ferromagnetic layers [46–48] across a thin insulating barrier, typically an ultrathin oxide spacer layer. If one considers spin conservation in the tunnel process, the tunneling occurs between majority and majority states as well as between minority and minority states of the two FM layers, if their magnetization directions are parallel. If they are antiparallel, majority electrons from one FM layer tunnel into minority states of the other layer, and vice versa. In general, the density of the involved states and the tunnel probability will be different in these two cases, leading to tunnel magnetoresistance. Systematic fundamental investigations [49–54] eventually helped to push the tunnel magnetoresistance ratio at room temperature up to 220 % [55].

<sup>&</sup>lt;sup>1</sup> The Nobel Prize in Physics 2007 was awarded to Albert Fert and Peter Grünberg for the discovery of Giant Magnetoresistance.

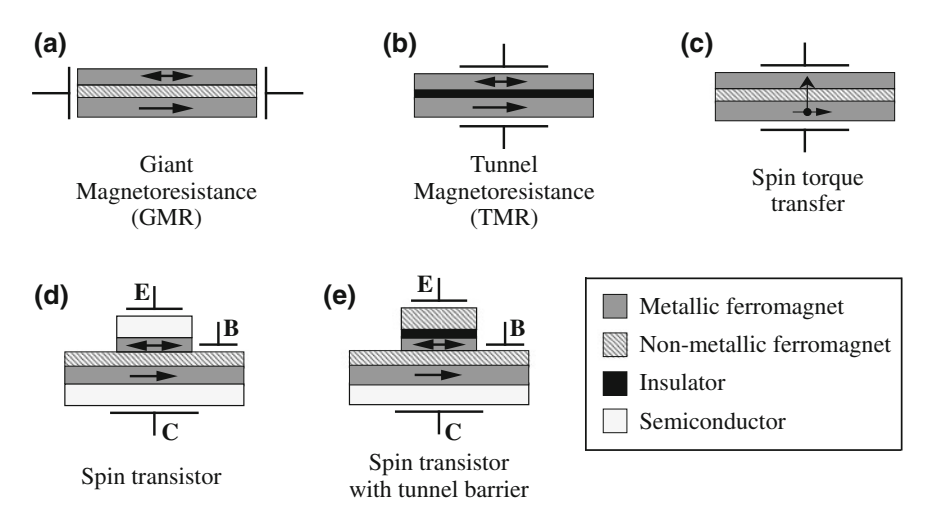
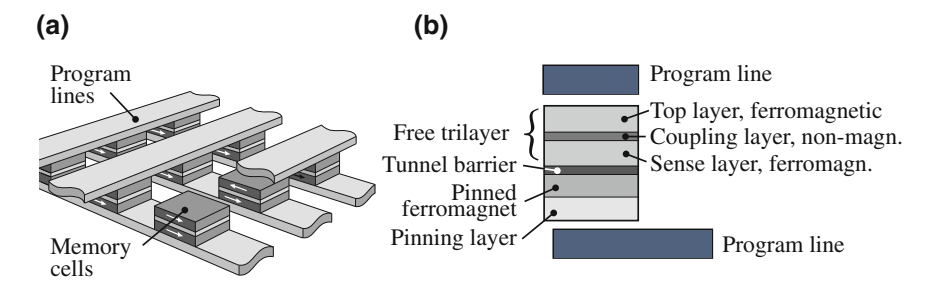


Fig. 1.1 Some modern concepts for devices based on thin film magnetism. a Giant magnetoresistance: Dependence of metallic conductivity in a stack of two or more ferromagnetic layers on the relative orientation of their magnetization directions. Soon after its discovery, this effect was applied in devices, for example, in read heads of hard disk drives. b Tunnel magnetoresistance: Dependence of tunnel current between two ferromagnetic layers across an insulating barrier layer on the relative orientation of the magnetization directions in the magnetic layers. This effect is, for example, currently applied in read heads of digital magnetic recording and will be used in future magnetic random access memories that are currently under development. c Spin torque transfer: Current-induced switching of the magnetization of a ferromagnetic layer in a nanostructured stack of two ferromagnetic layers by the torque exerted by the spin-polarized electrons on the magnetization of one of the layers. This is proposed as a means to switch the magnetization in magnetoresistive devices, and currently under intensive investigation. d Spin transistor: Three-terminal device in which the current between emitter (E) and collector (C) depends on the current between emitter and base (B) and, in addition, on the relative orientation of the two ferromagnetic layers. e Spin transistor with tunnel barrier: Three-terminal device like (d), in which in addition the emitter bias voltage can be used to tune the energy of electrons that are injected into the collector. The last two devices represent only two out of many approaches to the so-called field of spintronics, in which in future devices both the charge and spin of electrons are used for information processing

TMR elements have a higher resistance compared to GMR, which is desirable for certain applications, but the use of TMR requires the current to be run perpendicularly through the stack. In 2005, TMR-based spin valves have replaced GMR read elements in recording heads due to their higher magnetoresistance ratios and are in use up to now. Further downscaling, however, might enforce the use of current-perpendicular-to-plane GMR sensors in the near future as the high absolute resistance of TMR elements is a critical obstacle to downsizing such sensors [56]. Another possible application that is discussed in connection with the TMR effect is a magnetic random access memory (MRAM) (see Fig. 1.2). The idea is to have an array of small TMR elements like the one shown in Fig. 1.1b, which constitute the bits of the stored information, where "magnetization parallel" represents, for example, "0", and "magnetization antiparallel" stands for "1". The working principle is actually quite similar

4 1 Introduction



**Fig. 1.2** Scheme of an MRAM device. **a** Simplified sketch of the arrangement of memory cells in an MRAM device. Reading of the information stored in the individual memory cells is achieved by measuring their electrical resistivity using the program lines and underlying diodes (not shown). **b** Detail of a memory cell. The tunnel magnetoresistance is determined by the relative orientation of the magnetizations in the sense layer and the pinned ferromagnetic layer (*small arrows* in **a**). The purpose of the pinning layer is to make the pinned ferromagnet insensitive to magnetic fields. The *top* and *coupling layers* are needed for a certain scheme for magnetization reversal in the so-called "toggle MRAM" [57]

to the magnetic core memories of the early days of computing. The most remarkable difference is obviously the size. MRAMs are being advertised as making the boot process of computers obsolete<sup>2</sup> when replacing conventional random access memory chips, because the magnetic information is retained after the power is shut off [58, 59]. First prototype MRAMs are commercially available for niche applications.

Reading the information in a TMR-MRAM means measuring the resistance through the stack. Addressing the resistance of a certain element in an array of trilayered stacks requires an integrated scheme of crossing word and bit lines with additional diodes underneath each stack in order to read the tunneling resistance of a particular element. The "0" and "1" states are then to be distinguished by some readout electronics. Technically even more demanding is the write process. It requires a very local and quite high magnetic field at the place of the element that is to be switched from "0" to "1" or vice versa, which means reversing the magnetization direction of the soft layer. Proposed writing schemes include a crossed arrangement of writing word and bit lines, through which relatively high currents can be run. The element to be switched is then the one at the crossing of the two lines under current, because only there the Oersted fields of the two lines add up to reach and exceed the critical field for magnetic switching. It is obvious that for the realization of a highly integrated MRAM device severe requirements with respect to the switching field distribution of the elements and the need to avoid cross talk between neighboring elements have to be met. Analytical tools to characterize the switching characteristics of these elements are mandatory for this.

<sup>&</sup>lt;sup>2</sup> Note that the development of MRAM devices for applications in personal computers has to compete with the rapid progress in the development of semiconducting flash memories. It remains to be seen whether the use of MRAM will be restricted to niche applications, for instance where an insensitivity to strong radiation is required.

Another possibility of writing, i.e., of switching the magnetization in small elements, has been suggested after the discovery of current-induced effects on the magnetization. If a high current is vertically run through a multilayered stack as sketched in Fig. 1.1c, the electric current will be partially spin polarized after traversing the first magnetic layer. This spin polarized current exerts a torque on the magnetization of the other layer, and vice versa [60]. This can be used to reverse the magnetization of the soft layer, provided the current density is sufficiently high [61–66]. Typically  $10^7-10^8$  A/cm<sup>2</sup> are needed; this can be accomplished only if the area of the element is small enough.

### 1.1.2 Spintronics

Magnetoresistive effects and the generation of spin-polarized currents by ultrathin ferromagnetic layers have led to the vision of using not only the charge of the electrons for information processing, as in today's electronic circuits, but in addition also their spin [67–69]. This has been termed "spintronics". General fundamental questions regarding the efficiency of injecting spins into the FM layer (spin injection), the propagation of spin-polarized electrons (spin transport), the efficiency of detecting the spins (spin detection), and, generally, the inherent length scales of these processes (spin coherence length) are currently addressed in intensive fundamental studies. Recent reviews on spintronics can be found in [70] and [71]. A further emerging field of research, termed "spin caloritronics" [72], concentrates on the interplay between temperature and spin transport. This would allow to generate spin currents by temperature gradients, or use spin currents for heat transport.

Two possible logical elements that could be used as spin-sensitive logic devices are sketched in Fig. 1.1d, e. They are both three-terminal devices and have been termed "spin transistor" to emphasize the analogy to charge-based "conventional" electronics. Their working principle is as follows: A base current is run between emitter (E) and base (B). Due to the Schottky barrier formed at the semiconductormetal interface, this leads to the injection of hot electrons into the metallic trilayer that forms the base [73]. These electrons are spin-polarized by the upper FM layer. Hot electrons travelling to the collector (C) are then spin-analyzed by the lower FM layer, so that the collector current changes its magnitude significantly if the magnetization configuration of the FM layers is switched from parallel to antiparallel. More than 300 % current enhancement at room temperature have been achieved [74]. Integrating an insulating barrier layer in such a three-terminal device, as shown in Fig. 1.1e, gives the experimenter the flexibility to operate the same device at different bias voltages, and thus to inject hot electrons at variable energy [75]. Optimization of a similar structure as the one depicted in Fig. 1.1e has led to a magnetoresistance effect of 3,400 % at room temperature [76]. The transfer ratio, that is the ratio between base and collector currents of such devices, is presently smaller than unity (between  $10^{-6}$ and  $10^{-4}$  [75, 77]), so that no amplification like in a real transistor is obtained. Still, the idea of programming or controlling logical operations by magnetism is

6 1 Introduction

compelling and large efforts are dedicated to the development of more efficient spin injection into semiconductors [69, 78–86].

Another approach that is currently emerging involves the manipulation of magnetization in multiferroic systems by electrical fields. Multiferroic materials have coupled electric, magnetic, and structural order parameters that result in simultaneous ferroelectricity, ferromagnetism, and ferroelasticity [87–94]. With this coexistence, the magnetization can be influenced by an electric field and electrical polarization by a magnetic field, a property which is termed the "magnetoelectric effect". Aside from its fundamental importance, the mutual control of electric and magnetic properties is of significant interest for applications in magnetic storage media and spintronics, since the local application of electric fields to switch magnetic properties in nanoscale devices can be accomplished with much lower power dissipation than the application of magnetic fields. On a microscopic length scale it is expected that in ferroelectromagnets the coupled electric and magnetic ordering is accompanied by the formation of domains and domain walls, such that imaging techniques can contribute to the fundamental understanding of the interconnection of different order parameters.

### 1.1.3 Ferromagnetic-Antiferromagnetic Heterostructures

The coupling between an antiferromagnet and a ferromagnet at their interface is an issue that is important for the technical realization of magnetoresistive applications [38]. At the interface between ferro- and antiferromagnet the magnetic moments of both materials interact by exchange coupling. Studies of interfaces between a ferromagnet and non-magnetic adlayers have shown that the interaction with the ferromagnetic substrate may induce long-range ferromagnetic order in the adlayer, which by itself does not show ferromagnetic order [95–100]. The induced magnetization may be parallel or antiparallel to the magnetization of the ferromagnet, depending on the sign of the exchange interaction. This may lead to a ferromagnetic adlayer even for a material that in its bulk form is antiferromagnetic, as observed, e.g., for ultrathin Cr films on Fe [101–103]. In this case the long range order in the adlayer—be it an antiferromagnet or a non-magnetic metal in the bulk—is governed by the interaction with the ferromagnetic substrate and it may be expected to show the same temperature dependence. The temperature dependence of this induced magnetic order was in fact investigated for Mn on Ni and was found to be identical to that of the substrate [104]. Of course, as the antiferromagnetic layer thickness increases, the bulk antiferromagnetic state will prevail and each layer will show its own ordering temperature, approaching the bulk ordering temperatures for thick layers. It has been shown that the ordering temperature of the antiferromagnet may be influenced significantly by the presence of the ferromagnetic layer, as well as by its magnetization direction [105]. In addition, the exchange interaction at the interface can modify the magnetic behavior of the layered system in a characteristic way, which is known under the term "exchange bias".

Exchange bias was first observed in the 1950s on small Co particles covered with a Co oxide layer [106]. The hysteresis loop of these particles was shifted from being (inversion-) symmetric with respect to the magnetic field; instead, the inversion center of the hysteresis loop occurred at finite field, such as though some bias field was present in the sample, hence the term "exchange bias". The occurrence and magnitude of such a bias field depends on the history of the sample. To generate the bias field, the sample has to be cooled from above the Néel temperature—which has to be lower than the Curie temperature of the ferromagnet—in an external magnetic field. Obviously, this phenomenon is connected to the occurrence of magnetic moments in the antiferromagnet, which interact with those of the ferromagnet via exchange.

Exchange bias plays an important role for devices utilizing magnetoresistance effects or spin-dependent transport like the ones shown in Fig. 1.1. In such devices, one of the magnetic layers is required to have an increased coercive field for magnetization in a certain direction, which can be accomplished by exchange bias. Another example, the coupling of ferromagnetic nanoparticles to an antiferromagnetic material, was even suggested as a means of stabilizing the magnetic order at finite temperatures [107]. To take the full advantage of including antiferromagnetic/ferromagnetic interfaces into device structures, one needs to understand the underlying mechanisms governing the magnetic interaction at these interfaces.

Describing the exchange bias in terms of the magnetic moments of the antiferromagnet at the interface, which interact with the ferromagnetic moments by a typical exchange coupling [108], yields bias fields that are one to two orders of magnitude higher than observed experimentally. In the most simple model one assumes socalled uncompensated antiferromagnetic surfaces, i.e., surface orientations in which the atomic moments of the surface plane of the antiferromagnet add up to a nonvanishing net moment. The finite magnetization in the surface layer of the antiferromagnet interacts with that of the ferromagnet deposited on such a surface. The ferromagnet would then show a magnetization either parallel or opposite to the surface magnetization of the antiferromagnet, depending on the sign of the exchange interaction. However, it is not difficult to see why this simple picture is inadequate, because it does not take into account that any single-atomic step on the surface of the antiferromagnet will change the direction of the surface magnetization, which would enforce the formation of domains in the ferromagnet, or favor some other non-uniform state. Furthermore, exchange bias is also observed for interface orientations for which the antiferromagnet is not expected to have a net moment, the so-called compensated interfaces. This can not be accounted for by such a simple picture.

These aspects illustrate that the interaction between antiferromagnet and ferromagnet is rather complex. Therefore, the study of magnetic domains in such heterosystems [109, 110] provides an important input for modelling their behavior. By combining linear and circular magnetic dichroism in soft X-ray absorption, as will be explained in Sects. 2.7.1 and 2.7.3, layer-resolved magnetic imaging of both the magnetic domains in the ferromagnetic and in the antiferromagnetic layers is possible. Some examples will be presented in Sect. 4.4. The type of contrast—antiferromagnetic or ferromagnetic domains—is determined by the choice

8 1 Introduction

of light polarization and by the choice of the absorption edges or the spectroscopic features used for imaging. The layer-resolved information allows one to correlate the occurrence of antiferromagnetic and ferromagnetic domains in the layered anti-/ferromagnetic system and to draw conclusions about the interaction between the layers.

### 1.1.4 Need for Layer-Resolved Information

Although some of the principles explained in Fig. 1.1 as well as the exchange bias effect are already employed in devices or are under development for applications, fundamental knowledge about the processes and the physics behind the important effects is still highly demanded. This is true for the static magnetic properties, for which the interplay with structural, electronic, and chemical properties can greatly help to achieve desirable behavior for the operation of devices, and this is also true for the dynamic magnetic behavior. The ever increasing need for data storage space driven by the ever progressing digitalization of all kind of media goes hand in hand with the demand for faster access to the stored information.<sup>3</sup>

All of the effects sketched in Fig. 1.1 have in common that the structures in which they are observed contain two or more magnetic layers within a multi-layered thin film structure, and that the magnetization of these layers has to be controlled independently. Furthermore, since these samples are often laterally structured or confined, nanoscale magnetic effects are becoming increasingly important. Apart from electronic transport properties, the understanding and the control of the magnetic coupling between different magnetic layers, also considering micromagnetic effects, is thus a major issue. To address the different layers separately and to obtain microscopic magnetic information about each layer in a simple way is thus crucial for the investigation of such structures.

Imaging of magnetic domains has essentially contributed at all stages to our present level of understanding of micromagnetic phenomena [111–114] in bulk materials as well as in magnetic films. Magnetic imaging techniques allow the most direct view on magnetic properties on a microscopic scale. The local magnetization direction as a function of geometric and material properties can be studied immediately in a straightforward way. Imaging the magnetic domain structures of multilayered magnetic systems separately for each layer with high spatial resolution, and to study the dynamics of the spin structure with high temporal resolution is therefore the outstanding challenge to any magnetic microscopy technique applied to all the systems described above.

A number of layer-resolving magnetic imaging techniques have evolved in recent years, which can be used to address the different magnetic layers in layered magnetic structures separately. They consequently offer substantial advantages for the

<sup>&</sup>lt;sup>3</sup> While the length scales in devices approach the fundamental magnetic exchange length, the current time scales in magnetic applications are far from a fundamental limit (see Sect. 1.1.5).

microscopic investigation of layered magnetic structures compared to laterally or vertically averaging techniques. A review of these techniques is the objective of the present book, which intends to provide a comprehensive overview on the state-of-the-art imaging of magnetic domains in layered magnetic structures. It explains the fundamentals of the techniques and provides directions for potential users. Data and examples presented for each technique are (mostly) drawn from recent research, and are selected to illustrate the power for investigating complex multicomponent samples, such as ultrathin multilayers and nanostructures.

### 1.1.5 Need for Time Resolution

Beyond the static magnetic properties in nanoscale magnetic systems, the ultrafast spin dynamics in such systems is attracting more and more scientific and technological interest. The scientific goal is to understand magnetization dynamics on a fundamental time scale. Technologically the dramatic process of miniaturizing devices, e.g. in storage and sensor application, that has taken place over the last decade was by no means accompanied by a similar increase in speed of these devices. New concepts how to change the magnetization on a fast time scale need to be explored and are already being discussed, like the all-optical control of magnetization [115–117].

The general challenge to magnetic microscopies for studies of relevant layered systems is to reach simultaneously (i) nanometer length scales, (ii) ultrafast time scales, and (iii) depth or layer resolution. The time scales of interest in nanomagnetism cover several orders of magnitude from the micro- to nanosecond regime, where thermal processes and domain wall motion take place, to the nanosecond to picosecond regime, where precessional and relaxation processes occur, and down to the femtosecond regime, which is the fundamental time scale of exchange interaction, the strongest magnetic interaction.

The magnetization in a magnetic system can be changed, e.g., upon applying an external magnetic field. Since for the system this leads to a torque acting on the equilibrium magnetization, it will start a precessional motion that in turn relaxes after some time into the direction of the applied magnetic field. The same is true if a short current pulse exerts a spin transfer torque on the magnetization or if the effective magnetic field is temporarily changed by a short laser pulse. A phenomenological approach to describe the temporal development of the magnetization is provided by the Landau-Lifshitz-Gilbert equation

$$\frac{d\mathbf{J}}{dt} = \gamma \left[ \mathbf{J} \times \mathbf{H}_{\text{eff}} \right] - \frac{\alpha_{\text{G}}}{J} \left[ \mathbf{J} \times \frac{d\mathbf{J}}{dt} \right]$$
 (1.1)

accounting for both the precession of the magnetization in an effective magnetic field  $H_{\rm eff}$  with  $\gamma$  being the gyromagnetic ratio and J the vector of magnetic polarization, as well as for the relaxation and damping of the system. The latter is described by a phenomenological parameter  $\alpha_{\rm G}$  depending on the local geometry, anisotropy, and morphology. So far a complete microscopic understanding of relaxation processes

10 1 Introduction

is lacking although it is of paramount importance for understanding microscopic dynamic properties of magnetization.

Spin dynamics can be imaged by time-resolved high-speed microscopy [118]. In such pump-probe experiments, the sample is excited by a continuously changing or pulsed periodic magnetic field, a current pulse, or a laser pulse. At certain time delays relative to the excitation, the magnetization is microscopically probed in a finite time window. Shifting the time delay of the probing window yields a series of time-resolved images of the magnetization process. Time resolution is either obtained by a gated high-speed video camera using a constant light source for illumination or by a pulsed light source and continuous detection. An ideal dynamic experiment should deliver a time-delayed series of single-shot images, each of them representing the momentary magnetic state of the sample during the evolution of the magnetization process within the same excitation cycle. Single-shot imaging, however, requires a sufficient amount of signal to be accumulated in the detector during the probing time in order to obtain a sufficient signal-to-noise ratio. Very bright light sources and highly sensitive image detectors are therefore necessary. Also, the repetition rate of the experiment has to be fast enough to provide adequately short time delays for in-cycle imaging. Both conditions are increasingly difficult to meet with rising excitation frequency or if the magnetization response is too fast after pulse-field excitation. If both, detector sensitivity and repetition rate of the experiment are limited, time-resolved microscopy has to be performed in a different way, known as stroboscopic imaging. In a strobed system, image acquisition is precisely synchronized to a periodic excitation, so that images are captured in the same time period of successive cycles and accumulated over many cycles until a sufficient signal-to-noise ratio is achieved. The time delay is then periodically shifted to temporarily scan along the magnetization process. This accumulation technique, however, requires repetitive magnetization processes during successive cycles.

Stroboscopic magnetic microscopy on magnetic films and multilayers can be realized in two ways: (i) By imaging techniques using visible light in laboratory-based wide-field or laser-scanning Kerr microscopes [118] (see Sect. 3.1). Time-resolution can reach the femtosecond range by applying corresponding lasers as light source. The lateral resolution in such systems is limited, though, to some 100 nm owing to the wavelength of visible light and so far time-resolved Kerr microscopy has never

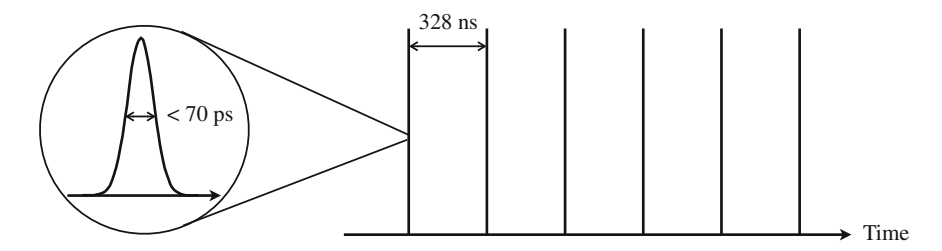


Fig. 1.3 Schematic of the time structure in two-bunch mode operation at the Advanced Light Source, Berkeley. The bunches are separated by 328 ns, while the width of each bunch determining the obtainable time resolution is  $\approx 70\,\mathrm{ps}$ 

been applied in a layer-resolved way although this would in principle be possible. (ii) By using X-ray illumination provided by a synchrotron radiation source. Here the lateral resolution is one or two orders of magnitude better, making synchrotron-based microscopy well suited for the investigation of micro- and nanostructures, and layer-resolved dynamic imaging has been realized already as will be demonstrated in Chaps. 4 and 5.

In recent years, the development of lab-based soft X-ray sources based on plasma sources and high harmonic generation has advanced significantly [119]. While these sources still can not compete with current synchrotron radiation facilities with respect to brightness, tunability to high photon energies, and polarization, their potential for the generation of femtosecond X-ray pulses with low jitter makes them very appealing for the study of dynamic processes [120, 121]. Although in principle imaginable, so far lab-based soft X-ray sources have not yet been used for layer-resolved magnetic imaging.

The X rays in a synchrotron radiation source are generated from electrons circulating the storage ring in short bunches at highly relativistic energies. At third generation synchrotron radiation sources the corresponding length of the X-ray pulses is in the sub-100-ps regime providing a time structure that is suitable for time-resolved studies of magnetism in layered structures. Since the intensity per bunch, however, is very low, such time-resolved studies have to be performed in a stroboscopic pumpprobe scheme limiting them to fully reproducible processes. Synchrotron radiation facilities serving a large variety of user experiments at the same time can be operated in many different modes. Generally, there are hundreds of relatively small electron bunches stored in the ring and the ring cavities are running at typical RF frequencies, e.g. 500 MHz, therefore each bunch is separated by 2 ns. However, most synchrotron radiation sources offer few-bunch operation modes, where only one (single-bunch mode) or two (two-bunch mode) bunches are injected into the storage ring. These are very convenient for time-resolved studies if, e.g., the detected signal cannot be separated from other X-ray pulses by a gated detector or if studies require a longer gap between subsequent X-ray pulses, such as time-of-flight experiments. To illustrate this, the time structure of the two-bunch mode of operation of the ALS is sketched in Fig. 1.3. In this mode, there are only two bunches stored in the ring separated by 328 ns with a bunch width of about 70 ps. The single bunch mode of BESSY II offers 70 ps long bunches every 800 ns. In a dedicated operation mode with compressed bunch lengths, the so-called low-alpha mode, pulse widths below 5 ps are achieved [122].

At many synchrotron radiation sources also a hybrid mode is available in which one bunch that is different from all others, a so-called camshaft bunch, is injected from the accelerator into the storage ring. It has a higher intensity and is normally set into the ring pattern so that there is a large gap before and after this bunch. At the ALS, a 70 ps bunch is surrounded by breaks of 80 ns, while during the other 640 ns bunches appear every 2 ns. The camshaft can be used for time-resolved experiments

12 1 Introduction

in which the other pulses can be blanked out,<sup>4</sup> serve as a marker, or can be used for special operations, such as the slicing mode offered at BESSY II in Berlin. In this slicing mode, femtosecond pulses are generated by modulating this bunch with a femtosecond laser pulse. This is an attempt to enable femtosecond dynamics experiments already with current synchrotron radiation sources. The drawback here is that the increased time resolution has to be paid with an enormous loss in intensity.

Next-generation sources using X-ray free electron laser systems will provide femtosecond pulses at very high intensity and therefore will enable studies of magnetism at femtosecond time scales that will not be restricted to pump—probe experiments, but will allow for single-shot experiments. Soft X-ray microscopies at such facilities hold the promise and the unique potential to cover both, fundamental length and time scales of magnetism, and provide elemental sensitivity, which is of paramount importance for studies of multicomponent systems.

There are several activities to combine X-ray-based layer-resolved magnetic imaging techniques with time resolution to study magnetization processes in multilayered magnetic systems on a microscopic length scale. This can be done by photoelectron emission microscopy (PEEM) or magnetic transmission X-ray microscopy in full-field (TXM) or scanning (STXM) mode by utilizing the time structure of synchrotron radiation sources as described above for soft X-ray pump—probe schemes. The results obtained so far are very encouraging since these time-resolved variants of the layer-resolved microscopic techniques overcome the limited spatial resolution of optical magnetic microscopy. Layer-resolved magnetic imaging by interference MOKE, on the other hand, has the prospect of combining the ultrafast laser pulses in the low femtosecond regime that are current state-of-the-art in the field of ultrafast laser technology with layer-resolved magnetic imaging. Some examples of time- and layer-resolved magnetic imaging using the three different techniques are presented in this book.

Chapters 4 and 5 close with some examples of time- and layer-resolved magnetic domain imaging. Using layer-resolved magnetic imaging for the investigation of fast magnetization reversal processes in multilayered or magnetically coupled systems is attracting more and more interest. One of the challenges for the further development of all kinds of magnetoresistive and spintronic devices will be to understand magnetization dynamics on a fundamental time scale in order to match the required increase in operation speed of applications.

<sup>&</sup>lt;sup>4</sup> Current developments aim to kick the camshaft into a different orbit, which would allow singlebunch experiments in multibunch mode operation of the storage ring (pseudo single bunch). The user would be thus enabled to turn time resolution on and off for his (imaging) experiment.

### 1.2 Approaches to Layer-Resolved Magnetic Imaging

The approaches to layer-resolved magnetic imaging presented in this book are based on various magneto-optical microscopies, and thus make use of the interaction of light with the local magnetization of the specimen. There are, in principle, two interaction mechanisms that can be employed to achieve layer-selectivity:

- In the first, interference effects in layered structures are utilized to enhance or diminish the response from a certain depth of the structure.
- In the second, the different electronic properties of the different layers are utilized in order to selectively address a particular layer and probe its magnetic properties.

### 1.2.1 Interference-Based Approach

The interference-based approach to layer-resolved magnetic imaging uses conventional magneto-optical microscopy. Here the magnetic microstructure is visualized by polarized light in the *visible* frequency range in an optical polarization microscope. To be suited for microscopy, a magneto-optical effect must change the polarization state of light. This applies to four effects: the Faraday and Kerr effects (also known as circular birefringence effects), the Voigt effect (linear birefringence), and the gradient effect (a birefringence that depends on magnetization gradients). Common to all these effects is the generation of a magnetization-dependent magneto-optical light amplitude by illumination with plane polarized light. The phenomenology of the effects is introduced in Chap. 2, followed by a description of the microscopic techniques required to transfer them into a domain contrast in Sect. 3.1.

All the aforementioned effects have a certain depth sensitivity. This is trivial for the transmission effects (Faraday and transmission-Voigt effect), which are anyway applied on optically transparent materials such as magnetic garnet films. But also the reflection effects (Kerr, reflection-Voigt, and gradient effect) are depth-sensitive, providing information on the magnetization in a depth range of the order of the penetration depth of light. In case of metallic materials the *information depth* is about 20 nm. Compared to microscopy techniques using electrons or electron tunneling for imaging [like SEMPA (scanning electron microscopy with polarization analysis), SPLEEM (spin polarized low energy electron microscopy), SP-STM (spin-polarized scanning tunneling microscopy), or PEEM (photo-emission electron microscopy)], which exhibit depth sensitivities between one and a dozen atomic layers at the surface, conventional magneto-optical microscopy has in fact to be considered as a

14 1 Introduction

depth-sensitive technique.<sup>5</sup> Within the penetration depth of light, phase differences between the magneto-optical contributions generated in different depths play a decisive role for the magneto-optical image. Usually these phase differences restrict the magneto-optical information depth to a stronger degree than absorption. In multilayer systems, however, the phase differences can be used to provide information on the magnetization of several ferromagnetic layers within the mentioned thickness range. Based on this "phase contrast", magneto-optical microscopy (notably Kerr microscopy) provides the possibility to image individual layers of a multilayer stack, even if the ferromagnetic layers are made of the *same material*. This is a fundamental difference to the second, electronic properties-based approach that relies on X-ray dichroism!

The physical basics of this information depth are described in Sect. 3.2, mainly for microscopy based on the Kerr effect, as this case has been most thoroughly investigated in the literature. Section 3.3 explains how the information depth of Kerr microscopy can be applied to obtain depth-selective information on magnetic domains in multilayer systems. Depth selectivity is achieved either by the phase adjustment of the different, interfering components of the reflected light wave by means of a rotatable compensator (like a quarter wave plate) or by tuning the photon energy or the angle of incidence of light. In this way the total Kerr signal from specific layers in a multilayer stack can be cancelled or enhanced, respectively, leading to images that represent the magnetic domain pattern at different depths of the sample or of different layers. Examples include the domain ground states of differently coupled epitaxial iron films that are interspaced by nonmagnetic layers as well as the switching of magnetic films which is dominated by stray-field interaction with domain walls in neighboring films of sandwich systems. Besides the Kerr effect, also the information depth of the magneto-optical Voigt and Gradient effects can be favorably applied to analyze coupling effects, especially in monocrystalline multilayers as reviewed in

The interference-based technique thus represents a lab-based approach to layer-resolved magnetic microscopy without the need for polarized soft X rays that are generally only available at large-scale facilities such as synchrotron radiation laboratories. In addition, the time resolution of conventional magneto-optical microscopy, if performed with laser illumination, exceeds that of present synchrotron radiation sources by about two orders of magnitude.

<sup>&</sup>lt;sup>5</sup> On the other hand, compared to integral techniques for the measurement of magnetization curves [like VSM (vibrating sample magnetometry) or SQUID (superconducting quantum interferometer device) magnetometry] the magneto-optical effects may be considered as surface-sensitive. As the Kerr effect is routinely used as a magnetization measuring tool particularly for ultrathin films, the acronym "SMOKE" [123–125] for "Surface magneto-optical Kerr effect" has been (somewhat misleadingly) invented for optical magnetometry based on the Kerr effect.

<sup>&</sup>lt;sup>6</sup> There are current developments for lab-based soft X-ray sources, e.g., based on plasma sources and high harmonic generation. However, for the time being, they are not competitive to the brightness, tunability to high photon energies, and polarization of current synchrotron facilities.

An interesting, but different interference-based approach to depth-resolved imaging that is recently being explored relies on the interference of soft X rays. It has been demonstrated that by using a multilayer substrate as a mirror for soft X rays, a vertical X-ray standing wave can be created in a sample deposited on top [126–128]. By tuning the wavelength, the intensity maxima (or nodes) can be moved to different depths of the sample, which may be used for depth-resolved imaging [129, 130]. So far, layer-resolved magnetic imaging using that technique has not yet been realized.

### 1.2.2 Electronic Properties-Based Approach

For the electronic properties-based approach to layer-resolved magnetic information, the magnetic effects in resonant X-ray absorption spectroscopy are most convenient to use. These effects, termed magnetic dichroisms, occur for polarized X rays and are dominantly located in the vicinity of elemental absorption lines. Hence, any technique based on these effects exhibits an inherent elemental specificity. These lines correspond to the resonant excitation of core electrons by X rays into unoccupied electronic states. Particularly in the soft X-ray regime (200 eV–2 keV), i.e., for the L edges of transition metals and the M edges of rare-earth elements, the XMCD effects are very large (up to tens of percent), whereas in the hard X-ray regime (>2 keV) the XMCD effect is typically weak, generally in the sub-percent range. The use of these effects requires the possibility for tuning the X-ray photon energy. With the increasing availability of high-quality synchrotron radiation sources worldwide, however, this demand nowadays is not too difficult to be satisfied. The element selectivity of this spectroscopic contrast mechanism can be directly turned into layer selectivity provided that different magnetic layers contain different elements.

Magnetic dichroism techniques require polarized X rays, which, however, are easily available at synchrotron sources by either using the radiation emitted offorbit at a bending magnet or by utilizing special insertion devices such as helical undulators. With regard to spatial resolution, X-ray based microscopies are advantageous. Compared to visible light microscopes, their shorter wavelength<sup>7</sup> pushes the diffraction-limited spatial resolution deep into the sub-10-nm regime. State-of-theart X-ray microscopies have demonstrated spatial resolutions approaching the range of 10 nm and below [131].

There are two ways for detecting the X-ray absorption. One can either detect X-ray absorption by measuring the amount of emitted electrons at the sample surface, or by measuring the transmitted intensity of X rays after transfer through the sample. In laterally integrating experiments the former is usually termed "total electron yield" detection of X-ray absorption. The latter is a more direct way of measuring the absorption. The limited penetration depth of soft X rays of about 100–200 nm requires sufficiently thin specimens, but also matches the maximum thickness of interest in

<sup>&</sup>lt;sup>7</sup> With  $\lambda$ [nm]  $\approx 1.24/E$ [keV] soft X rays have wavelengths of a few nanometers.

1 Introduction

layered systems. Although the penetration depth for hard X rays reaches into the micrometer regime, the fact that the XMCD effects are very weak has so far prevented any significant utilization of hard X rays for magnetic X-ray microscopies.

In imaging experiments these two approaches are realized by combining resonant excitation by polarized X rays and existing X-ray microscopy techniques. A photoelectron emission microscope (PEEM) can be used to create a magnified image of the sample from the emitted electrons at the surface after photon absorption. Complementary to that, in transmission X-ray microscopy (TXM),<sup>8</sup> an image of the bulk properties of the sample is obtained from the different local transmission of X rays. This information is integrated along the photon beam, but laterally depends on the local sample magnetization direction if circularly polarized X rays are used and tuned to element specific absorption edges. These two basic approaches are explained and described in Chaps. 4 and 5.

Chapter 4 first describes the use of a photoelectron emission microscope for the imaging of magnetic domains in layered systems by using X-ray magnetic circular dichroism (XMCD). Presented examples include the study of magnetic interlayer exchange coupling in trilayered systems in which two ferromagnetic layers are separated by a non-magnetic spacer layer, the observation of transitions between collinear and non-collinear magnetic configurations in such trilayers, and the identification and quantification of micromagnetic coupling mechanisms mediated by the local magnetostatic stray fields from domain walls. A separate section describes layerresolved imaging of antiferromagnetic materials in contact with ferromagnetic films by PEEM. The use of linear magnetic dichroism, as explained in Sect. 2.7.1, as a magnetic contrast mechanism for the imaging of domains in antiferromagnetic materials is explained. Examples of studies of the antiferromagnetic domain structure using linearly polarized synchrotron radiation are presented. By combining linear and circular dichroism, the correlation between the domain structure in the ferromagnet and in the antiferromagnet can be directly imaged and the coupling in combined ferromagnetic/antiferromagnetic systems can be studied.

In Chap. 5 the imaging of magnetic domains by magnetic transmission soft X-ray microscopy (M-TXM), which in contrast to the surface sensitivity of PEEM probes the volume magnetization in layered structures, is presented and reviewed. The strength of this technique is the high lateral resolution provided by Fresnel zone plates used as X-ray optical elements and the applicability of external magnetic fields during the image recording process, which allows detailed studies of magnetization reversal processes in layered systems. Layer sensitivity can be obtained both by the element-specific magnetic XMCD contrast mechanism and the different response of the magnetic domains to applied external fields. Presented examples include the layer-resolved imaging of magnetic domains in technologically relevant magnetically coupled systems and laterally patterned magnetic multilayers.

<sup>&</sup>lt;sup>8</sup> The acronym TXM was chosen in analogy to TEM (transmission electron microscopy) to emphasize the fundamental difference of these two high-resolution microscopy techniques, i.e., electron versus X rays.

Before we turn to the different variants for layer-resolved magnetic imaging, Chap. 2 first introduces the basics of magneto-optic effects which affect the transmission and reflection in the regime of visible light as well as the absorption of soft X rays in the vicinity of elemental absorption edges. Magneto-optic effects in both these wavelength regimes constitute the basics of all the magnetic imaging techniques suitable for layer-resolved magnetic imaging discussed in this book.<sup>9</sup>

<sup>&</sup>lt;sup>9</sup> A further technique, also capable of depth-selective imaging, is not treated in this book: By analyzing the backscattered electrons in a scanning electron microscope, a domain contrast (so-called Type II contrast) from depths of the order of 10 µm can be obtained, depending on the energy of the incident electrons. By tuning the electron energy, domain structures can be scanned at various depths [132, 133].

# **Chapter 2 Magneto-Optical Effects**

In this chapter the magneto-optical effects that are relevant for magnetic microscopy on layered structures are reviewed. This includes the conventional effects which occur at visible light frequencies as well as the X-ray-based effects. Before the phenomenology and physical origin of the different effects is presented, we firstly collect some optical and electromagnetic basics that are relevant for an understanding of the magneto-optical effects.

### 2.1 Overview

Magneto-optics describes the influence of magnetic fields or of a spontaneous magnetization on the emission or propagation of light in matter. The first magneto-optical phenomenon, now known as Faraday effect, was discovered in 1845 by Michael Faraday [134]. He found that the plane of linearly polarized light is rotated after passing through a glass rod in the presence of a magnetic field applied along the light propagation direction. This discovery was the first experimental evidence of the electromagnetic nature of light and played an important role in the development of the electromagnetic light theory. Some thirty years later Kerr [135, 136] discovered the corresponding effect in reflection (magneto-optical Kerr effect) by demonstrating light rotation upon reflection from the surface of iron. Two geometries have been investigated by Kerr: (i) the magnetization being perpendicular to the iron surface (polar Kerr effect [135]) and (ii) the magnetization being parallel to the surface and along the plane of incident light (longitudinal Kerr effect [136]). In 1896, Zeeman [137] proved the existence of a third variant in which the magnetization is in-plane but orthogonal to the plane of incidence (transverse Kerr effect). At that time Zeeman also discovered the splitting of emitted spectral lines of atoms in magnetic fields, now known as the Zeeman effect [138]. This effect has become a very valuable means for determining the structure of atoms, molecules and crystals. An early theoretical understanding of the Faraday and Kerr effect was proposed by Lorentz [139] in 1884, based on the idea that right- and left-circularly polarized light couples differently to classical electron oscillators in the material. For this reason the Kerr- and

Faraday effects are also known as circular birefringence effect (i.e. a birefringence of circularly polarized light—note that a plane polarized wave may be seen as being composed of two circularly polarized waves of opposite rotation sense). Further relevant discoveries were the occurrence of magnetic double refraction in vapor by Voigt [140] in 1898 and in paramagnetic liquids by Cotton and Mouton [141] in 1907. These effects are known as linear magnetic birefringence (i.e. a birefringence of linearly polarized light).

Magneto-optical imaging for the visualization of magnetic domains has first been applied in the 1950s by Williams et al. [142] and by Fowler and Fryer [143], all based on the Kerr effect. Since these earliest applications of Kerr microscopy, continuous methodical developments have greatly enhanced the capabilities of the traditional Kerr technique. Significant contrast enhancement was achieved by the application of interference layers [144], but the breakthrough of Kerr microscopy came with the introduction of video microscopy and digital image processing in the 1980s [145, 146]. For Faraday microscopy, which was also applied since the 1950s for transmission experiments mainly on magnetic garnet films [147] and orthoferrites [148], electronic contrast enhancement was not required as the Faraday effect is much stronger than the Kerr effect. The same was true for transmission microscopy based on the Voigt effect that was used for the observation of in-plane domains in garnets [149]. Later the Voigt effect was also discovered in reflection experiments on metals, together with the magneto-optical gradient effect [150] that shows up under similar experimental conditions. The gradient effect is a birefringence effect, which depends linearly on magnetization gradients. Both effects (in combination with the Kerr effect) are helpful in the analysis of domains in epitaxial multilayer systems with cubic magnetic anisotropy by considering the contrast laws and depth sensitivities of the effects [151]. The gradient effect can also favorably be applied to image fine transitions and domain modulations.

The phenomenological differences between Kerr, Voigt and gradient effects are compared in Fig. 2.1, in which a typical domain pattern of an iron-silicon crystal with two orthogonal easy axes of magnetization in the surface was imaged in an optical polarization microscope under different conditions as indicated. In each case a contrast was generated by choosing appropriate incidence of light and by properly setting the polarizer, analyser, and compensator in the microscope. The Kerr effect is linear in the magnetization vector, so the four domain phases in Fig. 2.1 show up in different colors. The same pattern imaged in the Voigt effect displays only two colors, one for each magnetization axis. This contrast is independent of the magnetization direction since the Voigt effect depends quadratically on the magnetization vector. The gradient effect is sensitive to changes in magnetization. Therefore domain boundaries show up in this effect with a contrast depending on the relative magnetization directions of the neighboring domains. Both, Voigt and gradient effects are strongest at perpendicular incidence of light (where a Faraday or Kerr contrast of in-plane domains is not possible), and they require a compensator (e.g. a rotatable quarter wave plate) for contrast adjustment.

All magneto-optical phenomena described so far are based on the interaction of light with magnetization in the *visible* frequency range. We therefore call the

2.1 Overview 21

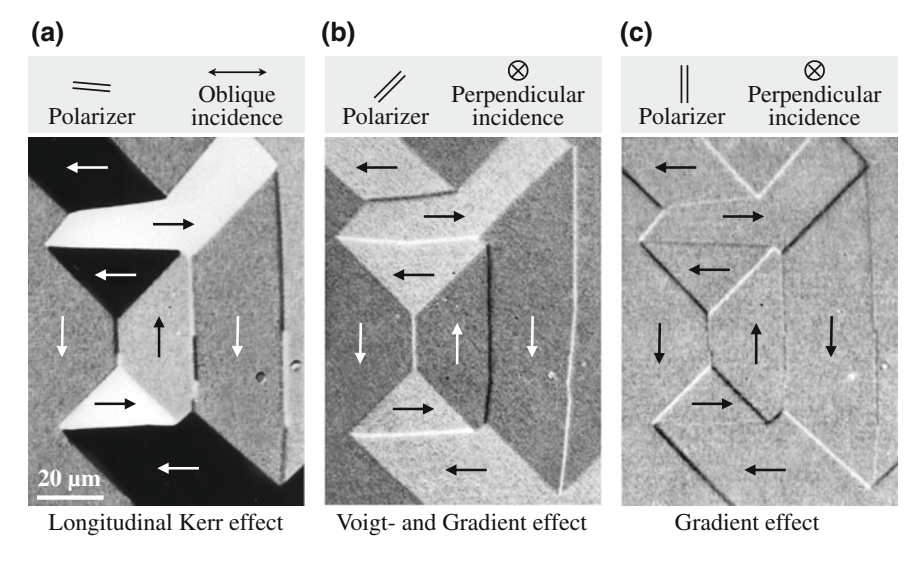


Fig. 2.1 Domains on a (100) surface of silicon-iron (Fe 3 wt% Si, a sheet of  $500\,\mu m$  thickness used as electrical steel), imaged using **a** the magneto-optical Kerr effect, **b** the Voigt and gradient effects, **c** the gradient effect [150]. Indicated is the polarizer setting, defining the polarization direction of the illuminating light, and the plane of incidence in case of the (longitudinal) Kerr effect. The local magnetization direction of each domain is represented by *arrows*. Images (**a**) and (**c**) show identical domain patterns, whereas a similar domain state was imaged in (**b**)

Kerr-, Voigt- and gradient effects conventional magneto-optic effects in the following. Effects analogous to the conventional effects also exist at shorter, X-ray wavelengths. The exploration of X-ray magneto-optical effects is a much younger field of science. While the effects can be much larger in the soft X-ray range [152] due to the resonant enhancement occurring close to absorption edges, the detection of the polarization state of reflected or transmitted X rays is more involved. Polarization analysis of the X rays after interaction with the sample for the detection of the X-ray Faraday effect [153–155], the longitudinal Kerr effect [156], the Voigt effect in transmission [157] or reflection [158] requires a sophisticated reflectometer set [159, 160]. This is the reason that in connection with X rays mostly intensity measurements are performed rather than polarization analysis, i.e., the absorption coefficient or the intensity of reflection are measured. Close to elemental absorption edges, the magneto-optical effects are large enough to lead to sizable changes in the absorption and reflection. In particular the lateral modulation of the local X-ray absorption can be applied for magnetic microscopy, as will be described in Chaps. 4 and 5. Layer resolution in soft X-ray absorption is achieved simply by the element-specificity of the binding energies of the electronic core levels. The magneto-optical effects in X-ray absorption are the X-ray magnetic linear dichroism (XMLD) and the X-ray magnetic circular dichroism (XMCD), categorized according to the polarization of the incoming X rays. They will be explained in Sects. 2.7.1 and 2.7.3, respectively, before some

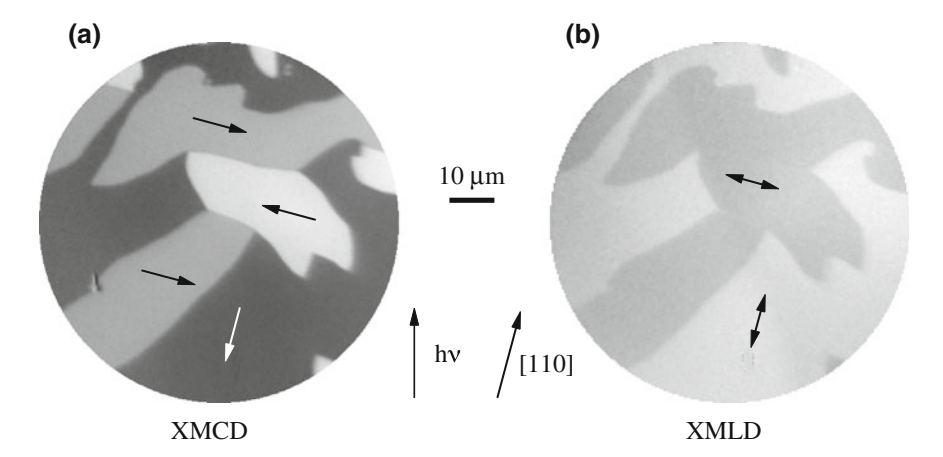


Fig. 2.2 Domains on a thin metallic Co film on the (001) surface of Cu, imaged by using **a** the X-ray magnetic circular dichroism and **b** the X-ray magnetic linear dichroism in the absorption of soft X rays at the Co  $L_3$  absorption edge in a photoelectron emission microscope (PEEM). The *arrow* labelled "hv" indicates the azimuthal direction of the incoming X rays, the *arrow* labelled "[110]" shows the crystallographic orientation of the Cu(001) substrate, while *arrows* in the images show the local magnetization directions in the domains. From [114]

quantitative considerations concerning the size of the respective magnetic contrast in different types of layered samples are discussed. It will be shown for which samples the two complementary methods of utilizing these magnetic contrast mechanisms in soft X-ray absorption, the yield of electrons emitted from the sample surface on the one hand and the intensity of transmitted X rays on the other hand, are suited best.

Figure 2.2 shows, in analogy to Fig. 2.1, the example of a magnetic domain pattern imaged by the two effects using the resonant absorption at the Co  $L_3$  absorption edge [161]. Here the sample was a thin cobalt film on copper. In panel (a), circularly polarized X rays were used, while panel (b) shows the result of the absorption of linearly polarized X rays at the same position of the sample. Like in Fig. 2.1a, b, the circular dichroism in panel (a) results in a contrast depending linearly on the cosine of the angle between the incident photons and the local magnetization direction, while the linear dichroism in panel (b) delivers a contrast proportional to the square of the cosine.

In the remainder of this book we will concentrate on the effects of a sample magnetization on the polarization of transmitted or reflected photons in the regime of visible light (called conventional magneto-optical effects), and on the effect of the absorption of photons in the regime of soft X rays (called magnetic dichroisms in the absorption of soft X rays), since these are the two classes of magneto-optical effects relevant for magnetic imaging. We will first discuss the basics of conventional magneto-optics, and come back to the X-ray dichroism effects in Sect. 2.7.

### 2.2 Optical Basics of Conventional Effects

To apply the conventional magneto-optical effects that are relevant for microscopy, linearly polarized light is used for illumination, which is then (in general) transformed to elliptically polarized light due to the magneto-optical interaction in the magnetic specimen. For a phenomenological description of the effects we therefore need an adequate description of different polarization states of light and how they change upon transmission or reflection. The coordinate systems used in this chapter for the definition of reflected and transmitted polarized light are introduced in Fig. 2.3a, together with an illustration of the sign convention in magneto-optics in Fig. 2.3b. This convention was proposed by Atkinson and Lissberger [162], and we will follow it throughout the chapter when discussing magneto-optics.

In this section some basics of optical phenomena are collected that are relevant for an understanding of the magneto-optical effects. Like many other optical properties of solids (e.g. selective absorption, double refraction, dispersion etc.), they can be treated within the framework of electrodynamic theory. We therefore start by briefly reviewing Maxwell's equations together with the relevant material equations and applying them to the propagation of light through solids. Following is a review on polarization optics, including the effects of birefringence, dichroism and optical activity. Magneto-optical effects represent special cases of optical activity, and they can be interpreted as birefringence or dichroism. Also the basic optical tool in depth-selective (conventional) magneto-optical microscopy, the compensator, is based on birefringence. We will furthermore recapitulate some basics of reflection and refraction, introducing Snell's law and Fresnel's formulas, which describe the behavior of light when it propagates between media of differing refractive indices. These equations will later be needed in the discussion of depth sensitivity in multilayers. For details we refer to textbooks on optics, e.g. [163–166].

### 2.2.1 Wave Equation

Conventional magneto-optical microscopy is applied to both, insulating materials like garnet films or ferrite samples as well as to metallic samples. In thin film systems, dielectric and metallic films may be stacked together. We therefore have to develop an understanding of the propagation of light in both types of media. Light propagation in matter, including the processes of transmission, reflection, and refraction, can be classically interpreted by scattering events on a submicroscopic level, in particular by the absorption and prompt re-emission of electromagnetic radiation by the electrons associated with atoms and molecules. In nonconducting, dielectric media (like glass) a polarization is constituted by the displacement of elastically bound electrons, which

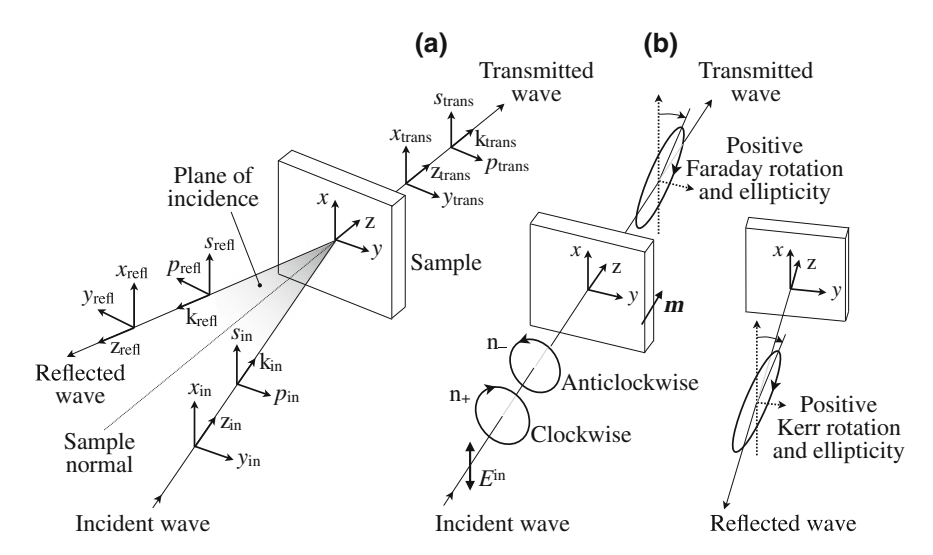


Fig. 2.3 a Definition of the coordinate systems used for the description of polarized light. The sample is defined by the right-handed cartesian (x, y, z)-system, in which the z-direction is the normal to the sample surface. Incident, reflected and transmitted light is defined by the righthanded (s, p, k)- or (x, y, z)-cartesian systems, where the direction of the light propagation is given by the wave vector direction k, z. The p-direction is in the plane of incidence (defined by the sample normal and the wave vector of obliquely incident light), the s-direction is perpendicular to the plane of incidence along x. b Illustration of the senses of rotation and ellipticity for both, Faraday and Kerr effect, according to Atkinson and Lissberger's sign convention (after [162]). Polar magnetization along the z-axis is assumed and the time-dependent part of the wave function is expressed by  $\exp(-i\omega t)$  in this scheme. The rotation senses of the propagating circularly polarized modes are defined with respect to their associated refractive indices:  $n_+(n_-)$  represents clockwise (anticlockwise) rotation of the E-vector looking along the sample's positive z-direction and the direction of magnetization m. The Faraday- and Kerr rotations are positive for a clockwise rotation of the polarization ellipse viewed along the positive z-direction. Likewise, the sign of the Faraday and Kerr ellipticity is positive for a clockwise rotation of the E-vector viewed along the positive z-direction. Note in advance: In the traditional convention on polarization that is used in general optics and which is based on the (x, y, z)-coordinate systems of incident, transmitted and reflected waves of (a), the illustrated Faraday ellipses would have a positive rotation but negative ellipticity, whereas the illustrated Kerr ellipse would have a negative rotation and positive ellipticity (compare Fig. 2.4)

are driven into oscillations by the oscillating electromagnetic field E of the light. Since the field within the material has been altered by the created dipoles, it is defined by a new field quantity, the displacement D. We will see below that in isotropic media D and E are related by a scalar quantity, i.e. they are always parallel. In anisotropic materials, however, they are related by a tensor so that their directions may deviate.

 $<sup>^{1}</sup>$  In the classical oscillator model, this deviation can be readily understood: due to the anisotropy of the binding forces, the charge will be displaced in the direction of the weakest restraint for a given force component and not in the direction of E which drives the charge. The field, induced in the material, will thus be oriented differently from E [166].

By treating the bound electrons as classical damped harmonic oscillators, phenomena like dispersion (the frequency dependence of the refraction index) can be derived (see, e.g., [163, 166]). Metals, on the other hand, are characterized by the presence of 'unbound' electrons, which are able to circulate within the material. The electron motion, driven by the electrical field E of the light, constitutes a circulating current, the density of which, j, is related to the electrical conductivity  $\sigma$  of the medium by Ohm's law ( $j = \sigma E$ ). In a "perfect" conductor with an assumed infinite conductivity, the electron oscillations would simply follow the field's alternations. There would be no restoring force and no absorption, the incoming light would be totally re-emitted by the vibrating oscillators. Real metals, however, are resistive and light will be converted to thermal energy, i.e it suffers a progressive attenuation (absorption) as it propagates through the medium with the strength of absorption depending on the electrical conductivity. Strong absorption is accompanied by high reflectivity, so that metallic surfaces act as excellent mirrors at the same time. We will see below that absorption can be treated by the introduction of a complex index of refraction.

A powerful approach to the propagation of electromagnetic fields in continua, which provides a far more complete description than scattering theory, is provided by electrodynamic theory. In this *phenomenological* theory, the fields, current and charge densities are macroscopically averaged to avoid the drastic changes of these quantities that occur on an atomistic scale. Starting point are the Maxwell equations:

$$\operatorname{div} \boldsymbol{D} = \nabla \cdot \boldsymbol{D} = \rho \tag{2.1a}$$

$$\operatorname{div} \mathbf{B} = \nabla \cdot \mathbf{B} = 0 \tag{2.1b}$$

$$rot \mathbf{E} = \nabla \times \mathbf{E} = -\dot{\mathbf{B}} \tag{2.1c}$$

$$rot \mathbf{H} = \nabla \times \mathbf{H} = \mathbf{j} + \dot{\mathbf{D}}, \tag{2.1d}$$

which connect the macroscopic electric and magnetic fields with each other. In these equations, E and H are the electric and magnetic field vector, respectively, and B is the vector of magnetic flux density or induction. The quantities  $\rho$  and  $\mathbf{j}$  are the electric charge and current density, respectively, which may be considered as the sources of the fields  $\mathbf{D}$  and  $\mathbf{H}$ . Non-zero solutions of Maxwell's equations also do exist if  $\rho$  and  $\mathbf{j}$  are set zero. Electromagnetic radiation can thus propagate also in regions of space where charges and currents are absent. Such electromagnetic fields are called electromagnetic wave. With the identity  $\operatorname{div}(\operatorname{rot} \mathbf{H}) = 0$ , the continuity equation

$$\operatorname{div} \mathbf{j} + \operatorname{div} \dot{\mathbf{D}} = \operatorname{div} \mathbf{j} + \frac{\partial}{\partial t} (\operatorname{div} \mathbf{D}) = \operatorname{div} \mathbf{j} + \dot{\rho} = 0$$
 (2.2a)

can be derived from (2.1a) and (2.1d). It describes the conservation of charge. In the following discussion we will exclude currents and external charges, we thus assume electrically neutral media. Then only the fields of the light wave can generate currents and charge-density fluctuations.

The field equations (2.1a–2.1d) are linked by material-specific relations between D and E, H and B, and between j and E. In the range of optical frequencies and conventional light intensities, local linear relations do apply, which are described by locally- and time-independent tensors  $\epsilon$ ,  $\mu$ , and  $\sigma$ :

$$\mathbf{D} = \epsilon_0 \mathbf{\epsilon} \mathbf{E} = \epsilon_0 \mathbf{E} + \mathbf{P} \tag{2.3a}$$

$$\mathbf{B} = \mu_0 \boldsymbol{\mu} \mathbf{H} = \mu_0 (\mathbf{H} + \mathbf{M}) \tag{2.3b}$$

$$j = \sigma E. \tag{2.3c}$$

Here P is the dipolar polarization per unit volume that is produced by the perturbation of the electron motion due to the presence of the electromagnetic field in matter, and M is the magnetization. The dielectric constant and permeability of vacuum,  $\epsilon_0$  and  $\mu_0$  respectively, are connected to the speed of light in vacuum,  $c_0$ , by

$$c_0 = 1/\sqrt{\epsilon_0 \mu_0}. (2.4)$$

The  $\epsilon$ ,  $\mu$ , and  $\sigma$  tensors are of rank two and known as dielectric- (or permittivity-), permeability- and conductivity tensors, respectively. While the dielectric tensor,  $\epsilon$ , is strongly frequency dependent in the visible light range, one may assume  $\mu=1$  at optical and near infrared frequencies<sup>2</sup> [167, 168]. All material-specific properties like absorption, dispersion, optical anisotropy, or optical activity, and also the magneto-optical effects are therefore incorporated in the  $\epsilon$ -tensor. According to (2.3a), it connects the electric vector E of the illuminating plane light wave with the induced dielectric displacement vector D. We will present this tensor for the magneto-optical Faraday, Kerr, and Voigt effects in Sect. 2.3.1. In isotropic media all tensors reduce to scalars.

With the material and Maxwell equations a general *wave equation* for the E field is obtained by taking the curl of (2.1c), the time derivative of (2.1d) and by eliminating H [163, 166, 169]:

$$\nabla \times (\nabla \times \mathbf{E}) = \nabla \times (-\dot{\mathbf{B}}) = -\mu_0 \mu (\nabla \times \dot{\mathbf{H}})$$
$$= -\mu_0 \mu \frac{\partial}{\partial t} (\dot{\mathbf{j}} + \dot{\mathbf{D}}) = -\mu_0 \mu (\sigma \frac{\partial \mathbf{E}}{\partial t} + \epsilon_0 \epsilon \frac{\partial^2 \mathbf{E}}{\partial t^2}). \tag{2.5}$$

In the case of dielectric media the term proportional to  $\epsilon$  is of importance, whereas for conducting materials the term proportional to  $\sigma$  becomes significant. The vector triple product in (2.5) can be simplified by using the operator identity  $\nabla \times (\nabla \times E) = \nabla(\nabla \cdot E) - (\nabla \cdot \nabla)E$ , arriving at the wave equation:

$$\nabla(\nabla \cdot \mathbf{E}) - \nabla^2 \mathbf{E} + \mu_0 \mu (\sigma \frac{\partial \mathbf{E}}{\partial t} + \epsilon_0 \epsilon \frac{\partial^2 \mathbf{E}}{\partial t^2}) = 0.$$
 (2.6)

 $<sup>^2</sup>$  The reason is that the Larmor-precession (<100 GHz) of the atomic moments cannot follow the high frequencies of the magnetic light vector, i.e. at optical frequencies the spins are too 'slow' to follow the alternating magnetic field of the electromagnetic wave.

The wave equation can be solved by assuming a (homogeneous) plane wave<sup>3</sup> solution for the electromagnetic wave, which is harmonic both in time, t, and position, r:

$$E = E^{0} \exp[i(\mathbf{k} \cdot \mathbf{r} - \omega t)]. \tag{2.7}$$

The frequency of light and the amplitude of the electric field are represented by  $\omega$  and  $E^0$ , respectively. The propagation vector  $\mathbf{k}$  defines the direction of the planes of constant phase for the light wave. The phase notation  $(\mathbf{k} \cdot \mathbf{r} - \omega t)$  with positive spatial-dependent and negative time-dependent parts represents a wave that propagates in the direction of the wave vector with a positive phase velocity. Due to the relations given above, also the fields  $\mathbf{D}$  and  $\mathbf{B}$  are described by plane waves.

The magnitude  $|\mathbf{k}|$ , the wave propagation number, is connected to the index of refraction n by

$$|\mathbf{k}| = n \, k_0 \tag{2.8}$$

with

$$k_0 = \omega/c_0 = 2\pi/\lambda_0.$$
 (2.9)

Here  $k_0$  is the wave propagation number in vacuum with  $\lambda_0$  being the vacuum wavelength of the (assumed) monochromatic, illuminating light. Analogous to (2.9), the wave propagation number in any material is described by  $|\mathbf{k}| = \omega/v$  where v is the speed of the light in the medium, which in general is different from that in vacuum. With (2.8) the wave velocity v is given by

$$v = -\frac{1}{n}c_0. {(2.10)}$$

The refraction index obviously describes the fact that the apparent wave velocity of light is different in different materials.

Absorption in conductive media is, as mentioned, formally expressed by considering a complex index of refraction in the electrodynamics theory. To recognize the relevance of complex quantities for the wave propagation, it is advantageous to rewrite the wave equation. With the ansatz (2.7) the differential operators can be replaced by algebraic functions:  $\nabla \cdot \Rightarrow i k \cdot , \nabla \times \Rightarrow i k \times \text{ and } \frac{\partial}{\partial t} \Rightarrow -i \omega$ , so that the Maxwell equations are simplified to a set of algebraic amplitude equations:

<sup>&</sup>lt;sup>3</sup> For linearly- (or plane-) polarized light the orientation of the electric field is constant, while its magnitude and sign vary in time.

$$\mathbf{k} \cdot \mathbf{D} = -\mathrm{i}\rho \tag{2.11a}$$

$$\mathbf{k} \cdot \mathbf{B} = 0 \tag{2.11b}$$

$$\boldsymbol{k} \times \boldsymbol{E} = \omega \boldsymbol{B} \tag{2.11c}$$

$$\mathbf{k} \times \mathbf{H} = -i\mathbf{j} - \omega \mathbf{D} = -\omega \epsilon_0 (\mathbf{\epsilon} + \frac{i\mathbf{\sigma}}{\epsilon_0 \omega}) \mathbf{E}.$$
 (2.11d)

With Ohm's law (2.3c) and the continuity equation (2.2a), now written as  $k \cdot j - \omega \rho = 0$ , (2.11a) can be transformed to

$$\mathbf{k} \cdot \epsilon_0 (\mathbf{\epsilon} + \frac{\mathrm{i}\sigma}{\epsilon_0 \omega}) \mathbf{E} = \mathbf{k} \cdot \epsilon_0 \tilde{\mathbf{\epsilon}} \mathbf{E} = \mathbf{k} \cdot \tilde{\mathbf{D}} = 0.$$
 (2.12)

The term

$$\epsilon + i\sigma/(\epsilon_0 \omega) = \widetilde{\epsilon} \tag{2.13}$$

represents an effective *complex* permittivity that consists of the true permittivity  $\epsilon$  and the conductivity  $\sigma$ . The imaginary part of  $\tilde{\epsilon}$  corresponds to the real part of  $\sigma$ . By the algebraic connections also the other quantities (like the dielectric displacement  $\tilde{D}$  and propagation vector  $\tilde{k}$ ) become complex in case of absorbing (i.e. electrically conductive) materials. Thus

$$\widetilde{k} = k' + ik'', \tag{2.14}$$

where k' and k'' are real vectors.

With the algebraic functions, the wave equation (2.6) can be re-written as

$$(\widetilde{k} \cdot E)\widetilde{k} - \widetilde{k}^2 E + \mu_0 \epsilon_0 \mu \omega^2 \widetilde{\epsilon} E = 0.$$
 (2.15)

Here  $\tilde{k}^2 = \tilde{k} \cdot \tilde{k}$  is a dyadic product, i.e. a tensor with the components  $k_i k_j$ . By setting  $\mu = 1$ , which is justified as mentioned, and with (2.9), (2.15) can then be further simplified and written as a system of three linear equations for the three vector components  $E_i$  of the E-field amplitude:

$$\widetilde{k}_{i}(\widetilde{k} \cdot E) - \widetilde{k}^{2} E_{i} + \sum_{j=1}^{3} k_{0}^{2} \widetilde{\epsilon}_{ij} E_{j} = 0.$$
(2.16)

With the now complex index of refraction [see (2.8)]

$$\widetilde{n} = |\widetilde{k}|/k_0 = \sqrt{\widetilde{k} \cdot \widetilde{k}}/k_0, \tag{2.17}$$

(2.16) becomes [170, 171]

$$\frac{\widetilde{k}_{i}(\widetilde{k} \cdot E)}{k_{0}^{2}} - \widetilde{n}^{2}E_{i} + \sum_{i=1}^{3} \widetilde{\epsilon}_{ij} E_{j} = 0.$$
(2.18)

The non-trivial solutions for E to this system of linear equations, the so-called *eigenmodes*, describe the propagable light waves in the medium. In order to find them, the determinant of the corresponding coefficient matrix must vanish. Under this condition a characteristic equation for the components  $k_i$  of the wave vector  $\tilde{k}$  as a function of the elements of the dielectric tensor is obtained. Once these  $k_i$ , and with them the "allowed" propagation directions are determined, the electrical amplitudes of the propagable waves are obtained as solutions of (2.18). The directional dependence of the refractive index on the real and imaginary parts of the wave vector leads to rather annoying algebraic problems when one considers light incidence obliquely on the surface of the medium. For perpendicular incidence, however, solutions of the wave equation can be easily obtained. We will present them in Sect. 2.3 for the examples of the polar Faraday effect and the Voigt effect by considering the proper magneto-optical dielectric tensors. When the electrical amplitudes of the propagable waves are known, their magnetic amplitudes are readily given by

$$\omega \,\mu_0 \,\mathbf{H} = (\widetilde{\mathbf{k}} \times \mathbf{E}). \tag{2.19}$$

Now back to the complex refractive index and its connection to absorption. In complex notation the index is written as

$$\widetilde{n} = n' + in'', \tag{2.20}$$

where n' and n'' are real numbers. The real part of the refractive index is the true refractive index and the imaginary part is the so-called *extinction coefficient*. This can be seen by entering (2.20) into the plane wave equation (2.7). With (2.9) and (2.17) the plane wave (2.7) is expressed by

$$E = E^{0} e^{i[\frac{\omega}{c_0}(n' + in'')z - \omega t]} = E^{0} e^{-\frac{\omega}{c_0}n''z} e^{i[\frac{\omega}{c_0}n'z - \omega t]}.$$
 (2.21)

The wave advances in the z-direction with a speed  $c_0/n'$ , precisely as if n' were the usual index of refraction. As the wave progresses into the conductor, its amplitude,  $E^0 exp(-\omega n''z/c_0)$ , is exponentially attenuated, i.e. the energy of the wave is absorbed by the medium. Remember that the damping is physically related to the electrical currents that are caused by the E-vector of the light in conducting media. The *irradiance*, i.e. the power of electromagnetic radiation per unit area (radiative flux), which is proportional to the square of the amplitude, is then given by

$$I(r) = I_0 e^{-\alpha z} \tag{2.22}$$

where  $I_0$  is the irradiance at the surface of the metal and

$$\alpha = 2\omega n''/c_0 \tag{2.23}$$

is called the absorption or attenuation coefficient that describes an exponential damping of the propagating wave. The flux density thus drops by a factor of  $e^{-1} \approx 1/3$  after the wave has propagated a distance of  $1/\alpha$ . This distance is known as the *skin or penetration depth*. To be transparent, a material has to be thinner than the penetration depth. For metals, the penetration depth is exceedingly small. Copper, for example, has a skin depth that varies between 0.6 nm and 6 nm for ultraviolet and infrared wavelengths, respectively. This accounts for the generally observed opacity of metals. The familiar metallic sheen corresponds to a high reflectance, which exists because the incident wave cannot effectively penetrate the material. The limited penetration depth in metals is nonetheless sufficient to obtain depth-sensitive magnetic information in metallic thin film systems as elaborated in detail in Sect. 3.2.

The particularly attractive feature of the electromagnetic theory is that all the derived formulae are valid for both, transparent (dielectric) media as well as absorbing (conductive) materials. The existence of conductivity is taken into account simply by introducing a complex dielectric constant and refraction index, instead of real ones. By the connecting relations presented above, also the wave vector and the field terms then become complex. If the conductivity tensor is set zero and if no external charges  $\rho$  and currents j are admitted, then no imaginary parts appear in the equations and all terms are real. This is the case for non-absorbing media. In the following we will always assume the general case of complex variables and we will not explicitly print the tilde for  $\epsilon$ , k and n.

## 2.2.2 Polarized Light

In the previous section we have seen that light may be treated as a transverse electromagnetic wave, which is described by an electrical field E and a magnetic field H. Both vectors are related by Maxwell equations (2.1a–2.1d), they are mutually perpendicular to each other and also perpendicular to the direction of the wave's motion which is represented by the propagation vector E. As the electrical field acts much stronger with matter than the magnetic field, the polarization direction of the light wave is conventionally described by its E-vector (or—in anisotropic media—by the vector of dielectric displacement E). Due to the transverse nature of the wave, the variation of the electric field vector is confined in a plane perpendicular to E. It can thus be expressed in a 2D-basis with the E-and E-directions (defined in Fig. 2.3a) as unit vectors. If we assume that the light is propagating in E-direction, the E-vector will thus lie on the E-plane. In complex function representation, the time and spatial dependences of the E-and E-components of this wave's E-vector are generally expressed by

$$E_{j}(z,t) = \operatorname{Re}(\boldsymbol{e}_{j}E_{j}^{0} \exp[\mathrm{i}(\boldsymbol{k}_{z}z - \omega t)]),$$
with  $E_{j}^{0} = E_{j}^{\max} \exp[\mathrm{i}\delta_{j}]$  and  $j = \{x, y\}.$  (2.24)

In (2.24) the real part of the complex function (2.7) is taken, which describes the measurable component of the electric field, where  $e_x$  and  $e_y$  are the unit vectors along the positive x- and y-axes, respectively. The maximum amplitudes of the electric field components in x- and y-directions,  $E_j^{\max}$ , have phase retardations  $\delta_j$  (defined for t, z = 0).

As illustrated in Fig. 2.4a, the wave described by (2.24) consists of two linearly polarized partial waves, the vibration directions of which are along the x- and y-directions and which are shifted in phase in the most general case. The end point of the E-vector describes an elliptic trajectory as time evolves. In the xy-plane this trajectory traces out the so-called polarization ellipse which fully specifies the

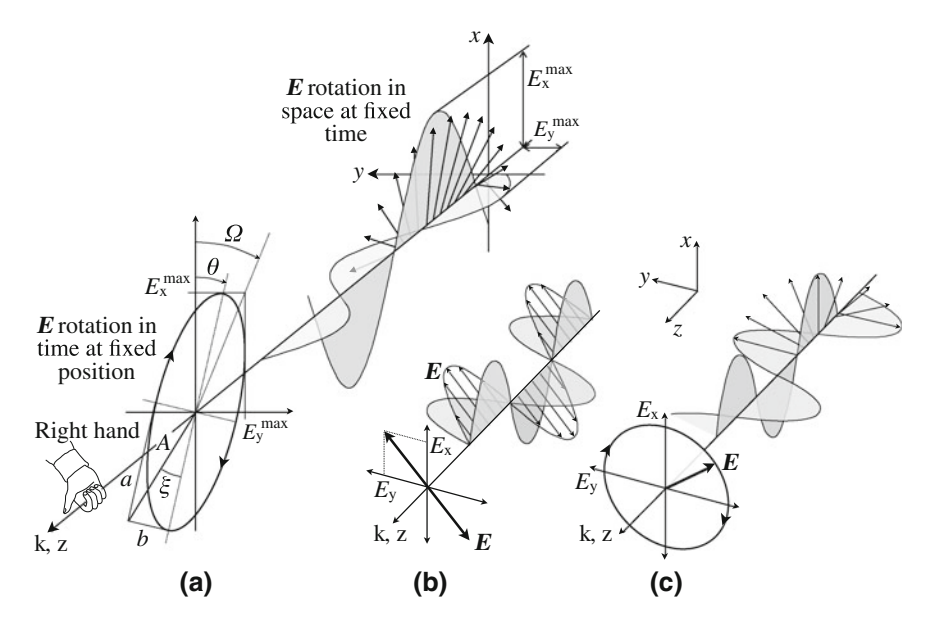


Fig. 2.4 a Visualization of (right-handed) elliptically polarized light as being generated by the phase-shifted superposition of two partial waves polarized in the (x, z)- and (y, z)-planes. Shown is the spatial and time evolution of the electric field vector E. The presented polarization ellipse has a negative azimuth  $\theta$  and a positive ellipticity  $\xi$  according to traditional convention in optics (note that the ellipse would have a positive azimuth in the Atkinson and Lissberger convention because there it would be related to the (x, y, z)-coordinate system of the *sample*, compare Fig. 2.3b). **b** Plane-polarized light can be seen as being composed of two orthogonally polarized waves which are in-phase (or phase-shifted by 180°, not shown). **c** A phase shift of 90° between the partial waves generates a circularly polarized wave, which is a special case of elliptically polarized light. The case of right-circularly polarized light is shown and, like in (a), the polarization circle represents the rotation of the E-vector in time at a fixed spatial position

polarization state of the light. Elliptic polarization is characterized by the following quantities:

- The ratio between the maximal values of the electric field in y- and x-directions, expressed by  $\tan \Omega = \left| E_y^{\text{max}} \right| / \left| E_x^{\text{max}} \right|$ .
- The *phase shift* (or phase angle) between the x and y modal amplitudes:

$$\delta = \delta_{\rm v} - \delta_{\rm x}.\tag{2.25}$$

The phase angle is defined in the range  $-\pi < \delta < +\pi$ .

- The *azimuth*  $\theta$ , which is the rotation angle between the major axis of the polarization ellipse and the *x*-direction, defines the orientation of the ellipse in its plane. By traditional convention, a positive azimuth is characterized by a clockwise rotation of the polarization ellipse when looking along the light beam.
- The *ellipticity*  $\xi$  relates the minor and major axes of the ellipse by

$$\tan \xi = b/a. \tag{2.26}$$

For small ellipticity,  $\xi \approx b/a$ . By traditional convention, a positive ellipticity corresponds to a anticlockwise rotation of the *E*-vector when looking along the light beam.

• Related to the ellipticity is the *amplitude* (or 'size') of an elliptical vibration that is defined as

$$A = \sqrt{(a^2 + b^2)}. (2.27)$$

• The "handedness" of the ellipse determines the sense in which the ellipse is described. Close inspection of Fig. 2.4a reveals that the rotation sense of the wave is opposite in space and time. The handedness can be determined by applying the right and left hand rule to the *spatial* motion of *E*: When the thumb of the right hand points in the direction of the wave vector *k*, the *E*-vector rotates in space according to the right hand rule for a right-handed wave (i.e. positive ellipticity). Similarly, the rotation sense in space for a left-handed wave (negative ellipticity) is determined by the left hand rule. Note that this definition of handedness is typically used in the optics community, for further definitions see [172].

The variables  $\xi$ ,  $\theta$ ,  $\Omega$  and  $\delta$  are connected by the following independent relations [164, 173]:

$$\tan 2\theta = (\tan 2\Omega)\cos \delta,\tag{2.28a}$$

$$\sin 2\xi = -(\sin 2\Omega)\sin \delta,\tag{2.28b}$$

$$\tan \Omega e^{i\delta} = \frac{E_y}{E_x} = \frac{\tan \theta - i \tan \xi}{1 + i \tan \theta \tan \xi}.$$
 (2.28c)

Two special cases are of significant importance: If the two orthogonal partial waves are in-phase ( $\delta=m\pi$ , with m=0, 1 and  $-\pi<\delta<\pi$ ), the ratio of the strengths of the two components is constant and so the direction of the electric vector (the vector sum of these two components) is constant. The polarization ellipse then degenerates into a straight line and the resulting wave is *linearly* polarized with its vibration direction rotated depending on the relative amplitudes of the two components. For partial waves with equal amplitudes, the polarization plane is rotated by 45° against the x- and y-axes as illustrated in Fig. 2.4b. Here the two partial waves are in-phase, whereas a phase shift of 180° would result in a linearly polarized wave that is rotated by 90° compared to the shown case.

The other special case is that of *circularly* polarized light: the ellipse reduces to a circle if the partial waves have equal amplitudes ( $E^0 = E_x^{\rm max} = E_y^{\rm max}$ ) and are shifted in phase by  $\delta = \pm \pi/2$ . In this case one component is zero when the other is at maximum or minimum amplitude. There are two possible phase relationships that satisfy this requirement: the *y*-component can be ninety degrees ahead ( $\delta = -\pi/2$ ) or ninety degrees behind ( $\delta = +\pi/2$ ) the *x*-component. The case of  $\delta = -\pi/2$ , which corresponds to right-handed circularly polarized light according to traditional convention, is illustrated in Fig. 2.4c. The electric field of a circularly polarized wave, propagating along the positive *z*-direction, can be written in complex form as

$$E_{\pm}(z,t) = \frac{1}{\sqrt{2}} \left[ e_{x} E^{0} e^{i(k_{z}z - \omega t)} + e_{y} E^{0} e^{i(k_{z}z - \omega t \pm \pi/2)} \right], \tag{2.29}$$

or, by employing the identity  $e^{i\pi/2} = i$ , as

$$\boldsymbol{E}_{\pm}(z,t) = \frac{1}{\sqrt{2}} E^{0} (\boldsymbol{e}_{x} \pm i \boldsymbol{e}_{y}) e^{i(\boldsymbol{k}_{z}z - \omega t)}. \tag{2.30}$$

The normalization factor  $1/\sqrt{2}$  is explained below. If the wave is traveling along the positive z-direction, then right- (left-) circularly polarized light corresponds to  $E_-$  ( $E_+$ ) in (2.29) and (2.30). Under time inversion left-circularly polarized light becomes right-circularly polarized, and vice versa. Also, upon reflection, an incident left- (right-) circularly polarized wave becomes reflected as right- (left-) circularly polarized wave. A device that introduces a relative phase shift of  $\pi/2$  between two orthogonal components of linearly polarized light is known as quarter wave plate (see Sect. 2.2.4).

<sup>&</sup>lt;sup>4</sup> It may appear somewhat counterintuitive that a phase lead is described by a negative phase angle. This is owed to the fact that we use the notation  $(\mathbf{k} \cdot \mathbf{z} - \omega t)$  for the phase [see (2.7)]. Had we used  $(\omega t - \mathbf{k} \cdot \mathbf{z})$ , the signs for the phase angles would have been interchanged.

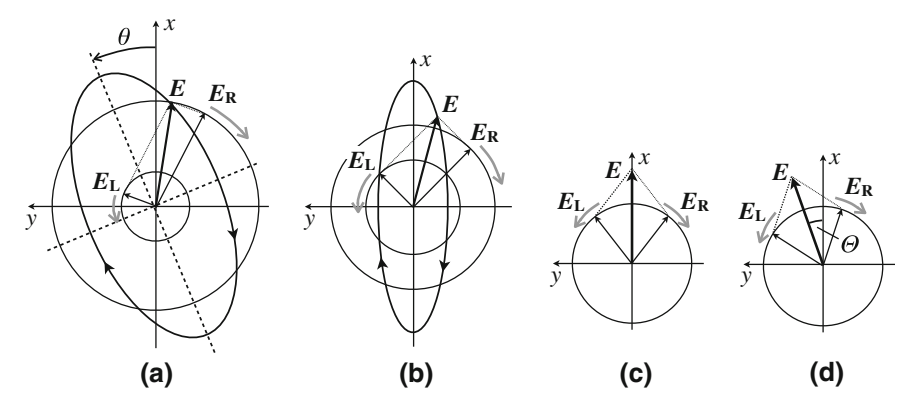


Fig. 2.5 a Representation of a general elliptically polarized wave as superposition of right- and left-handed circularly polarized waves with different amplitudes and different phase. Like in Fig. 2.4a, the angle  $\theta$  defines the azimuth between the (x,z)-plane and the major axis of the polarization ellipse. Along the minor axis the field vectors of the two circular waves are antiparallel, along the major axis they are parallel. The left-polarized wave then has the phase  $+\theta$ , the right-polarized wave  $-\theta$ . As both waves have the same rotational frequency, the major axis is the angle bisector between the left- and right-circularly polarized components of the momentary field vectors at any time. b A non-rotated ellipse is created if the two circular modes are in-phase (for a 90° phase shift the ellipse would be aligned along the y axis). c If also the amplitudes of the two circular waves are equal, a linearly polarized wave emerges by superposition. This is shown in c and d to demonstrate the effect of circular birefringence. In c the superposition of right- and left-handed circularly polarized waves of equal phase leads to a linearly polarized wave along the x-axis, which shall represent the wave at z=0 at the surface of the birefringent material. In traversing the optically active medium, the two circular waves get out-of-phase and the resultant linear wave at a depth z' appears rotated (d). (After [166, 169])

The "Cartesian" decomposition of the electric field into *x* and *y* components, which was applied so far, is arbitrary though. Plane waves of any polarization can as well be described by combining waves of opposite circular polarization as basis [173]. If the two circular waves have different amplitudes, elliptically polarized light will result (Fig. 2.5a, b), whereas for equal amplitudes linearly polarized light is created (Fig. 2.5c, d). A phase shift between the two circular modes leads to rotation (compare Fig. 2.5a, d)

An efficient way to describe the polarization state of light is the *Jones formalism* [166, 173]. In this representation, the electrical field vector of the light wave is expressed in terms of its complex amplitudes in a two-element column vector, the *Jones vector*:

$$\mathbf{J} = \begin{pmatrix} E_{\mathbf{x}} \\ E_{\mathbf{y}} \end{pmatrix} = \begin{pmatrix} \begin{vmatrix} E_{\mathbf{x}}^{\text{max}} \\ E_{\mathbf{y}}^{\text{max}} \end{vmatrix} e^{\mathbf{i}\delta_{\mathbf{x}}} \\ e^{\mathbf{i}\delta_{\mathbf{y}}} \end{pmatrix}. \tag{2.31}$$

The spatial and temporal phase,  $e^{i(k_z z - \omega t)}$ , is common to both components and is therefore omitted. The Jones vector contains complete information about the phases

and amplitudes of the E-field vector components. As we are only interested in the polarization state of the wave rather than in its exact amplitudes and phases, it is convenient to normalize the irradiance to unity. The Jones vector then has to satisfy the condition  $\mathbf{J} \cdot \mathbf{J}^* = 1$ , meaning that the sum of the squares of the vector components is one—the asterix (\*) denotes the complex conjugate. A linearly polarized wave whose E-vector vibrates along a given axis can then be represented by the normalized Jones vector

$$\mathbf{J_{lin}} = \begin{pmatrix} \cos \alpha_{\text{pol}} \\ \sin \alpha_{\text{pol}} \end{pmatrix}. \tag{2.32}$$

Here  $\alpha_{\rm pol}$  is the azimuth angle of the electric field vector oscillation, defined by the polarizer setting with respect to the x-axis (see Fig. 2.7b below). When  $\alpha_{\rm pol}=0$  represents a linearly polarized wave with its E-vector oscillating along the x-axis, the normalized Jones vectors for waves polarized along the coordinate axes and in diagonal direction are given by

$$\mathbf{J_x} = \begin{pmatrix} 1 \\ 0 \end{pmatrix}, \quad \mathbf{J_y} = \begin{pmatrix} 0 \\ 1 \end{pmatrix} \quad \text{and} \quad \mathbf{J_{45^\circ}} = \frac{1}{\sqrt{2}} \begin{pmatrix} 1 \\ 1 \end{pmatrix}.$$
 (2.33)

The Jones vector for general elliptic polarization can be derived by rewriting (2.31):

$$\mathbf{J_{elp}} = E_{\mathbf{x}}^{\max} e^{\mathrm{i}\delta_{\mathbf{x}}} \begin{pmatrix} 1 \\ \frac{E_{\mathbf{y}}^{\max}}{E_{\mathbf{x}}^{\max}} e^{\mathrm{i}(\delta_{\mathbf{y}} - \delta_{\mathbf{x}})} \end{pmatrix} = E_{\mathbf{x}}^{\max} e^{\mathrm{i}\delta_{\mathbf{x}}} \begin{pmatrix} 1 \\ \frac{\sin\Omega}{\cos\Omega} e^{\mathrm{i}\delta} \end{pmatrix}. \tag{2.34}$$

Multiplication with  $\cos \Omega/(E_x^{\rm max} {\rm e}^{{\rm i}\delta_x})$  leads to the normalized Jones vector

$$\mathbf{J_{elp}} = \begin{pmatrix} \cos \Omega \\ \sin \Omega \, \mathrm{e}^{\mathrm{i}\delta} \end{pmatrix} \tag{2.35}$$

that satisfies  $J_{elp} \cdot J_{elp}^* = 1$  and which describes a vibration like in Fig. 2.4a. For right-circular light,  $\delta = -\pi/2$  and  $\Omega = \arctan{(E_y^{max}/E_x^{max})} = \arctan{1 = \pi/4}$ , yielding the normalized Jones vector

$$\mathbf{J}_{\mathbf{R}} = \frac{1}{\sqrt{2}} \begin{pmatrix} 1\\ e^{-i\frac{\pi}{2}} \end{pmatrix} = \frac{1}{\sqrt{2}} \begin{pmatrix} 1\\ -i \end{pmatrix}. \tag{2.36}$$

For left-circular light, with  $\delta = \pi/2$  and  $\Omega = \pi/4$ , we get

$$\mathbf{J_L} = \frac{1}{\sqrt{2}} \begin{pmatrix} 1\\ e^{i\frac{\pi}{2}} \end{pmatrix} = \frac{1}{\sqrt{2}} \begin{pmatrix} 1\\ i \end{pmatrix}. \tag{2.37}$$

As  $J_R^* \cdot J_L = 0$ , these two circular polarizations are mutually orthogonal. The basic linear polarizations  $J_X$  and  $J_Y$  can be resolved into circular polarizations  $J_R$  and  $J_L$ , and vice versa:

$$\begin{split} \mathbf{J_R} &= \frac{1}{\sqrt{2}}(\mathbf{J_x} - \mathrm{i}\mathbf{J_y}), \quad \mathbf{J_L} = \frac{1}{\sqrt{2}}(\mathbf{J_x} + \mathrm{i}\mathbf{J_y}), \\ \text{and} \quad \mathbf{J_x} &= \frac{1}{\sqrt{2}}(\mathbf{J_R} + \mathbf{J_L}), \quad \mathbf{J_y} = \frac{\mathrm{i}}{\sqrt{2}}(\mathbf{J_R} - \mathbf{J_L}). \end{split} \tag{2.38}$$

As mentioned before already, circular polarizations obviously consist of linear vibrations along the x- and y-axes with equal amplitudes  $1/\sqrt{2}$  and a phase difference of  $\pm \pi/2$ . Similarly, a linear polarization can be seen as a superposition of two oppositely sensed circular polarizations (Fig. 2.5c).

#### 2.2.3 Birefringence, Dichroism, and Optical Activity

Many crystalline substances like calcite or quartz are optically anisotropic, i.e. their optical properties are not the same in all directions within the crystal. One of the consequences is that the propagation speed of a light wave in the crystal is a function of the direction of propagation and the polarization of the light. In a classical picture this can be ascribed to an anisotropy in the atomic binding forces: In a transparent substance, light propagates by exciting the atoms within the medium. The electrons are driven by the electrical field of the light wave, they then reradiate secondary wavelets which, following Huygen's principle, recombine in a resultant refracted wave that continues propagation. The speed of the wave, and with it the refraction index.5 are determined by the difference between the frequency of light and the natural electronic frequency. An anisotropy in the electronic binding forces, which depends on the symmetry of the atomic crystal lattice, will thus cause an anisotropy in the index of refraction. Substances with hexagonal, tetragonal, and trigonal crystal structure are typical examples for optically anisotropic materials. They are known as uniaxial with the optical axis corresponding to a direction about which the atoms are arranged symmetrically. Due to the anisotropic refraction index, a ray of natural light entering the crystal at a nonzero acute angle to the optical axis is decomposed into two rays, called ordinary and extraordinary ray, when it passes through the material. The two rays are mutually perpendicularly polarized (the ordinary wave is polarized perpendicular to the optic axis, the extraordinary wave has both, parallel and perpendicular components to the axis) and they propagate in different directions. On leaving the medium, the two partial rays are spatially separated so that an object observed through the medium appears doubled. This effect is therefore known as double refraction.

<sup>&</sup>lt;sup>5</sup> The absolute index of refraction  $n = c_0/v$  is defined by the ratio of the speed  $c_0$  of an electromagnetic wave in vacuum to the speed v in matter, see (2.10).

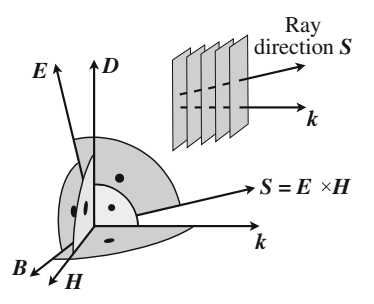
In general, a material that displays two different indices of refraction is said to be birefringent. For the mentioned uniaxial materials the birefringence magnitude is defined by  $\Delta n = (n_e - n_o)$ , where  $n_o = c_0/v_{\perp}$  and  $n_e = c_0/v_{\parallel}$  are the two principal refractive indices for the ordinary and extraordinary wave, which propagate with velocities  $v_{\perp}$  and  $v_{\parallel}$ , respectively, according to their polarization direction with respect to the optic axis. In calcite, for instance,  $\Delta n$  is negative, meaning that  $v_{||} > v_{\perp}$ . The wave whose electrical field vibrates parallel to the optic axis travels fastest, so that the optic axis is referred to as the fast axis in this case, and the direction perpendicular to it is the slow axis. For quartz  $\Delta n$  is positive and the slow axis corresponds to the optic axis. A birefringent material that absorbs the orthogonally polarized waves with different strengths is dichroic. In its broadest sense, the term dichroism refers to the phenomenon of anisotropic optical absorption, which means that one of the two orthogonal polarization state components is more strongly absorbed than the other.<sup>6</sup> Orthorhombic, monocline, and triclinic systems have two optic axes and are said to be biaxial. A typical example is mica [KH<sub>2</sub>Al<sub>3</sub>(SiO<sub>4</sub>)<sub>3</sub>]. Such substances have three different principal refraction indices and the birefringence is measured as the numerical difference between the largest and smallest index. The magneto-optical Kerr-, Faraday-, and Voigt effects can also be interpreted as birefringence effects as explained below.

Also *optical activity* can be interpreted as birefringence effect. Any material that causes the electrical field of an incident linearly polarized wave to be rotated on passing through is said to be optically active. A dextrorotatory or right-handed substance causes a clockwise rotation of the polarization plane while looking in the direction of the source, and vice versa for a *levorotatory* or left-handed material. Crystalline quartz, for instance, can be either right- or left-handed depending on its crystal structure. A simple phenomenological description of optical activity was proposed by Fresnel: Since the incident linear wave can be represented by the superposition of right- and left-circularly polarized partial waves (see Fig. 2.5c), Fresnel suggested that these two circular waves propagate in the active medium at different speeds. An optically active material thus shows circular birefringence, i.e., it possesses two indices of refraction, one for right  $(n_{-})$  and one for left  $(n_{+})$  circularly polarized light. When propagating through an optically active specimen, the two circular waves get out-of-phase and the resultant linear wave appears rotated (Fig. 2.5d). The rotation angle is proportional to the length of the traversed path and to the difference  $(n_+ - n_-)$  of the two refractive indices. An analytical derivation of light rotation in optically active media is presented in Sect. 2.4.1 using the example of the Faraday effect.

The electromagnetic description of crystal optics [163, 164, 168] starts from the general wave equation (2.18). The solution of this system of linear equations leads to an equation of second order for  $n^2$  and thus to two physically relevant solutions for n

<sup>&</sup>lt;sup>6</sup> The two attenuation coefficients may be frequency-dependent and vary in different ways with the frequency. If white light enters the crystal, the crystal will in general appear colored with the color depending on the vibrational direction of the incident light. For uniaxial crystals there are two characteristic colors, leading to the term 'dichroism'.

Fig. 2.6 Relative orientations of the field- and propagation vectors for a transparent, anisotropic material. While the *D*-vector is perpendicular to the propagation vector, the *E*-vector strongly deviates from this direction. (After [169])



(we will present such solution for special magneto-optical conditions in Sect. 2.3.2). For certain directions of k these two solutions can coincide; such directions are the mentioned optical axes. The fact that in an optically anisotropic medium there exist, in general, two different plane waves for every propagation direction is what we have met as birefringence.

At this point it is instructive to have a closer look at the electromagnetic description of wave propagation in anisotropic media. The propagation vector  $\mathbf{k}$ , which defines the propagation direction of the planes of constant phase of the light wave, is generally not in the same direction as the energy flow in the material. The energy flow, which corresponds to the ray direction, is given by the Poynting vector  $S = E \times H$ . The connection between the different vectors is illustrated in Fig. 2.6. According to (2.11a) and (2.11b) and ignoring electrical charges  $\rho$ , the **D**- and **B**-vectors lie in the plane perpendicular to the wave vector k. By (2.11c), E together with k are aligned in the plane perpendicular to B, and by (2.11d) the vectors H and k are aligned perpendicular to D (if external currents are zero). The Poynting vector S is by definition perpendicular to E and H. If we further assume  $\mu = 1$ , the directions of B and H coincide, the vectors E, D, S, and k lie in the plane perpendicular to Band the vectors D, B, and k are forming a right-handed coordinate system. While **D** is perpendicular to k, this is obviously not true for the E-vector, which is rather perpendicular to S—the planes of constant phase are inclined to their direction of motion as indicated in the inset of Fig. 2.6. For anisotropic, transparent materials the (transverse) **D**-vector is therefore used for description and not the **E**-vector as usual. Only if the direction of propagation is along an optical axis of the crystal, S and k have the same directions. Otherwise their directions deviate and double refraction is observed. In optically isotropic or amorphous materials the directions of **D** and **E** coincide (the connecting dielectric constant is a scalar quantity rather than a tensor) and there is no birefringence. In materials with very strong absorption the light within the material is in general elliptically polarized and the D-vector deviates from orthogonal alignment with k [164]. We will come back to such phenomena at the end of Sect. 2.3.

There are a number of optical effects that are related to birefringence and optical activity, but which are somehow *externally induced* [166]. By exerting an external influence (e.g. a mechanical force, an electric or magnetic field) on an otherwise

optically isotropic medium, the way in which the medium transits light may change. If under mechanical compression or tension a substance takes on the properties of an optically active crystal, the phenomenon of stress birefringence or *photoelasticity* is observed. The stress creates an optical axis in the direction of stress and the induced birefringence is proportional to the stress. Photoelasticity can be applied for imaging the stress distribution in transparent and opaque mechanical structures. In polarization microscopy, the optical elements have to be selected for stress freedom to avoid the disturbing effects of photoelasticity.

Also in the presence of a magnetic field a (non-magnetic) isotropic dielectric like glass may become optically active, a phenomenon that was discovered by *Faraday* in 1845. The amount of rotation  $\theta_F$  of the plane of polarization of the light is proportional to the component of magnetic induction B in propagation direction and to the length I of traversed medium:

$$\theta_{\rm F} = V B l, \tag{2.39}$$

where the proportionality constant V is called Verdet constant. Although the Faraday effect is reminiscent of optical activity, there is an important distinction: The Faraday rotation is irreversible, i.e., the rotational sense of the polarization plane is opposite if the light propagates parallel or antiparallel to the magnetic field direction. If the light is reflected after having passed the material, the resulting rotation is thus doubled compared to a single passage. The Faraday effect can be used to realize optical insulators and modulators. In magneto-optical microscopy the Faraday effect plays a role in two ways: (i) Optical elements in the microscope, like the objective lens, can cause a Faraday rotation in the presence of magnetic fields that is superimposed to any light rotation being caused by the magnetism of the specimen. In quantitative Kerr microscopy [174], where saturated sample states of well defined directions are created by external magnetic fields for calibration purpose, this disturbing Faraday effect has to be considered. (ii) More important is the intrinsic Faraday effect created by the magnetization of (optically transparent) ferro- or ferrimagnetic materials itself, which can be applied for domain imaging as explained in Sect. 2.4. As the intrinsic Faraday effect of magnetically ordered material is associated with the *magnetization* rather than with the applied magnetic field, the concept of a Verdet constant is not applicable here. In Sect. 2.4 we will show that the Faraday effect can be discussed as circular birefringence in the same fashion as Fresnel's treatment of optical activity. This also applies to its analogue in reflection, the *magneto-optical Kerr effect*.

In a similar sense, the *Cotton-Mouton effect* arises when a constant magnetic field is applied to a transparent medium (vapors or liquids) *perpendicular* to the propagation of light. The medium then becomes birefringent and behaves like a uniaxial crystal with its optic axis in the direction of the dc magnetic field, i.e. normal to the light beam. One of the two refraction indices then corresponds to the wave's vibration plane normal to the magnetic field, the other one parallel. Their difference  $\Delta n$  (i.e. the birefringence) is proportional to the square of the applied magnetic field. The same effect can also be caused by the magnetization of ferro- or ferrimagnets, where it is usually called *Voigt effect* (Sect. 2.5).

The Cotton-Mouton effect is the magnetic analogue to the *electro-optic Kerr effect*. In 1875, John Kerr discovered that an isotropic transparent substance becomes birefringent in the presence of an electric field. The medium takes over the characteristics of a uniaxial crystal whose optic axis matches the direction of the applied field. The birefringence  $\Delta n = n_{\parallel} - n_{\perp} = \lambda_0 K E^2$  is proportional to the square of the electric field analogous to the magnetic field dependence of the Cotton-Mouton and Voigt effect. The two refraction indices,  $n_{\parallel}$  and  $n_{\perp}$ , are associated with the two vibration planes parallel and perpendicular to the applied electric field and K is the Kerr constant. The electro-optic Kerr effect is utilized to produce a high-speed light modulator known as Kerr cell.

### 2.2.4 The Compensator

In polarization microscopy, birefringent material may be used to *modify* elliptically polarized light as it emerges from birefringent samples including magnetic samples. For this purpose a transparent birefringent plate of suitable thickness and material is placed in the ray path emerging from the specimen. The plate allows to change the path difference between the two mutually orthogonal vibration directions of the elliptical wave (see Fig. 2.4). Such a device is called a *compensator*, as its function is to compensate phase differences. Compensators are commonly used for qualitative applications, such as control of background illumination or to improve the contrast and visibility in weakly birefringent specimens. For magneto-optical microscopy, phase compensation can be essential as only linearly polarized light can be converted into a contrast by means of an analyser. For many materials (notably Permalloy, Fe<sub>20</sub>Ni<sub>80</sub>) a reasonable domain contrast can only be obtained if a compensator is used in the reflection path, and the Voigt- and Gradient effects would not be detectable without phase adjustment. A compensator is furthermore the basic element of layerselective Kerr microscopy! It is therefore worth to spend an extra chapter on this important optical element. Of the many different types of compensators, we shall consider only those two that are used most widely in magneto-optical experiments: the Babinet and the Brace-Köhler compensator, which are applied in magneto-optical magnetometry and wide-field magneto-optical microscopy, respectively.

The *Babinet compensator* is a device containing two opposed quartz (or calcite) wedges of equal angle, one wedge being movable along its length by a micrometer screw. The wedges are cut so that their optic axes are along and perpendicular to the direction of motion, respectively (see Fig. 2.7a). A ray that traverses vertically through the device at any point will pass a thickness  $d_1$  in the upper and a thickness  $d_2$  in the lower wedge. The o- and e-rays (see Sect. 2.2.3) in the upper wedge become the e- and o-rays, respectively, in the bottom wedge. The separation of the two rays can be neglected as the compensator is thin. The *retardance*, i.e. the total phase difference, is then [166]

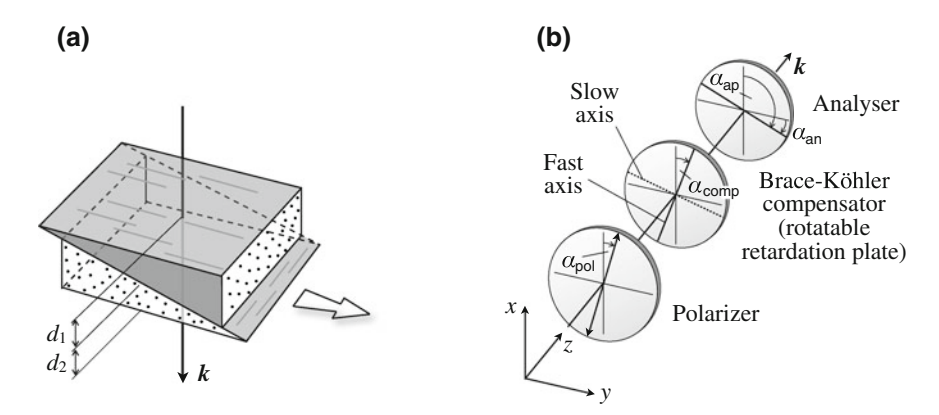


Fig. 2.7 a Babinet compensator, consisting of two quartz wedges whose optic axes are indicated by *lines* and *dots* (after [166]). **b** A Brace-Köhler compensator contains a  $N\lambda$ -retardation plate as defined in the text, having the optical axis parallel to the plate plane (see Sect. 2.2.3 for the definition of the fast axis). For adjustment, the retardation plate is rotated around the propagation axis (k-direction) of the light. The azimuth angles of polarizer, compensator and analyser are defined relative to the x-axis. The sample is omitted in the drawing—in a magneto-optical experiment it is placed between polarizer and compensator

$$\Delta \varphi = \frac{2\pi}{\lambda_0} (d_1 - d_2)(|n_0 - n_e|). \tag{2.40}$$

At the center of the device, where  $d_1=d_2$ , the effect of one wedge is exactly canceled by the other, and  $\Delta\varphi=0$ . Otherwise the retardation varies from point to point over the surface, being constant in narrow regions across the width of the compensator along which the wedge thicknesses are themselves constant.

For wide-field microscopy, where the compensator is typically located in a position of parallel light between specimen and analyser (see Fig. 3.1), Babinet compensators cannot be used due to their line-characteristics. Here *Brace-Köhler* compensators are better suited as they cause a homogeneous phase retardation across the whole field of view. A Brace-Köhler compensator is a rotatable retardation plate, that is a piece of birefringent, uniaxial (or uniaxial appearing) material like mica or calcite. As shown in Fig. 2.7b, the crystal is cut so that the optic axis lies in the plane of the plate. The o- and e-rays are retarded relative to each other and the path difference between the two rays is given by  $N\lambda_0 = d(|n_0 - n_e|)$ , where d is the physical thickness of the plate. Variable N can be seen as retardation, expressed in fractions of a wavelength. For example, a quarter wave (or  $\lambda_0/4$ ) plate is represented by  $N = \frac{1}{4}$ , a half wave (or  $\lambda_0/2$ ) plate by  $\frac{1}{2}$ , etc.. The phase difference between two rays traveling through the retardation plate is  $2\pi/\lambda_0$  times the path difference, so

<sup>&</sup>lt;sup>7</sup> Today, retarders are also made of polyvinyl alcohol sheets that have been stretched so as to align their long-chain organic molecules. A permanently birefringent substance is created in this way even though the material is not crystalline. The foil is cemented between two glass plates by a filler with suitable refraction index.

that the phase retardation  $\Delta \varphi$  is [175]

$$\Delta \varphi = 2\pi N = \frac{2\pi}{\lambda_0} d(|n_0 - n_e|). \tag{2.41}$$

Thus, phase differences of  $\pi/2$  and  $\pi$  are introduced between the o- and e-beams in quarter-wave and half-wave plates, respectively. When the compensator is rotated around the k-axis, the value of retardation R is given by

$$R = \Delta \varphi \sin \left( 2 \left| \alpha_{\text{pol}} - \alpha_{\text{comp}} \right| \right), \tag{2.42}$$

where  $\alpha_{pol}$  and  $\alpha_{comp}$  are the rotation angles of polarizer and compensator according to Fig. 2.7b. Apparently, linear light incident parallel to either principal axis of the compensator (the fast axis, i.e.  $\alpha_{comp} = \alpha_{pol}$ , or the slow axis, i.e.  $\alpha_{comp} = \alpha_{pol} + 90^{\circ}$ ) will be unaffected by the compensator—a *relative* phase difference always requires two components. When linear light, polarized at 45° to either principal axis is incident on a quarter-wave plate, its *o*- and *e*-components have equal amplitudes. Then a 90° phase shift converts the wave into circular light and, vice versa, an incoming circular wave front will emerge linearly polarized (see Fig. 2.4c). For any other orientation of the quarter-wave plate, linear light is converted to elliptical light with varying degrees of ellipticity, depending upon the degree of relative phase retardation *R*. Vice versa, any elliptically polarized wave can be converted into a linearly polarized wave by a properly rotated compensator! Established retardation plates used as Brace-Köhler compensators are  $\lambda/10$ - or  $\lambda/4$ -plates. In mica crystals, the birefringence shows little dependence on the wavelength of light, so that a broadband application of compensators made of such material is possible.

In a magneto-optical experiment, the compensator is part of a train of optical elements consisting of (in order) polarizer, sample, compensator and analyser, perhaps extended by some electro-optical device. To achieve good sensitivity or contrast, each of these optical elements is oriented at a certain azimuth angle as illustrated for the polarizer, analyser, and compensator in Fig. 2.7b. An efficient technique to describe the polarization state of light along this train of optical elements is provided by *Jones matrix* algebra [165, 166]. In Jones algebra, the electrical field vector of the light wave is represented by the Jones vector (2.31), while each optical element is represented by a  $2 \times 2$  matrix, the Jones matrix  $\Gamma$ . If  $E = (E_x, E_y)$  is the Jones vector of the incident light defined along the (x, y, z)-coordinate system of Fig. 2.3a, the light emerging from the optical element,  $E' = (E'_x, E'_y)$ , is then given by [163]

$$\mathbf{E}' = \boldsymbol{\Gamma} \mathbf{E} \quad \text{with} \quad \boldsymbol{\Gamma} = \begin{pmatrix} a & b \\ c & d \end{pmatrix}. \tag{2.43}$$

<sup>&</sup>lt;sup>8</sup> In magneto-optical microscopy the light beams behind the objective lens emerge in parallel bundles, so that the polarization vectors of each beam can be assumed to be co-planar to the polarization elements on the observation side (compensator and analyser), as well as to the image plane. All polarization aspects can therefore be treated two-dimensionally in a plane perpendicular to the optical axis of the microscope.

If the light is sent through a train of n optical elements, the result is obtained by multiplication of all the matrices in sequence:

$$\begin{pmatrix} E_{\mathsf{x}}' \\ E_{\mathsf{y}}' \end{pmatrix} = \begin{pmatrix} a_n \ b_n \\ c_n \ d_n \end{pmatrix} \cdots \begin{pmatrix} a_2 \ b_2 \\ c_2 \ d_2 \end{pmatrix} \begin{pmatrix} a_1 \ b_1 \\ c_1 \ d_1 \end{pmatrix} \begin{pmatrix} E_{\mathsf{x}} \\ E_{\mathsf{y}} \end{pmatrix}. \tag{2.44}$$

For a Brace-Köhler compensator the transformation of light is written as [165]

$$\begin{pmatrix} E_{\mathbf{x}}' \\ E_{\mathbf{y}}' \end{pmatrix} = \boldsymbol{\Gamma}_{\text{comp}} \begin{pmatrix} E_{\mathbf{x}} \\ E_{\mathbf{y}} \end{pmatrix}, \tag{2.45}$$

where the Jones matrix  $\Gamma_{
m comp}$  of the rotatable retardation plate is given by

$$\Gamma_{\text{comp}} = \Gamma_{\text{rot}}(-\alpha_{\text{comp}}) \begin{pmatrix} e^{-\frac{1}{2}i\Delta\varphi} & 0\\ 0 & e^{+\frac{1}{2}i\Delta\varphi} \end{pmatrix} \Gamma_{\text{rot}}(\alpha_{\text{comp}})$$
with 
$$\Gamma_{\text{rot}}(\alpha_{\text{comp}}) = \begin{pmatrix} \cos\alpha_{\text{comp}} & \sin\alpha_{\text{comp}}\\ -\sin\alpha_{\text{comp}} & \cos\alpha_{\text{comp}} \end{pmatrix}.$$
(2.46)

Here  $\Delta \varphi$  is the phase retardation (2.41) and the angle  $\alpha_{comp}$  defines the azimuthal rotation of the fast axis of the retardation plate with respect to the *x*-axis. The central matrix in (2.46) is the Jones matrix of the retardation plate itself, the outer two are rotation matrices:  $\Gamma_{rot}(\alpha_{comp})$  represents a coordinate transformation from xy to eo, i.e. the x- and y-components of the incoming light ( $E_x$ ,  $E_y$ ) are transformed to the axes e and o of the normal modes of the retardation plate. As mentioned, the two normal mode components will propagate with their own phase velocities and one component is retarded relative to the other due to the difference in phase velocity. This phase retardation changes the polarization state of the emerging light. The electric field vector of the polarization state of the emerging beam in the xy coordinates ( $E_x'$ ,  $E_y'$ ) is obtained by transforming back from the crystal eo-coordinate system, which is achieved by the rotation matrix  $\Gamma_{rot}(-\alpha_{comp})$  in (2.46).

In order to visualize the effect of the compensator, let us discuss the case of a quarter-wave plate ( $\Delta \varphi = \pi/2$ ). The previously discussed transformations of light can be conveniently calculated by Jones algebra. Suppose that the azimuth angle of the plate is  $\alpha_{comp} = 45^{\circ}$  and the incident beam is vertically polarized along the x-axis,  $E_{in} = (1,0)$ . According to (2.46) the Jones matrix for this arrangement is

$$\Gamma_{\text{qw}} = \frac{1}{\sqrt{2}} \begin{pmatrix} 1 & -1 \\ 1 & 1 \end{pmatrix} \begin{pmatrix} e^{-\frac{i\pi}{4}} & 0 \\ 0 & e^{+\frac{i\pi}{4}} \end{pmatrix} \frac{1}{\sqrt{2}} \begin{pmatrix} 1 & 1 \\ -1 & 1 \end{pmatrix} = \frac{1}{\sqrt{2}} \begin{pmatrix} 1 & -i \\ -i & 1 \end{pmatrix}. \quad (2.47)$$

The Jones vector  $\mathbf{E}'$  of the emerging beam is then obtained by

$$\mathbf{E}' = \mathbf{\Gamma}_{qw} \begin{pmatrix} 1 \\ 0 \end{pmatrix} = \frac{1}{\sqrt{2}} \begin{pmatrix} 1 \\ -i \end{pmatrix}. \tag{2.48}$$

As expected, vertically (x-) polarized light is thus converted to right-handed circularly polarized light [compare (2.36)] by a  $45^{\circ}$ -oriented quarter-wave plate. If the incident beam is vertically polarized along the x-axis, the emerging beam will be left-handed circularly polarized. These two transformations together with some others are illustrated in Fig. 2.8. In the figure also the effect of an (ideal) analyser is indicated. Its Jones matrix is given by

$$\Gamma_{\rm an} = \begin{pmatrix} \cos \alpha_{\rm ap} - \sin \alpha_{\rm ap} \\ \sin \alpha_{\rm ap} & \cos \alpha_{\rm ap} \end{pmatrix} \begin{pmatrix} 1 & 0 \\ 0 & 0 \end{pmatrix} \begin{pmatrix} \cos \alpha_{\rm ap} & \sin \alpha_{\rm ap} \\ -\sin \alpha_{\rm ap} & \cos \alpha_{\rm ap} \end{pmatrix}, \quad (2.49)$$

with  $\alpha_{\rm ap} = \alpha_{\rm pol} + 90^{\circ} + \alpha_{\rm an}$ . Here it is assumed that the analyser is first crossed relative to the polarizer and then opened by a small angle  $\alpha_{\rm an}$  (relative to the x-axis in Fig. 2.7b) as usual in a magneto-optical experiment.

Also the change of the polarization state, caused by reflection or transmission on a sample, can be described by corresponding Jones matrices:

$$\begin{pmatrix}
E_{\mathbf{x}}^{\text{refl}} \\
E_{\mathbf{y}}^{\text{refl}}
\end{pmatrix} = \mathbf{R} \begin{pmatrix}
E_{\mathbf{x}}^{\text{in}} \\
E_{\mathbf{y}}^{\text{in}}
\end{pmatrix} \quad \text{and} \quad \begin{pmatrix}
E_{\mathbf{x}}^{\text{trans}} \\
E_{\mathbf{y}}^{\text{trans}}
\end{pmatrix} = \mathbf{T} \begin{pmatrix}
E_{\mathbf{x}}^{\text{in}} \\
E_{\mathbf{y}}^{\text{in}}
\end{pmatrix},$$
with  $\mathbf{R} = \begin{pmatrix}
r_{\mathbf{xx}} & r_{\mathbf{xy}} \\
r_{\mathbf{yx}} & r_{\mathbf{yy}}
\end{pmatrix} \quad \text{and} \quad \mathbf{T} = \begin{pmatrix}
t_{\mathbf{xx}} & t_{\mathbf{xy}} \\
t_{\mathbf{yx}} & t_{\mathbf{yy}}
\end{pmatrix}.$ 
(2.50)

In the (s, p, k)-coordinate system (Fig. 2.3) these equations are conventionally written as

$$\begin{pmatrix}
E_{p}^{\text{refl}} \\
E_{s}^{\text{refl}}
\end{pmatrix} = \mathbf{R} \begin{pmatrix}
E_{p}^{\text{in}} \\
E_{s}^{\text{in}}
\end{pmatrix} \quad \text{and} \quad \begin{pmatrix}
E_{p}^{\text{trans}} \\
E_{s}^{\text{trans}}
\end{pmatrix} = \mathbf{T} \begin{pmatrix}
E_{p}^{\text{in}} \\
E_{s}^{\text{in}}
\end{pmatrix},$$
with  $\mathbf{R} = \begin{pmatrix}
r_{pp} & r_{ps} \\
r_{sp} & r_{ss}
\end{pmatrix} \quad \text{and} \quad \mathbf{T} = \begin{pmatrix}
t_{pp} & t_{ps} \\
t_{sp} & t_{ss}
\end{pmatrix}.$ 
(2.51)

Here R and T are the reflection and transmission matrices, respectively, and the matrix elements  $r_{ij}$  and  $t_{ij}$  are the reflection and transmission coefficients for the electrical field amplitudes. The first index, i, describes the reflected or transmitted component, the second index, j, is for the corresponding components of the incident light. Expressions for the diagonal coefficients are given in the next section. The transfer matrices contain the complete information about the optical properties of a sample including the magneto-optical properties. We will return to such description in Sect. 2.4A.

# 2.2.5 Reflection and Transmission of Polarized Light

In the previous sections we have seen that any polarization state of an electromagnetic wave, propagating along the z-axis, can be treated by resolving its E-field

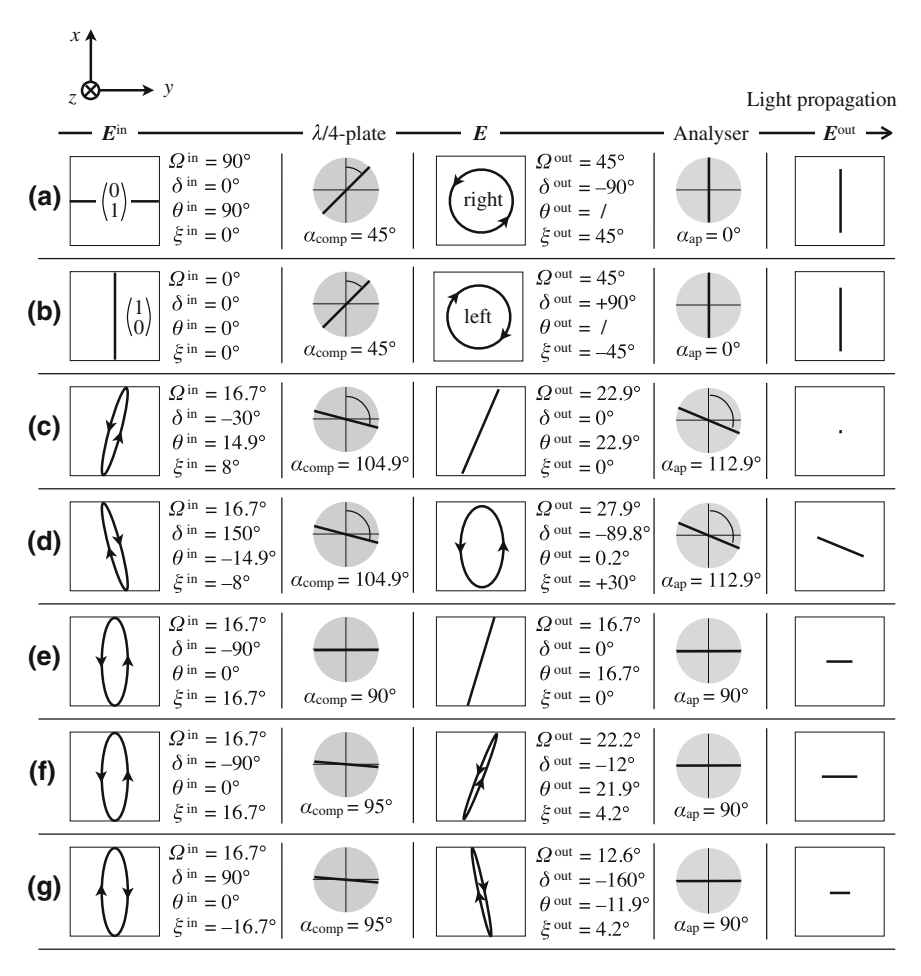


Fig. 2.8 Transformation examples of a quarter-wave plate in combination with an analyser. Shown are the traces of the light polarization by looking along the propagation direction according to Fig. 2.7b. The rotation sense according to traditional convention is indicated by *arrows* that show the *E*-vector rotation in time at a fixed position like in Fig. 2.4. **a, b** Transformation of linearly polarized light into *circular light*. **c** Rotated elliptical light (as it is principally generated by the Kerr- or Faraday effect can be linearized by rotating the compensator by  $90^{\circ} + \theta^{\text{in}}$ . The linear wave is then rotated by  $\theta^{\text{out}} = \dot{\xi}^{\text{in}} + \theta^{\text{in}}$ . **d** A wave of opposite rotation and ellipticity as in (c) is transformed into a strongly elliptical wave under the same compensator setting. **e** A 90° phase shift between the *x*- and *y*-components leads to an *upright ellipse* (like in the Voigt effect) that can be linearized by a transversely oriented compensator. **f**, **g** Opening of the compensator by leaving the analyser crossed to the polarizer leads to a contrast behind the analyser. (Developed together with *L. Lokamani*, Dresden)

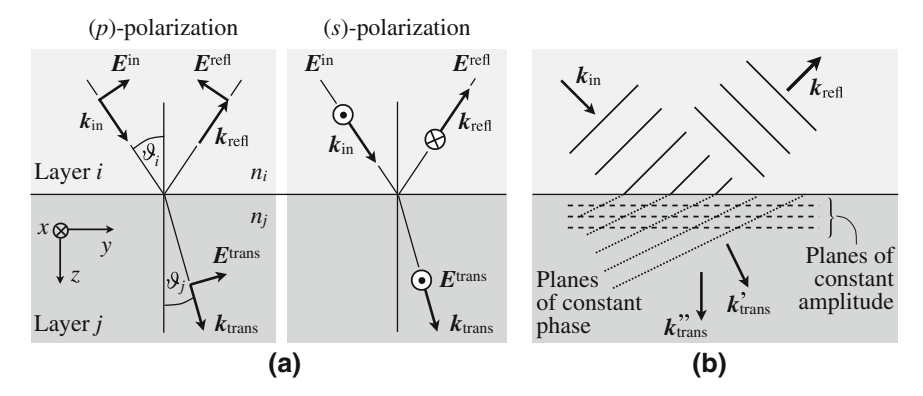


Fig. 2.9 a The two standard situations of s- and p-polarized plane waves incident on the boundary between two homogenous and isotropic media. The waves are represented by their electrical field, where  $E^{\rm in}$ ,  $E^{\rm refl}$  and  $E^{\rm trans}$  are the incident, reflected and transmitted light amplitudes, respectively. On the left, the E-field of the incoming wave is parallel to the plane of incidence (the yz plane), on the right it is normal. The component of E normal to the plane of incidence undergoes a phase shift of  $180^\circ$  upon reflection when the incident medium has a lower refraction index than the transmitting medium. Under this condition no phase shift occurs for field components parallel to the incidence plane (note that two fields in the incidence plane are in-phase if their z components are parallel). E Real and imaginary parts of the wave vector in an absorbing material, illustrating the difference between the directions of phase propagation and amplitude damping

into components along the x- and y-axes and by discussing these constituents separately. In polarization microscopy with a chosen angle of incidence it is convenient to switch to the (s, p, k)-coordinate system (Fig. 2.3) and treat an electromagnetic wave in terms of the components parallel (p) and perpendicular (s) to the plane of incidence. Figure 2.9a illustrates the two cases.

In Sect. 2.3 we will describe how the light propagates within a magnetic sample and how it is influenced by the magnetization. This will finally lead to the magneto-optical effects. Before the light can propagate within the sample, however, it has to enter the material and, after some interaction, leave it again for detection. Although the physical properties (characterized by the dielectric tensor  $\epsilon$  and the magnetic permeability tensor  $\mu$ ) may change abruptly across the interface, there do exist *continuity relationships* for some of the components of the field vectors at the boundary, which can be directly derived from the Maxwell equations [164]. These boundary conditions require that the *tangential components* of the electric field E are always continuous across the interface. In other words, the total tangential component of E on one side (consisting of the incident and reflected amplitudes  $E^{\rm in}$  and  $E^{\rm refl}$ , respectively—see Fig. 2.9) must be equal to that on the other side (the transmitted amplitude  $E^{\rm trans}$ ). The same condition applies to the magnetic field E. For the dielectric displacement vector E0 and for the magnetic flux density E1 the *normal components* are continuous across the interface.

From the boundary conditions of electromagnetic theory, the reflection and transmission coefficients for the two principal cases of p- and s-polarization can be derived

[164, 166]. For optically isotropic media (i.e. ignoring magneto-optical effects or other optical activity for the moment) only the diagonal terms,  $r_{pp}$  and  $r_{ss}$ , appear in the reflection and transmission matrices (2.51). Pure s- and pure p-waves therefore remain linearly polarized on reflection with the plane of polarization being along the same direction as that of the incident light. The reflection coefficients for the two cases are given by

$$r_{\rm pp}^{ij} = \left(\frac{E^{\rm refl}}{E^{\rm in}}\right)_{\rm p} = \frac{n_i \cos \vartheta_j - n_j \cos \vartheta_i}{n_i \cos \vartheta_j + n_j \cos \vartheta_i} = |r_{\rm pp}| \exp(i\delta_{\rm rp})$$

$$r_{\rm ss}^{ij} = \left(\frac{E^{\rm refl}}{E^{\rm in}}\right)_{\rm s} = \frac{n_i \cos \vartheta_i - n_j \cos \vartheta_j}{n_i \cos \vartheta_i + n_j \cos \vartheta_j} = |r_{\rm ss}| \exp(i\delta_{\rm rs}), \tag{2.52}$$

and the transmission coefficients by

$$t_{pp}^{ij} = \left(\frac{E_{trans}}{E_{in}}\right)_{p} = \frac{2n_{i}\cos\vartheta_{i}}{n_{i}\cos\vartheta_{j} + n_{j}\cos\vartheta_{i}} = |t_{pp}|\exp(i\delta_{tp})$$

$$t_{ss}^{ij} = \left(\frac{E_{trans}}{E_{in}}\right)_{s} = \frac{2n_{i}\cos\vartheta_{i}}{n_{i}\cos\vartheta_{i} + n_{j}\cos\vartheta_{j}} = |t_{ss}|\exp(i\delta_{ts}).$$
(2.53)

These so-called *Fresnel equations* can be generally applied to dielectric as well as absorbing materials (remember: for the latter the refraction index and refraction angle of the absorbing medium have to be taken complex. A complex angle has no simple physical meaning, though). Index i represents the layer from which the light originates. This can be a ferromagnetic or dielectric layer in a multilayer system, or an environment like air or immersion oil. The light then enters (and is reflected from) from layer j that is in direct contact to layer i. Each layer is characterized by its (in general complex) index of refraction,  $n_i$  or  $n_j$ . The constants  $r_{pp}^{ij}$  and  $r_{ss}^{ij}$  are the amplitude reflection coefficients from layer i to layer j for parallel and perpendicular polarization, and  $t_{pp}^{ij}$  and  $t_{ss}^{ij}$  are the corresponding transmission coefficients from layer i to layer j. These coefficients describe the fraction of wave amplitude that is reflected and transmitted, respectively, by passing the interface between layer i and j. The coefficient  $t_{pp}^{ij}$ , for instance, represents the wave fraction transmitted on entering layer j from layer i, and  $t_{pp}^{ji}$  represents the fraction transmitted when a wave leaves layer j again across the same interface. The angles of incidence in layer i and j,  $\vartheta_i$  respectively  $\vartheta_j$ , are related to the refraction indices by Snell's law:

$$n_i \sin \vartheta_i = n_j \sin \vartheta_j. \tag{2.54}$$

The absolutes of the reflection and transmission coefficients in (2.52, 2.53) specify the amplitude changes and the  $\delta$ 's the associated phase shifts on reflection or transmission. For absorbing materials (metals), s- and p-polarized light experiences different phase shifts on reflection (compare the two cases in Fig. 2.9a). The light is therefore reflected elliptically when the incident light has both, s- and p-components.

Purely *s*- and *p*-light is only reflected if the incident wave is polarized perpendicular or parallel, respectively, to the plane of incidence as mentioned. In absorbing materials there is also a difference between the directions of phase propagation and amplitude damping as illustrated in Fig. 2.9b. This difference is a consequence of the complex nature of the wave vector and refraction index in the metal together with the boundary conditions at the interface. With (2.9), (2.17), and (2.21) we can employ the following notations for the three plane waves in Fig. 2.9b (neglecting the amplitudes) [163]:

$$e^{i(k_{in}r-\omega t)}$$
 (incident wave)  
 $e^{i(k_{refl}r-\omega t)}$  (reflected wave)  
 $e^{-k''_{trans}r}e^{i(k'_{trans}r-\omega t)}$  (refracted wave)

where the complex propagation vector of the refracted wave in the absorbing medium is given by  $\mathbf{k}_{\text{trans}} = \mathbf{k}'_{\text{trans}} + \mathrm{i}\mathbf{k}''_{\text{trans}}$  [see (2.14)]. The continuity conditions require constant ratios of the fields at the interface, leading to

$$k_{\text{in}} \cdot r = k_{\text{refl}} \cdot r$$
  
 $k_{\text{in}} \cdot r = k_{\text{trans}} \cdot r = (k'_{\text{trans}} + i k''_{\text{trans}}) \cdot r$ 

at the boundary. The first equation leads to Snell's law (2.54) and the second equation yields

$$\mathbf{k}_{\text{in}} \cdot \mathbf{r} = \mathbf{k}'_{\text{trans}} \cdot \mathbf{r}$$
 (2.55a)  
 $0 = \mathbf{k}''_{\text{trans}} \cdot \mathbf{r}$  (2.55b)

after equating real and imaginary parts. This result shows that, in general,  $\mathbf{k}'_{\text{trans}}$  and  $\mathbf{k}''_{\text{trans}}$  have different directions—the wave is said to be *inhomogenous*. As shown in Fig. 2.9b, the direction of planes of constant amplitude, defined by  $\mathbf{k}'_{\text{trans}}$ , is always normal to the boundary according to (2.55b), whereas the planes of constant phase, defined by  $\mathbf{k}'_{\text{trans}}$ , may have any direction. The wave thus moves in the direction of the wave vector  $\mathbf{k}'_{\text{trans}}$ , but its amplitude is exponentially diminished with the distance from the boundary plane as shown in the figure. The amplitude of an inhomogeneous wave consequently varies over the wave front, whereas a homogenous wave is defined as a wave whose amplitude is constant over the plane-wave front and varies in the direction of propagation [176]. The reflection and transmission behavior of a thin film or multilayer is more complicated as an incident light beam will interact not just with the first boundary but rather with a number of boundaries. We will discuss this situation in Sect. 3.2.2.

So far we have collected some background on the polarization of light, thus providing the basis for the magneto-optical effects to be discussed in the following sections. Two different approaches will be used: one is related to the propagation of light and its interaction with matter, so it stresses more the physical aspects (Sect. 2.3). The other description is based on the permittivity tensor, which allows phenomenologically to

derive the symmetry of the effects (Sect. 2.4). In any case, we will restrict ourselves to a descriptive way of presentation. For a full mathematical derivation we refer to the literature.

## 2.3 Electromagnetic Basics of Conventional Effects

In Sect. 2.2.1 we have provided the electrodynamic basics for the propagation of light in continua. From Maxwell's and the material equations a general wave equation was derived, the solutions of which describe the propagable light waves in the medium. All material-specific properties of light propagation (including absorption, dispersion, optical anisotropy, and optical activity, as well as the magneto-optical effects) are completely included in the complex dielectric  $\epsilon$ -tensor. We therefore have a closer look at the magneto-optical tensor first before presenting solutions of the wave equation for the magneto-optical tensors in Sect. 2.3.2.

#### 2.3.1 The Dielectric Permittivity Tensor

According to (2.3a), the dielectric permittivity tensor  $\epsilon$  connects the electric vector E of the illuminating plane light wave with the induced dielectric displacement vector D in the illuminated medium. The D-vector represents the direction of the oscillatory electron motion and thus determines the vibration direction of the light transmitted through or reflected from the medium. In case of *non-magnetic* materials, the permittivity tensor is expressed as a sum of several contributions:

$$\epsilon_{\text{cryst}} = \epsilon^0 + \epsilon_{\text{br}} + \epsilon_{\text{oa}}, \quad \text{with} \quad \epsilon^0 = \begin{pmatrix} \epsilon_{\text{iso}} & 0 & 0 \\ 0 & \epsilon_{\text{iso}} & 0 \\ 0 & 0 & \epsilon_{\text{iso}} \end{pmatrix}.$$
 (2.56)

The first term,  $\epsilon^0$ , is an *isotropic* tensor, followed by an arbitrary traceless matrix  $\epsilon_{\rm br}$  that describes conventional crystalline *birefringence*, and a tensor for *optical activity*,  $\epsilon_{\rm oa}$ . Here  $\epsilon_{\rm iso}$  represents the dielectric constant of an isotropic, non-magnetic material. If only the isotropic tensor  $\epsilon^0$  would be active, the displacement vector would be along the same direction as the *E*-vector (under the assumption that no further optical anisotropies are present, i.e.  $\epsilon^0_{11} = \epsilon^0_{22} = \epsilon^0_{33}$ ). The light would then interact with the matter without rotation of its polarization plane. A rotation of the vibrational plane or ellipticity in the out-coming light requires non-zero off-diagonal elements in the tensor. They are contained in the  $\epsilon_{\rm oa}$  tensor, for instance, but also in the magneto-optical tensors shown below.

In analogy to (2.56), also the dielectric  $\epsilon$ -tensor of the magneto-optical effects can be split into the magnetization-independent, isotropic part  $\epsilon^0$  and a part that

depends on magnetization. If we just consider ferro- and ferrimagnetic materials, the magnetization-dependence can be seen as dependence on the magnetization direction, because the magnitude of magnetization always corresponds to the saturation magnetization. The magnetic parts to the dielectric tensor are relatively small, so that the discussion can be restricted to contributions that depend linearly or quadratically on the unit vector of magnetization m [171]:

$$\epsilon_{ij} = \epsilon_{ij}^0 + \sum_{k=1}^3 K_{ijk} m_k + \sum_{k=1}^3 \sum_{l=1}^3 G_{ijkl} m_k m_l.$$
 (2.57)

The subscription represents the three cubic axes and  $m_i$  are the components of the magnetization vector  $\mathbf{m}$ . The number of independent components of the linear magneto-optic  $\mathbf{K}$ -tensor and the quadratic  $\mathbf{G}$ -tensor can be reduced to a few material parameters by symmetry considerations [171]. For cubic crystals,  $^9$  the magneto-optic tensor then writes

$$\epsilon = \epsilon_{\text{iso}} \begin{pmatrix} 1 & -iQ_{V}m_{3} & iQ_{V}m_{2} \\ iQ_{V}m_{3} & 1 & -iQ_{V}m_{1} \\ -iQ_{V}m_{2} & iQ_{V}m_{1} & 1 \end{pmatrix} + \begin{pmatrix} B_{1}m_{1}^{2} & B_{2}m_{1}m_{2} & B_{2}m_{1}m_{3} \\ B_{2}m_{1}m_{2} & B_{1}m_{2}^{2} & B_{2}m_{2}m_{3} \\ B_{2}m_{1}m_{3} & B_{2}m_{2}m_{3} & B_{1}m_{3}^{2} \end{pmatrix}.$$
(2.58)

Here  $Q_V$  is the (Voigt) magneto-optical constant, a material parameter that describes the strength of the linear magneto-optical effects, the Kerr- and Faraday effects. It is roughly proportional to the saturation magnetization.  $B_1$  and  $B_2$  are the corresponding constants for the (intrinsic) Voigt effect. For isotropic and amorphous materials,  $B_1$  and  $B_2$  are identical. The constants  $Q_V$ ,  $B_1$  and  $B_2$  are generally frequency-dependent and complex numbers (i.e.  $Q_V = Q_V' + i Q_V''$  etc.), for which the real part is usually dominating. Exact numbers for the constants are insufficiently known—the absolute values for  $Q_V$  are of the order of  $10^{-2}$  and for B around  $10^{-4}$ .

#### 2.3.2 Solutions

The system of linear equations (2.16) or (2.18), derived from the general wave equation (2.6), has non-trivial solutions if the determinant of its coefficient matrix vanishes. This leads to a characteristic equation for the components of the wave vector as a function of the elements of the dielectric tensor, which finally defines the

 $<sup>^{9}</sup>$  The term "cubic crystal" is used in the sense that the crystal symmetry is cubic neglecting magnetization.

 $<sup>^{10}</sup>$  Another widely used convention [177] postulates a zero trace for the second matrix. This amounts in a ferromagnet (because of |m| = 1) to adding an isotropic term, which is shifted into the first matrix in (2.58).

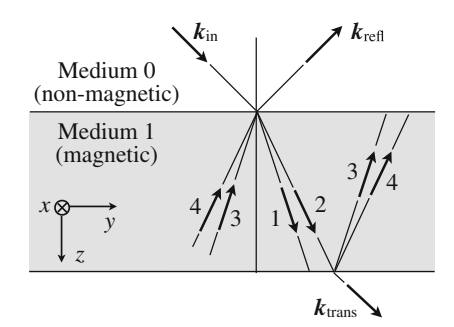


**Fig. 2.10** Illustration of the eigenmodes of the light wave in a magnetized medium for a given wave vector  $\mathbf{k}_{\text{in}}$ . Four waves with different wave vectors add to the electric field at the boundary between the non-magnetic and magnetic media. The two retrograde waves (3 and 4) would not occur in case of a single boundary, but have to be considered in films and multilayers. (After [179])

"allowed" propagation directions (eigenmodes) of the light waves in the magnetic medium. Due to the degree of freedom of a selectable light incidence, the characteristic equation is initially not unique. For a selected direction of incidence, however, the lateral components of the wave vector are defined by Snell's refraction law (2.54). For the remaining component of the wave vector an equation of fourth order is obtained in the most general case. The associated four (complex) solutions describe generalized elliptically polarized waves, for which the directions of phase propagation and amplitude damping do not coincide in case of oblique incidence, i.e. inhomogeneous waves (see Fig. 2.9b). Always, however, two waves can be assigned to forwardly propagating light and two to retrogradely advancing light (Fig. 2.10). For light incidence obliquely on the surface of the medium rather annoying algebraic equations are obtained due to the inhomogenous character of the waves (see Sect. 2.2.5). For simple geometries, however, the characteristic equations and associated eigenmodes can be easily specified. This is presented here exemplarily for the so-called "polar" (Faraday or Kerr) effect, where a homogeneous wave (real and imaginary part of k parallel to each other) is propagating along the direction of M, and for the quadratic effect (Voigt effect) occurring when a homogeneous wave propagates at right angles to M. For a thorough review of such solutions, also for other geometries, see Višňovský's book [178].

For the polar effect, the light incidence, magnetization, and surface normal vector are all parallel to the z-axis of the cubic coordinate system. Then we get  $m_3 = m_z = |\boldsymbol{m}| = 1$  and  $k_3 = k_z = |\boldsymbol{k}|$ . Inserting the magneto-optical tensor (2.58) into the wave equation (2.16) yields a system of three equations for the cartesian components of the vector field amplitude  $E_{\mathbf{x},\mathbf{y},\mathbf{z}}^0$ :

$$(k_0^2 \epsilon_{iso} - k_z^2) E_x^0 - k_0^2 \epsilon_{iso} i Q_V E_y^0 + 0 \cdot E_z^0 = 0,$$

$$k_0^2 \epsilon_{iso} i Q_V E_x^0 + (k_0^2 \epsilon_{iso} - k_z^2) E_y^0 + 0 \cdot E_z^0 = 0,$$

$$0 \cdot E_x^0 + 0 \cdot E_y^0 + (k_0^2 \epsilon_{iso} + B_1) E_z^0 = 0.$$
(2.59)

The characteristic equation, obtained from the determinant of the coefficient matrix of (2.59), is biquadratic in  $k_z$ :

$$(\epsilon_{\rm iso} + B_1) [(\epsilon_{\rm iso} - k_{\rm z}^2/k_0^2)^2 - (Q_{\rm V}\epsilon_{\rm iso})^2] = 0,$$
 (2.60)

and leads to the solutions

$$k_z^2 = k_0^2 \epsilon_{\rm iso} (1 \pm Q_{\rm V})$$
 or (2.61a)

$$k_{\rm z} \approx \pm k_0 \sqrt{\epsilon_{\rm iso}} (1 \pm Q_{\rm V}/2).$$
 (2.61b)

For approximation (2.61b) it was assumed that the non-diagonal terms of the first  $\varepsilon$ -tensor in (2.58) are small with respect to the diagonal terms ( $|Q_V| \ll 1$ ). The first plus and minus signs in (2.61b) correspond to waves propagating in forward and retrograde directions according to Fig. 2.10. In both cases we obtain

$$E_{y}^{0} = \pm i E_{x}^{0} \tag{2.62}$$

by inserting (2.61b) in (2.59). The plus and minus signs in (2.62) correspond to those in the bracket of (2.61b). From (2.62) we see that the amplitudes  $E_x^0$  and  $E_y^0$  are equal but  $\pi/2$  apart. According to (2.37) and (2.36) these are left- and right-circularly polarized waves corresponding to the plus and minus signs, respectively, in the bracket of (2.61b) and in (2.62). With  $k_z = nk_0$  [see (2.8)] and under the assumption that the wave propagates in the positive ( $+k_z$ ) direction, (2.61b) is written as

$$n_{\pm} = \sqrt{\epsilon_{\rm iso}} (1 \pm Q_{\rm V}/2). \tag{2.63}$$

With these two refractive indices, the two forward and two retrograde circular waves are explicitly given by [178]

$$E_{1,+} = \frac{1}{\sqrt{2}} (e_{x} + ie_{y}) E_{1}^{0} e^{i(+k_{0}n_{+}z - \omega t)},$$

$$E_{2,-} = \frac{1}{\sqrt{2}} (e_{x} - ie_{y}) E_{2}^{0} e^{i(+k_{0}n_{-}z - \omega t)},$$

$$E_{3,+} = \frac{1}{\sqrt{2}} (e_{x} + ie_{y}) E_{1}^{0} e^{i(-k_{0}n_{+}z - \omega t)},$$

$$E_{4,-} = \frac{1}{\sqrt{2}} (e_{x} - ie_{y}) E_{2}^{0} e^{i(-k_{0}n_{-}z - \omega t)},$$
(2.64)

using (2.30) and (2.8). Subscripts 1, 2 belong to the forward waves and 3, 4 to the retrograde waves according to Fig. 2.10.

The crucial point of this solution is that for light propagating along the magnetization the normal modes are two oppositely rotating, *circularly* polarized waves. They are propagating as though the magnetic material has refractive indices  $n_+ = \sqrt{\epsilon_{\rm iso}}(1 + Q_{\rm V}/2)$  for left-circularly polarized radiation and  $n_- = \sqrt{\epsilon_{\rm iso}}(1 - Q_{\rm V}/2)$ 

for right-circularly polarized radiation. If  $Q_V$  would be zero (which is true for isotropic, non-magnetic media),  $n_+$  and  $n_-$  would be identical and there would be no restriction on  $E_y^0$  relative to  $E_x^0$ —any polarization state could propagate in the crystal, feeling an isotropic refractive index  $n = \sqrt{\epsilon_{\rm iso}}$ . As soon as  $Q_V$  appears, only the normal modes, right and left circularly polarized waves, propagate. If the medium is absorptive,  $n_+$  and  $n_-$  are complex:

$$n_{\pm} = n'_{+} + i n''_{+}, \tag{2.65}$$

where  $n'_{\pm}$  and  $n'_{\pm}$  are real quantities. The absorption coefficient, which is the reciprocal of the distance in which the intensity of the light is reduced by a factor  $e^{-1}$ , is  $\alpha_{\pm} = 4\pi n''_{\pm}/\lambda_0$  [compare (2.23)].

A different situation arises if the light propagates perpendicular to the magnetization. Let us discuss the most important case of in-plane magnetization (here along x) at perpendicular incidence, i.e.  $m_1 = m_x = |\boldsymbol{m}| = 1$  and  $k_3 = k_z = |\boldsymbol{k}| = nk_0$ . These are conditions for the magneto-optical *Voigt effect*. For this geometry the wave equation (2.18) yields

$$(\epsilon_{iso} + B_1 - n^2)E_x^0 + 0 \cdot E_y^0 + 0 \cdot E_z^0 = 0,$$

$$0 \cdot E_x^0 + (\epsilon_{iso} - n^2)E_y^0 - \epsilon_{iso} i Q_V E_z^0 = 0,$$

$$0 \cdot E_x^0 + \epsilon_{iso} i Q_V E_y^0 + \epsilon_{iso} E_z^0 = 0,$$
(2.66)

with the characteristic equation

$$(\epsilon_{\rm iso} + B_1 - n^2) [\epsilon_{\rm iso} (1 - Q_{\rm V}^2) - n^2] = 0.$$
 (2.67)

Here both tensors in (2.58) have been considered because they can both lead to a magneto-optical effect in the symmetry of the Voigt effect as elaborated in Sect. 2.5. The solution of (2.67) then yields

$$n_{\parallel}^2 = \epsilon_{\rm iso} + B_1, \quad E = \begin{pmatrix} 1 \\ 0 \\ 0 \end{pmatrix}$$

and

$$n_{\perp}^2 = \epsilon_{\rm iso}(1 - Q_{\rm V}^2), \quad \boldsymbol{E} = \begin{pmatrix} 0\\1\\-\mathrm{i}Q_{\rm V} \end{pmatrix}.$$
 (2.68)

for the index of refraction and the corresponding electric field. For the intrinsic Voigt effect, which is purely based on the quadratic tensor in (2.58) (i.e.  $Q_V = 0$ ), the solutions are obviously *linearly* polarized waves with polarization planes parallel and perpendicular to the magnetization direction. These two waves see refraction indices  $n_{\parallel}$  and  $n_{\perp}$ , respectively. For the Voigt effect derived from the gyroelectric

tensor in (2.58) (i.e.  $Q_V \neq 0$ ), the E-vector in case of the perpendicular wave is not strictly perpendicular to the direction of propagation though it is approximately so (remember that  $|iQ_V| \ll 1$ ). This, however, does not apply for D, which is strictly perpendicular to k (for non-absorbing media) as explained in Fig. 2.6. In any case, the two waves propagate parallel and antiparallel to the incident wave like for the case of circular polarization. For the gyroelectric Voigt effect the four waves are explicitly given by [178] [compare (2.64)]

$$\begin{aligned} E_{1,3,\parallel} &= e_{x} E_{\parallel}^{0} e^{i(\pm k_{0} n_{\parallel} z - \omega t)}, \\ E_{2,4,\perp} &= (e_{y} + e_{z} i Q_{V}) E_{\perp}^{0} e^{i(\pm k_{0} n_{\perp} z - \omega t)}. \end{aligned}$$
(2.69)

## 2.4 Faraday and Kerr Effect

After having introduced the electromagnetic basics of the magneto-optical effects, we will now have a closer look at the circular magneto-optical birefringence—the Faraday effects in transmission and the Kerr effects in reflection. The Kerr effect applies to any metallic or otherwise light-absorbing magnetic material, whereas the Faraday effect occurs in optically transparent media. Nevertheless, both are *rotational* effects that follow the same phenomenology. Therefore the two effects are discussed together in this section with emphasis on the Kerr effects. Two approaches of phenomenological description will be used: In Sect. 2.4.1 the discussion is based on circular polarization, leading finally to a derivation of the Kerr amplitude. In Sect. 2.4.2 the Kerr amplitude is then used as one of the components of the electrical field on a cartesian basis, which allows to derive the geometry of the Kerr effects in a descriptive way.

# 2.4.1 Phenomenological Description

The Faraday rotation and Faraday ellipticity can be interpreted as circular birefringence and circular dichroismeffects, respectively, in the same sense as optical activity introduced in Sect. 2.2.3. This can be directly derived from the electromagnetic treatment presented at the end of Sect. 2.3. From (2.62) we have seen that for light propagating along the magnetization the normal modes are two oppositely rotating circular polarizations. Linearly polarized light entering the medium is resolved into these two modes which travel along without interaction. Each circular mode has its own index of refraction  $n_+$  and  $n_-$  as given in (2.63). If the wave has a wavelength of  $\lambda_0$  in vacuum, then the wave lengths of its circular components in the medium are  $\lambda_0/n_\pm$  according to (2.8) and (2.9). Since  $n_+$  and  $n_-$  may differ in both real and imaginary parts [see (2.65)], the two partial waves will generally propagate with different dispersion (i.e. with different velocities  $c_0/n_+$  and  $c_0/n_-$ ) and different absorption. Due to the difference in dispersion the two circular waves cover different optical paths  $ln_+$  and  $ln_-$  while propagating a distance l. The optical retardation of

 $l(n_+ - n_-)$  finally results in a rotation<sup>11</sup> of the polarization vector by an angle  $\theta$  (see Fig. 2.5c, d for illustration). The difference in absorption causes different amplitudes of the two circular modes which leads to ellipticity (compare Fig. 2.5a).

An analytical treatment is presented here for the *polar Faraday effect*. Consider a plane electromagnetic wave propagating along the positive z-direction in a magnetic medium with polar magnetization ( $|\mathbf{k}| = k_3$  and  $|\mathbf{m}| = m_3 = 1$ ). At the point z = 0 at the surface the wave shall be linearly polarized along the x-axis, i.e.

$$E_{\rm x} = E^0 e^{i(k_z z - \omega t)}, \quad E_{\rm y} = 0, \quad E_{\rm z} = 0.$$
 (2.70)

In the magnetic medium, the propagating wave can be written as the sum of right-and left-circularly polarized waves. According to (2.64) the x- and y-components of this wave are given by [170, 178]

$$E_{x} = \frac{1}{2}E^{0}(e^{i(k_{0}n_{-}z-\omega t)} + e^{i(k_{0}n_{+}z-\omega t)}) = E^{0}e^{i(k_{0}\bar{n}z-\omega t)}\cos(\frac{\rho}{2}),$$

$$E_{y} = \frac{1}{2}iE^{0}(-e^{i(k_{0}n_{-}z-\omega t)} + e^{i(k_{0}n_{+}z-\omega t)}) = E^{0}e^{i(k_{0}\bar{n}z-\omega t)}\sin(\frac{-\rho}{2}).$$
(2.71)

Here the sum of the two circular modes was expressed with the help of the normalized Jones vectors (2.36) and (2.37), i.e. the term  $(e_x \pm ie_y)$  in (2.64) is replaced by the vector  $\frac{1}{\sqrt{2}}(1, \pm i)$ , where the minus sign corresponds to right circular polarized light. For the final notations in (2.71) we have used the average refraction index

$$\bar{n} = \frac{1}{2}(n_+ + n_-) \tag{2.72}$$

and the phase difference

$$\rho = k_0 z (n_+ - n_-) \tag{2.73}$$

that has been introduced between  $E_x$  and  $E_y$  by the birefringence of the medium.

Let's assume for the moment that  $n_+$  and  $n_-$  are real, i.e. there is no absorption. From the notations on the right in (2.71) it is evident that at every depth z the wave is linearly polarized with its direction of polarization turned through an angle  $\theta = -\rho(z)/2$  from the positive x-axis to the negative y-axis to the negative <math>to the negative of the polarized at <math>to the negative of the negative of the negative of the negative <math>to the negative of the negative of the negative <math>to the negative of the negative of the negative <math>to the negative of the negative of the negative <math>to the negative of the negative of the negative <math>to the negative of the negative of the negative of the negative of the negative <math>to the negative of the negative <math>to the negative of the nega

 $<sup>^{11}</sup>$  As mentioned in Sect. 2.2.2, the Faraday rotation is non-reciprocal: if the light passes the material again in reversed direction, the rotation does not cancel but is rather doubled. This is different to the circular birefringence of optically active media. The reason is that the Faraday rotation is tied to the direction of the magnetization. In Sect. 2.4.2 we will see that the magnitude of rotation is proportional to the projection of M on the direction of propagation.

<sup>&</sup>lt;sup>12</sup> This is the situation illustrated in Fig. 2.5d. The rotation angle  $\theta$  is defined by  $\tan \theta = \frac{E_y}{E_x} = \frac{\sin(-\rho(z)/2)}{\cos(\rho(z)/2)} = -\tan \frac{\rho(z)}{2}$ , so that  $\theta = -\frac{\rho(z)}{2}$ .

polarized with its azimuth rotated by a complex angle

$$\theta_{\rm F}^{\rm c} = \theta_{\rm F} + i\xi_{\rm F} = -\frac{\rho(l)}{2} = -\frac{k_0 l}{2} [n'_{+} + in''_{+} - n'_{-} - in''_{-}]$$

$$= -\frac{\pi l}{\lambda_0} [(n'_{+} - n'_{-}) + i(n''_{+} - n''_{-})]. \tag{2.74}$$

The major axis of the ellipse is thus rotated by the angle  $Re(\theta_F^c)$ , which can be written as [170, 171]

$$\theta_{\rm F}/l = -\frac{\pi}{\lambda_0} \operatorname{Re}(n_+ - n_-) = -\frac{\pi}{\lambda_0} (n'_+ - n'_-)$$
 (2.75)

per unit thickness. This situation is illustrated in Fig. 2.11a for two oppositely magnetized domains under the assumption of no absorption of the partial waves. The angle  $\theta_F/l$  is called the *specific Faraday rotation* or *magnetic circular birefringence*—a birefringence of circularly polarized light. The difference in absorption results in an ellipticity of the polarization that is given by

$$\xi_{\rm F}/l = -\frac{\pi}{\lambda_0} \operatorname{Im}(n_+ - n_-) = -\frac{\pi}{\lambda_0} (n''_+ - n''_-)$$
 (2.76)

in case of small ellipticity (for strong ellipticity the exact term would apply which writes  $\tan \xi_{\rm F} = -\tanh(\frac{\pi l}{\lambda_0}) \, {\rm Im}(n_+ - n_-)$  [170, 176]). The angle  $\xi_{\rm F}/l$  is known as *specific Faraday ellipticity* or *magnetic circular dichroism*. With (2.9) and (2.23) it can be expressed as

$$\xi_{\rm F}/l = \frac{1}{4} (\alpha''_{-} - \alpha''_{+}),$$
 (2.77)

showing that the Faraday ellipticity is simply defined as the difference of the absorption coefficients of the two circular modes. Figure 2.11b illustrates the effect under the assumption of pure dichroism (i.e. the two circularly polarized partial waves are absorbed differently without retardation). In the general case both, circular birefringence and dichroism, will be relevant. The two partial waves will thus be out of phase and unequal in amplitude on leaving the medium, producing rotated elliptical waves as illustrated in Fig. 2.11c (also compare Fig. 2.5a). This is the same situation as depicted in Fig. 2.4, where instead of a circular basis a cartesian decomposition was chosen. Two phase-shifted, perpendicularly polarized partial waves of different amplitude also produce a rotated ellipse. Below we will call the high-amplitude wave the 'normal' component and the low-amplitude wave the 'Faraday' (or 'Kerr') component. Note that in case of the Kerr effect the ellipses and rotations illustrated in Figs. 2.4 and 2.11 would be drawn strongly exaggerated—real Kerr rotations and ellipticities are much weaker. For iron, for instance, rotation- and ellipticity angles of  $-0.05^{\circ}$  and  $+0.01^{\circ}$ , respectively, are found at 450 nm wavelength [180].

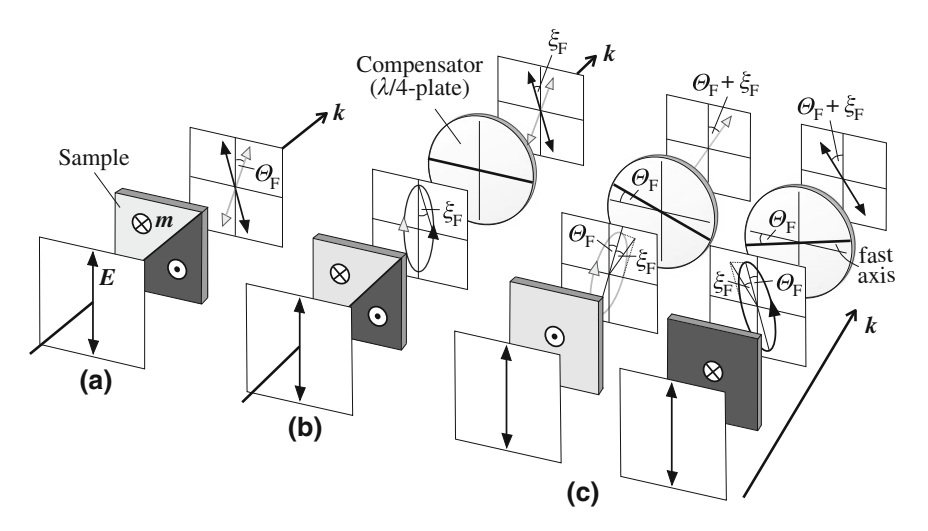


Fig. 2.11 Magnetically-induced circular birefringence (a), circular dichroism (b) and superimposition of the two effects (c), illustrated for linearly polarized light incidence and transmission (polar Faraday geometry). Shown is the trace of light polarization in the plane perpendicular to the direction of propagation. The magnetization of the sample is subdivided into two out-of-plane domains, which have different influences on the polarization state of the light as indicated by *black* and *gray arrows* that correspond to the domain color. In the birefringent sample the linear polarization is preserved (see Fig. 2.5c, d for illustration), though rotated in opposite directions (Faraday rotation  $\theta_F$ ) according to the corresponding magnetization direction. In case of a dichroic sample the two domains generate elliptically polarized light of different handedness (Faraday ellipticity  $\xi_F$ , compare Fig. 2.5a, b for illustration). Here a compensator is required to obtain linear light that can be converted into a contrast by means of an analyser. In c an opening of the compensator's fast axis by  $|\theta_F|$  leads to rotation of  $|\theta_F + \xi_F|$  if a quarter wave plate is used (compare Fig. 2.8). For the sign convention of the Faraday rotation and ellipticity see Fig. 2.3b

With the approximation in (2.63), the average complex refraction index  $\bar{n}$  is written as

$$\bar{n} = \frac{1}{2} (n_+ + n_-) = \sqrt{\epsilon_{\rm iso}},$$
 (2.78)

which corresponds to the "optical" index of refraction in the absence of magnetization, i.e. in case of a ferromagnet to the state above the Curie temperature. The specific Faraday rotation (2.75) and ellipticity (2.76) can then be expressed as

$$\theta_{\rm F}/l = -\frac{\pi}{\lambda_0} \operatorname{Re}(\bar{n} \ Q_{\rm V}) \quad \text{and} \quad \xi_{\rm F}/l = -\frac{\pi}{\lambda_0} \operatorname{Im}(\bar{n} \ Q_{\rm V})$$
 (2.79)

by using (2.63). In a reasonably transparent material (i.e. only moderate absorption,  $\bar{n}' \gg \bar{n}''$ ), it is the real part of the Voigt parameter  $Q_V$  that gives rise to circular dichroism while it is the imaginary part of  $Q_V$  that gives the circular birefringence [note that the Voigt parameter was introduced as  $iQ_V$  in the off-diagonal elements

of the  $\epsilon$ -tensor (2.58), so that its true real part becomes imaginary and vise versa]. On transmission through a specimen with a substantial circular dichroism only one circular polarization will survive.

The two effects discussed so far, the magnetic circular birefringence and dichroism, can be measured in transmission using the polar geometry mentioned above. For arbitrary orientation of sample and magnetization the wave equation (2.18) becomes fairly intractable because the two circular effects are mixed with the effects of magnetic linear dichroism and birefringence. A brief discussion of such mixed conditions will be given at the end of Sect. 2.5.

The magneto-optical *Kerr effects*, occurring when light is reflected on strongly absorbing magnetic media (like metals), are much weaker than the transmission effects as the light only interacts with the magnetization within a relatively thin surface layer given by the penetration depth of light. By taking the reflection coefficients into account, the Kerr rotation and ellipticity can—like the Faraday effect—be discussed as circular birefringence and dichroism effects. Like for the Faraday effect, we restrict the discussion to the *polar Kerr effect* ( $|\mathbf{k}| = k_3$  and  $|\mathbf{m}| = m_3 = 1$ ) for the moment to keep it simple. <sup>13</sup> Reviews on various ways to derive the Kerr effect on the basis of circular light, also including the cases of oblique incidence and in-plane magnetization, can be found in Sokolov's [176] and Višňovský's [178] books.

For the polar conditions, we have already established that the normal modes of propagation in the sample are right- and left-handed circular waves with refraction indices  $n_-$  and  $n_+$ , respectively. Outside the sample these are also possible modes, so that the reflection coefficients can be simply calculated by applying the usual Fresnel relations (2.52) for normal light incidence to each of the circular components (and assuming air as the incident medium, i.e.  $n_i = 1$  in the Fresnel formula) [171]:

$$r(n_{+}) = \frac{1 - n_{+}}{1 + n_{+}}$$
 and  $r(n_{-}) = \frac{1 - n_{-}}{1 + n_{-}}$ . (2.80)

Considering the complex nature of  $n_{\pm}$  [see (2.65)] and recalling notation (2.30) for the electromagnetic amplitudes for circularly polarized light, the reflection coefficients (2.80) of circularly polarized light may as well be noted in terms of x- and y-components

$$r(n_{+}) = r_{x} + i r_{y}$$
 and  $r(n_{-}) = r_{x} - i r_{y}$ . (2.81)

<sup>&</sup>lt;sup>13</sup> The analysis of the Kerr effect at oblique light incidence, which is generally required to obtain a Kerr signal on in-plane domains (see Sect. 2.4.2), is more complicated [170]: Here the wave in the medium is a mixture of linearly and circularly polarized eigenmodes. For normal incidence, however, and with the magnetization either parallel or perpendicular to the surface, the symmetry is high enough so that these polarizations do give pure eigenmodes in the medium.

From (2.81) we obtain

$$r_{\rm x} = \frac{1}{2} [r(n_+) + r(n_-)]$$
 (2.82a)

$$r_{y} = \frac{1}{2} i[r(n_{+}) - r(n_{-})],$$
 (2.82b)

which can be written as

$$r_{\rm x} = \frac{1 - \bar{n}}{1 + \bar{n}} \equiv N \tag{2.83a}$$

$$r_{\rm y} = \frac{-i\,\bar{n}\,Q_{\rm V}}{(1+\bar{n})^2} \equiv K$$
 (2.83b)

by making use of (2.80) together with (2.63) and (2.78) and ignoring terms of higher order in  $Q_V$ . For an incident linearly polarized wave along the x-axis

$$E = \begin{pmatrix} E_{\mathbf{x}}^{\text{in}} \\ 0 \end{pmatrix}, \tag{2.84}$$

the reflected wave is, according to (2.50), given by

$$\begin{pmatrix} E_{\rm x}^{\rm refl} \\ E_{\rm y}^{\rm refl} \end{pmatrix} = \begin{pmatrix} r_{\rm xx} \ r_{\rm xy} \\ r_{\rm yx} \ r_{\rm yy} \end{pmatrix} \begin{pmatrix} E_{\rm x}^{\rm in} \\ 0 \end{pmatrix} = \begin{pmatrix} r_{\rm xx} E_{\rm x}^{\rm in} \\ r_{\rm yy} E_{\rm x}^{\rm in} \end{pmatrix} = \begin{pmatrix} N E_{\rm x}^{\rm in} \\ K E_{\rm x}^{\rm in} \end{pmatrix} \equiv \begin{pmatrix} R_{\rm N} \\ R_{\rm K} \end{pmatrix}, \quad (2.85)$$

where  $r_{xx}$  and  $r_{yy}$  correspond to  $r_x$  and  $r_y$  in (2.82a, 2.82b) and (2.83a, 2.83b), respectively.

The important point to note from this discussion is that an impinging linear wave, polarized along the x-axis, will generate a reflected wave that has a (small) y-component, and this is due to the different  $n_+$  and  $n_-$ ! Regularly reflected light is polarized in the same plane as the incident light. We therefore call the x-component of the reflected amplitude (2.85) the regular component  $R_N$ , which is defined by the regular Fesnel reflectance N of demagnetized material, and the magneto-optically induced y-component the Kerr component R<sub>K</sub> that is defined by the Kerr coefficient K. In Fig. 2.12 the two coefficients are visualized in terms of the reflection of circularly polarized light by making use of (2.82a, 2.82b). As both orthogonally polarized components,  $R_{\rm N}$  and  $R_{\rm K}$ , are in general out of phase, the light reflected from a magnetic specimen will be elliptically polarized. This holds for the Kerr effect and to a much stronger degree for the Voigt effect that will be described by the Voigt component  $R_{\rm V}$  and discussed in Sect. 2.5. On basis of the two phase-shifted orthogonal components an elliptical wave is described as sketched in Fig. 2.4a. Making use of (2.28c), <sup>14</sup> the ratio of the Kerr- and regular light components can be expressed as a function of ellipticity  $\xi_K$  and azimuth  $\theta_K$ :

<sup>&</sup>lt;sup>14</sup> and considering the different sign conventions used in Fig. 2.4a and in the representation of the Kerr ellipses according to Fig. 2.3b. The angles in both conventions are related as  $\theta_{\rm K}=-\theta$  and  $\xi_{\rm K}=\xi$ .

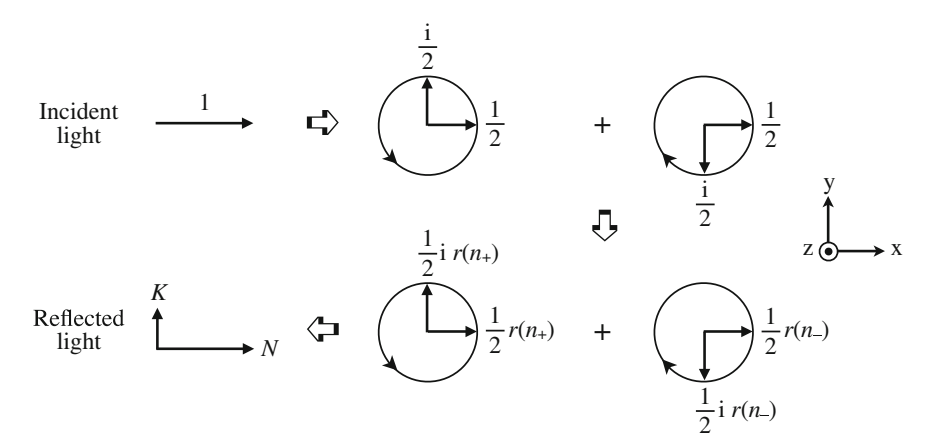


Fig. 2.12 Representation of the polar magneto-optical Kerr effect in terms of the reflection of circularly polarized light. The incident linear wave, polarized along x, is split into two counterrotating circularly polarized waves which then interact with the magnetic medium. According to (2.82b) a Kerr component K is generated that is polarized along the y-axis and which interferes with the regularly reflected component N (after [181])

$$\frac{R_{\rm K}}{R_{\rm N}} = \frac{K}{N} = \frac{-E_{\rm y}}{E_{\rm x}} = -\frac{\tan\theta - i\tan\xi}{1 + i\tan\theta\tan\xi} = \frac{\tan(\theta_{\rm K}) + i\tan(\xi_{\rm K})}{1 - i\tan(\theta_{\rm K})\tan(\xi_{\rm K})}$$
(2.86)

with the azimuth being defined relative to the polarization plane of the regularly reflected light. As the angles  $\xi_K$  and  $\theta_K$  are very small (at least in bulk samples where transmission effects can be excluded), the tangent terms in (2.86) can be replaced by their arguments and the term of second order can be neglected, leading to the *complex Kerr rotation*  $\theta_K^c$ :

$$\frac{K}{N} \approx \theta_{\rm K} + i \, \xi_{\rm K} = \theta_{\rm K}^{\rm c}.$$
 (2.87)

Since the Kerr rotation is complex, the vibration is transformed from linear into elliptical on reflection from a ferromagnet, and the semi-major axis is at an angle to the direction of the incident plane-polarized vibration. The real angle of rotation  $(\theta_K)$  of the semi-major axis of the vibration ellipse corresponds to the real part of  $\theta_K^c$ , and the Kerr ellipticity to its imaginary part. As magneto-optical effects are described by amplitude ratios, we can always normalize properly so that N becomes real, and write the Kerr effect in its polar form:

$$\theta_{K}^{c} = K_0 \exp(i \delta_{K}). \tag{2.88}$$

Here  $K_0$  is the magnitude of the Kerr amplitude and  $\delta_K$  the Kerr phase. If  $\delta_K$  is positive, the Kerr amplitude lags behind the regular amplitude. The polar form can be favorably applied in Hamrle's description of depth selective Kerr microscopy (Sect. 3.2.6).

For the polar geometry and with K and N defined in (2.83a, 2.83b), the complex Kerr rotation can now be written as

$$\theta_{K}^{c} = \theta_{K} + i \xi_{K} = \frac{K}{N} = -i \frac{\bar{n} Q_{V}}{1 - \bar{n}^{2}}.$$
 (2.89)

by using (2.87). Due to the imaginary unit in front of the fraction, the real angle of rotation is obviously a result of the imaginary part of the fraction, which is non-zero only in absorbing media:

$$\theta_{K} = \text{Re}(\theta_{K}^{c}) = \text{Im}\left(\frac{\bar{n} Q_{V}}{1 - \bar{n}^{2}}\right), \tag{2.90}$$

and the ellipticity is accordingly given by

$$\xi_{K} = \operatorname{Im}(\theta_{K}^{c}) = -\operatorname{Re}\left(\frac{\bar{n} \ Q_{V}}{1 - \bar{n}^{2}}\right), \tag{2.91}$$

looking along the positive z-direction. Note particularly that the rotation on reflection comes primarily from the imaginary part and the ellipticity from the real part of the off-diagonal elements of the magneto-optical matrix. This is reverse to the situation on transmission, compare (2.79). The Kerr rotation thus corresponds to the Faraday ellipticity and the Kerr ellipticity to the Faraday rotation. Recalling that the imaginary part of  $\bar{n}$   $Q_V$  is zero for non-absorbing materials, we see that the rotation on reflection is zero for a transparent medium. The reflected light is then just elliptically polarized with the major axis parallel to the plane of polarization of the incident light. Rotation in reflection requires a non-vanishing imaginary part and thus absorption. For highly transparent magnetic garnets, for example, no domain observation truly based on the Kerr effect has been reported (domains in garnets are observed in transmission by the Faraday effect, perhaps using a mirror for reflection observations [111]).

For the general case of oblique incidence, the plane of incidence can be defined according to Fig. 2.3a. It is then convenient to use the *sp*-representation (2.51) of the Fresnel reflection matrix. Solving Maxwell equations for the linear magneto-optical tensor in (2.58) in a more general way than before, leads to the following reflection coefficients [179, 182–184]

$$r_{\rm pp} = \frac{n_0 \cos \vartheta_1 - n_1 \cos \vartheta_0}{n_1 \cos \vartheta_0 + n_0 \cos \vartheta_1} - \frac{i 2n_0 n_1 \cos \vartheta_0 \sin \vartheta_1 m_{\rm x} Q_{\rm V}}{(n_1 \cos \vartheta_0 + n_0 \cos \vartheta_1)^2},$$
 (2.92a)

$$r_{\rm sp} = \frac{\mathrm{i} \, n_0 n_1 \cos \vartheta_0 (m_z \cos \vartheta_1 + m_y \sin \vartheta_1) \, Q_{\rm V}}{(n_1 \cos \vartheta_0 + n_0 \cos \vartheta_1) (n_0 \cos \vartheta_0 + n_1 \cos \vartheta_1) \cos \vartheta_1},\tag{2.92b}$$

$$r_{\rm ss} = \frac{n_0 \cos \vartheta_0 - n_1 \cos \vartheta_1}{n_0 \cos \vartheta_0 + n_1 \cos \vartheta_1},\tag{2.92c}$$

$$r_{\rm ps} = -\frac{\mathrm{i}\,n_0 n_1 \cos\vartheta_0 (m_{\rm z}\cos\vartheta_1 - m_{\rm y}\sin\vartheta_1) Q_{\rm V}}{(n_1\cos\vartheta_0 + n_0\cos\vartheta_1)(n_0\cos\vartheta_0 + n_1\cos\vartheta_1)\cos\vartheta_1}. \tag{2.92d}$$

Here  $n_0$  is the refractive index of the environment (air or an immersion medium),  $n_1 = n_1' + i n_1''$  is the complex index of refraction of the magnetic material,  $Q_V$  is its magneto-optical Voigt constant,  $\vartheta_0$  is the angle of incidence (measured from the surface normal) and  $\vartheta_1$  is the (complex) angle of incidence in the magnetic medium, to be calculated from  $\vartheta_0$  by Snell's law (2.54)  $\cos \vartheta_1 = \sqrt{1 - (n_0 \sin \vartheta_0/n_1)^2}$ . Like in the previous discussion, above equations are valid within the first-order approximation of the Voigt constant. By generalizing previous arguments, the complex Kerr effect is then defined by the ratios of the off-diagonal elements to the diagonal elements of the reflection matrix. For the two standard geometries of s- and p-polarized incident light these ratios are given by

$$\theta_{\rm K}^{\rm p} \equiv \frac{r_{\rm sp}}{r_{\rm pp}}$$
 and  $\theta_{\rm K}^{\rm s} \equiv \frac{r_{\rm ps}}{r_{\rm ss}}$ . (2.93)

As an example, let us have a closer look at the polar configuration ( $m_z = 1$  and  $m_x = m_y = 0$ ) with s-polarized, obliquely incident light. By substituting (2.92d) and (2.92c) in (2.93), the complex Kerr rotation is obtained:

$$(\theta_{K}^{s})^{pol} = \left(\frac{r_{ps}}{r_{ss}}\right)^{pol} = \frac{-i n_{0} n_{1} \cos \vartheta_{0} Q_{V}}{(n_{1} \cos \vartheta_{0} + n_{0} \cos \vartheta_{1})(n_{0} \cos \vartheta_{0} - n_{1} \cos \vartheta_{1})}. (2.94)$$

For normal incidence ( $\vartheta_0 = \vartheta_1 = 0^\circ$ ) and  $n_0 = 1$  this expression is identical with (2.89). With the Fresnel formulae (2.52) and (2.53), the complex Kerr rotation (2.94) can be written as

$$(\theta_{K}^{s})^{pol} = \frac{-i n_1 Q_V t_{ss}^{01} t_{pp}^{01}}{4 n_0 \cos \vartheta_0} \frac{1}{r_{ss}^{01}}.$$
 (2.95)

Here we have also considered the upper indices in the Fresnel coefficients according to (2.52) and (2.53). Recalling that the Kerr rotation is the ratio between Kerr coefficient and coefficient of the normally reflected amplitude [here given by  $N_{\rm s}=r_{\rm ss}^{01}$ , where  $r_{\rm ss}^{01}$  is the regular reflection coefficient of the demagnetized material as defined in the Fresnel equation (2.52)], the Kerr coefficient  $K_{\rm ps}^{\rm pol}$  is finally given by the first fraction in (2.95):

$$K_{\rm ps}^{\rm pol} = \frac{-i n_1 Q_{\rm V} t_{\rm ss}^{01} t_{\rm pp}^{01}}{4 n_0 \cos \vartheta_0}.$$
 (2.96)

This coefficient is interpreted as follows: the incident light is s-polarized, resulting in a p-polarized Kerr amplitude as indicted by the lower index ps in  $K_{ps}^{pol}$ . The portion of the incident light, which penetrates into the metal ( $t_{ss}^{01}$ ), generates the Kerr amplitude by interaction with the magnetization. Its size depends on the material constant  $Q_V$  and the angle of incidence  $\vartheta_0$ . The p-polarized Kerr amplitude has to leave the material to be detected, actually described by the transmission coefficient

 $t_{\rm pp}^{10}$ . In (2.96) this coefficient is hidden in  $t_{\rm pp}^{01}$ , which is related to  $t_{\rm pp}^{10}$  by identity  $t^{\rm ji}/t^{\rm ij} = n_{\rm j}\cos\vartheta_{\rm j}/n_{\rm i}\cos\vartheta_{\rm i}$  according to the Fresnel formulae (2.53). If the polarization direction of the incident light is rotated by 90°, the sign of the polar Kerr coefficient (now  $K_{\rm sp}^{\rm pol}$ ) is inverted.

The Kerr coefficients for in-plane magnetization ( $m_z = 0$ ,  $m_{x,y} \neq 0$ ) can be derived in a similar way from (2.92a–2.92d) and (2.93). In vector notation all Kerr coefficients are summarized as [185]:

$$K_{\rm ps}^{\rm bulk} = \frac{iQ_{\rm V}t_{\rm pp}^{01}t_{\rm ss}^{01}}{4\cos\vartheta_0} \left(0, \frac{\sin\vartheta_0}{\cos\vartheta_1}, \frac{-n_1}{n_0}\right),\tag{2.97a}$$

$$K_{\rm sp}^{\rm bulk} = \frac{i Q_{\rm V} t_{\rm pp}^{01} t_{\rm ss}^{01}}{4 \cos \vartheta_0} \left( 0, \frac{\sin \vartheta_0}{\cos \vartheta_1}, \frac{+n_1}{n_0} \right), \tag{2.97b}$$

$$K_{\rm pp}^{\rm bulk} = \frac{iQ_{\rm V}t_{\rm pp}^{01}t_{\rm pp}^{01}}{4\cos\vartheta_0} \left(-2\sin\vartheta_0\,,\,0\,,\,0\right). \tag{2.97c}$$

As indicated by the upper index, these coefficients are valid for bulk magnetic material. The coefficient  $K_{\rm pp}^{\rm bulk}$  is derived from  $r_{\rm pp}^{\rm (mag)}/r_{\rm pp}^{\rm (0)}$  in (2.92a), where  $r_{\rm pp}^{\rm (0)}$  is the first fraction and  $r_{\rm pp}^{\rm (mag)}$  the (magnetization-dependent) second one. In the next section we will make use of the Kerr coefficients to describe the geometry of the rotation effects.

## 2.4.2 Geometry of the Rotation Effects

The dependence of the Faraday and Kerr effects on the direction of magnetization, light incidence and polarization can be rigorously derived from the dielectric magneto-optical tensor, Maxwell's equations, and the proper boundary conditions. Examples of such solutions and a detailed analysis for the example of the polar Faraday and Kerr effects have been presented in the previous Sect. (2.4.1). The discussion was based on circular polarization, which finally led to a derivation of the Kerr amplitude. The symmetry of the solutions, however, can also be derived by simple arguments based on the *Lorentz concept*.

To see this, let us recall the dielectric law of the Kerr- and Faraday effects. With (2.3a) and (2.58) we have seen that, in the regime of optical frequencies, the "rotational" nature of these two effect is phenomenologically described by

$$\mathbf{D} = \epsilon_0 \epsilon \mathbf{E} = \epsilon_0 n^2 \begin{pmatrix} 1 & -iQ_V m_3 & iQ_V m_2 \\ iQ_V m_3 & 1 & -iQ_V m_1 \\ -iQ_V m_2 & iQ_V m_1 & 1 \end{pmatrix} \mathbf{E},$$
 (2.98)

with the refractive index of the medium being related to the isotropic dielectric constant by  $n=\sqrt{\epsilon_{\rm iso}}$ . If the off-diagonal elements of the antisymmetric  $\epsilon$ -tensor would be zero, the displacement vector would be along the same direction as the E-vector. The light would then interact with the matter without rotation of its polarization plane. A rotation of the vibrational plane requires the off-diagonal elements, which contain the components of the magnetization vector. By rewriting the dielectric law (2.98) as

$$\mathbf{D} = \varepsilon_0 n^2 [\mathbf{E} + i O_V(\mathbf{m} \times \mathbf{E})] \tag{2.99}$$

it becomes obvious that the E-vector of the illuminating light interacts with the magnetization vector m in a cross-product fashion in the same symmetry as a Lorentz force that acts on the light-agitated electrons, thus revealing the gyroelectric nature of the Kerr and Faraday effects. A magnetization-dependent contribution to the D-vector is obviously only generated if  $m \times E$  is non-zero.

This Lorentz concept leads to simple derivation of the symmetry of the rotation effects as illustrated in Fig. 2.13. Let us first assume perpendicular magnetization and oblique incidence of light (Fig. 2.13a). According to the Lorentz concept, the E-vector of the incident light wave excites electrons in the specimen to an oscillation motion parallel to its plane of polarization. The oscillatory motion acts as source for the emitted light in terms of a Hertz dipole. Regularly reflected or transmitted light is polarized in the same plane as the incident light. In Sect. 2.4.1 we have called this the regular component  $R_N$  of the emerging light. At the same time, the Lorentz force induces a small component of vibrational motion perpendicular to the primary motion and to the direction of magnetization. This secondary motion is proportional to the 'Lorentz velocity'  $v_{Lor} = -m \times E$ . Because of Huygens' principle, the secondary motion creates secondary amplitudes: the Kerr amplitude  $R_{\rm K}$  for reflection and the Faraday amplitude  $R_{\rm F}$  for transmission. Due to the transverse nature of electromagnetic waves, these magneto-optic light amplitudes are obtained by projecting the Lorentz movement  $v_{Lor}$  onto the plane perpendicular to the propagation direction of the light wave used in observation. It was shown by Wenzel et al. [186] that this simple recipe describes for small  $Q_{\rm V}$  all possible cases: transmission, reflection, all directions of the magnetization, and even magnetic diffraction by nonuniform magnetization fields. The superposition of  $R_N$  with  $R_K$  (or  $R_{\rm F}$ ) finally leads to magnetization-dependent polarization rotations if  $R_{\rm N}$  and  $R_{\rm K}$  (or  $R_{\rm F}$ ) are in phase. In case of a phase shift elliptically polarized light emerges. This is a situation as illustrated in Fig. 2.4a (the x- and y-components of the cartesian decomposition of the E-vector in this figure correspond to  $R_N$  and  $R_K$  or  $R_F$ ). Ellipticity can be eliminated, e.g., with a compensator, but let us ignore this complication for the moment.

Depending on the relative orientation of magnetization, polarization-direction of the illuminating light, and the plane of light incidence, three fundamental geometries are traditionally defined for the rotation effects: the polar, longitudinal, and transverse Faraday- and Kerr effects:

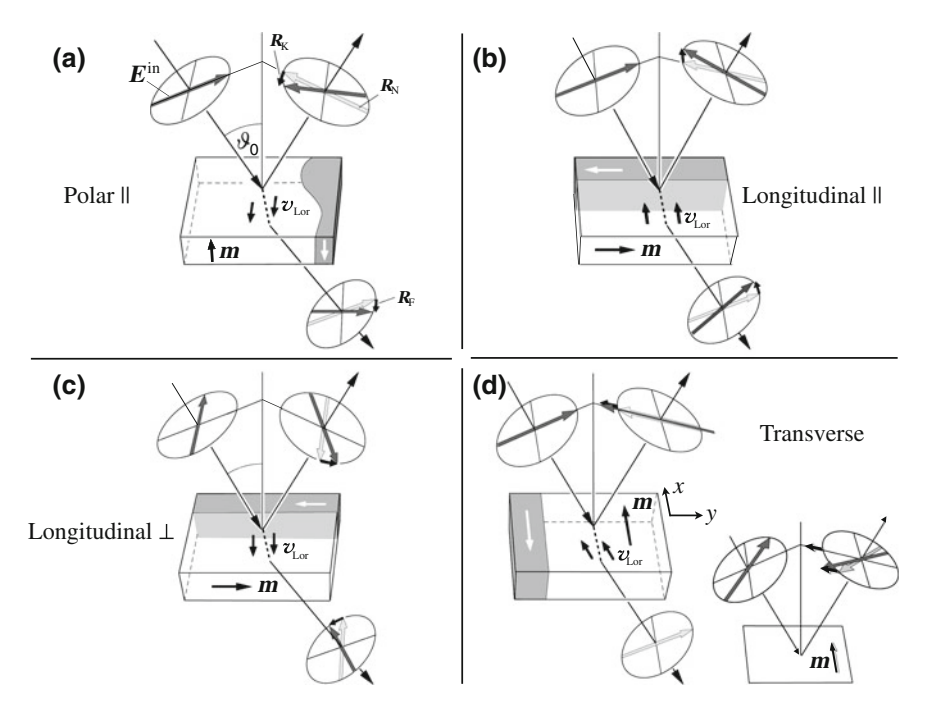


Fig. 2.13 Illustration of the basic magneto-optical rotation effects.  $R_N$  is the regularly reflected (or transmitted) electric field amplitude. The magneto-optical amplitudes  $R_K$  and  $R_F$  are generated by the Lorentz motion  $v_{Lor}$ . The polar effects (a) would also occur for a vanishing angle of incidence  $\vartheta_0$ , and they are independent of the direction of polarization  $E^{in}$  (chosen here parallel to the plane of incidence). The longitudinal effects, possible with parallel (b) and perpendicular (c) polarization directions, increase proportional to  $\sin \vartheta_0$ . The magnitude of the longitudinal effects is the same in (b) and (c), but of opposite sign. In the transverse case (d), only parallel polarization yields an effect, and only in reflection. A detectable rotation is obtained by polarizing the light at 45° as illustrated in the right figure of (d). Both, longitudinal and transverse effects, require a non-vanishing angle of incidence. After [111]

- In case of the *polar* effect (Fig. 2.13a) the magnetization is oriented perpendicular to the sample surface. This effect is strongest at perpendicular incidence ( $\vartheta_0 = 0^\circ$ ). It results in a rotation of the plane of polarization, which (for  $\vartheta_0 = 0^\circ$ ) is by symmetry the same for all polarization directions of the incident beam.
- If the magnetization is oriented parallel to the sample surface and along the plane of incidence, the *longitudinal* effects are obtained (Fig. 2.13b, c). To create a Lorentz force for in-plane magnetization, oblique incidence of light is required. For the longitudinal effect this yields a magneto-optical rotation for both, light that is polarized parallel and perpendicular to the plane of incidence. The rotation sense is opposite in the two cases. For  $\vartheta_0 = 0^\circ$  the Lorentz force either vanishes (Fig. 2.13b), or points along the beam (Fig. 2.13c), thus not generating a detectable rotation.

• For transverse orientation (Fig. 2.13d) the in-plane magnetization is perpendicular to the plane of incidence. No magneto-optical effect is possible in transmission because the cross-product (2.99) is either zero or points along the propagation direction. In reflection, however, p-polarized light will generate a Kerr amplitude, since the reflected beam has a different direction. It is again proportional to  $\sin \vartheta_0$ , but its polarization direction is the same as that of the regularly reflected beam. The transverse Kerr effect therefore causes an amplitude variation of the light, which can be used for measuring purposes, whereas in a microscopic image the contrast is very little. The amplitude modulation can be verified by comparing the Fresnel reflection coefficients for p- and s-polarization: the coefficient for the s-wave (2.92c) is equal to that of a non-magnetic material given in (2.52), whereas that of a p-wave (2.92a) contains an additional term that is proportional to  $Q_{\rm V}$  and  $m_{\rm x}$ . The *intensity* of the reflected wave thus becomes dependent on the magnetization direction—it changes sign by magnetization reversal even if one works with unpolarized light and without analyser. To generate a measurable rotation also in the transverse case, the light has to be polarized at 45° to the plane of incidence. Then the perpendicular light component is not affected by the magnetization, while the parallel component receives an amplitude modulation. Altogether this leads to a detectable rotation as illustrated in the inset of Fig. 2.13d. Note that the transverse Kerr effect has to be distinguished from the Voigt effect which occurs under similar geometric conditions. The transverse Kerr effect is odd in the magnetization direction, the Voigt effect is rather even (see Sect. 2.5).

The geometry of the magneto-optical rotation effects can be summarized as follows: The Kerr- and Faraday effects cause a rotation of light, which is proportional to the magnetization component parallel to the reflected or transmitted light beam. According to (2.98), both effects are *linear* in the magnetization. Consequently the Kerr- and Faraday rotation is inverted when the magnetization direction is inverted. Oppositely magnetized domains thus rotate plane-polarized light in opposite directions as illustrated in Fig. 2.14a for the longitudinal Kerr effect. A domain contrast in the Kerr microscope is obtained if the reflected light from different domains is blocked differently with an analyser as indicated in Fig. 2.14b. The theory of the Kerr contrast and its optimization is presented in Sect. 2.4.3.

A general formula [111, 174] for the signal amplitude of the Kerr effect is obtained by combining the three effects in a quantitative way. The polarizer of setting  $\alpha_{\rm pol}$ , measured from the axis perpendicular to the plane of incidence, defines the polarization plane of the incoming light (Fig. 2.14c). On reflection from the sample the light experiences regular reflection coefficients  $N_{\rm p}$  and  $N_{\rm s}$  for the amplitude components  $R_{\rm N}^{\rm p}$  and  $R_{\rm N}^{\rm s}$  parallel (index p) and perpendicular (index s) to the plane of incidence, respectively. At the same time the Kerr amplitudes  $R_{\rm K}^{\rm pol}$ ,  $R_{\rm K}^{\rm lon}$ , and  $R_{\rm K}^{\rm tra}$  with the coefficients  $K^{\rm pol}$ ,  $K^{\rm lon}$ , and  $K^{\rm tra}$  for the polar, the longitudinal and the transverse cases are excited [compare (2.85)], depending on the magnetization components  $m_{\rm pol}$ ,  $m_{\rm lon}$ , and  $m_{\rm tra}$ . Finally the light passes through an analyser (with the setting  $\alpha_{\rm an}$  measured from the the plane of incidence), leading to the total signal amplitude

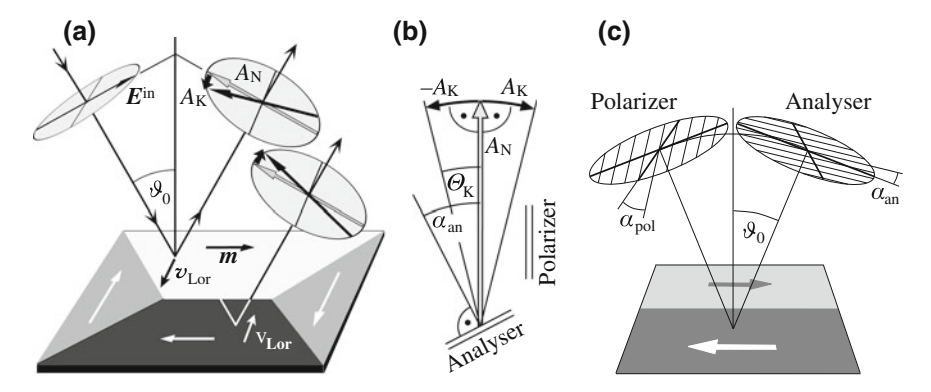


Fig. 2.14 a The elementary magneto-optical interaction of oppositely magnetized domains for the longitudinal Kerr effect. The Lorentz force in antiparallel domains acts in reversed direction so that the Kerr amplitude  $A_K$  changes sign [note that regular and Kerr amplitudes are denoted here by 'A' which stands for the generalized amplitudes defined in (2.100)]. b The interference of the normally reflected component  $A_N$  and the Kerr amplitude  $A_K$  results in a magnetization-dependent light rotation by the (small) angle  $\Theta_K$ , which, by using an analyser, leads to the domain contrast. The analyser should actually be set at an angle  $\alpha_{an} > \Theta_K$  to optimize the domain visibility. For the sketch it is assumed that a possible phase shift between  $A_N$  and  $A_K$  (ellipticity) is eliminated by a compensator. c Polarizer and analyser in a Kerr setup with definition of the respective angels (compare Fig. 2.7b)

$$A_{\text{tot}} = A_{\text{N}} \pm A_{\text{K}},\tag{2.100}$$

with

$$\begin{split} A_{\mathrm{N}} &= R_{\mathrm{N}}^{\mathrm{p}} \sin \alpha_{\mathrm{pol}} \cos \alpha_{\mathrm{an}} - R_{\mathrm{N}}^{\mathrm{s}} \cos \alpha_{\mathrm{pol}} \sin \alpha_{\mathrm{an}}, \\ A_{\mathrm{K}} &= R_{\mathrm{K}}^{\mathrm{pol}} \cos \left(\alpha_{\mathrm{an}} - \alpha_{\mathrm{pol}}\right) m_{\mathrm{pol}} - R_{\mathrm{K}}^{\mathrm{lon}} \cos \left(\alpha_{\mathrm{an}} + \alpha_{\mathrm{pol}}\right) m_{\mathrm{lon}} \\ &+ R_{\mathrm{K}}^{\mathrm{tra}} \sin \alpha_{\mathrm{pol}} \cos \alpha_{\mathrm{an}} m_{\mathrm{tra}}. \end{split}$$

This equation can also be used for a general magnetization direction different from the conventional polar, longitudinal, and transverse orientations. The total signal amplitude  $A_{\text{tot}}$  is the sum of the regular signal amplitude  $A_{\text{N}}$  and the *effective* Kerr amplitude  $A_{\text{K}}$ . The regular reflection coefficients,  $N_{\text{p}}$  and  $N_{\text{s}}$ , are those of demagnetized material as defined in the Fresnel equations (2.52) [see Sect. 2.4.1]:

$$N_{\rm p} = r_{\rm pp}^{01}$$
 and  $N_{\rm s} = r_{\rm ss}^{01}$ , (2.101)

and the Kerr coefficients for the three basic geometries are [111, 144, 177]:

$$K_{\rm sp}^{\rm pol} = \frac{\mathrm{i} Q_{\rm V} n_1}{4 n_0 \cos \vartheta_0} t_{\rm ss}^{01} t_{\rm pp}^{01}, \quad K_{\rm ps}^{\rm pol} = -K_{\rm sp}^{\rm pol},$$
 (2.102a)

$$K_{\rm sp}^{\rm lon} = \frac{iQ_{\rm V}\sin\vartheta_0}{4\cos\vartheta_0\cos\vartheta_1} t_{\rm ss}^{01} t_{\rm pp}^{01}, \quad K_{\rm ps}^{\rm lon} = K_{\rm sp}^{\rm lon}, \tag{2.102b}$$

$$K_{\rm pp}^{\rm tra} = -\frac{iQ_{\rm V}\sin\vartheta_0}{2\cos\vartheta_0} t_{\rm pp}^{01} t_{\rm pp}^{01}, \tag{2.102c}$$

according to (2.97a-2.97c).

Interesting is the relative strength of the longitudinal and polar Kerr effects. With Snell's law (2.54), the longitudinal Kerr coefficient can be written as  $K_{\rm sp}^{\rm lon}=(iQ_{\rm V}n_1t_{\rm ss}^{01}t_{\rm pp}^{01}\tan\vartheta_1)/(4n_0\cos\vartheta_0)=K_{\rm sp}^{\rm pol}\tan\vartheta_1$ . The polar and longitudinal Kerr effects thus differ just by the factor  $\tan\vartheta_1$ . At optical frequencies the refractive indices of metals are relatively large, i.e.  $\vartheta_1$  and therefore  $\tan\vartheta_1$  are typically of the order of 0.1. The polar Kerr effect is consequently by an order of magnitude stronger than the longitudinal (and transverse) Kerr effect.

#### 2.4.3 Kerr Contrast and Signal

The most important characteristics in magneto-optical microscopy are *contrast* and *signal-to-noise ratio*. Let's have a closer look at these parameters as they demonstrate the importance of the Kerr amplitude as a "figure of merit" in magneto-optics. The discussion in this section is specified to the Kerr contrast, but it equally well applies to the Voigt effect (Sect. 2.5) by simply replacing the generalized Kerr amplitude  $A_{\rm K}$  [defined in (2.100)] by a corresponding Voigt amplitude  $A_{\rm V}$ .

A domain contrast in the Kerr microscope is obtained if most of the reflected light from one domain type is blocked by the analyser as indicated in Fig. 2.14b. The light emerging from domains with other magnetization directions will then more or less pass the analyser and the rotation of the polarization plane is transferred to a detectable difference in intensities. Strongest contrast is expected between domains that create an opposite change of the polarization state (this is the situation assumed in Fig. 2.14b). In case of the Kerr effect these are domains with antiparallel magnetization<sup>15</sup> as shown in Fig. 2.11. If extinction is not possible due to elliptical contributions in the emerging light, the light can be made linear by means of a phase shifter (compensator, see Sect. 2.2.4). Elliptically polarized light is generated when the magneto-optical light component is phase-shifted relative to the regular component as discussed previously. Metallic reflection at oblique incidence always generates elliptical light if the polarization direction of the incident light is not perpendicular or parallel to the plane of incidence (like for the transverse Kerr effect at 45° polarization). But even if this is the case like in the longitudinal effects, an intrinsic Kerr ellipticity can occur as shown in Sect. 2.4.1. It is, however, usually small. In Kerr microscopy, ellipticity can often sufficiently be compensated by slightly rotating the polarizer [144], without the need of a compensator.

According to Fig. 2.14b, it seems reasonable to chose an analyser setting that would exactly extinguish the light coming from one of the domain phases,

<sup>&</sup>lt;sup>15</sup> In case of the Voigt effect, orthogonally magnetized domains lead to the strongest contrast as shown in Sect. 2.5.

i.e.  $\alpha_{\rm an}=\theta_{\rm K}$ . This domain phase will then appear dark, whereas all other domain phases will appear more or less bright. In practice, however, analyser angles of a few degrees are typical, which is much more than the typical Kerr rotations of less than a degree. This can also be reasoned theoretically: Let us assume the general case of a phase shift between  $A_{\rm N}$  and  $A_{\rm K}$ , so that  $A_{\rm K}$  is a complex number (if the phases of regular and magneto-optical amplitude would be equal, then  $A_{\rm N}$  and  $A_{\rm K}$  could be taken as real numbers). For an opening angle  $\alpha_{\rm an}$ , by which the analyser is rotated away from the crossed position relative to the polarizer, the intensities of the domains become [111, 187]:

$$I_{1} = [A_{N} \sin(\alpha_{an}) - A_{K} \cos(\alpha_{an})][A_{N} \sin(\alpha_{an}) - A_{K} \cos(\alpha_{an})]^{*} + I_{0},$$

$$(2.103a)$$

$$I_{2} = [A_{N} \sin(\alpha_{an}) + A_{K} \cos(\alpha_{an})][A_{N} \sin(\alpha_{an}) + A_{K} \cos(\alpha_{an})]^{*} + I_{0}.$$

$$(2.103b)$$

Here  $I_1$  and  $I_2$  are the intensities of the "dark" and "bright" domain, respectively, and  $I_0$  is a background intensity that is, e.g., caused by an imperfect polarization degree of the polarizers, the use of a finite illumination aperture and by depolarizing effects at lenses and the sample. The star (\*) denotes the conjugate complex. The products in (2.103a, 2.103b) sensitively depend on the phase difference  $\delta_K$  between  $A_N$  and  $A_K$  that was defined in (2.88). For the Kerr effect, the "intrinsic" phase difference is usually small, whereas for the Voigt effect (see Sect. 2.5) it can amount to  $\pi/2$ . The phase difference can also depend on possibly present interference layers, which have a different influence on the magneto-optical and regular light amplitudes [144].

The Kerr signal is largest if the phase difference  $\delta_K$  is an integer multiple of  $2\pi$ . To fulfill this condition in a magneto-optical experiment, the phase shift between  $A_N$  and  $A_K$  has (possibly) to be adjusted. This can be achieved, for instance, with a Babinet compensator with controllable phase difference  $\Delta \varphi$  (2.40). For maximum signal, the optical axes of the compensator have to be aligned perpendicular and parallel, respectively, to the polarization plane of the regularly reflected light. Then the phase  $\delta_K$  of the Kerr amplitude  $A_K$  can be exactly compensated by  $\Delta \varphi$ . This applies to the Kerr amplitudes of both domains (see Fig. 2.14b) simultaneously in case of a Babinet compensator. The relative Kerr signal  $S_K$ , which is the difference between the two domain intensities (2.103a, 2.103b), is then written as [187]:

$$S_{K} = 2\cos(\delta_{K} + \Delta\varphi)\sin(2\alpha_{an})A_{K}A_{N}, \qquad (2.104)$$

where the cos-term considers the degree of phase adjustment.

A Babinet compensator cannot be favorably used in wide-field microscopy (see Sect. 2.2.4). Here rather compensators of the *Brace-Köhler* type are applied, i.e. phase-plates with a fixed phase difference between ordinary and extraordinary beam. A variable phase shift is obtained by rotating the phase plate around its normal axis. There is, however, no neutral position which leaves *both* amplitudes unaffected. In case of a quarter-wave plate with  $\Delta \varphi = \pi/2$ , which is oriented at an angle of 45°

between its optical axis and  $A_N$ , a signal

$$S_{K} = 2\sin(\delta_{K} + 2\alpha_{an})A_{K}A_{N} \tag{2.105}$$

is obtained. In both cases (2.104, 2.105) the Kerr signal is a linear function of the Kerr amplitude and therefore, according to (2.98), also linear in the magnetization vector. This is very unusual for microscopy in general, where mostly quadratic effects are observed and the phase information is lost. The Kerr signal can be optimized by increasing the analyser angle. However, at the same time the brightness rises, which might not always be of an advantage.

To see the problem, let us again consider the application of a Babinet compensator for simplicity. It allows to compensate the ellipticity in such a way that plane-polarized light from both domains in Fig. 2.14b is obtained simultaneously. The signal then gets maximum for  $\alpha_{\rm an}=45^\circ$  according to (2.104). The high brightness for such wide opening, however, does not lead to an optimized contrast for visual observation. The contrast C is given by

$$C = (I_2 - I_1)/(I_2 + I_1). (2.106)$$

Optimization with respect to the analyser angle  $\alpha_{an}$  gives the maximum contrast

$$C_{\text{opt}} = \frac{A_{\text{K}} A_{\text{N}}}{\sqrt{(A_{\text{K}}^2 + I_0)} \sqrt{(A_{\text{N}}^2 + I_0)}} \approx \frac{A_{\text{K}}}{\sqrt{(A_{\text{K}}^2 + I_0)}},$$
 (2.107)

which is achieved already at an angle  $\alpha_{an} = \alpha_{opt}^{C}$  smaller than 45°:

$$\tan \alpha_{\text{opt}}^C = \sqrt{\frac{A_{\text{K}}^2 + I_0}{A_{\text{N}}^2 + I_0}}.$$
 (2.108)

As the background  $I_0$  is much smaller than  $A_N^2$ , the optimum contrast can be approximated by the second term in (2.107). For large  $A_N$ , the optimum contrast obviously depends on the background intensity and on the Kerr amplitude only—not on the regular amplitude  $A_N$  or the Kerr rotation  $\theta_K = A_K/A_N$ .

In todays Kerr microscopy, however, the contrast is not the decisive criterion. By image processing (Sect. 3.1.1) it can be easily enhanced with electronic means. For video microscopy, a large signal-to-noise ratio,  $r_{SN}$ , is rather important in order to obtain good domain visibility. This ratio is maximized by increasing the signal, which again requires larger opening angles  $\alpha_{an}$  than necessary for optimum contrast (with increasing angle  $\alpha_{an}$  the image intensity increases with  $\alpha_{an}^2$ ). The optimum analyser angle  $\alpha_{opt}^{SN}$  depends on the ratio of the different noise contributions. Three sources of noise have to be taken into account: (i) Temperature-dependent noise of the detection electronics that is usually independent of the image intensity.

(ii) Fluctuations in the light source, in the optical path, and in the sample (in magneto-optical recording this noise is called "media noise"), which will be proportional to the image intensity. (iii) Shot noise based on the quantized nature of light. This unavoidable noise contribution can be reduced by averaging over a large number of photons due to its statistical character. Shot noise varies with the square root of the photon number in the image. The less the noise depends on the average detected intensity, the better are larger opening angles. In the limiting case of an intensity-independent detector noise as sole noise mechanism, the optimum angle  $\alpha_{\text{opt}}^{\text{SN}}$  is 45°, i.e. the angle for maximum signal according to (2.104). An optimum signal then also results in an optimum  $r_{\text{SN}}$ . If, on the other hand, those fluctuations are dominating that are proportional to the intensity, a maximum  $r_{\text{SN}}$  is obtained by maximizing the contrast at  $\alpha_{\text{opt}}^{\text{SN}} = \alpha_{\text{opt}}^{\text{C}}$ .

An ideal image processing is only limited by the unavoidable shot noise. In this case the optical noise may be written as

$$N_{\text{shot}} = \sqrt{\frac{1}{2} F_{\text{inc}}(I_1 + I_2)},$$
 (2.109)

where  $F_{\text{inc}}$  is the incident number of photons. With the absolute signal  $S_{\text{mo}} = F_{\text{inc}}(I_1 - I_2)$  we obtain

$$r_{\rm SN} = S_{\rm mo}/N_{\rm shot} = \sqrt{F_{\rm inc}}(I_1 - I_2)/\sqrt{\frac{1}{2}(I_1 + I_2)}.$$
 (2.110)

Inserting (2.103a, 2.103b) and minimizing with respect to the analyser angle  $\alpha_{an}$  we obtain for the maximum signal-to-noise ratio [187]:

$$r_{\rm SN}^{\rm opt} = \frac{4A_{\rm K}A_{\rm N}\sqrt{F_{\rm inc}}}{\sqrt{A_{\rm N}^2 + I_0} + \sqrt{A_{\rm K}^2 + I_0}} \approx 4A_{\rm K}\sqrt{F_{\rm inc}},$$
 (2.111)

if the analyser is opened beyond the setting of optimum contrast to

$$\tan \alpha_{\text{opt}}^{\text{SN}} = \sqrt[4]{\frac{A_{\text{K}}^2 + I_0}{A_{\text{N}}^2 + I_0}}.$$
 (2.112)

As long as  $I_0 \ll A_{\rm N}^2$ , the second part of (2.111) is valid. The maximum value of  $r_{\rm SN}$  is thus determined by the Kerr amplitude and the illuminating number of photons, but again not by the Kerr rotation. A rise of the illuminating intensity is often limited by a closely connected heat load of the specimen. If electronic noise contributions and/or fluctuations are added, the signal-to-noise ratio is reduced and the analyser angle determined in (2.112) is shifted within the boundaries  $\alpha_{\rm opt}^C < \alpha_{\rm opt}^{\rm SN} < 45^\circ$  as mentioned before. The proportionality between  $r_{\rm SN}$  and the magneto-optical amplitude  $A_{\rm K}$  is preserved, however.

An important point of this thorough discussion is that the *magneto-optical amplitude* is a direct measure for the magneto-optical properties of the sample in both cases, for visual observation (2.107) as well as for electronic image processing (2.111). By proper microscope settings in either case a signal maximum is obtained that is proportional to the magneto-optical amplitude, but completely independent of the regularly reflected amplitude  $A_N$ . This statement, which can be verified by inserting reasonable values for the parameters, confirms the role of the Kerr amplitude as the meaningful material quantity in magneto-optics. It is also called the "figure of merit" [177, 188, 189] and often expressed somewhat indirectly in the form  $\theta_K \sqrt{I}$ .

If there is a phase shift between  $A_{\rm K}$  and  $A_{\rm N}$ , it is sufficient to remove the ellipticity of the darker domains by the compensator. Once this is achieved, the formulae (2.104, 2.107, 2.108) for the signal and the contrast remain valid if the magneto-optical amplitude is replaced by its absolute value [144]. In practice, the compensator and the analyser are adjusted "simultaneously", leaving the polarizer fixed, until an image of satisfactory contrast and brightness is obtained. When using a video system, it is often advisable to perform this adjustment first directly in the microscope, and then to "open" the analyser as far as necessary to obtain best results on the video screen.

The often rather weak Kerr contrast can be enhanced by *dielectric antireflection coatings*, which reduce the regularly reflected light while enhancing the Kerr component [144, 190]. To see this, let us rewrite the Kerr coefficients (2.102a, 2.102b, 2.102c) in terms of the so-called *intensity reflectance* coefficients  $R_p$  and  $R_s$ . They are connected to the intensity transmittances,  $T_p$  and  $T_s$ , by R + T = 1 and to the Fresnel coefficients (2.52, 2.53) by  $R_s = r_{ss}^2$  and  $R_p = r_{pp}^2$ . With  $T_s = (n_1 \cos \vartheta_1)/(n_0 \cos \vartheta_0)t_{ss}^2$  and  $T_p = (n_1 \cos \vartheta_1)/(n_0 \cos \vartheta_0)t_{pp}^2$  [166] the absolute values of the Kerr coefficients (which are the values important for usable magneto-optical signals) can be expressed as [111]

$$|K_{\rm sp}^{\rm pol}| = (|Q_{\rm V}|/4n_1)\sqrt{n_1'^2 + n_1''^2}\sqrt{(1-R_{\rm s})(1-R_{\rm p})},$$
 (2.113a)

$$|K_{\rm sp}^{\rm lon}| = (|Q_{\rm V}|/4n_1) n_0 \sin \vartheta_0 \sqrt{(1 - R_{\rm s})(1 - R_{\rm p})},$$
 (2.113b)

$$|K_{pp}^{tra}| = (|Q_V|/2n_1) n_0 \sin \vartheta_0 (1 - R_p),$$
 (2.113c)

where  $n'_1 + in''_1$  is the complex refractive index of the magnetic medium. If the regular reflectivities  $R_p$  and  $R_s$  are reduced to zero, the Kerr coefficients K and thus the Kerr amplitudes assume their largest values. This fact can be interpreted in the following way: The useful Kerr amplitude is largest when all light is absorbed inside the magnetic sample, and if the generated Kerr amplitude can freely exit in turn [177]. If light is uselessly reflected from the surface, it cannot contribute to the Kerr amplitude. The same applies if the generated Kerr amplitude is reflected on its way out. The Kerr effect can thus be enhanced by effective dielectric antireflection coatings (avoiding any absorption in the coating itself) for the particular material. In practice it is sufficient to minimize the reflectivity at normal incidence, because large angles of incidence are hardly used. For metals a suitable dielectric in ZnS, and for

magnetic oxides  $MgF_2$  or  $SiO_2$  layers can be applied. For a descriptive explanation of antireflection coatings based on multiple beam interference see [111].

### 2.4.4 Microscopic Origin of the Kerr Effect

So far we have discussed the phenomenology of the classical magneto-optical Kerrand Faraday effects based on a macroscopic theory, in which all the material properties are included in the dielectric  $\epsilon$ -tensor. The *microscopic* origin of the conventional magneto-optical effects can be traced back to optical transitions in the valence-band energy regime. The appearance of these effects, and also of the X-ray magnetic circular dichroism, which will be presented in Sect. 2.7, requires the simultaneous presence of exchange splitting and spin-orbit splitting. Let us again consider the case of the polar Kerr effect and normal incidence of circularly polarized light. Figure 2.15 schematically explains the situation in a (general) bulk ferromagnet in which d states are responsible for the ferromagnetism. Selection rules for electric dipole transitions allow transitions from occupied exchange-split states with d character to unoccupied states of p character. The m selection rule (here m is the magnetic quantum number) for transitions excited by circularly polarized light reads  $\Delta m = \pm 1$ , where the sign depends on the direction of photon helicity. The relevant quantization axis in the case of normal incidence is along the surface normal. For simplicity, we are considering the case in which also the magnetization is along the surface normal, such that no further projection of the electronic states on the quantization axis is necessary. Initial d and final p states are displayed as horizontal lines in Fig. 2.15, and labelled according to their orbital and spin quantum numbers, using the nomenclature  $|l m \uparrow\rangle$  and  $|l m \downarrow >$ . Here l is the orbital quantum number (l = 1 for p states and l = 2 for dstates) and ↑↓ indicate the spin orientation. Levels for spin up (↑, majority, left) and spin down (\( \psi, \) minority, middle) are separated in energy by exchange splitting. The exchange splitting for the unoccupied p states has been neglected. In addition to the exchange splitting, also the (in valence bands generally smaller) spin-orbit splitting contributes to the separation of levels. It lifts the degeneracy of states with different m. For spin up, a more positive m is lower in energy, while for spin down, the lowest energy corresponds to the state with the most negative m.

The vertical arrows show possible  $d \to p$  transitions obeying the dipole selection rules, both for left- and right-circularly polarized light ( $\Delta m = +1$  and  $\Delta m = -1$ , respectively). Electric dipole transitions conserve the spin. It is evident from the different lengths of these arrows for the two opposite light helicities, and thus the different photon energies, that there is a dichroism in absorption upon helicity reversal. The right hand side of Fig. 2.15 demonstrates this for the case of transitions from the  $|2 \pm 1>$  levels, indicated by solid lines of the arrows. For left-circular polarization, ( $\Delta m = -1$ ) transitions from  $|2 \ 1 \ >$  and  $|2 \ 1 \ >$  are possible, while for right-circular polarization, ( $\Delta m = +1$ ) transitions originate from  $|2 \ 1 \ >$  and  $|2 \ 1 \ >$ . The two different resulting absorption spectra for the two helicities are shown schematically on the right hand side of Fig. 2.15. Two peaks in each spectrum

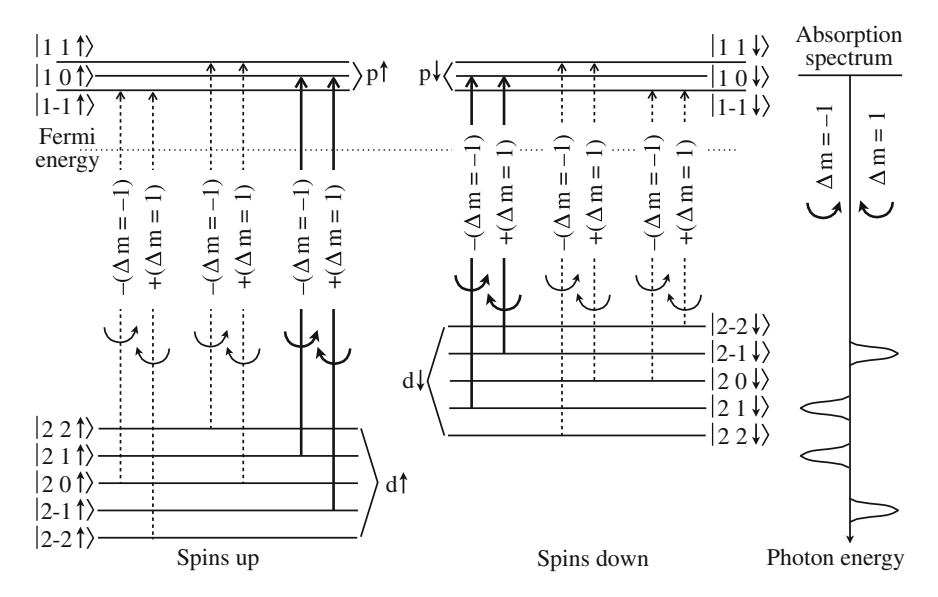


Fig. 2.15 Schematic representation of the electronic structure of p and d states in a ferromagnetic solid, including exchange splitting of the occupied d states and spin–orbit splitting of p and d states. Levels are labelled  $|l m \uparrow\rangle$  according to their orbital and magnetic quantum numbers as well as their spin. *Vertical arrows* indicate dipole-allowed transitions for right- $(\Delta m = +1)$  and left- $(\Delta m = -1)$  circularly polarized light. The *right hand side* schematically depicts absorption spectra for the two opposite circular polarization directions for transitions from  $|2 \pm 1\rangle$  states. After [191, 192]

result from the two allowed transitions from  $|2\pm1\rangle$  states. Although the dichroism in this sketch looks like a one-hundred percent effect, in reality, by including all possible transitions and considering the energetic width of the states in a solid, the asymmetry in the absorption is typically not more than a few percent.

It can be easily verified from Fig. 2.15 that this dichroism vanishes if either the exchange splitting or the spin-orbit splitting is reduced to zero. Magneto-optical effects, which include also the magnetic dichroism in X-ray absorption treated in Sect. 2.7, generally only occur if both, exchange splitting and spin-orbit splitting, are simultaneously present either in the initial or the final states. Note that spin-orbit splitting of the unoccupied p states included in Fig. 2.15 would not be necessary to obtain magnetic dichroism as long as there is spin-orbit splitting of the occupied initial d states.

If the magnetization is not along the direction of light helicity, either because of a magnetization in the surface plane, or because the light is incident under an oblique angle, the electronic states have to be projected onto the quantization axis defined by the light helicity axis. The resulting states will have a lower symmetry, but still can be separated with respect to the resulting orbital moment component along the new quantization axis. Transitions from these states then follow the same dipole selection rules as discussed before. All the above considerations are consequently also valid

in such cases, as long as the projection of the magnetization on the light helicity direction does not vanish.

The imaginary part of the complex dielectric constant  $\epsilon''$  can be related to the electronic transitions by

$$\epsilon''_{\pm}(\omega) \propto \frac{1}{\omega^2} \sum_{i,f} f(\mathcal{E}_i) \left[ 1 - f(\mathcal{E}_f) \right] |\langle i|p_{\pm}|f \rangle|^2 \delta(\omega_f - \omega_i - \omega).$$
 (2.114)

Here  $\omega$  is the light frequency,  $\mathcal{E}_i = \hbar \omega_i$  is the energy of the initial state and  $\mathcal{E}_f = \hbar \omega_f$  the energy of the final state. The plus and minus signs in  $n''_\pm$  refer to left- and right-circular polarization, respectively.  $f(\mathcal{E})$  is the Fermi function at energy  $\mathcal{E}$ , and  $p_\pm$  the dipole transition operator for right- and left-circular polarization. The sum has to be taken over all initial and final states, while the delta function on the right hand side assures energy conservation. The real part of the dielectric constant,  $\epsilon'_\pm$ , is linked to the imaginary part,  $\epsilon''_+$ , by the Kramers-Kronig relation.

Equation (2.114) thus connects the microscopic picture illustrated by Fig. 2.15 to the discussion in Sects. 2.3 and 2.4. The real and imaginary parts of the complex index of refraction n' and n'', respectively, are connected to  $\epsilon'$  and  $\epsilon''$  by

$$(n'_{+} + in''_{+})^{2} = \epsilon'_{+} + i\epsilon''_{+}. \tag{2.115}$$

In particular, from (2.63) and (2.78) follows that the Voigt constant  $Q_V$ , which was used for the description of the Faraday and Kerr effects before, can be expressed in terms of  $n_+$  and  $n_-$  by

$$Q_V = 2\frac{n_+ - n_-}{n_+ + n_-}. (2.116)$$

The absorption coefficient  $\alpha$ , as defined in (2.22), is directly connected to the imaginary part of the complex index of refraction, n'', by  $\alpha = 2n''\omega/c_0$  where  $c_0$  is the vacuum speed of light [see (2.23)]. By equating real and imaginary part in (2.115) it follows that  $\epsilon''_{\pm} = 2n'_{\pm}n''_{\pm}$ . Since in the soft X-ray regime  $n' \approx 1$ , (2.114) thus directly describes the absorption of X rays.

## 2.5 Voigt Effect

The Kerr- and Faraday effects, presented in Sect. 2.4, are effects to first order in the magneto-optical parameter  $Q_V$  and in the components  $m_i$  of the magnetization vector. This becomes immediately evident from the dielectric tensor—the first tensor in (2.58)—which represents these effects. The Voigt effect is a second-order effect that is often considered an independent effect with its own material coefficients  $B_1$  and  $B_2$  according to the second matrix in (2.58). This *intrinsic (or true) Voigt effect*,

however, is not the only conceivable second-order magneto-optical effect. As elaborated below, quadratic effects may also occur as a consequence of the elementary gyrotropic interaction, which is responsible for the Kerr- and Faraday effects and which is characterized by the material parameter  $O_{\rm V}$  according to the first matrix in (2.58). Second-order effects differ from first-order effects not only in their dependence of the magnetization vector, but also in their optical symmetry behavior [193]. Typical for first-order effects is the primary rotation of the polarization direction of the light, which may be superimposed by some ellipticity. This means that the magneto-optical amplitudes differ in their polarization plane relative to the incident light. In terms of the general reflectivity matrix (2.51), (2.93) indicates an effect in the off-diagonal elements,  $r_{sp}$  or  $r_{ps}$ , of this matrix. A typical quadratic effect, on the other hand, may contribute a modification of the regular reflectivity, i.e. the diagonal elements (like  $r_{ss}$ ) of the reflectivity matrix. It can thus be interpreted as a magnetically induced birefringence. Note, however, that these features depend on the "coordinate system" used to describe the polarization state of the light. The conventional Kerr and Faraday effects can as well be understood as a "circular magnetic birefringence". This was explained in the previous section, where we have seen that parallel to the magnetization direction a light wave can only propagate in two circularly polarized eigenmodes. The transmittance or reflectivity of circularly polarized light is thus modified by magnetism depending on the rotation sense of the light.

A different situation arises if the k-vector of the light wave is perpendicular to the magnetization vector, which is the condition for the Voigt effect. As shown at the end of Sect. 2.3.2, the eigenmodes are two *linearly polarized* waves in this case, the vibrational plane of one being aligned along and that of the other perpendicular to the magnetization. According to (2.68), both eigenmodes are feeling different refraction indices  $n_{\parallel}$  and  $n_{\perp}$ , respectively. Their difference is approximately [187]

$$\Delta n \approx (B_1 + \epsilon_{\rm iso} Q_{\rm V}^2)/(2\,\bar{n}),\tag{2.117}$$

where  $\bar{n} = \frac{1}{2}(n_{\parallel} - n_{\perp})$  is again the "optical" index of refraction, compare (2.78). An incident light wave, linearly polarized along or perpendicular to the magnetization direction, will thus not alter its polarization plane when it propagates in the magnetic medium. If the polarization plane of the incident light is at an angle to the magnetization direction, however, the polarization state of the light will be changed with the strongest effect occurring at an angle of  $45^{\circ}$ .

This situation is depicted in Fig. 2.16. The components of the wave's electrical field, which are parallel and perpendicular to the magnetization vector, may proceed in the medium with different velocities and with different attenuations (in case of a complex refractive index). The light thus experiences a birefringence proportional to  $\text{Re}(\Delta n)$  and a dichroism proportional to  $\text{Im}(\Delta n)$ . The first effect is called Voigt effect or *magnetic linear birefringence*—a birefringence of linearly polarized light, where the word "linear" refers to the polarization mode of the incident light and not to the order of the effect. As the two partial waves are retarded relative to each other, the outgoing vibration is elliptically polarized by an amount  $\sim m^2$  and with a

2.5 Voigt Effect 77

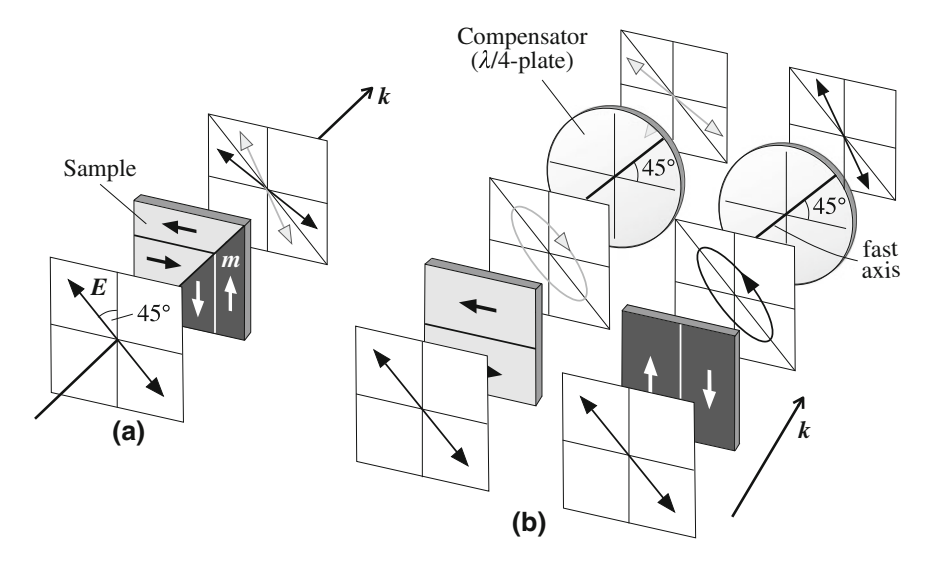


**Fig. 2.16** Illustration of magnetically-induced linear dichroism (**a**) and linear birefringence (**b**) effects. For both effects the domain axis is relevant rather than the domain direction, i.e antiparallel domains cannot be distinguished. In the sketches, a relative orientation of the two domain axes of 90° is assumed. If the polarization plane of the incident light is at 45° relative to the domain axes, the linear dichroism leads to a magnetization-dependent rotation of the polarization plane, whereas the linear birefringence causes elliptical light of opposite rotation sense for the two domain axes. Here a compensator is required for linearization. The action of the compensator can be verified by Jones calculus, see Fig. 2.8

handedness depending on the relative orientation of magnetization *axis* and polarization plane (Fig. 2.16b). Oppositely magnetized domains, which follow the same axis, can therefore not be distinguished in their birefringence effect. The second effect for *k* perpendicular to *m* is called *magnetic linear dichroism* and results in a rotation of the emerging light (Fig. 2.16a) due to the different amplitudes of the partial waves. <sup>16</sup> In practice, rotation of the polarization due to dichroism often superimposes on the ellipticity resulting from birefringence. Like for the Faraday- and Kerr effect, a rotation effect may thus also be found in case of the Voigt effect. The birefringence effect is usually dominating, however. As both classes of effects contribute to different elements in the reflectivity matrix, they can be separated experimentally as shown below. Note that the Voigt effect should be distinguished from the *Cotton-Mouton effect* mentioned in Sect. 2.2.3 [167]. Here anisotropic, diamagnetic molecules align themselves in an external magnetic field. As a result of this alignment, the material becomes birefringent. Phenomenologically this effect is identical to the Voigt effect, but it has a different microscopic origin.

<sup>&</sup>lt;sup>16</sup> The phenomenology is thus opposite to that of the magnetic *circular* birefringence and dichroism: there birefringence causes a rotation, whereas the dichroism leads to ellipticity (compare Fig. 2.11).

The dominating ellipticity of the emerging light in case of the magnetic linear birefringence requires a compensator to obtain detectable linearly polarized light. In the geometry of Fig. 2.16b, the fast axis of the compensator has to be along or perpendicular to the polarizer axis (zero position). In either case this causes planepolarized light, which is rotated relative to the incoming light and which can be converted into a contrast by means of an analyser. In practice, the analyser may be crossed to the polarizer. The Voigt contrast then appears when the compensator is "opened" by some degrees. This causes elliptical light of different ellipticity for the two domain axes, which passes the crossed analyser with different intensity—see Fig. 2.8f, g. The contrast can be inverted by rotating the compensator through its zero position thus interchanging the degrees of ellipticity for the two domain axes. Also an opening of the analyser will give a contrast, if the compensator is left at its zero position (Fig. 2.8e). The experimental conditions are different for the Kerr contrast: as the Kerr ellipticity is usually small, a Kerr contrast is mainly generated and inverted by rotating the analyser—the compensator is just used to linearize the light emerging from one domain type, <sup>17</sup> see Fig. 2.8c, d.

The Voigt contrast and signal can be treated along the same line as for the Kerr effect presented in Sect. 2.4.3. The magneto-optical interaction can again be seen as a superposition of magneto-optical amplitude  $A_{\rm V}$  (instead of  $A_{\rm K}$  for the Kerr effect) and regularly reflected (or transmitted) amplitude  $A_{\rm N}$ . Different to the Kerr effect, however, both amplitudes are shifted in phase by  $\xi=\pi/2$  in case of the linear birefringence, whereas the "intrinsic" phase difference is usually small in case of the circular birefringence (Kerr- and Faraday effects. The relation between  $A_{\rm V}$  and  $A_{\rm N}$  is illustrated in Fig. 2.17 in an analogous presentation as for the Kerr effect in Fig. 2.14b. A Voigt signal thus requires the introduction of an additional phase by means of a compensator as mentioned. Otherwise the same formula as in Sect. 2.4.3 do apply.

The essential difference between Voigt and Kerr contrast is the dependence on the magnetization vector: Different to the Faraday or Kerr rotation, which is directional-sensitive, the Voigt effect is *quadratic* in the magnetization vector due to its axial sensitivity. The symmetry (not the magnitude) of the Voigt effect can best be understood as a strain birefringence of a magnetostrictively distorted medium, because also magnetostriction is a quadratic effect. In the same sense as a cubic crystal is characterized by two magnetostriction constants to lowest order, the linear magnetic birefringence of a cubic material is characterized by two independent material parameters, the frequency-dependent and complex constants  $B_1$  and  $B_2$  in the dielectric tensor [second term in (2.58)]. As expected, the tensor also contains the squares of the magnetization vector components. The symmetry of the dielectric tensor also reveals that two perpendicularly magnetized domains, the axes of which are oriented at  $\pm 45^{\circ}$  relative to the polarizer axis, generate maximum domain contrast. This is the geometry chosen in Fig. 2.1b. For the circular birefringence (Kerr- and

<sup>&</sup>lt;sup>17</sup> In materials with a strong Kerr ellipticity (like Permalloy) it is, consequently, the other way round: here the Kerr effect is mainly adjusted by the compensator, whereas the Voigt effect requires an opening of the analyser.

2.5 Voigt Effect 79

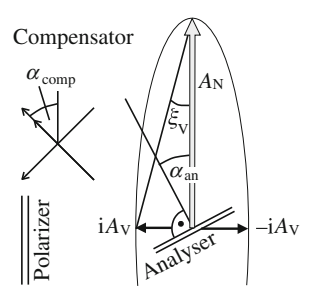


Fig. 2.17 Visualization of the light amplitudes for the Voigt effect (see Sect. 2.4.3 for a quantitative discussion). By interference of the regular amplitude  $A_{\rm N}$  with one of the two Voigt amplitudes  $iA_{\rm V}$  or  $-iA_{\rm V}$  a left- or right-handed elliptical wave is generated, each of them corresponding to one of the two emerging partial waves. The angle  $\xi_{\rm V}$  characterizes the ellipticity, and  $\alpha_{\rm an}$  and  $\alpha_{\rm comp}$  are the opening angles of analyser and compensator. Compare with Fig. 2.14b for the analogous representation of the Kerr effect

Faraday effects) the conditions are different: here maximum contrast is obtained for antiparallel domains, and the polarizer has to be parallel or orthogonal to the domain magnetization for the longitudinal effect or at an arbitrary angle for the polar effect.

As mentioned, a second-order effect with the same symmetry as the intrinsic Voigt effect can as well be derived from gyrotropic interaction and Maxwell equations, i.e. the linear term in the dielectric  $\epsilon$ -tensor (2.58—first matrix) can not just lead to the Kerr and Faraday effects, but also to a magneto-optical effect of second order and therefore add to the linear birefringence [168, 194]. This is illustrated in Fig. 2.18. Assume that the polarizer sends some  $E_y$ -component along the z-direction. According to the gyroelectric tensor this will cause a Lorentz motion along z, i.e. a first-order displacement [195, 196]

$$D_{\rm z} = +i\epsilon_{\rm iso} Q_{\rm V} m_{\rm x} E_{\rm v}, \tag{2.118}$$

which will lead to a first-order depolarizing field

$$E_{\rm z} = -D_{\rm z}/\epsilon_{\rm iso} = -iQ_{\rm V}m_{\rm x}E_{\rm y} \tag{2.119}$$

to keep  $D_z = 0$ . The depolarizing field then induces a second-order displacement

$$D_{y}' = -i\epsilon_{iso}Q_{V}m_{x}E_{z} = -\epsilon_{iso}(Q_{V}m_{x})^{2}E_{y}, \qquad (2.120)$$

which corresponds to a Lorentz motion along -y, opposite to the zero-order  $D_y = \epsilon_{iso} E_y$ . If E points between x and y (best at 45°), the polarization plane rotates towards m, i.e. the D-component along m is longer. The same contrast phenomenology as in Fig. 2.18 can be derived from the second matrix in (2.58) for the intrinsic Voigt effect. A detailed description of second order effects is given in [193].

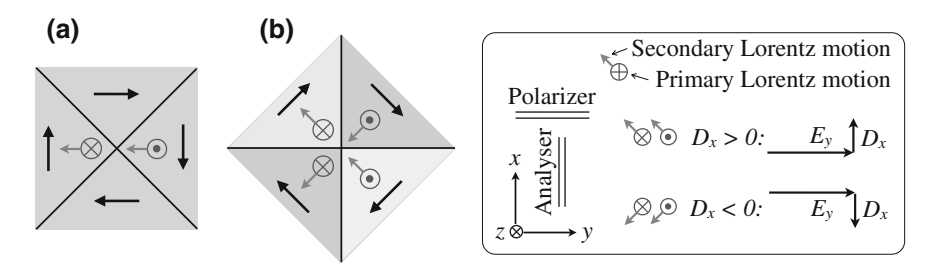


Fig. 2.18 Explanation of the secondary quadratic effect that has the same symmetry as the Voigt effect, but which is derived from gyrotropic interaction like the Kerr effect. a Horizontally polarized light (see inset) creates an out-of-plane Lorentz motion in the vertically magnetized domains. This primary motion generates a secondary motion that is polarized antiparallel to  $E_y$ . b A 45° rotation of the domain magnetization relative to  $E_y$  leads to antiparallel  $D_x$ -components for domains magnetized along different axes. The dielectric displacement is responsible for magneto-optical  $E_x$ -components in the reflected light. Due to their phase shift relative to the ordinary reflected  $E_y$ , a black/white microscopic contrast is created by matching the phase of one of the two  $E_x$  vectors with that of  $E_y$  by means of the compensator

The Voigt effect plays an established role for the visualization of in-plane domains in transparent crystals like magnetic garnet films [149, 197]. In [150] it was proven that, with the help of digital image processing, the Voigt effect can also be observed in reflection on metals. (An analogous reflection effect was very recently also seen in X-ray spectroscopy [158]). An example for the reflection observation of in-plane domains in the Voigt effect is shown in Fig. 2.1b. The quadratic dependence on the magnetization vector is immediately evident in this image, opposite to the linear magnetization dependence of the Kerr effect that is shown for comparison in Fig. 2.1a. As the Voigt effect is weaker than the rotational effects, it can usually only be observed if the Kerr or Faraday effects are suppressed. For Voigt microscopy on in-plane domains like in Fig. 2.1, the specimen has to be illuminated with plane-polarized light at perpendicular incidence to avoid contributions from the Kerr effect. This geometry was also considered in the sketches of Fig. 2.16. By rotating the sample or polarizer by 45° (Fig. 2.1c), the Voigt contrast disappears and reappears again with inverted contrast after a further rotation of 45° (not shown). The Voigt contrast thus changes sign every 90° due to its quadratic magnetization dependence. This is different for the Faraday and Kerr contrast: due to the linear magnetization dependency of these effects the sample has to be rotated by 180° to achieve opposite, but equally intensive contrasts.

In the general case of arbitrary angles between k-vector and magnetization, there is a superposition of linear and circular birefringence. If the sample is illuminated along or transverse to the magnetization, just the circular or linear birefringence, respectively, will be active. For any other direction there is *elliptical birefringence* and dichroism, i.e. two elliptical partial waves (rather than circular or linear) do propagate with slightly different refraction indices [170]. When going from parallel to perpendicular illumination the ellipses change from circles to elongated (linear)

2.5 Voigt Effect 81

shapes. If, in addition, the magnetic medium is strongly absorbing (i.e. if  $n' \approx n''$ ), also the real and imaginary parts of the components of the magneto-optical  $\epsilon$ -tensor are mixed and the total magneto-optical signal emerging from the sample gets highly complicated [171].

#### 2.6 Gradient Effect

The magneto-optical gradient effect [150] is sensitive to changes (gradients) in the magnetization. It therefore stresses fine magnetization modulations relative to the large-scale features of a domain pattern. The strongly modulated surface domains of heavily branched domain patterns, which occur on strongly misoriented surfaces, can e.g. be favorably visualized in the gradient effect.

Magnetization gradients are strongest across domain walls. For this reason also domain walls reveal a strong contrast if imaged in the gradient effect, which, however, is different from the wall contrast seen by the Kerr effect. Let us again refer to the example shown in Fig. 2.1: In the Kerr effect (Fig. 2.1a), which senses the magnetization directly, the 180° domain walls show up in a color that depends on the (in-plane) rotation sense of the wall magnetization. Imaged under conditions of the gradient effect (Fig. 2.1b), the same walls appear in a homogeneous black or white contrast. This contrast is independent of the wall rotation sense, and it does not depend on the wall width as could be proven by measurements on a variety of materials [198]. Therefore the gradient effect arising at domain walls is better called "boundary" contrast rather than wall contrast. The boundary contrast is primarily determined by the magnetization jump from one domain to the other, i.e. by the magnetization gradient across the wall, and not by the properties of the actual wall. It consequently alternates for neighboring walls in dependence of the surrounding domain magnetization. The boundary contrast changes sign when the walls are rotated by 90°. The same rotational symmetry applies to the Voigt contrast, which is detected at the same experimental conditions as the gradient effect and which is also visible in Fig. 2.1b. By rotating the polarizer by 45° as in Fig. 2.1c (alternatively the sample may be rotated by 45°), the Voigt contrast disappears together with the 180° boundary contrast. Now the 90° domain boundaries show up in an alternating black and white gradient contrast, whereas a residual double contrast is left at the 180° walls that can be traced back to a superposition of Voigt contrast and local gradient contrast due to the wall magnetization [198]. A further example, again comparing the gradient and Voigt contrast with the Kerr contrast, is presented in Fig. 2.19. The cross-tie character of the central wall in the Landau pattern is better visible in the gradient image.

The contrast symmetry of the gradient effect for the elementary wall geometries of *in-plane* magnetized materials, including those of Figs. 2.1 and 2.19, is schematically summarized in Fig. 2.20. Thin films as well as bulk samples are considered in the graphics—different symmetry rules may apply to these two cases as elaborated below. To isolate the gradient contrast from the Kerr contrast, perpendicular incidence of

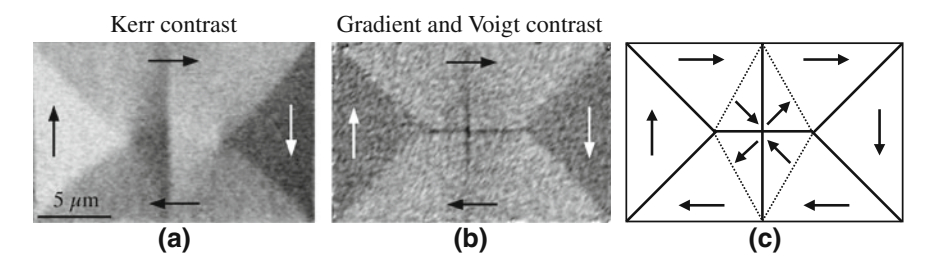


**Fig. 2.19** Landau domain pattern with cross-tie wall, imaged in the longitudinal Kerr effect (a) at oblique illumination along the vertical direction and by gradient/Voigt microscopy (b) at perpendicular incidence. The polarizer was oriented vertically for the Kerr image, and at  $+45^{\circ}$  for the gradient/Voigt image. The dashed lines in the "domain" model (c) are in reality continuous transitions [111]. The sample is a Ta (5 nm)/FeMn (10 nm)/NiFe (50 nm) trilayer, in which the domains in the NiFe film are visualized. The Ta/FeMn cover layers are sufficiently transparent for all three magneto-optical effects. Sample courtesy *R. Kaltofen*, Dresden

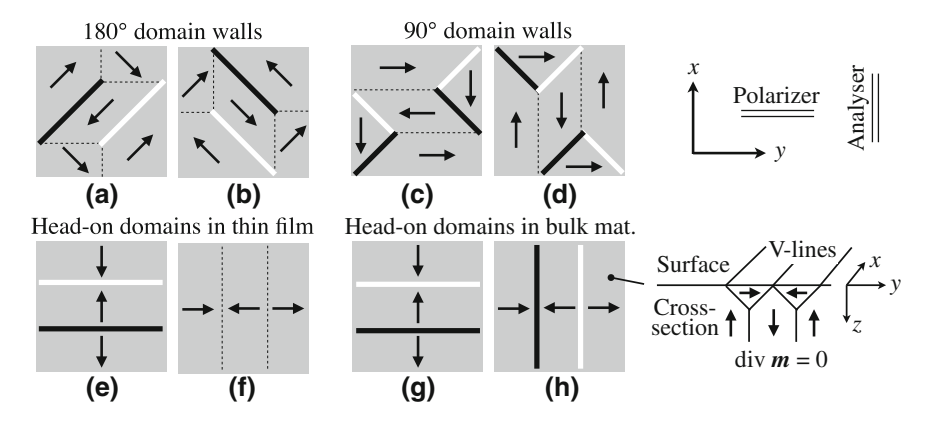


**Fig. 2.20** Presence (*thick lines*) or absence (*dashed lines*) and sign of the gradient effect at domain boundaries, illustrated for the elementary geometries of in-plane magnetized domains. Horizontal polarization direction and perpendicular incidence of light is assumed. For each wall type the contrast before and after rotating the sample by 90° is shown. The contrast symmetry for the 180° and 90° walls (**a-b** and **c-d**, respectively) applies to bulk material as well as magnetic films. The boundary contrast symmetry of head-on domains, on the other hand, is different for films (**e-f**) and bulk samples (**g-h**). In bulk material, head-on domains are usually of the V-line type (inset) for which perpendicular subsurface gradients add to the gradient contrast

light is required for in-plane materials. A Kerr contrast is not possible then, neither for the domains nor the walls. A separation of gradient and Voigt contrast is not possible, because both effects appear under the same experimental conditions and

<sup>&</sup>lt;sup>18</sup> Note that in thin films the domains walls are of the Néel type with an in-plane rotation of magnetization. The same applies to the Néel cap of vortex walls in low-anisotropy bulk material [111]. In case of high-anisotropy materials, perpendicular components at domain walls might be present. But here the wall width is far below resolution anyway, so that the polar Kerr effect does not play a role.

2.6 Gradient Effect 83

follow the same rotational symmetry (i.e. the contrast can be obtained by rotating the compensator and it can be inverted by either rotating the sample by 90°, the polarizer by 45°, or by rotating the compensator through its extinction position—see Sect. 2.5). This indicates a phase shift of the magneto-optical amplitude of the gradient contrast of roughly 90° relative to the phase of the Kerr amplitude [150], similar to that of the Voigt effect (compare Fig. 2.17 and Fig. 2.14b).

The physical origin of the gradient effect can be traced back to the same gyrotropic interaction ( $D \propto m \times E$ ) that is also responsible for the Kerr- or Faraday effect and which can be used to derive quadratic effects (see Fig. 2.18). This was shown by magneto-optical diffraction analysis in a series of articles by Kamberský [185, 195, 199, 200]. The symmetry of the gradient effect is, however, strongly affected by the micromagnetic conditions in the underlying domain structure. Two cases have to be distinguished:

• Specimens with strict *in-plane* magnetization, including magnetically charged micromagnetic objects. Thin magnetic films with in-plane anisotropy are typical examples for this class. Under this condition, the *x*-component of the displacement vector **D**, which is responsible for the gradient effect at the in-plane domain geometries presented in Fig. 2.20, is written as:

$$D_{\mathbf{x}} = P\left(-\partial m_{\mathbf{x}}/\partial x\right) E_{\mathbf{v}},\tag{2.121}$$

where y and x are the coordinates along the E- and H-vectors of the incident light wave, respectively, and  $\partial m_x/\partial x$  is the gradient of the magnetization vector m along the x-axis. The material constant P scales with that of the Kerr effect.

• Samples with subsurface perpendicular magnetization gradients, for which the condition  $\operatorname{div} \boldsymbol{m} \approx 0$  is fullfilled. The polar gradients have to be present within the information depth of the magneto-optical experiment, which is, for example, the case in so-called V-line configurations occurring in thick specimens. For such micromagnetic objects the  $D_x$ -component writes

$$D_{x} = P \left( \frac{\partial m_{y}}{\partial y} - \frac{\partial m_{x}}{\partial x} \right) E_{y}. \tag{2.122}$$

Both laws can be derived from gyrotropic interaction within the framework of Kamberský's diffraction theory. Consider a  $180^{\circ}$  domain wall as presented in Fig. 2.21. For the given polarization direction of light along the *y*-axis, a nonvanishing cross product in the domains does exist for the wall orientations (a), (b), and (d) in the figure. In these three cases, the incident light thus generates in each domain an oscillating gyrotropic polarization normal to the sample surface, the amplitude of which depends on the magnetization direction of the illuminated domain. It varies between zero (if m is along the y-axis) and 1 (if m is along the x-axis). In the neighboring domain a similar oscillation is generated that is out-of-phase to the first one by  $180^{\circ}$  since the  $m_x$ -component, which causes the gyrotropic interaction, changes sign (i.e. has a gradient across the boundary). The pairs of out-of-phase oscillating electric dipoles produce a quadrupolar dielectric displacement with a component

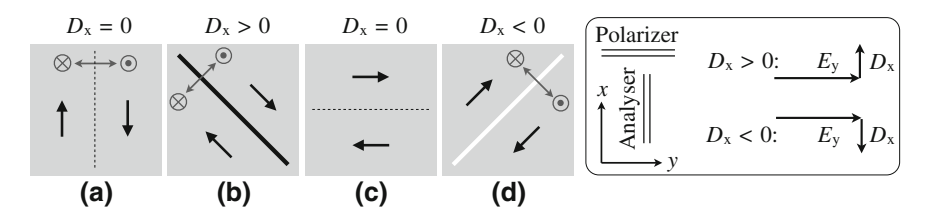


Fig. 2.21 Gradient contrast symmetry of a  $180^\circ$  wall that is rotated by  $135^\circ$  from **a** to **d**. The oscillating Lorentz motion across the wall, excited by gyrotropic interaction, is indicated. It causes a dielectric displacement vector, the positive and negative  $D_{\rm x}$  components of which are aligned along the analyser axis, but at opposite directions (see inset). Parallel to  $D_{\rm x}$  are the magneto-optically reflected  $E_{\rm x}$ -components. Due to their phase shift relative to the ordinary reflected  $E_{\rm y}$ , a black/white microscopic contrast is created by matching the phase of one of the two  $E_{\rm x}$  vectors with that of  $E_{\rm y}$  by means of the compensator

perpendicular to the domain boundary, which results in an electric field component along the same direction in the reflected light. In the experiment, the component of this transverse field parallel to the analyser axis ( $E_x$ -component) can be detected. It is proportional to the component  $\partial m_x/\partial x$  of the magnetization gradient and may be expressed as [201]:

$$E_{\rm x}^{1(x,y)}(x,0) \sim -G(\partial m_{\rm x}/\partial x) E_{\rm v}^0, \tag{2.123}$$

with some constant G. This law also comprises the case in Fig. 2.21c where  $m \times E$  vanishes—like in Fig. 2.21a, the gradient  $\partial m_x/\partial x$  and thus  $E_x$  is zero in this case. The x-component of the displacement vector D, which is the source of  $E_x$ , is thus written as in (2.121). This law describes qualitatively the magneto-optical gradient effect of strictly in-plane magnetization gradients. This also includes the magnetically charged boundaries between head-on domains in thin films (Fig. 2.20e, f—note that such boundaries are normally zigzag-folded in ordinary films to reduce the stray-field energy [111]).

A different situation arises if also polar subsurface gradients do exist in the sample. This is the case for the V-line structure illustrated in Fig. 2.20g, h. V-lines are the surface intersections of internal domain walls that are arranged in shape of the letter V (see Fig. 2.20, inset). Around a V-line the m-vectors of the surface domains are head- or foot-on, but underneath the surface the magnetization flow points away from (or towards) the surface. In this way the magnetic flux of the surface domains is distributed in a stray-field free manner (a stray-field-free magnetization field, i.e. div  $m \approx 0$ , is naturally enforced in low-anisotropy materials, including iron [111]). Surprisingly, a gradient contrast is observed at V-lines [150] even when the surrounding domains are magnetized along the polarization direction of the light (Fig. 2.20h). The term  $(\partial m_y/\partial y)$  in the dielectric law (2.121) takes this fact into account. This law was originally derived empirically [150] based on experimental observations.

2.6 Gradient Effect 85

In successive articles on the diffraction analysis [195, 200–203], Kamberský has shown that the interpretation of this (necessary) term requires the consideration of polar gradients  $(\partial m_z/\partial z)$ . The crucial point is the divergence-free micromagnetic structure of a V-line: As there is an in-plane contribution to the divergence  $\partial m_y/\partial y$ , it must be compensated by an almost equal but opposite  $\partial m_z/\partial z$  to fulfill the condition div  $m \approx 0$ . Even if the  $m_z$ -component is zero at the surface, it must rise below the surface and give rise to a non-uniform polar Kerr effect according to its limited, but signifiant information depth of about 20 nm in metals [177]. In fact, by considering both, diffraction due to planar and perpendicular gradients in the analysis [195], it was possible to derive the empirically observed symmetry of the gradient effect including the critical case of Fig. 2.20h if the condition div m = 0 is valid.

This can be verified by extending our previous analysis: Polar magnetization components cause a gyrotropic interaction for any wall orientation, so that the x-component of the electric field can be written as

$$E_{\rm x}^{1(z)} \sim -\frac{1}{2} G(\partial m_{\rm z}/\partial z) E_{\rm y}^{0}.$$
 (2.124)

The proportionality of the two constants in (2.123, 2.124) follows from the symmetry of the magneto-optic interaction considered in the diffraction theory [202]. In bulk low-anisotropy materials, the flux-closing condition div  $m \approx 0$  implies

$$\partial m_{\rm x}/\partial x + \partial m_{\rm y}/\partial y + \partial m_{\rm z}/\partial z = 0,$$
 (2.125)

so that in this case (2.124) may be replaced by

$$E_{\rm x}^{1(z)} \sim \frac{1}{2} G(\partial m_{\rm x}/\partial x + \partial m_{\rm y}/\partial y) E_{\rm y}^0.$$
 (2.126)

The full detectable x-component then is the sum of (2.123) and (2.126):

$$E_{\rm x}^{1(x,y,z)} \sim \frac{1}{2} G(\partial m_{\rm y}/\partial y - \partial m_{\rm x}/\partial x) E_{\rm y}^0,$$
 (2.127)

which is consistent with (2.122). A more systematic analysis of domain diffraction phenomena, including the gradient effect, was presented in a later article [185] that has completed a series of papers [177, 186, 204, 205] dealing with magneto-optical interference and diffraction effects in magnetic multilayers. The pioneering paper [177] of this series, in which the concept of magnet-optical depth sensitivity was introduced, also contains a descriptive explanation of the subsurface gradient contribution based on the depth sensitivity function.

We will return to the gradient effect in Sect. 3.4, showing that it can be favorably applied to obtain layer-selective information in epitaxial multilayers.

#### 2.7 X-Ray Magnetic Dichroism

We now turn to the magneto-optic effects in the resonant absorption of soft X rays. These effects are sizable only in the vicinity of elemental absorption edges. It is therefore necessary to tune the wavelength of the X rays to an absorption edge of the respective element. Tunable X rays are nowadays conveniently available at synchrotron radiation sources. The X rays emitted from a synchrotron radiation source are, in addition, always polarized, a necessary prerequisite for their use in connection with magneto-optic effects. The polarization can be either linear, which is the "native" polarization of synchrotron radiation, or circular, which requires some additional measures to be taken, see Sect. 2.7.2.

We will in the next section first discuss the case of linear polarization, following the historic development of X-ray magnetic dichroism, and then come to the more important case of circular polarization in Sect. 2.7.3, after shortly discussing the generation of circularly polarized X rays at synchrotron radiation sources in Sect. 2.7.2.

#### 2.7.1 X-Ray Magnetic Linear Dichroism

The transfer of magneto-optical techniques from the visible to the X-ray regime appeared for a long time impossible due to the difficulty of generating and manipulating polarized light in this wavelength regime. In 1986, it was realized that the linear polarization of synchrotron radiation generated in a bending magnet could be put to use for investigating magnetic phenomena, and the first studies of magnetic dichroism in the X-ray regime were carried around this time using linear light polarization [206]. In an effort to understand the fine structure of soft X-ray absorption spectra of rare earth materials, it was realized that the X-ray absorption spectrum, which has an intrinsic characteristic width on the scale of an electron volt because of lifetime broadening, is very sensitive to the precise character of the ground state, whose characteristic energy scale is governed by interactions of the order of meV. An example is the spin-orbit splitting of the 4f states in cerium. Calculations indicated that the spectrum should show characteristic changes depending on the relative weight of J = 5/2 and J = 7/2 in the ground state, where J is the total angular momentum of the electrons. As systems which allowed experimental verification of such phenomena, calculations identified magnetically ordered dysprosium or terbium. These calculations predicted strongly different 3d absorption spectra for the electric field of the radiation being either parallel or perpendicular to the magnetic moment of the rare earth [207]. Soon after, these predictions were verified by polarization-dependent studies of ultrathin dysprosium films grown on nickel [208], or for terbium-iron garnet [206].

The first 3d system for which linear dichroism was established was Fe<sub>2</sub>O<sub>3</sub> [209]. This material shows a spin reorientation transition, the Morin transition, at 263 K [210]. This transition was utilized to obtain  $L_{2,3}$  absorption spectra with the magnetic

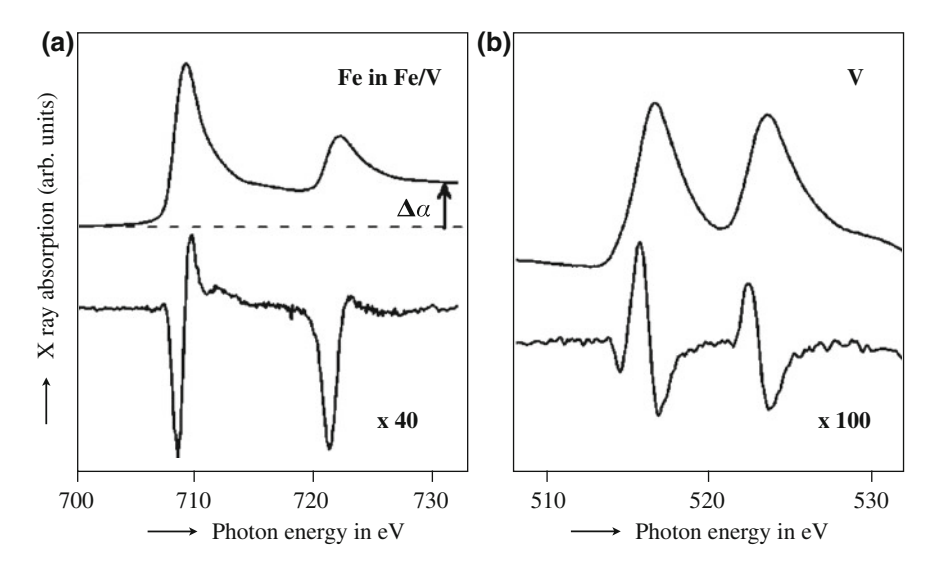


**Fig. 2.22** X-ray absorption spectra for a  $[V/Fe]_{40}$  multilayer with 1.5 Å vanadium and 7.5 Å iron layer thickness. Panel **a** shows absorption spectra at the Fe  $L_{2,3}$  edges, panel **b** those at the V  $L_{2,3}$  edges. In each panel, the absorption line (top) is shown together with the difference between absorption with orthogonal linear polarization of the exciting X rays (bottom), magnified in the vertical direction by factors of 40 and 100, respectively. Reprinted with permission from [211]. Copyright (1998) by the American Physical Society

moments parallel and perpendicular to the light polarization. The results were in good agreement with calculations treating the 3d states as highly localized with distinct angular and spin moment [209].

For metallic systems with delocalized d states, the optical properties in principle also show a difference between light polarization parallel or perpendicular to the magnetization. However, this difference is much smaller than in localized systems, which makes the study of magnetic properties utilizing this effect much more difficult. Figure 2.22 shows an experimental result for Fe/V multilayers [211]. The spectra for the different light polarizations are very similar in appearance, and only the difference spectrum reveals the dichroism.

In both examples, the X-ray absorption spectrum can distinguish between the sample being magnetized parallel or perpendicular to the light polarization. In contrast, circular dichroism, which is discussed in Sect. 2.7.3, distinguishes between magnetization parallel and antiparallel to the light propagation direction. Therefore, the two techniques are complementary, compare also Fig. 2.2. Figure 2.23 depicts the different geometries.

Another form of magnetic linear dichroism is the transverse magneto-optical Kerr effect. Here the reflectivity changes for p-polarized light under oblique incidence upon switching the magnetization between the two orientations perpendicular to the plane of incidence (see Sect. 2.4.2). From the theory of magneto-optics it is

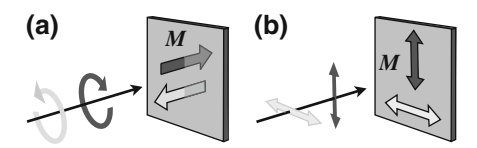


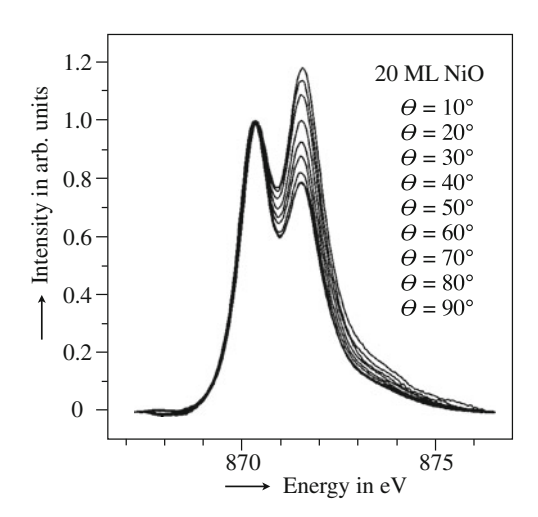
Fig. 2.23 a XMCD detects the difference in absorption for the projection of the sample's magnetization onto the propagation direction of circularly polarized X rays. b XMLD detects the difference in absorption of the axis of magnetization aligned parallel or perpendicular to the E field of the X rays

evident that the transverse Kerr effect is governed by the same elements of the dielectric tensor as circular dichroism. This effect does not require a polarization analysis of the reflected beam. The small reflectivity in the X-ray regime is not a real problem, since one may choose a grazing incidence angle for which there is still sufficient reflectivity at the wavelength to be used. For the 3p edges of the 3d elements, the effect is easily measurable up to incidence angles of  $45^{\circ}$  [212, 213]. For imaging purposes, the question is whether this change of reflectivity leads to a change of absorption, which could be used as a contrast mechanism. 19 The continuity relation for the incident light stipulates that the fraction of light which is not reflected is transmitted across the interface into the medium. Therefore, a change in reflectivity with change of magnetization changes the intensity transmitted into the sample. If the mean reflectivity is not too small, this may generate a contrast in the transmitted photon intensity or in the electron yield which could be used for imaging oppositely magnetized domains. In a photoelectron emission microscope (PEEM), this effectively limits the applicability of this contrast mechanism to the 3p edges of the 3d elements, since the typical incidence angle for the light in photoelectron emission microscopy is  $15^{\circ}$  or more, so that only the 3p edge regime offers sufficient reflectivity.

An important ingredient for the study of magnetic domains in transition metal compounds using magnetic linear dichroism is an understanding of the soft X-ray absorption spectra of transition metal (TM) ions with highly localized *d* states. In general terms, the absorption spectra of such transition metal compounds show rich structures, which can be adequately described by atomic multiplet theory. The understanding of the line shapes of absorption edges has reached a remarkable level during recent years, as illustrated by the good agreement between experimental spectra and theoretical calculations based on an atomic description. The solid-state environment induces some hybridization between the localized *d* states and delocalized states, and may modify the spectra due to the presence of the crystal field. Both these effects can be incorporated in the modeling of spectra by empirically reducing the magnitude of the Slater-Coulomb and exchange integrals, and by incorporating the crystal field into the calculation. Furthermore, the solid state environment introduces a lowering

<sup>&</sup>lt;sup>19</sup> For the classical transverse Kerr effect in the visible light regime, a Kerr contrast is generated by polarizing the light at 45° to the plane of incidence, which results effectively in a rotation of light (see Sect. 2.4.2, Fig. 2.13d).

Fig. 2.24 Polarization dependence of the Ni  $L_2$ X-ray absorption spectra of a 20 monolayer NiO(001) film at T = 298 K.  $\Theta$  is the angle between the (001) surface normal and the electric vector of the linearly polarized light. The spectra are normalized at the first peak of the  $L_2$  edge spectrum. Strong linear dichroism can be observed. Reprinted with permission from [214]. Copyright (1998) by the American Physical Society



of the symmetry, which can be taken into account by incorporating crystal field splitting.

Atomic multiplet calculations including such a crystal-field splitting [207] indicated that for magnetically ordered materials, large dichroic effects should occur in core-level absorption spectra. The term dichroism in this context means a dependence of the absorption on the relative orientation of the light polarization and the ordered magnetic moment. The first experimental demonstrations of this effect were performed on ferrimagnetic rare earth systems and hematite [206, 209]. In these cases, the direction of the magnetic moment can be fixed either by an external field, or by utilizing a spin reorientation transition. For antiferromagnets, it is more difficult to establish a uniform orientation throughout the sample. In thin films, however, one may anticipate that the quasi two-dimensional character of the sample may lower the energy of a subset of the possible domains with respect to the remaining ones. This was indeed found to be the case for thin NiO films grown epitaxially on MgO [214]. For (100)-oriented films grown by molecular beam epitaxy, four out of the twelve possible domain phases have a large component of the magnetic moment perpendicular to the surface, while for the others the largest component is in the surface. If one of these two sets is preferred, then this should be detectable in the X-ray absorption spectrum as magnetic dichroism. The experimental finding of Alders et al. for NiO thin films [214] is reproduced in Fig. 2.24. The spectra show two absorption edges, caused by the excitation from the Ni  $2p_{1/2}$  level to the unoccupied valence states. There are a number of differences between spectra taken at normal and grazing incidence. The spectra differ in the relative height of the absorption signal in the two peaks. By comparison to calculated spectra, this can be identified with a preferred spin orientation normal to the surface.

The absorption spectrum is different for normal incidence (E vector parallel to the surface, s polarization) and grazing incidence (E vector nearly perpendicular to the surface, p polarization). This polarization dependence vanishes at the NiO

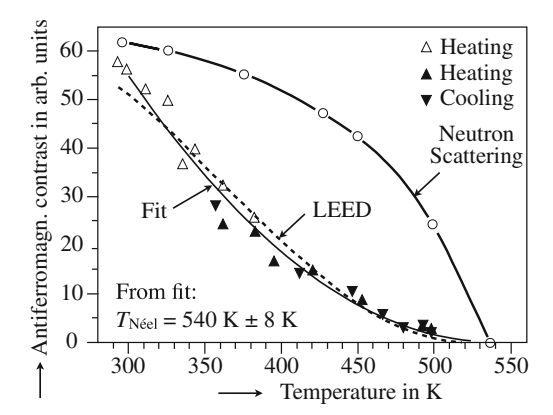


Fig. 2.25 Temperature dependence of antiferromagnetic contrast in XMLD observed on NiO(001). Experimental XMLD data are indicated by triangles, the solid line through the data is a parabolic fit. Circles represent neutron scattering data of bulk NiO [225], the dashed line low-energy electron diffraction data [226]. After [215]

Néel temperature, confirming the connection to antiferromagnetic order of the film. Figure 2.25 shows the temperature dependence of the contrast between the two Ni  $L_2$  absorption features for a NiO(001) single crystal [215]. The contrast decreases gradually and disappears at a temperature above 500 K. The close proximity of this temperature to the bulk Néel temperature of NiO shows that the contrast is caused by the magnetic order of NiO. A fit of the observed behavior yields a parabolic temperature dependence with a Néel temperature of  $(530\pm8)$  K. The determination of the Néel temperature from this experiment is not precise enough to confirm or rule out an enhancement of the surface Néel temperature by 6 K, which has been claimed from metastable Helium diffraction experiments [216].

Later it has been discovered that the shape of XMLD difference spectra depends on the crystallographic direction under which the measurement is conducted, i.e., the crystallographic orientation of the magnetization and the polarization of the probing X rays [217]. Subsequent measurements on Fe<sub>3</sub>O<sub>4</sub> [218], (Ga, Mn)As [219], LaFeO<sub>3</sub> [220], NiFe<sub>2</sub>O<sub>4</sub> [221], CoFe<sub>2</sub>O<sub>4</sub> [222] as well as on metallic Fe [223] and Co films [224] all showed a strong dependence of the XMLD on the crystallographic orientation. If we limit ourselves for the discussion of these effects to cases in which the XMLD is taken as the difference between spectra acquired with the polarization vector parallel and perpendicular to the magnetization axis, the result for transition metal oxides, confirmed by atomic multiplet calculations [218, 221, 222], can be summarized as follows: The XMLD at the  $L_2$  edge measured for magnetization directions along  $\langle 100 \rangle$  and  $\langle 110 \rangle$  exhibits more or less identical spectral shape, but the opposite sign. The dichroism at the  $L_3$  edge, in contrast, exhibits also a considerably different shape for these two cases. Since before 2006 mostly—like in the examples presented above—the XMLD at the L2 edge was used for an evaluation of the spin structure, and always had been interpreted in terms of multiplet calculations performed for  $\langle 100 \rangle$  magnetization directions, this had led to wrong interpretations, and several of the conclusions drawn from XMLD measurements had to be reanalyzed [221]. An example will be presented in connection with the layer-resolved magnetic imaging of Co/NiO(001) in Sect. 4.4.2.

#### 2.7.2 Circularly Polarized X-rays

The obvious requirement for the detection of magneto-optic effects in the absorption of circularly polarized X rays is the availability of circularly polarized X rays in the soft X-ray regime covering the L absorption edges of 3d transition metals such as Fe, Co and Ni as well as the M absorption edges of 4f systems, such as Gd and Tb, which are the most prominent components in ferromagnetic systems.

Polarized X-rays are nowadays abundantly available at synchrotron radiation laboratories. At bending magnet stations (Fig. 2.26), the radiation emitted in the orbital plane is horizontally linearly polarized, while the radiation emitted off orbit at an angle of a few millirad yields a significant circular degree of polarization with reversed polarity above and below the orbital plane. The gain in circular polarization is accompanied by a reduction in intensity, therefore a typical configuration views the X rays at 3–5 mm above or below the synchrotron plane yielding about 60–80 % circular polarization at about half the intensity compared to the center position [227].

At third-generation storage rings, dedicated insertion devices, such as helical undulators in the soft X-ray energy range [228, 229], provide high-brilliant sources of polarized X rays (Fig. 2.27). They consist of arrays of permanent magnets which force the path of the electron beam into certain shape so as to tailor the polarization of the emitted radiation. Mechanically shifting the magnet arrays against each other one can deliberately modulate the polarization of the X rays. It is possible to reverse

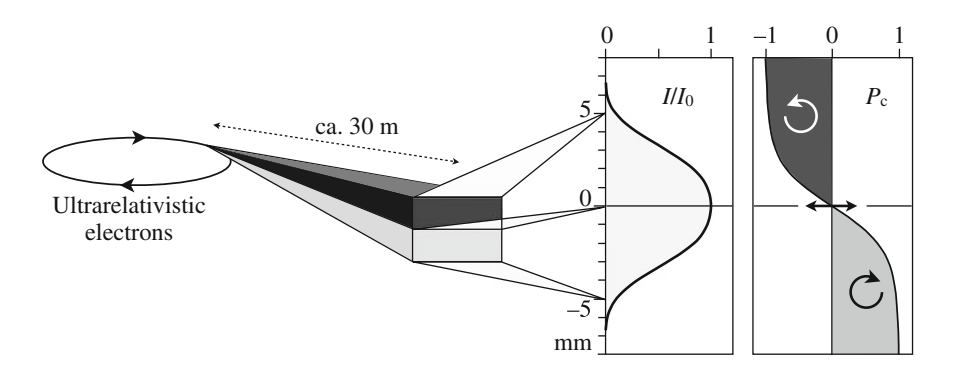


**Fig. 2.26** Circularly polarized X rays are emitted above and below the orbital plane at a bending magnet station with reversed helicity. The graph at the *right hand side* shows the intensity of the emitted photon beam  $(I/I_0)$  as well as the degree of circular polarization  $(P_C)$  as a function of the vertical position of the entrance slit with respect to the ring plane

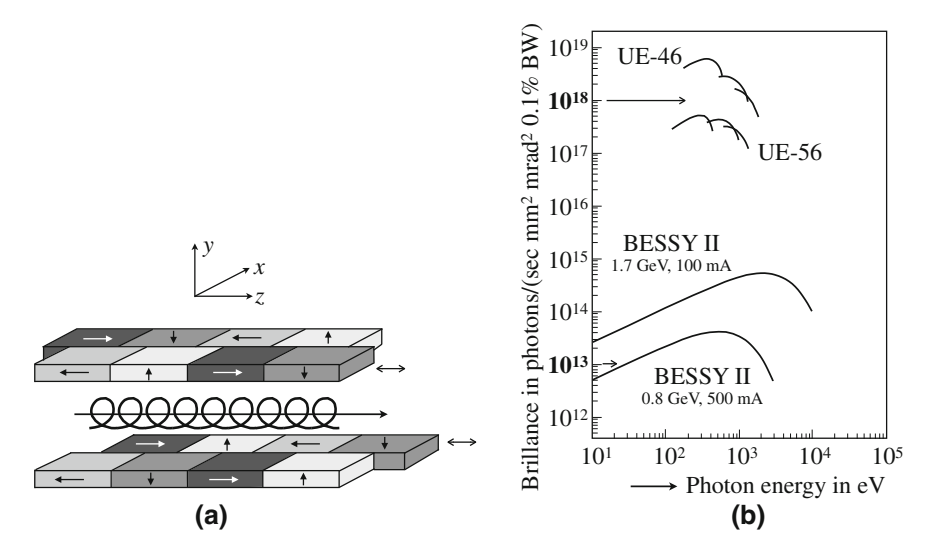


**Fig. 2.27** a Scheme of a helical undulator. Mechanically shifting the magnet arrays allows to tune the polarization to circular and linear. **b** Brilliance of X rays versus photon energy for synchrotron sources (UE46 and UE56 helical undulator beamlines at BESSY II compared to bending magnet beamlines at BESSY I and BESSY II)

the helicity of circular polarization within several seconds, or even to tune to linear polarization with its orientation pointing in any direction. This enables the study of ferromagnetic/antiferromagnetic systems by utilizing both, the effect of magnetic linear dichroism [230], as described in the previous section, and of magnetic circular dichroism, which will be explained in the following section.

## 2.7.3 X-Ray Magnetic Circular Dichroism

In the case that circularly polarized X rays are being absorbed in ferromagnetic systems, the cross section for X-ray absorption depends not only on the thickness and chemical composition of the sample, but also on the orientation of magnetization direction with respect to the helicity of the circularly polarized X rays. This effect is called X-ray magnetic circular dichroism (XMCD), which was first experimentally observed in 1987 [231]. Depending on the relative orientation between the helicity of the incoming photons and the projection of the magnetization onto the photon propagation direction, the absorption cross section, which is equivalent to the experimentally measurable absorption coefficient  $\alpha(\mathcal{E})$  at photon energy  $\mathcal{E}$ , is increased  $(\alpha^+)$  or decreased  $(\alpha^-)$ . With

$$\alpha_{\pm}(\mathcal{E}) = \alpha_0(\mathcal{E}) \pm \frac{1}{2} \Delta \alpha(\mathcal{E})$$
 (2.128)

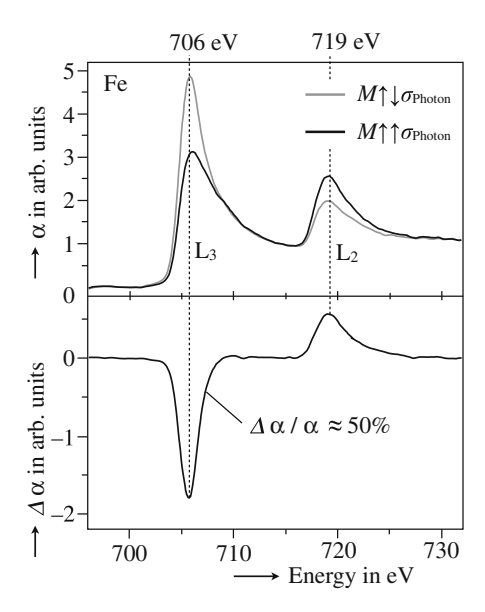


Fig. 2.28 X-ray magnetic circular dichroism at the Fe  $L_{3,2}$  absorption edges. *Top* X-ray absorption spectra for different orientation of the sample magnetization relative to the helicity of the exciting x-rays. *Bottom* Difference between the two curves shown in the top panel. The maximum of the difference curve amounts to nearly 50 % of the helicity-averaged absorption

the dichroic signal  $\Delta\alpha(\mathcal{E})$  can thus be described by

$$\Delta \alpha(\mathcal{E}) = \alpha_{+}(\mathcal{E}) - \alpha_{-}(\mathcal{E}). \tag{2.129}$$

A typical example of XMCD observed in ferromagnetic iron is shown in Fig. 2.28: The top panel shows the absorption coefficient  $\alpha(E)$  as a function of incoming photon energy for the two cases of parallel and antiparallel alignment between the helicity and magnetization of the specimen. The photon energy is varied in the region of the  $L_2$  and  $L_3$  absorption edges of iron, which correspond to absorption by resonant transitions from  $2p_{1/2}$  and  $2p_{3/2}$  core levels, respectively, and the unoccupied part of the 3d states just above the Fermi energy. The lower panel displays the difference between these two profiles,  $\Delta\alpha(E)$ . It is seen that the maximum difference at the Fe  $L_3$  edge amounts to nearly 50 % of the helicity-averaged absorption.

The following features can be observed. The XMCD effect is localized around the absorption edges, i.e. the  $L_3$  and  $L_2$  edges, which are separated by the spin-orbit coupling. The XMCD signal furthermore reverses its sign and yields a different amplitude at the  $L_3$  and  $L_2$  edges, respectively. In the case of 3d transition metals such as Fe, Co, or Ni, the additional magnetic contribution to the absorption cross section yields values up to  $25\,\%$ , i.e. a change up to  $50\,\%$  between the negative and positive saturated magnetization states.

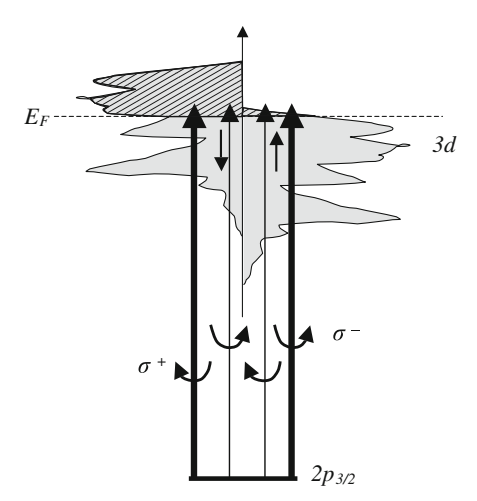


Fig. 2.29 Sketch illustrating the principle of X-ray magnetic circular dichroism. The *gray* and *hatched gray areas* represent the density of occupied and unoccupied 3d states, respectively. The *left* and *right* part of the figure refer to minority and majority spin directions. Transitions excited by circularly polarized X rays of helicity  $\sigma_+$  and  $\sigma_-$  are shown by *arrows*, the line thickness of which corresponds to the transition probability determined by the spin polarization of dipole transitions

Although in the beginning XMCD was used as a sensitive spectroscopic tool only, it was soon realized that it could also serve as huge magnetic contrast mechanism in combination with high-resolution microscopy. So far two real-space imaging techniques have been realized using either a photoelectron emission microscope (PEEM) [232], which will be described in Sect. 4.4, or a transmission X-ray microscope (TXM) [233], which will be the topic of Chap. 5.

The physical origin of XMCD and its global characteristics can be discussed in the frame of a simple vector coupling model. Within the dipole approximation for the transition process of a right- (left)-handed photon being absorbed, the photoelectron is going out with a finite spin  $\langle \sigma_z \rangle$  and orbital  $\langle l_z \rangle$  polarization in photon beam direction z, taking into account angular momentum conservation and spin–orbit coupling in the initial state. In particular, for the transition from an initial  $2p_{1/2}$  and  $2p_{3/2}$  spin–orbit-split state into a d-like final state (which corresponds to the  $L_2$  and  $L_3$  absorption edges),  $\langle \sigma_z \rangle$  amounts to -1/2 and +1/4, respectively, while  $\langle l_z \rangle = +3/4$  for both cases [234]. For very low photoelectron energies (E < 20 eV) and itinerant final states, the absorption coefficient is described by Fermi's Golden Rule, see (2.114) and (2.23) and the discussion in Sect. 2.4.4, where the dipole matrix element  $|e| p_{\pm} |f| > |^2$  contains the XMCD effect.

In a ferromagnetic system, the absorbing atom reveals a magnetic spin moment if the majority (minority) band final states are shifted below (above) the Fermi level due to exchange splitting. This is schematically shown in Fig. 2.29. The hatched areas of the 3d density of states, plotted to the left and right for minority and majority electrons, respectively, indicate the unoccupied states available for  $2p \rightarrow 3d$ 

transitions. Thus a local magnetic spin moment is induced, given by the excess of one spin direction in the density of states above the Fermi energy. Now due to Pauli's exclusion principle the spin/orbital-polarized photoelectrons created in the absorption process by a circularly polarized photon can be seen as a probe for the final-state spin/orbital polarization projected onto the photon k vector. The spin polarization can be shown in the sketch of Fig. 2.29 by drawing arrows between the spin-orbit split 2p states and the unoccupied 3d states in the left and right part of the figure. Symbols  $\sigma_+$  and  $\sigma_-$  refer to transitions excited by positive and negative helicity of circular polarization, respectively. The thickness of the arrows indicates the transition probability as a consequence of this spin polarization. Applying an external magnetic field, it is possible to adjust the sample's magnetization and to align the magnetic moments. The spins of the majority electrons are thus either parallel or antiparallel to the z-direction. According to Fermi's Golden rule an integration of the dichroic signal, which is related to the difference in spin-up and spin-down densities of states, measures then directly the local spin moment. In other words, when the spin polarization of the electronic transition matches the minority spin, the highest absorption is observed. A similar consideration holds for the orbital momentum. The unique potential of XMCD, however, is the possibility to address local magnetic moments separated into spin and orbital contributions applying the sum rules by Thole [235] and Carra [236] to the dichroic signals at spin-orbit-coupled edges, like  $L_{2,3}$ , or  $M_{4.5}$ . In particular the information that can be obtained on the orbital contribution to the local magnetic moments is crucial to understand, for example, the origin of magnetic anisotropies. Although the general applicability of the sum rules is still discussed [237–240], at least for the itinerant transition-metal systems like Fe, Co, Ni the results are satisfying [16, 239–242].

As discussed in Sect. 2.4.4, the absorption coefficient  $\alpha$  is related to the imaginary part of the complex refractive index n'' according to (2.23), and the XMCD effect introduces a magnetic contribution to n''. Following the causality reflected by a Kramers-Kronig relationship, which connects the real and the imaginary part of a complex quantity, a magnetic contribution to the real part of the refractive index n' should occur as well [243]. Therefore one expects to observe a similar magnetic dichroism effect also for the phase, which makes magnetic phase contrast mechanisms possible [244].

# **Chapter 3 Depth-Sensitive Conventional Magneto-Optical Microscopy**

In this chapter depth-sensitive magneto-optical microscopy, based on the conventional Kerr-, Voigt- and gradient effects, is reviewed. Following some experimental aspects of conventional magneto-optical microscopy and magnetometry in Sect. 3.1, the main part of the chapter (Sect. 3.2) is devoted to the depth sensitivity of the *Kerr effect* that is the most commonly applied effect. The concept of depth sensitivity functions will be introduced, followed by a detailed treatment of magnetic films and multilayers on the basis of a multiple beam formalism and magneto-optic diffraction analysis, which provides an intuitive understanding of depth sensitivity. Experimental depth-selective Kerr microscopy will then be presented in Sect. 3.3, followed by a section on Voigt and gradient microscopy and their favorable application on multilayer films (Sect. 3.4).

## 3.1 Magneto-Optical Microscopy and Magnetometry

Two types of polarization microscopes are in use for magneto-optical imaging: Wide-field ("regular") microscopes, which immediately provide an image of a certain sample area, and laser-scanning microscopes, in which a laser spot is scanned along the sample surface building up the image sequentially. Both are suited for the study of layered structures. In this section the two types of microscopes are introduced with emphasis on wide-field reflection microscopy as it is the most commonly applied and most versatile technique. The description is restricted to features that are important for depth-selective imaging. Comprehensive reviews on *Kerr* microscopy are given in the monograph Magnetic Domains [111] and in a more recent review article [118] that includes extended bibliographies. At the end of the section we introduce magneto-optical magnetometry, which has been successfully applied for layer-selective measurement of the magnetization curves in multilayers (e.g. in [245]).

#### 3.1.1 Wide-Field Microscopy

#### 3.1.1.1 Microscope

Standard wide-field Kerr microscopes are reflected light microscopes with strain-free optics to allow for polarization microscopy. Homogeneously illuminated images are obtained by applying the Köhler illumination technique that is explained by ray-diagrams in Fig. 3.1. The lamp is focused onto the plane of the aperture diaphragm, passes through the field diaphragm, is then linearly polarized and deflected downward into the objective lens by a partially reflecting plane glass mirror. After reflection from the sample, the light is collected by the objective and then passes through the half-mirror again. Most optical microscopes are built with infinity-corrected objectives, i.e. the reflected light rays leave the objective in parallel bundles from every azimuth and are projected to infinity. These bundles enter the tube lens, which

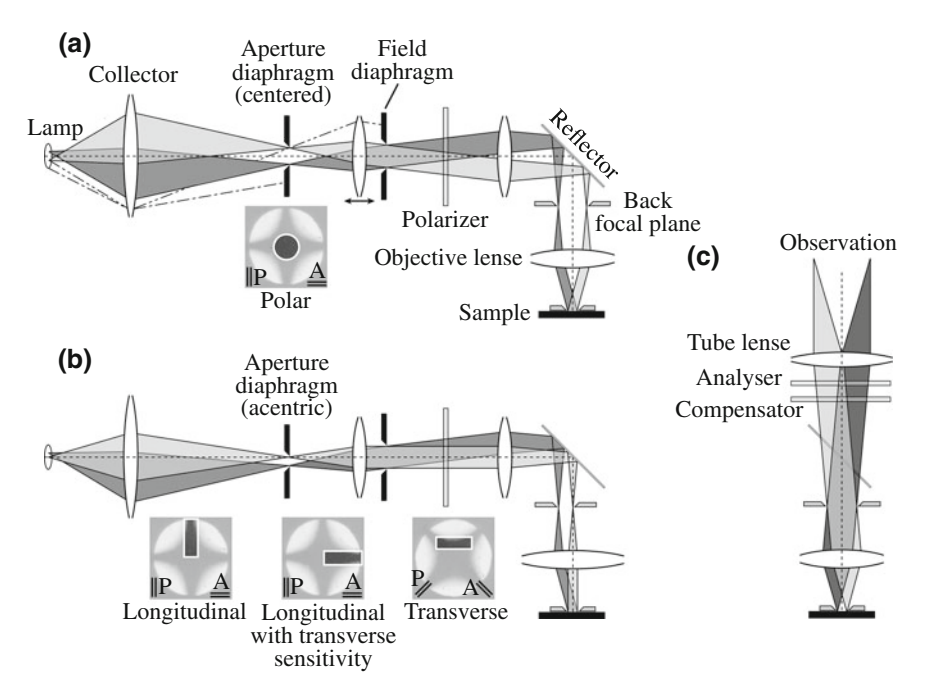


Fig. 3.1 Ray paths and essential components of a wide-field magneto-optical reflection microscope. The illumination- and image-formation ray paths are illustrated separately for clarity. a Illumination path for perpendicular light incidence. Oblique incidence (b) requires a displaced aperture slit. The insets in (a) and (b) show the diffraction plane of the microscope. Here the aperture diaphragm can be viewed and adjusted to fulfill the requirements for the polar Kerr effect (centered iris diaphragm) or longitudinal and transverse effects (displaced slit diaphragm). The orientation of the extinction cross depends on the polarizer setting, indicated by (P), with the analyser (A) and eventually the compensator being adjusted for maximum extinction. The image forming path is shown separately in (c). After [118]

forms an intermediate image that is further processed towards camera or eyepiece. In the infinity space, accessories like reflector mirror, analyzer, and compensator are added without distorting the image. Polarizers and analysers are usually made of dichroic polarizing foils, but also grid polarizers or Glan-Thompson prisms can be used.

The field diaphragm with variable opening and adjustable lateral position is imaged on the specimen. It thus determines which part of the sample is illuminated without having an affect on the resolution or intensity of illumination. The latter is rather controlled by the aperture diaphragm. Closing or opening this diaphragm varies not only the light intensity, but also the angle of the light rays that reach the specimen. The aperture diaphragm is thus crucial for magneto-optical microscopy as it allows to select the direction of incidence: A centered aperture iris (Fig. 3.1a) results in an illumination cone that strikes the sample vertically. Due to symmetry, the Kerr amplitudes resulting from in-plane magnetization components cancel each other, so that in this case a sole sensitivity to out-of-plane magnetization is given as required for the polar Kerr effect. A centered aperture iris also provides optimum conditions for Voigt- and Gradient microscopy of in-plane domains. An off-centered aperture diaphragm (Fig. 3.1b) leads to an obliquely incident bundle of rays as necessary for longitudinal and transverse Kerr sensitivity. Here the angle-of-incidence dispersion ranges between perpendicular and a maximum angle that is limited by the numerical aperture of the objective.

The plane of the aperture diaphragm is conjugate to the back focal plane of the objective lens, also known as diffraction plane or pupil of the objective. The pupil can be seen in the so-called conoscopical image of the microscope by applying a builtin, focusable Bertrand lens or by replacing the eye-piece by an auxiliary telescope. When analyser, polarizer, and compensator are crossed for maximum extinction, the diffraction image is characterized by a cross-shaped extinction zone (Fig. 3.1, insets), which is owed to the fact that a convergent light bundle is used in wide-field microscopy. All beams not lying in a central incidence plane along or perpendicular to the polarization plane cannot be extinguished [111] as they are reflected in an elliptical and rotated polarization state due to differential transmission of the p- and s-components at the steep optical interfaces of the lenses. This depolarization results in four bright quadrants, separated by the cross. For best Kerr contrast conditions, the illumination should be restricted to the area of maximum extinction in the conoscopic image by properly positioning the aperture stop as illustrated in the insets of Fig. 3.1. For the polar Kerr effect a centered iris diaphragm is used, while the longitudinal effect is preferably adjusted by an off-centered slit aperture that is oriented parallel to the plane of incidence. For the transverse Kerr effect, the polarizer and consequently also the extinction cross are rotated by 45° (due to depolarization at the reflector the use of a compensator is mandatory in this case to obtain a closed extinction cross). Here a displaced slit perpendicular to the plane of incidence or a V-shaped slit [118] are the best solutions. Transverse sensitivity can also be obtained with the longitudinal Kerr effect by placing the slit aperture on the sideward-branch of the extinction cross, thus causing a transverse plane of incidence.

The lateral resolution in optical microscopy is determined by the numerical aperture of the objective lens and by the wavelength of light. According to the Rayleigh criterion, the smallest distance between two objects that can be resolved is given by  $d_{min} = \frac{1}{2}\lambda(NA)^{-1}$ . Here  $\lambda$  is the wavelength of light and  $NA = n_0 \sin \alpha$  is the numerical aperture with  $\alpha$  being half the opening angle of the objective (i.e. half the angle of the cone of light from the specimen that is accepted by the objective) and  $n_0$  being the refractive index of the medium between objective and object ( $n_0 = 1$  for air;  $n_0 \approx 1.5$  for immersion oil). The higher  $\alpha$  and  $n_0$ , the more orders of diffracted light are collected by the objective and the higher the resolution. The highest numerical aperture available is 1.4, obtained with oil-immersion objectives of 100x magnification. Using such an objective and blue light for illumination, domains as narrow as 150 nm can be resolved [246]. Smaller magnetic objects like domain walls down to a size of some ten nanometers may also become visible by digital contrast enhancement, but their image is diffraction-broadened. Recently it was shown [247] that a Kerr signal can also be obtained from nanowires with a width of just 30 nm.

#### 3.1.1.2 Setup and Image Processing

Due to the smallness of the magneto-optical signals, magnetic images can be strongly obscured by polarization effects from imperfect surfaces. Magnetic contrast enhancement is possible by the interference layers mentioned at the end of Sect. 2.4.3. A more powerful way, however, is the implementation of digital image processing [145, 146]. Magnetic materials are ideally suited for difference imaging, because the magnetization can be manipulated by external magnetic fields without changing the topography of the specimen. The standard procedure starts with a digitized, averaged image of the magnetically saturated state, where in an external d.c. magnetic field all domains are eliminated. Alternatively, an alternating field of moderate amplitude can be applied, which mixes up the domains during averaging with the advantage that forces on the sample may be smaller than in the high fields required for d.c. saturation. This domain-free background (reference) image is subsequently subtracted from a state containing domain information. The difference image then displays a micrograph of the domain pattern, which can be improved by averaging and digital contrast enhancement, free of topographic contrasts. All domain images shown in this chapter have been obtained by such technique. Often it is desirable to study identical domains in different aspects, e.g. under Kerr- and Voigt-contrast conditions or with different analyser and compensator settings to obtain depth selectivity (see Sect. 3.3). This is possible by a combination experiment: After having created a regular difference image of a certain domain pattern, an image of the same pattern, but under different contrast conditions, is stored as a reference image that is then subtracted from an image of the saturated state obtained under the same contrast conditions. So two difference images of the same domain pattern, but with different contrast aspects, are obtained. The images in Fig. 2.1a, c have been generated in this way and for layer-selective imaging the combination technique is essential as shown for a number of examples in Sect. 3.3.

Also the recording of magnetization loops ("MOKE magnetometry") is easily possible in a digitally enhanced wide-field Kerr-microscope. Plotting the average difference-image intensity in a sample area, which is defined by the field diaphragm or selected in the image processing software, as a function of the applied magnetic field yields a local magneto-optical hysteresis curve. At the same time the domain images can be recorded, thus providing a visualization of the underlying magnetization process (see Fig. 3.18 for an example). In this aspect *microscopic* magnetometry is superior to the laser-based systems described in Sect. 3.1.3.

The complete experimental setup for video-enhanced, wide-field magneto-optical microscopy is schematically shown in Fig. 3.2. Light sources with a high luminous density are mandatory as most of the light is thrown away due to the small relative opening of polarizer and analyser. High-pressure mercury arc lamps offer sufficient brightness and a color spectrum that can be monochromatically used in the yellow-green as well as blue range by suitable spectral filters. The use of monochromatic light is prerequisite for depth-selective Kerr microscopy as elaborated in Sect. 3.2. The disadvantage of the mercury lamp is its instability and short lifetime. More stable are xenon-arc lamps, which offer white light at a luminous density of just one quarter of the mercury lamp. This is still sufficient if the lack of light is compensated by a highly sensitive video camera. Laser illumination [146] for wide-field microscopy is problematic [118]: the coherence of the laser leads to diffraction patterns (speckle) due to interference at surfaces and dirt particles in the optics. The elimination of such artifacts, which may be orders of magnitude stronger than any magneto-optical contrast, requires special means of de-speckling [248, 249]. Never-

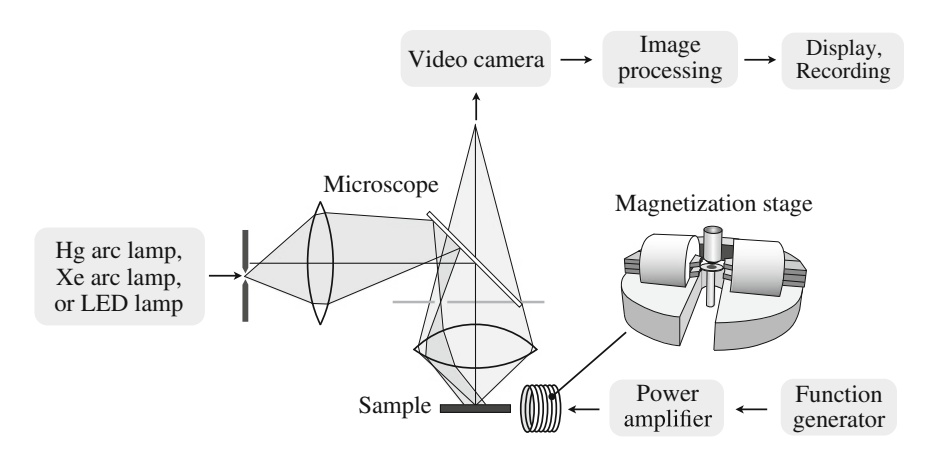


Fig. 3.2 Experimental setup for wide-field Kerr microscopy. Image processing and function generator are usually implemented in a computer. In-plane magnetic fields of arbitrary direction can be applied by a rotatable electromagnet as sketched. Here the specimen is mounted on a stamp that is placed between the split pole pieces to enable a reasonable sample displacement. Magnetic fields  $\mu_0 H$  up to some tenths of a Tesla can be achieved in such setups, reaching the Tesla regime at proper pole-tip geometry and close pole distance. Also perpendicular magnetic fields (i.e. parallel to the objective) can be generated by specially designed electromagnets [118]

theless, satisfactory results with laser-illuminated microscopes are only obtained in multi-frame accumulated images where residual laser effects are sufficiently averaged out. A promising light source for future applications are high-intensity lightemitting diodes (LEDs). They offer monochromatic light of high stability and have already reached intensities that make them suitable for magneto-optical microscopy. Placing an array of LEDs directly in the plane of the aperture diaphragm makes the diaphragm needless as a centered or displaced slit can be simulated by running different LEDs of the array. Recently the simultaneous wide-field imaging of different magnetization components was demonstrated by using monochromatic LEDs of different color and placing them at selected positions in the diffraction plane [250]. Using some dichroic device for the separation of the corresponding reflected Kerr images results in wide-field images that are complementary sensitive to selected in-plane or out-of-plane magnetization components. This method of dichromatic imaging will substantially improve the technique of quantitative Kerr microscopy [174] and might have the potential for convenient layer-selective Kerr microscopy based on wavelength selection (see Sect. 3.2.6).

Image processing for contrast enhancement requires digital image acquisition. Digital CCD (Charge-Coupled Device) or CMOS (Complementary Metal Oxide Semiconductor) cameras directly provide a digitized data stream, while for video-rate CCD cameras the analogous output has to be converted by an analog-to-digital converter. Digital CCD cameras are suitable for Kerr microscopy if their frame rate is fast enough (some 10 Hz) to allow real-time imaging. Cooling of the CCD chip improves the signal-to-noise ratio and image intensifiers can further increase the sensitivity. In practice, the image brightness has to be adapted properly to meet the optimum dynamic range of the camera. Increasing the analyser angle  $\alpha_{an}$  (Fig. 2.14b—the intensity increases with  $\alpha_{an}^2$ ) or opening the aperture stop beyond the width of the extinction cross, thus increasing the background intensity, are practical means to achieve a large signal-to-noise ratio (see Sect. 2.4.3). A possible loss in contrast is not a severe problem, as contrast can be enhanced electronically by difference imaging. To create a difference image, first an averaged reference image is stored by summation of repeated images of the same sample state. The reference image is then continuously subtracted from all following images. As the visual observation of domain motion is fundamental for any kind of domain analysis, it is advantageous if the subtraction process is performed in "real time" without averaging. For presentation and recording purposes, noise can be reduced by adding a number of digitized images in a recursive procedure to produce a running average of the incoming images. Because noise is random and the signal is not, a running average both reduces the noise contribution and enhances the signal component of the output digital image. The result is an image of constant brightness, the noise of which is continuously reduced with increasing averaging time. By difference-image processing, contrasts below 0.1 % can be visualized (the contrast sensitivity of the human eye is some percent at best). A high mechanical, thermal, and electrical stabilization of the microscope is indispensable to obtain optimal results.

# 3.1.2 Laser-Scanning Microscopy

In a laser-scanning Kerr microscope a polarized laser beam is scanned across the specimen surface and its polarization state after reflection is analyzed using a photo detector. The domain information is attained by sophisticated detection schemes that even have the capability of vector magnetometry [251–254]. Figure 3.3a illustrates the principle of such an advanced microscope. The collimated and polarized laser beam is focused on the specimen surface by an infinity-corrected objective lens. The sample is moved in a raster-like way by using a precision XY stage. Although this stage scanning is relatively slow (the acquisition time for an image is of the order of tens of seconds), it is more favorable for Kerr microscopy than beam scanning as it ensures that the polarization state as well as the angle of incidence of the illuminating ray bundle are constant over the entire scan. By scanning, the image is constructed in a point-by-point manner with a lateral resolution that is basically determined by the size of the probing laser beam. Using a 100x oil immersion objective with a numerical aperture of 1.3, a laser spot size of 0.8  $\mu$ m is obtained. A smaller

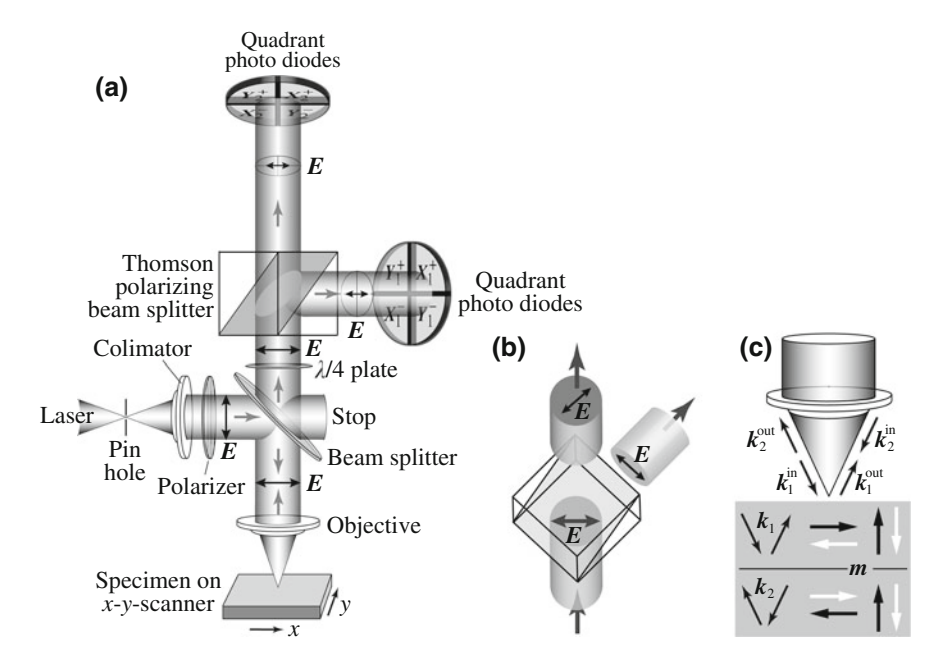


**Fig. 3.3** a Principle of Laser-Scanning Kerr Microscopy (based on setups realized by Wright et al. [255] and Freeman and Hiebert [256]). The polarization plane of light is indicated by the **E**-vector. Sketch **b** shows a perspective view from top to illustrate the orthogonal polarization directions of the two beams leaving the polarizing beam splitter. **c** Contrast of in- and out-of plane magnetization components in dependence of the direction of the **k**-vector. After [118]

focused spot size of  $0.16 \mu m$  is achieved if the beam diameter is first increased by beam expansion to completely fill the objective aperture before it is focused on the sample [248].

The reflected light is collected by the same objective lens and passes a rotatable quarter-wave plate to compensate ellipticity before it finally enters a Thomson polarizing beam splitter. To maximize sensitivity, the splitter is set at 45° to the incident (undisturbed) polarization. The splitter provides two beams of orthogonal polarization direction (Fig. 3.3b) that hit a pair of quadrant photodiodes. Each pair of opposing quadrants is aligned along the projection of the sample's x and y axes, respectively. The two beams are of equal intensity for the case of undisturbed 45° polarization, while any sample-induced polarization rotation leads to equal but opposite intensities (45° is the angle most sensitive to small polarization changes). By suitably combining the outputs of the eight photodiode quadrants, the three orthogonal components of magnetization can be simultaneously detected and separated, provided that they are sampled nearly equally, which is true for objectives with a high numerical aperture. As illustrated in Fig. 3.3c, the longitudinal Kerr contrast changes sign if excited by two beams of opposite directions of incidence, while the polar contrast remains unchanged. By adding the signals of all four diodes of one quadrant detector, the longitudinal components will cancel while the polar components are added. As the total intensity that reaches each detector is reduced and enhanced, respectively, by equal amounts due to the beam splitting, the pure polar contrast can thus be separated by subtracting the two sum signals [i.e. taking the quadrant combinations  $(X_1^+ + X_1^- + Y_1^+ + Y_1^-) - (X_2^+ + X_2^- + Y_2^+ + Y_2^-)$ ], whereas a non-magnetic surface-contrast image is generated by simply adding the signals. The longitudinal Kerr contrast of magnetization components along the x-axis is revealed by combining  $(X_1^+ - X_1^-) - (X_2^+ - X_2^-)$ , and that along the y-axis by  $(Y_1^+ - Y_1^-) - (Y_2^+ - Y_2^-)$ . Since all data are collected from the quadrants simultaneously, the three magnetization components at one sample spot are captured at the same time. This elegant method of vector magnetometry requires a highly symmetrical beam profile so that each quadrant receives the same quarter of the beam. Enhancement of the signal-tonoise ratio can be achieved by applying lock-in techniques: The illuminating laser beam is modulated and the reflected light is measured by a phase-sensitive detection amplifier, thus selecting only signals that are proportional to the Kerr amplitude. See [118] for further possibilities.

The biggest potential of laser-scanning microscopes lies in their predestination for stroboscopic imaging of fast dynamic processes [118]. They fall short in replacing conventional microscopy for routine domain research as real-time imaging of domain motion cannot be realized. Of advantage is the capability to simultaneously image all three magnetization components (vector magnetometry) and to easily eliminate background contrast by lock-in techniques [118]. Static Kerr images of satisfactory quality, both of in- and out-of-plane domains, can therefore be obtained. Also other quantities like permeabilities or magnetization curves can conveniently be measured on a microscopic scale, thus probing the spatial variation of magnetic properties. Laser-scanning microscopy also offers the potential of layer-selective imaging, although this option has not yet been applied.

### 3.1.3 Magneto-Optical Magnetometry and Ellipsometry

In magneto-optical *microscopy* the different effects described in Sects. 2.4–2.6 are employed for the purpose of domain *imaging*. The most widely-used magneto-optical measuring systems, however, are laser-based setups as schematically shown in Fig. 3.4. Mostly they make use of the Kerr effect and are known under the acronym "MOKE" for Magneto-Optical Kerr Effect. MOKE setups can simply be operated as magnetometers to obtain magnetization loops by plotting the Kerr intensity as a function of the magnetic field. In fact, the Kerr effect is in principle well-suited for magnetometry due to its linear dependence on the magnetization vector. In a more sophisticated way, MOKE setups can be run as Kerr spectrometers to measure Kerr rotation and ellipticity as a function of wavelength. Also layer-selective measurements are possible in magnetic multilayer systems as will be elaborated in Sect. 3.2.6.

In optical magnetometry, a light beam is focused on the sample with a spot size of several micrometers and the reflected Kerr signal is then measured with an optical detector. Because of their better stability, laser light sources or high-intensity LEDs are preferred to arc lamps. In bulk materials, optical magnetometry must be applied with care as light scans the surface domains, which may differ drastically from interior domains. For thin films, however, the optical method has many advantages: the measured magnetization is usually relevant for the whole film thickness. Due to its high sensitivity, MOKE magnetometry can be performed on extremely thin films down to the monolayer regime. The method is direct, it can be fast, but also quasistatic measurements can be performed. Space-resolved measurements are possible by scanning over the surface as discussed in the previous section. Magneto-optical magnetometry can also be performed in situ during the preparation or treatment of a material e.g. in a vacuum chamber. A useful magnetometer that is able to detect even weak signals needs some means of suppressing non-magnetic noise. One way to achieve this is to feed a split-off part of the laser light as a reference signal into the

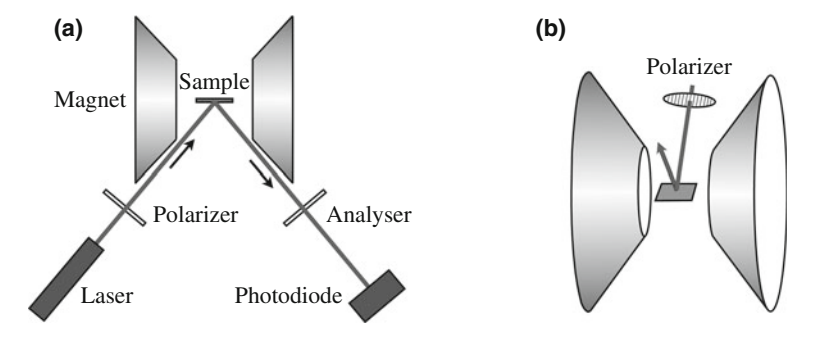


**Fig. 3.4** a Schematic drawing of a magneto-optical magnetometer that allows to record magnetization loops or to measure Kerr rotation and ellipticity. **b** A design that makes use of the transverse Kerr effect offers advantages in magnetometry as explained in the text

amplifier. If the polarization of the light is modulated by a spinning analyser or an electro-optical device [257–259], the magnetic signal can be detected by a lock-in amplifier, thus achieving virtually unlimited sensitivity.

An optical magnetometer needs some care in calibration and adjustment. The signal strength depends on the precise settings of polarizer and analyser and on surface conditions, i.e. on the presence or absence of surface layers. The safest procedure is therefore to normalize the optical signal with the saturation signal, taking the saturation magnetization from other measurements. Sometimes the Faraday effect in the optical components of the magnetometer can be superimposed to the Kerr signal, leading to a linearly increasing signal with the magnetic field after the sample is already saturated. Such effects can be easily corrected. Another problem lies in the exact dependence of the signal on the magnetization direction. For every polarizer/analyser setting at oblique incidence a certain in-plane magnetization direction yields the maximum Kerr signal, while the transverse direction is inactive. The "sensitivity direction" has to be adjusted to agree with the desired measuring direction. The difficulty of determining the sensitivity direction can be avoided by using the pure transverse Kerr effect. The polarizer is set parallel to the plane of incidence and the analyser can be omitted (Fig. 3.4b). Then only the component of the magnetization perpendicular to the plane of incidence causes a variation of the reflected intensity, which can be detected electronically. An advantage of the transverse design is that it fits nicely into a magnet. The transverse optical magnetometer also avoids possible influences of magneto-optical effects that are quadratic in the magnetization components and which may lead to asymmetrically distorted magnetization loops [260, 261].

A number of techniques have been developed to measure the Kerr rotation and ellipticity. The simplest ellipsometer is based on the setup of Fig. 3.4a [262]. Consider linear p-polarized light falling on the sample. As discussed in Sect. 2.4.2 (Fig. 2.14b), the reflected light due to the Kerr effect then consists of a small s-component (the Kerr amplitude  $A_{\rm K}$ ) in addition to the dominant p-component (the regularly reflected amplitude  $A_{\rm N}$ ), with  $A_{\rm K}/A_{\rm N}$  being the Kerr rotation according to (2.87). Goal of the experiment is the measurement of the complex Kerr component. This can be achieved by saturating the sample in opposite directions along the sensitivity axis (p-direction) and measuring the intensities  $I_1$  and  $I_2$  of these two states by the detector. After having passed the analyser, which is opened by an angle  $\alpha_{\rm an}$  from extinction (see Fig. 2.14b), the two intensities are given by (2.103a, 2.103b). For small  $\alpha_{\rm an}$ , intensity  $I_1$  can be approximated:

$$I_1 = |A_N \sin \alpha_{an} - A_K \cos \alpha_{an}|^2 + I_0 \approx |A_N \alpha_{an} - A_K|^2 + I_0.$$
 (3.1)

With (2.87) we get

$$I_{1} = |A_{N}|^{2} |\alpha_{an} - \theta_{K} - i \xi_{K}|^{2} + I_{0}$$

$$= |A_{N}|^{2} (\alpha_{an} - \theta_{K} - i \xi_{K}) (\alpha_{an} - \theta_{K} + i \xi_{K}) + I_{0}$$

$$\approx |A_{N}|^{2} (\alpha_{an}^{2} - 2\alpha_{an}\theta_{K}) + I_{0}$$
(3.2)

by ignoring the quadratic terms of rotation and ellipticity. With

$$I_2 \approx |A_{\rm N}|^2 (\alpha_{\rm an}^2 + 2\alpha_{\rm an}\theta_{\rm K}) + I_0 \tag{3.3}$$

and  $\Delta I = I_1 - I_2$ , the Kerr rotation is finally given by

$$\theta_{\rm K} = \frac{\Delta I}{4|A_{\rm N}|^2 \alpha_{\rm an}} \tag{3.4}$$

The Kerr ellipticity  $\xi_K$  is obtained by placing a quarter-wave plate in the reflected beam before the analyser, with its optical axis parallel to the  $A_K$ -direction. This adds an additional phase difference of  $\pi/2$  between  $A_N$  and  $A_K$ , i.e.  $A_K$  in (3.1) is replaced by  $iA_K$ . Calculating the relative Kerr intensity  $\Delta I$  as before it becomes evident that rotation and ellipticity are interchanged now and one measures the ellipticity

$$\xi_{\rm K} = -\frac{\Delta I}{4|A_{\rm N}|^2 \alpha_{\rm an}}.\tag{3.5}$$

Instead of a retardation plate also a photoelastic modulator can be employed [258, 263]. It provides a time-dependent phase shift between 0 and  $\pi/2$  (at a typical frequency of 50 kHz) between  $A_N$  and  $A_K$  if the principal axis of the modulator coincides with either of them. The intensity is then measured by means of lock-in detection of the detector output. The intensity component at the lock-in frequency is proportional to the Kerr ellipticity  $\xi_K$  and the component at the double frequency is proportional to the rotation  $\theta_K$ . The advantage of this technique is that  $\xi_K$  and  $\theta_K$  can be measured simultaneously. Polarization modulation and related optical techniques are described in a general reference [264].

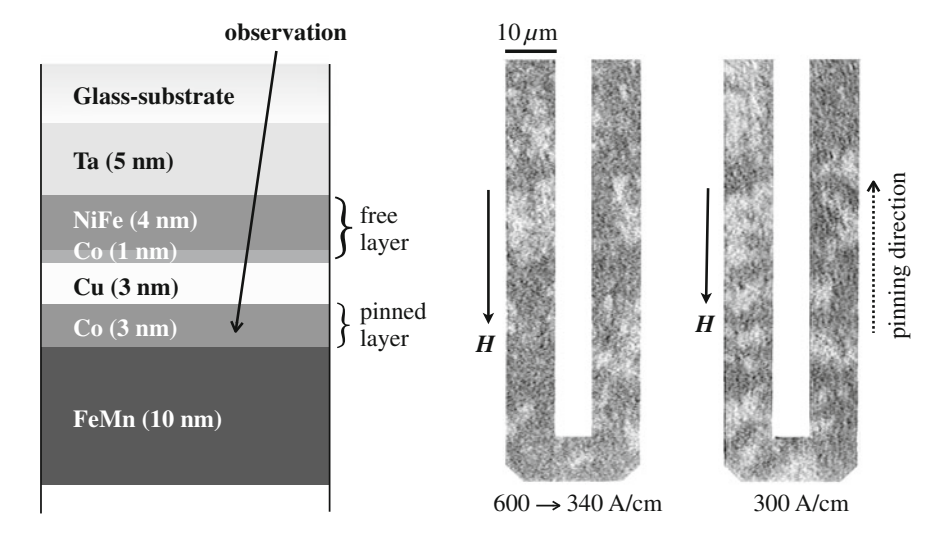
MOKE spectroscopy involves the determination of wavelength-dependent properties [265]. The main instrumental additions are a white light source (like a xenon arc lamp) and a monochromator. Different detectors are used, depending on the wavelength: InSb- or Si-diodes for the infrared to red spectral range, or photomultipliers for the visible to ultraviolet range can be applied. As the maximum light intensity is usually much lower than for lasers, modulation techniques are generally used for noise suppression. See [266] for representative work and basic descriptions of spectrometers.

# 3.2 Depth Sensitivity of Conventional Magneto-Optics

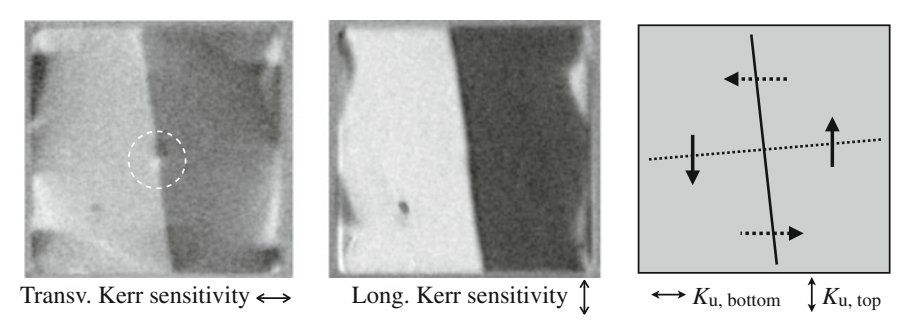
After proving the depth sensitivity of magneto-optical microscopy by simply presenting experimental examples in Sect. 3.2.1, an introduction to the theory of the effect is given in Sect. 3.2.2. The discussion is (mainly) restricted to Kerr microscopy in this section.

# 3.2.1 Experimental Proof of Depth Sensitivity

Magneto-optic microscopy on metallic materials is (restrictedly) depth-sensitive. This fact is proven in the following three figures that show domain images and magnetization processes in typical metallic multilayer systems. All images were obtained in the longitudinal Kerr effect with standard microscope settings, i.e. analyser and compensator were set for good contrast regardless of layer selectivity. In Fig. 3.5 the magnetization process in a burried cobalt film of a spin-valve layer stack, which is covered by 13 nm of metallic material, was imaged. Despite the coverage, the domains in the ferromagnetic film are clearly visible. The other ferromagnetic NiFe/Co bilayer within the stack, which is transmitted by the light at a lower depth, contributes even stronger to the Kerr signal. It switches, however, at applied magnetic fields almost two orders of magnitude lower in strength and is thus saturated in the course of the shown images. In the example of Fig. 3.6 a trilayer film was imaged at two orthogonal longitudinal Kerr sensitivities. The two ferromagnetic films, which are decoupled by a non-magnetic spacer film, have orthogonal induced anisotropies so that a vertically oriented 180° domain structure is present in the top layer, and a horizontally oriented one in the bottom layer. In both pictures, however, there is just contrast from the top layer. A contrast from the bottom layer should be visible as domain contrast in the



**Fig. 3.5** Kerr microscopy on a spin-valve meander for GMR sensor applications. As schematically indicated, the layer stack consists of a "free" ferromagnetic double layer that is interspaced by a non-magnetic interlayer from another, "pinned" ferromagnetic layer. Pinning is achieved by exchange-coupling to an antiferromagnetic layer. Shown are two domain images during the reversal of the pinned layer. At the indicated field values the free layer is saturated and does not contribute to the domain contrast. The domains were observed through a transparent glass substrate and several metal layers of 13 nm total thickness. Sample preparation: *K.U. Barholz* and *R. Mattheis*, Jena. After [267]



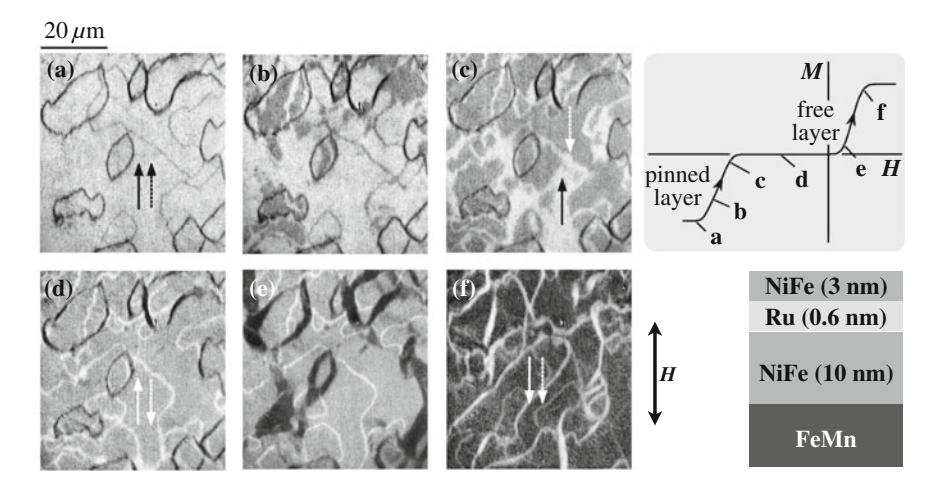
**Fig. 3.6** Kerr images of an amorphous CoFeSiB (80 nm)/SiO<sub>2</sub> (20 nm)/CoFeSiB (80 nm) sandwich element, taken under two orthogonal sensitivity conditions thus revealing two different aspects of the same domain structure. The schematics shows orthogonally oriented basic domains in the top and bottom layers marked by full and dashed arrows, respectively, while the edge domains are ignored. With kind permission of *J. McCord*, Dresden (imaging) *E. Quandt* and *A. Gerber*, Bonn (sample preparation)

image with transverse sensitivity. Obviously the 80 nm thick top layer is too thick to allow a direct contrast from the bottom layer. The presence of the horizontal domains in the bottom layer is only indirectly visible by charge-compensating magnetization excursions in the top layer. They are formed on the left and right edges, and especially at the crossing point of the domain walls in the middle of the element as marked by a circle in the transverse Kerr image.

Another example of a spin-valve-type layer system, proving the depth sensitivity again, is presented in Fig. 3.7. Here two Permalloy films of different thickness are interspaced by a non-magnetic ruthenium layer, which provides a weak ferromagnetic coupling at the given thickness. Both ferromagnetic films are remagnetized independently by the growth of domains that are nucleated at 360° walls. The 360° walls and domains in the bottom layer have a weaker contrast than those in the top layer due to a stronger absorption of light. Also for this experiment the longitudinal Kerr effect was adjusted without paying attention to layer selectivity. The magnetization process in both layers can be distinguished because they have different switching fields. This would not be possible in case of a strong ferromagnetic coupling between two films and simultaneous switching.

# 3.2.2 Theoretical Approaches to Depth Sensitivity in Magneto-Optics

The depth sensitivity of magneto-optics can theoretically be treated in two principal ways: in a rigorous way by numerical solutions of Maxwell's equations using optical matrix methods, or by magneto-optic diffraction analysis based on a multiple beam formalism. Here we introduce the basic ideas of both methods, which are to first order mathematically equivalent. Emphasis will be on the second method as it is more attractive for an intuitive understanding of depth sensitivity.



**Fig. 3.7** Magnetization process in the two ferromagnetic layers of an extended trilayer system as indicated. The longitudinal Kerr images correspond to labels in the schematic magnetization curve. Reducing the field from saturation, two sets of grey and black 360° walls appear in the two layers (a). From **b** to **d** the bottom layer is remagnetized by growth of dark domains nucleating at the grey 360°-walls. When the bottom layer is almost saturated (apart from residual, white 360°-walls), the black walls of the top layer are still unaffected (**d**). They then act as nucleation sites for the magnetization of the top layer (**e–f**). The field is applied along the axis of the pinning direction. After [268]

#### 3.2.2.1 Optic Matrix Methods

Optical matrix methods, as they are known from the optics of thin dielectric films [269, 270], were introduced into magneto-optics by Smith [271]. Today they are the standard methods to characterize the magneto-optics of magnetic multilayers. Mostly these methods are used to calculate the Kerr rotation and ellipticity obtained from multilayer structures [179, 272–274], but also the depth sensitivity of magneto-optical effects can be treated by such calcuations [177]. A thorough review on matrix methods was recently presented in the monograph by Višňovský [178]. In the following overview [187] we just outline the basics of this procedure.

Let the field distribution of light be represented by

$$E(\mathbf{r}) = \sum_{i=1}^{4} C_i U_i \exp[i(\mathbf{k}_i \cdot \mathbf{r} - \omega t)], \qquad (3.6)$$

where  $E_i = C_i U_i$  are the amplitudes of the four eigenmodes introduced in Sect. 2.3.2 (Fig. 2.10), here expressed in terms of unit amplitudes  $U_i$ . In every film of the multilayer, as well as in the (isotropic) half spaces above and below the layer stack, the coefficients  $C_i$  are initially unknown. Goal of the method is to connect the coefficient vector  $C^{\text{top}}$  of the eigenmodes of the upper half space with the

corresponding vector  $C^{\text{bottom}}$  of the lower half space by means of matrix algebra. For a layer system with surface normal parallel to the z-axis of the cartesian coordinate system, the basic steps are the following:

• The propagation of light in every layer of the stack is described by the proper eigenmodes in that layer, which are obtained by solving the wave equation (2.15) for a chosen external angle of incidence. When the wave vectors  $k_i^{(n)}$  of the eigenmodes in layer n of thickness  $D_n$  are known, the eigenmode amplitudes at the upper side of the layer (D=0), can be connected with those at the bottom side  $(D=D_n)$ :

$$C_i^{(n)}(0) = \sum_{j=1}^4 P_{ij}^{(n)} C_j^{(n)}(D_n),$$
with  $P_{ij}^{(n)} = \exp(-ik_i^{(n)}D_n), \quad P_{i,j\neq i}^{(n)} = 0,$  (3.7)

where  $P_{ij}^{(n)}$  are the components of the *medium propagation matrix*  $\boldsymbol{P}$ .

• The eigenmodes of the adjacent layers are coupled by the continuity condi-

• The eigenmodes of the adjacent layers are coupled by the continuity conditions that are valid for the lateral components of the E- and H-fields at the layer interfaces (see Sect. 2.2.5). Collecting these components in the vector  $F = (E_1, E_2, H_1, H_2)$ , the vector components of F at the boundary between layer n and (n + 1) are given by

$$F_i^{(n)} = \sum_{j=1}^4 Q_{ij}^{(n)} C_j^{(n)} = \sum_{j=1}^4 Q_{ij}^{(n+1)} C_j^{(n+1)} = F_i^{(n+1)}, \tag{3.8}$$

where  $Q_{ij}^{(n)}$  are the components of the *medium boundary matrix* Q. The elements of Q for i = 1, 2 are derived from (3.6), and for i = 3, 4 they are derived from (3.6) in connection with (2.19).

• General N-layer systems can now be described by a system matrix S, which is calculated by matrix multiplication from (3.7) and (3.8) and which couples the coefficient matrix  $C^{\text{top}}$  with  $C^{\text{bottom}}$ :

$$C^{\text{top}} = S C^{\text{bottom}}, \tag{3.9a}$$

$$S = (Q^{\text{top}})^{-1} \left[ \prod_{n=1}^{N} Q^{(n)} P^{(n)} (Q^{(n)})^{-1} \right] Q^{\text{bottom}} = \begin{pmatrix} S_1 & S_2 \\ S_3 & S_4 \end{pmatrix}.$$
(3.9b)

In this matrix equation eight unknowns are connected by four equations, so that four variables can be freely chosen. These four degrees of freedom are in fact to be expected, as the sample can be illuminated from both sides so that two elements in  $C^{\text{top}}$  and  $C^{\text{bottom}}$ , respectively, can be fixed.

• In the isotropic half spaces the solutions of the characteristic equation are degenerate, so that in each space two arbitrary orthogonal, elliptically polarized waves are the eigenmodes. By choosing *s*- and *p*-polarized incident light, and by collecting the amplitudes of the incident (i), reflected (r) and transmitted (t) light properly in the coefficient vectors,

$$C^{\text{top}} = (E_s^{(i)}, E_p^{(i)}, E_s^{(r)}, E_p^{(r)}) \text{ and } C^{\text{bottom}} = (E_s^{(t)}, E_p^{(t)}, 0, 0),$$
 (3.10)

the reflection coefficients  $r_{ss} = E_s^{(r)}/E_s^{(i)}$ , etc. and transmission coefficients  $t_{ss} = E_s^{(t)}/E_s^{(i)}$ , etc. [compare (2.52) and (2.53)] can be determined from the sub-matrices of S:

$$\begin{pmatrix} r_{\rm ss} & r_{\rm sp} \\ r_{\rm ps} & r_{\rm pp} \end{pmatrix} = S_3 S_1^{-1} \quad \text{and} \quad \begin{pmatrix} t_{\rm ss} & t_{\rm sp} \\ t_{\rm ps} & t_{\rm pp} \end{pmatrix} = S_1^{-1}. \tag{3.11}$$

The magneto-optical observables, the Kerr rotation and ellipticity, are then obtained from the quotients of the off-diagonal to the diagonal elements [see Sect. 2.4.1, (2.93)].

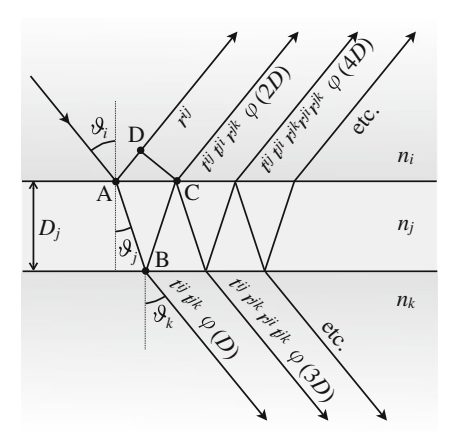
This matrix method can always be applied if the considered effects are described by a temporarily and (within each layer) spatially constant dielectric tensor. General solutions for the magneto-optical effects in multilayers can be implemented in a computer program and simulations can be performed with moderate computing time: the characteristic equation of fourth order can be solved analytically and the application of  $(2 \times 2)$  matrices, introduced by Mansuripur [274], provides a good numerical stability. The disadvantage of matrix methods, however, is the fact that the influence of the material parameters of the individual layers as well as of the whole layer setup on the magneto-optical behavior is not directly seen, but only from the final result of the simulation. In this sense the multiple beam method, presented in the next section, is more favorable.

#### 3.2.2.2 Multiple Beam Formalism

Multiple beam formalisms as alternative to matrix methods can be applied favorably in cases where the propagation vector of the eigenmodes and the transmission- and reflection coefficients of the associated amplitudes can be easily determined. This applies, for example, to isotropic non-magnetic films. But also the magneto-optics of magnetic films and multilayers can be described advantageously by multiple beam analysis. Here the (weak) magneto-optical interaction is treated in the sense of a perturbation of the isotropic light propagation. We will present such an analysis in Sect. 3.2.4.

The basic concept of multiple beam methods is based on the following physical picture: In a (general) thin film or multilayer system, an incident light beam will interact not just with the first boundary (like in Fig. 2.9) but rather with a number of

Fig. 3.8 Multiple beam interference from a parallel film, including a schematics for the derivation of the optical path length between adjacent reflected rays (see text) [166]



boundaries. For a thin film these are the two film surfaces, in case of a multilayer it will be the surface and several interfaces within the penetration depth of the light. At each boundary the beam will generate a cascade-like multitude of transmitted and reflected beams that will interfere to add up to the total electromagnetic field. The situation is schematically depicted in Fig. 3.8 for a general, absorbing thin film with refraction index  $n_j$ , embedded in two media with indices  $n_i$  and  $n_k$ . The incident beam is partially reflected and partially transmitted at the first interface. The transmitted part is subsequently reflected back and forth between the two interfaces as shown. The global reflection and transmission coefficients of the complete film can be obtained by adding the amplitudes of the successive reflected and transmitted rays.

In doing this it is important to include the phase factor that accounts for the geometric, "optical" path difference between any two successive reflected or transmitted rays. Between two adjacent reflected rays, this path difference  $\Lambda$  can be derived from Fig. 3.8: For the first two reflected beams it is given by  $\Lambda = n_j [\overline{AB} + \overline{BC}] - n_i \overline{AD}$ . With  $\overline{AB} = \overline{BC} = D_j/\cos\vartheta_j$  we get  $\Lambda = 2n_j D_j/\cos\vartheta_j - n_i \overline{AD}$ . With  $\overline{AD} = \overline{AC}\sin\vartheta_i$  and Snell's law (2.54) the path length difference is finally given by  $\Lambda = 2n_j D_j \cos\vartheta_j$ . The corresponding *phase* difference associated with the optical path length difference is the product of the free-space propagation number  $k_0 = 2\pi/\lambda_0$  and  $\Lambda$ , that is,  $k_0 \Lambda$ . The phase difference is taken into account by the *phase factor*  $\varphi$ 

$$\varphi(D_j) = \exp(\frac{2\pi i \cos \vartheta_j n_j}{\lambda_0} D_j), \qquad (3.12)$$

<sup>&</sup>lt;sup>1</sup> In a medium of constant refractive index n, the "optical" path length for a path of physical length d is nd. A wave that travels a path of given optical path length arrives with the same phase shift as if it had traveled a path of that physical length in vacuum [166].

which comprises phase changes and absorption (by using a complex refraction index in case of metals) when the light passes the film thickness  $D_j$ . Adding the amplitudes of the reflected rays according to Fig. 3.8 and considering the phase factor we obtain the total reflection coefficient of the film

$$r^{ik} = r^{ij} + t^{ij}t^{ji}r^{jk}\varphi(2D_j) + t^{ij}t^{ji}r^{jk}r^{ji}r^{jk}\varphi(4D_j) + \cdots$$

$$= r^{ij} + \frac{t^{ij}t^{ji}r^{jk}\varphi(2D_j)}{1 - r^{ji}r^{jk}\varphi(2D_j)}.$$
(3.13)

In a similar way the transmission coefficient  $t^{ik}$  is obtained. By using the reversibility conditions,  $r^{ji} = -r^{ij}$  and  $t^{ij}t^{ji} - r^{ij}r^{ji} = 1$  [165], we finally obtain *Airy's recursion formulae* [164]:

$$r^{ik} = \frac{r^{ij} + r^{jk} \varphi(2D_j)}{1 - r^{ji}r^{jk} \varphi(2D_j)}, \quad t^{ik} = \frac{t^{ij}t^{jk} \varphi(D_j)}{1 - r^{ji}r^{jk} \varphi(2D_j)}, \tag{3.14}$$

which describe the multiple reflections inside the film by geometric series. Here k>j=(i+1) are the corresponding layer indices. Analogous formulae apply for the other directions with k< j=(i-1). These formulae allow to describe the global reflection and transmission of the system by "effective" reflection and transmission coefficients  $r^{ik}$  and  $t^{ik}$ . The denominators in (3.14) combine the multiple reflections within the film. With Airy's formulae, for example, the positive influence of dielectric coatings on the Kerr rotation (see end of Sect. 2.4.3) can be explained [144, 190]: If the reflected light is assumed to consist of a system of "primary" beams (which are not influenced by the magnetization) and a system of magneto-optically generated light beams, the enhancement of the Kerr amplitude can be explained by constructive interference of the two light systems.

If more layers are added to form a multilayer system, the effective reflection and transmission coefficients are obtained by a recursive application of Airy's formulae (3.14). Consider, as an example, two films marked with index 1 and 2 with thickness  $D_1$  and  $D_2$ , respectively, that are sandwiched between a semi-infinite cover layer (index 0) and a semi-infinite substrate (index 3). The effective reflection coefficient is then given by:

$$r^{03} = \frac{r^{01} + r^{13} \varphi(2D_1)}{1 - r^{10}r^{13} \varphi(2D_1)}, \quad \text{with} \quad r^{13} = \frac{r^{12} + r^{23} \varphi(2D_2)}{1 - r^{21}r^{23} \varphi(2D_2)}. \tag{3.15}$$

The coefficients for adjacent layers  $(r^{01}, r^{12}, \text{ etc.})$  are calculated by the Fresnel equations (2.52). Airy's formulae are valid for both, s- and p-polarization directions, and they can be applied to dielectric (n real) as well as metallic films, where the complicated phase changes are considered in the complex refraction index.

In magneto-optics, multiple beam analysis was established by Lissberger [190]. The method is intuitively attractive as it leads to simple, analytic formulae that directly reveal the influence of the material parameters of the dielectric or magnetic

layers. In particular, these formulae allow an intuitive approach to the phenomenon of magneto-optic diffraction and they can be easily extended to cases of inhomogeneous magnetization distributions [185, 204]. Therefore they are well suited for magneto-optic image simulations. Most applications of the magneto-optic effects can be treated by such methods of perturbation theory—multiple beam analysis leads in linear approximation to the same results as the much more elaborate matrix methods!

# 3.2.3 Depth Sensitivity Function

A quantification of the depth sensitivity of the magneto-optical effects in arbitrary magnetic materials (including bulk material, thin films, and multilayers) was developed by Hubert and coworkers in a number of sequential articles [177, 185, 186, 193, 204, 205]. The authors introduced the concept of *depth sensitivity functions*, which describe the sensitivity of a given magneto-optical observation or measurement to the magnetization as a function of depth beneath the surface. To calculate these functions, the magneto-optic interaction of the incident light with a hypothetical thin "elementary" layer is computed. This slice with thickness  $\Delta z$  is buried at a depth z in the material as indicated for a bulk ferromagnet in Fig. 3.9a. For the simulation, the elementary slice is assumed to be magnetic and embedded in a (hypothetic) non-magnetic environment of otherwise identical optical properties. Initially [177], the depth sensitivity functions for the Kerr effects were derived on basis of the matrix

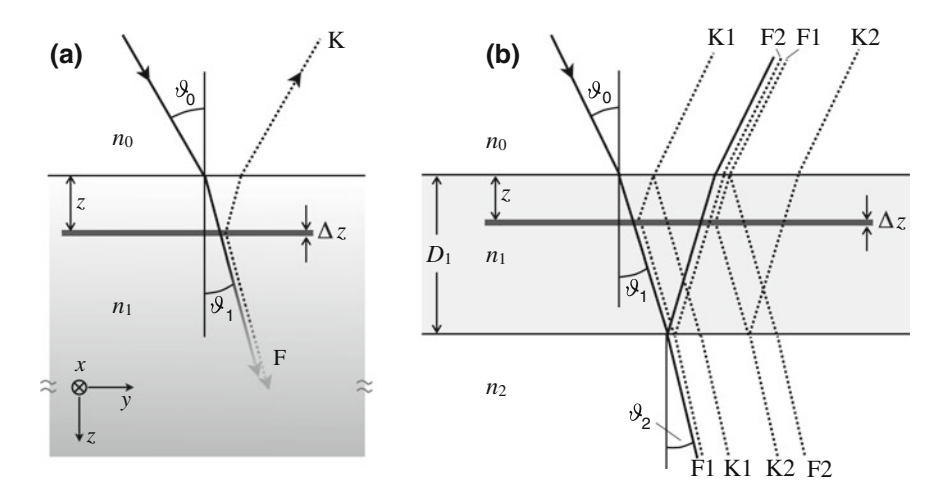


**Fig. 3.9** Partial beams contributing to the differential Kerr- and Faraday amplitudes of a thin buried layer in the depth z in a bulk magnetic material (**a**) and a magnetic thin film (**b**). The *solid lines* represent regular light beams, the *dashed lines* the magneto-optical contributions. In **b** there are further multiple reflections both of the regular and of the magneto-optical amplitudes that have been omitted. The four "first-order" magneto-optic beams shown for the reflected light (K1 and K2 for the Kerr effect) and for the transmitted light (F1 and F2 for the Faraday effect) differ in their phase as described in the text. After [193]

method explained in Sect. 3.2.2. Subsequently [193], the same sensitivity functions were obtained analytically by multiple beam arithmetics, put on an analytic basis in [186] and finally reduced to a geometrically interpretable form [185, 205] that is presented in Sect. 3.2.4.

From such simulations the authors found that the differential contribution  $\Delta e_{\rm K}$  of an individual buried layer to the magneto-optical *Kerr* amplitude<sup>2</sup> of *bulk* material can be expressed by a complex exponential function:

$$\Delta e_{\text{bulk}}^{\text{K}}(z) = -K_{\text{bulk}} 2 \eta \varphi(2z) m_i(z) \Delta z$$
 with 
$$\varphi(z) = \exp(\eta z) \text{ and } \eta = k_0 i \cos \theta_1 n_1.$$
 (3.16)

Here  $K_{\rm bulk}$  is the conventional Kerr coefficient for uniformly magnetized bulk material, which is given in (2.102a–2.102c) for the three standard magnetization directions—the polar, the longitudinal, and the transverse Kerr effects. The corresponding component  $m_i$  of the magnetization vector is  $m_z$ ,  $m_y$ , and  $m_x$ , respectively. The complex index of refraction of the material,  $n_1$ , and the angle of incidence within the sample,  $\vartheta_1$ , have already been defined in the context of the Kerr amplitudes in Sect. 2.4.2. The depth z is measured from the surface and  $k_0 = 2\pi/\lambda_0$  is the wave propagation number with  $\lambda_0$  being the vacuum wavelength of the (assumed) monochromatic, illuminating light. The phase factor  $\varphi(z)$  has been introduced in (3.12). Plotted as a function of the depth z (Fig. 3.10a), the differential Kerr amplitude follows the expected 1/e-decay and looks like a simple damped oscillation.<sup>3</sup>

Equation (3.16), which can be interpreted as the information depth profile or sensitivity function of the Kerr effect, has an intuitive interpretation: When the light wave enters the material, its amplitude is exponentially damped and at the same time shifted in phase according to the complex exponential function. At a certain depth z it generates a Kerr amplitude (Fig. 3.9a), which has to travel back to the surface, thus being absorbed and shifted again by the same amount. The information depth is therefore one half the penetration depth of the light! The total Kerr amplitude can be seen as a superposition of the phase-shifted contributions from different depths and can be derived from the complex amplitude penetration function (3.16) and a given magnetization profile by integration.

For a quantification of the *information depth* we have to take into account the contrast formation in magneto-optical microscopy, which was introduced in Sect. 2.4.2. In a magneto-optical experiment, the magneto-optical amplitude has to be converted into a detectable signal. In case of the Kerr effect, light rotation is generated by interference of the regularly reflected light amplitude and the Kerr amplitude that

<sup>&</sup>lt;sup>2</sup> With the nomenclature ' $e^{K}$ ' we anticipate the nomenclature for the Kerr amplitude to be used later in this chapter (Sect. 3.2.4). In Chap. 2 the Kerr amplitude was denoted by  $R_K$  [see (2.85)] and  $A_K$  [see (2.100)].

<sup>&</sup>lt;sup>3</sup> Note that the *conjugate complex* of (3.16) has to be plotted to obtain the same curves as in the first publications [177, 193]. This is owed to the fact that in these articles the Atkinson-Lissberger sign convention [162] was not used.

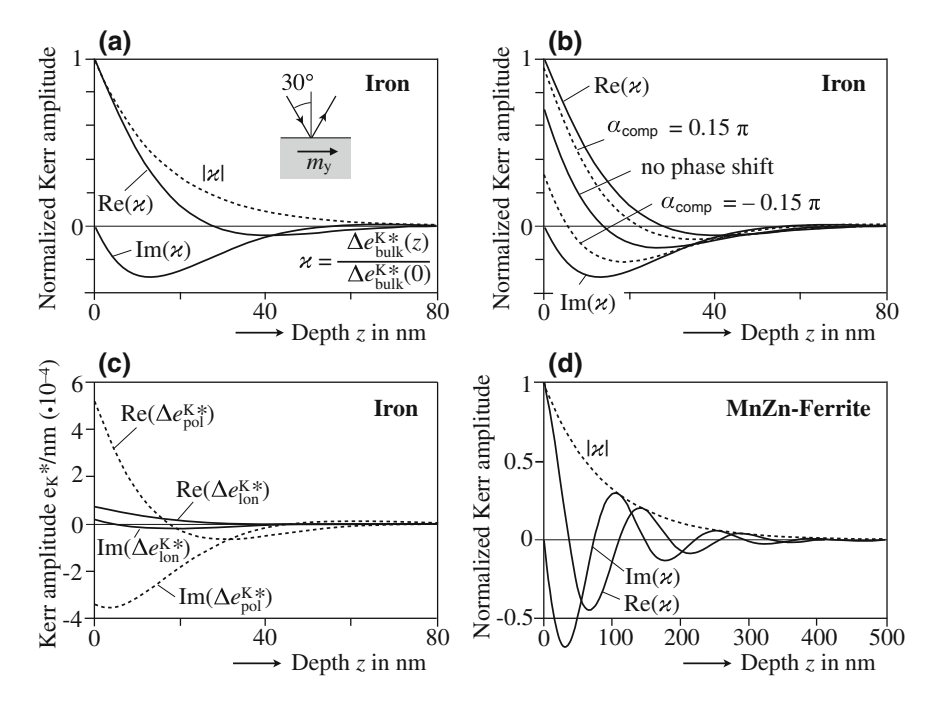


Fig. 3.10 Depth dependence of the Kerr amplitude (at  $\vartheta_0=30^\circ$ ) for bulk iron ( $n_1=2.893+i3.069$ ,  $Q_V=0.042+i0.012$  [193]) and bulk MnZn-Ferrite ( $n_1=2.205+i0.548$ ,  $Q_V=0.0007+i0.00023$  [185]). The wavelength of a red HeNe-laser ( $\lambda_0=633$  nm) and p-polarized incident light was assumed for the simulations. **a** Real part, imaginary part and absolute value of the longitudinal Kerr amplitude in iron, normalized to the amplitude at the surface as indicated. **b** Like (**a**), with curves for three different compensator settings added [275]. **c** Kerr amplitudes of iron for the longitudinal and polar effects, not normalized. **d** Like (**a**), but for MnZn-ferrite. Note that the conjugate complex of (3.16) is plotted in each case

is polarized perpendicular to the regular amplitude. A *detectable* rotation is only obtained if the two light components are in phase so that they can interfere to a plane-polarized wave. In the case of a phase shift between regular and Kerr amplitude we would have to add a phase shifter (compensator) in order to shift the phases properly. With a compensator, however, the phase difference can be selected freely. One choice is to select the relative phase in such a way that the magnetization at the surface is detected optimally, meaning that the regular amplitude is allowed to interfere with the Kerr amplitude generated right at the surface. The real part curve of the (normalized) amplitude in Fig. 3.10a applies to this case. The magnetization at a certain depth where this amplitude passes zero will then be invisible, and magnetization contributions from deeper layers may even reduce the overall signal. The first zero crossing of the real part curve  $\text{Re}[\Delta e_{\text{K}}(z)/\Delta e_{\text{K}}(0)]$  is therefore a meaningful "information depth" parameter. According to (3.16) it is found at

$$z_0 = \lambda_0 / 8n_1', \tag{3.17}$$

where  $n_1'$  is the real part of the complex refraction index  $n_1$ . For iron ( $n_1' = 2.89$ ) the information depth  $z_0$  is around 20 nm for visible light, depending on the wavelength. The 1/e-decay length of the absolute value of the signal is according to (3.16) equal to  $z_d = \lambda_0/4\pi n_1''$ .

By selecting another relative phase angle by proper adjustment of the compensator, any linear combination between the real part and the imaginary part of the differential Kerr amplitude can be realized within a depth frame given by the absorption. For instance, adjusting the phase sensitivity at 90° to the phase of the surface contribution, the curve of the imaginary part in Fig. 3.10a will become the real part curve. Then the surface sensitivity will be zero and one will "focus" on subsurface magnetization components. So in principle any differential Kerr amplitude within the absorption limit can be selected to interfere with the regular component, allowing to focus on certain depth-magnetizations or to intentionally blind out the magnetization in a certain depth by adjusting the Kerr amplitude out of phase with respect to the regular light. Examples for three different compensator settings are shown in Fig. 3.10b. The linear combinations were obtained by  $\Delta e_{\rm K}(z) = \cos(\pi/4 - \alpha_{\rm comp}) {\rm Re}(\kappa) +$  $\sin(\pi/4 - \alpha_{\rm comp}) \text{Im}(\kappa)$ . Without compensator ( $\alpha_{\rm comp} = 0$ ) the zero crossing of the Kerr amplitude is at a depth of about 14 nm. Although in a given experiment only a specific phase can be detected, the absolute value of the differential Kerr amplitude (plotted in Fig. 3.10a) indicates the potential of observing the magnetization in a certain depth if the phase sensitivity of the microscope or magnetometer is adjusted for this depth.

Curves (c) and (d) in Fig. 3.10 give some further insights in the depth sensitivity of the Kerr amplitude: In (c) the (unnormalized) amplitudes of the polar and longitudinal effects are plotted, clearly showing the expected relative strength of the two effects (see end of Sect. 2.4.2). In (d) the differential Kerr effect is shown for a typical oxide. Here the decay length  $z_d$  is much larger than the position of the first zero  $z_0$ . Due to this large information depth and the many oscillations in the depth-dependent Kerr signal, the inner contributions will reduce the contributions from the surface region so that the integral Kerr effect of oxides is usually quite weak.

For all curves shown in Fig. 3.10, an incidence angle of  $\vartheta_0=30^\circ$  was chosen. It turns out that the factor  $|\cos(\vartheta_1)|$  in (3.16) differs usually from unity only by a small amount (for example, for iron at  $\vartheta_0=45^\circ$  in air this quantity is 0.98, and at  $\vartheta_0\to90^\circ$  it approaches 0.95). This reflects the fact that metals are optically denser than vacuum so that light in the metal is always refracted towards the normal. The dependence of the information depth profile of the Kerr effect on the angle of incidence may therefore as well be ignored, at least in metallic materials. In principle, however, the factor  $\cos(\vartheta_1)$  can as well become significant. Such a case was analysed in [177]: For bulk magnetic oxides with their oscillating information depth it was shown that observation with a large numerical aperture (e.g. by using a highly refractive immersion medium or suitable antireflection coatings) can significantly enhance the surface sensitivity. In an angular range that corresponds to the total reflection angle,  $\cos(\vartheta_1)$  becomes imaginary and thus strongly contributes to the damping. A simple exponential information depth profile, as in a metal, is then obtained and at the same time the magnitude of the total Kerr amplitude is increased.

# 3.2.4 Depth Sensitivity in Magnetic Films

The theory of depth sensitivity in magnetic films and multilayers, underlying the layer-selective experiments to be presented later, is more complicated than for bulk material. In bulk samples, only the Kerr beam indicated by K in Fig. 3.9a has to be taken into account to calculate the differential Kerr amplitude. In films and multilayers, however, also the Faraday effect has to be incorporated and, by reflection on the surfaces of the film and interfaces in case of multilayers, there may be interference between a number of Kerr and Faraday amplitudes. Some of the partial beams in a single thin film, contributing to the differential magneto-optical amplitudes of a thin layer buried in the depth z, are indicated in Fig. 3.9b. Beam K1 represents the reflected elementary Kerr amplitude. Together with K1 an elementary Faraday amplitude is generated that differs from the Kerr amplitude in its propagation direction. The Faraday amplitude leads to a transmitted beam F1 and—due to reflections at the interfaces—to further contributions to the overall Kerr and Faraday amplitudes. The depth sensitivity function of the film is finally obtained by summing over all elementary beams.

A generalized multiple beam analysis for the Kerr- and Faraday effects in thin film systems was presented by Kamberský, Wenzel, and Hubert [185, 187, 205]. The theory applies to first-order magneto-optical effects, i.e. effects that are linear in the amplitude of the electrical field (excluding second harmonic generation), linear in the magnetization (excluding the Voigt effect and the second order gyrotropic effect), and linear in the magneto-optical interaction parameter  $Q_{v}$  (excluding large rotations and ellipticities as they may occur in thick transparent media). Under these restrictions the magneto-optical interaction may be treated in the sense of a perturbation theory<sup>4</sup> [193, 276]. The rigorous and explicit expressions derived from this theory can be applied in a straightforward manner to arbitrary thin-film systems and to arbitrary magnetization configurations. In this section we just present an outline of this formalism and apply it to some specific examples of depth-sensitivity functions in single films. The extension to multilayers is introduced in Sect. 3.2.5. We also restrict the discussion to magnetization distributions that are laterally homogeneous. For inhomogeneous magnetization and the related diffraction effects we refer to [185, 186].

In the perturbation theory, first the magnetization is assumed to be zero and the "primary" field distribution ( $E_{m=0}$ ,  $H_{m=0}$ ) is obtained from the superposition of solutions of the wave equation (2.6). The magneto-optical "perturbation", generated by the magneto-optical interaction, is then treated separately as a source of secondary light waves (e, h) that propagate in the otherwise unperturbed system. Both together add up to the total electromagnetic field [187]:

<sup>&</sup>lt;sup>4</sup> The perturbation calculation takes over the concept that was already introduced in Sect. 2.4.2: the total electromagnetic amplitude can be described as a superposition of a magnetically unaffected, primary light field (without the magneto-optical terms, called normally reflected amplitude  $R_{\rm N}$  or  $A_{\rm N}$  in Sect. 2.4.2) and a magnetically induced perturbation contribution (the magneto-optical amplitude  $R_{\rm K}$  or  $A_{\rm K}$  in the previous nomenclature).

$$E = E_{m=0} + e$$
,  $H = H_{m=0} + h$ . (3.18)

The secondary field e is proportional to the Voigt parameter  $Q_V$ . Due to our limitation to linear effects in m and  $Q_V$ , and with (3.18), the dielectric law (2.99) is explicitly given by:

$$\mathbf{D} = \varepsilon_0 n^2 [\mathbf{E}_{m=0} + \mathbf{e} + i O_V (\mathbf{m} \times \mathbf{E}_{m=0})]. \tag{3.19}$$

With (3.18), (3.19), and the Maxwell equations (2.1a–2.1d), a wave equation analogous to (2.6) can be set up for the secondary amplitudes:

$$\nabla(\nabla \cdot \mathbf{e}) - \nabla^2 \mathbf{e} + \mu_0 \sigma \dot{\mathbf{e}} + \epsilon_0 \mu_0 n^2 \ddot{\mathbf{e}} = -i\epsilon_0 \mu_0 n^2 Q_V(\mathbf{m} \times \ddot{\mathbf{E}}_{\mathbf{m}}). \tag{3.20}$$

This equation differs from the "non-magnetic" wave equation (2.6) by an optical source term that correspond to a current density  $j \sim Q_V(m \times E_{m=0})$  [186] that has the symmetry of a Lorentz force (see Sect. 2.4.2). So the perturbation ansatz has split up the problem: first the field distribution of the primary light  $E_{m=0}$  together with the source term can be determined. With the source term, the system of partial, nonlinear and inhomogeneous differential equations (3.20) can be solved in a second step.

To determine the magneto-optical amplitude by the perturbation approach [185], one elementary slice of thickness  $\Delta z$  at the depth z inside the magnetic film is picked (Fig. 3.9b). Then the first-order Lorentz current density of the slice, which represents its magneto-optical response, is calculated. From the current density the source functions of the magneto-optical amplitudes in this slice are derived from Maxwell's equations. These source functions are then converted into differential magneto-optical signals of the Kerr- and Faraday type by using the boundary conditions for light reflection and transmission. Finally, integration over the contributions from all slices of the film yields its total Kerr amplitude  $e^K_\rho$  [185]:

$$e_{\rho}^{\rm K} = \int_0^D \Delta e_{\rho}^{\rm K}(z) \, \mathrm{d}z \quad \text{with} \quad \Delta e_{\rho}^{\rm K}(z) = s_{\rho\sigma}^{\rm K}(z) \cdot \boldsymbol{m}(z) \, E_{\sigma}^{\rm in} \Delta z. \tag{3.21}$$

Here  $\Delta e^{\rm K}_{\rho}(z)$  is the differential contribution of the buried elementary slice to the Kerr signal, m(z) is the magnetization vector,  $E^{\rm in}_{\sigma}$  the incident amplitude and  $s^{\rm K}_{\rho\sigma}(z)$  the *vectorial* depth-sensitivity function.

The electromagnetic field is assumed to be separated into two contributions, which are polarized perpendicular (s) and parallel (p) to the plane of incidence (see Fig. 2.9). The index  $\rho$  thus assumes the values (s, p) for the two polarization states in the secondary beam system, as  $\sigma$  for the primary light. The depth sensitivity functions can be written in a compact and explicit form [185]:

$$\mathbf{s}_{\mathrm{ps}}^{\mathrm{K}}(z) = P_{0}(0, a_{\mathrm{x}}a_{\mathrm{z}}, -a_{\mathrm{x}}a_{\mathrm{y}}), \quad \mathbf{s}_{\mathrm{sp}}^{\mathrm{K}}(z) = P_{0}(0, a_{\mathrm{x}}a_{\mathrm{z}}, a_{\mathrm{x}}a_{\mathrm{y}}), 
\mathbf{s}_{\mathrm{pp}}^{\mathrm{K}}(z) = -2P_{0}(a_{\mathrm{y}}a_{\mathrm{z}}, 0, 0), \quad \mathbf{s}_{\mathrm{ss}}^{\mathrm{K}}(z) = \mathbf{0},$$
(3.22a)

with 
$$P_0 = \frac{\pi n_1^2 Q_V}{\lambda_0 n_0 \cos \theta_0}$$
, (3.22b)

$$a_{\rm x} = t_{\rm ss}^{01} V_{\rm s} f_{\rm s}^{+}(z), \ a_{\rm y} = \gamma t_{\rm pp}^{01} V_{\rm p} f_{\rm p}^{+}(z), \ a_{\rm z} = \beta t_{\rm pp}^{01} V_{\rm p} f_{\rm p}^{-}(z),$$
 (3.22c)

$$a_{x} = t_{ss}^{01} V_{s} f_{s}^{+}(z), \ a_{y} = \gamma t_{pp}^{01} V_{p} f_{p}^{+}(z), \ a_{z} = \beta t_{pp}^{01} V_{p} f_{p}^{-}(z),$$

$$V_{\sigma} = \frac{1}{1 - r_{\sigma\sigma}^{10} r_{\sigma\sigma\sigma}^{12} \varphi(2D)}, \quad f_{\sigma}^{\pm}(z) = \varphi(z) \pm r_{\sigma\sigma}^{12} \varphi(2D - z).$$
(3.22d)

The polarization-independent prefactor  $P_0$  contains the off-diagonal element  $n_1^2 Q_V$ of the magneto-optical dielectric tensor (2.99) thus describing the magneto-optical interaction. It further contains the refractive index  $n_0$  and the cosine of the incidence angle  $\theta_0$  which is the z-component of the wave vector  $\mathbf{k}_0 = (0, \sin \theta_0, \cos \theta_0)$  in the incident medium. For the magnetic film the propagation vector is modified by refraction to  $k_1 = (0, \beta_1, \gamma_1)$  with  $\beta_1 = (n_0\beta_0)/n_1$  and  $\gamma_1 = \sqrt{1 - \beta_1^2}$  according to Snell's law (2.54) that requires continuity of the lateral component  $n_0\beta_0k_0$  of the wave vector k across the interfaces. The primary and magneto-optical field amplitudes with s- and p-polarization at a depth z are expressed by vectorial amplitude transfer functions that are contained in the components  $(a_x, a_y, a_z)$  of the vector variable a. The transmitted contribution of the incident light is considered by the Fresnel coefficient  $t_{\sigma\sigma}^{01}$  in  $a_i$ . The function  $f_{\sigma}^{\pm}(z)$  describe two elementary contributions to the primary, exciting amplitude: the first is the direct wave, the second results from reflection at the lower interface. It differs from the first term by the additional reflection coefficient  $r_{\sigma\sigma}^{12}$  and by the longer optical path, which is expressed by the difference between  $\varphi(z)$  and  $\varphi(2D-z)$  in the phase factor. The latter describes the depth-dependent phase change and absorption according to (3.12). Further, multiple reflections at the upper and lower boundaries of the magnetic film lead to a geometrical sum that is expressed by the multiple reflection coefficient  $V_{\sigma}$ . An analogous sensitivity function  $s^F$  can be derived for the Faraday amplitude that leaves the film after transmission [185].

The sensitivity vector  $s^{K}$  defines the magnetization direction which contributes most to the Kerr signal for a given sample and experimental setup. Its vector components (x, y, z) directly represent the sensitivity for the transverse, longitudinal and polar magnetization components in the traditional terminology. It thus generalizes the classical observation on transparent volume crystals according to which the Faraday effect is proportional to the magnetization component along the propagation of light [149]. For the longitudinal Kerr effect, for example, the sensitivity function of a magnetic film can explicitly be written as:

$$\begin{split} s_{\rm ps}^{\rm lon}(z) &= s_{\rm sp}^{\rm lon}(z) = \\ \frac{\pi n_1^2 Q_{\rm V,1} \beta_1}{\lambda_0 n_0 \gamma_0} t_{\rm ss}^{01} t_{\rm pp}^{01} \frac{\left[\varphi(z) + r_{\rm ss}^{12} \varphi(2D-z)\right] \left[\varphi(z) - r_{\rm pp}^{12} \varphi(2D-z)\right]}{\left[1 - r_{\rm ss}^{10} r_{\rm ss}^{12} \varphi(2D)\right] \left[1 - r_{\rm pp}^{10} r_{\rm pp}^{12} \varphi(2D)\right]}. \end{split} \tag{3.23}$$

For  $D \to \infty$ , equations (3.22a) yield the same results as the bulk sensitivity function (3.16). A comparison of (normalized) longitudinal Kerr sensitivities for different iron film thicknesses with the corresponding functions of bulk iron is presented in

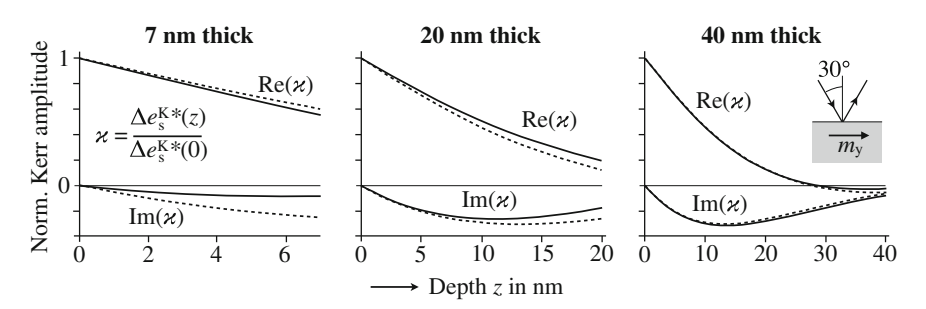


**Fig. 3.11** Thickness dependence of the longitudinal Kerr amplitude of iron films of different thicknesses (*full lines*). Like in Fig. 3.10, the amplitude is normalized to the Kerr sensitivity at the surface and the incident light is *p*-polarized. For comparison the corresponding curves of bulk iron are plotted (*dashed lines*)

Fig. 3.11. The difference between the curves becomes the stronger the thinner the films, which is a consequence of the multiple reflections in case of the films.

The previous formulae show that integration of the depth sensitivity functions over the film thickness (see 3.21) leads to a direct connection between polarization and direction of the incident light and the resulting magneto-optical amplitude that leaves the film. Under the given assumption of a uniform magnetization vector  $\mathbf{m}$  within film, the Kerr coefficients are obtained by rewriting (3.21):

$$e_{\rho}^{K} = \mathbf{K}_{\rho\sigma} \cdot \mathbf{m} \, E_{\sigma}^{\text{in}}, \quad \mathbf{K}_{\rho\sigma} = \int_{0}^{D} \mathbf{s}_{\rho\sigma}^{K}(z) \, \mathrm{d}z.$$
 (3.24a)

The x, y, and z components of  $\mathbf{K}_{\rho\sigma}$  are the classical Kerr coefficients for the transversal, longitudinal and polar magnetization direction and for the given combination of incident and detectable polarization,  $\sigma$  and  $\rho$ , respectively. In vector notation they can be written as

$$\mathbf{K}_{ps}(z) = t_{ss}^{01} t_{pp}^{01} V_s V_p [0, \beta_1(c_s^- + d^-), -\gamma_1(c_s^+ + d^+)],$$
 (3.25a)

$$\mathbf{K}_{\rm sp}(z) = t_{\rm ss}^{01} t_{\rm pp}^{01} V_{\rm s} V_{\rm p}[0, \, \beta_1(c_{\rm s}^- + d^-), \, +\gamma_1(c_{\rm s}^+ + d^+)],$$
 (3.25b)

$$\mathbf{K}_{\rm pp}(z) = t_{\rm pp}^{01} t_{\rm pp}^{01} V_{\rm p} V_{\rm p} [-2\beta_1 \gamma_1 c_{\rm p}^-, 0, 0],$$
 (3.25c)

with

$$c_{\sigma}^{\pm} = \frac{iQ_{V}n_{1}}{4n_{0}\gamma_{0}\gamma_{1}} \left[1 - \varphi(2D)\right] \left[1 \pm r_{\sigma\sigma}^{12} r_{pp}^{12} \varphi(2D)\right], \tag{3.25d}$$

$$d^{\pm} = P_0 D\varphi(2D) [r_{\rm ss}^{12} \pm r_{\rm pp}^{12}]$$
 (3.25e)

Equivalent analytic equations were derived and experimentally confirmed by Višňovský et al. [277] for the special case of polar magnetization and perpendicular light incidence. These authors, however, used a perturbation approach on the basis of circularly polarized light eigenmodes [181] which proved favorable for this case.

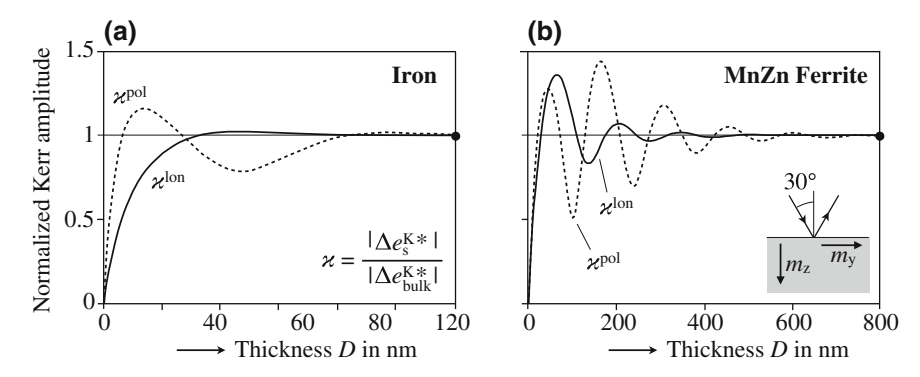


Fig. 3.12 Dependence of the Kerr amplitude on the thickness of magnetic films that are deposited on glass substrates ( $n_2=1.5$ ). Compared are iron films (**a**) and MnZn-ferrite films (**b**) with both, longitudinal (*full lines*) and polar magnetization (*dashed*). All curves are normalized to the corresponding Kerr amplitudes of bulk material (indicated by *dots*). The absolute polar extreme values are about eight times larger than the longitudinal values in case of iron, and four times larger for the ferrite. The simulations were performed with the optical parameters of bulk materials (see caption of Fig. 3.10) at a wavelength  $\lambda_0=633$  nm and at an incidence angle  $\vartheta_0=30^\circ$  of p-polarized light. After [185, 205]

Typical curves for the longitudinal and polar Kerr amplitudes as a function of the film thickness are shown in Fig. 3.12. Compared is iron as an example of a strongly absorbing material with a weakly absorbing manganese-zink-ferrite. Both are single layers, deposited on a glass substrate. In a medium thickness range the periodic oscillations of the Kerr amplitude are a sign of interference effects, which result from reflections from the layer backside and from intrinsic phase differences of the magneto-optical depth contributions (see Fig. 3.10a). In (3.25d, 3.25e) the backside reflection  $(r_{\sigma\sigma}^{12})$  appears in  $d^{\pm}$  and in the third term of  $c_{\sigma}^{\pm}$ , the influence of the depth-sensitive phase difference is located in the second term of  $c_{\alpha}^{\pm}$ . Depending on absorption, both the reflected beams as well as those contributions generated deeper in the film are more or less significantly contributing to the total amplitude, so that the oscillations are more pronounced for the weakly absorbing material. Beyond a certain film thickness, the amplitudes known from bulk samples are approximately assumed. For iron the limit is at about 100 nm, whereas for the semi-transparent ferrite bulk crystal behavior is not reached below 600 nm. In the bulk limit of  $D \to \infty$  the phase factor  $\varphi(2D)$  in (3.25a-3.25e) vanishes and the equations reduce to the classical expressions (2.102a-2.102c) for the three standard magnetization directions—the polar, the longitudinal, and the transverse Kerr effects. In Fig. 3.12 these conventional bulk coefficients were used for normalization.

From the depth sensitivity function (3.16) and Fig. 3.10 we have seen that for bulk material the Kerr contributions from different depths differ in phase. In general, this fact reduces the overall efficiency of the Kerr effect. This disadvantage of bulk materials can be overcome in *ultrathin film systems* [177, 190, 271]: such layers can produce *more* signal than bulk material, because in a very thin film all of the

magneto-optic amplitude is generated with (almost) the same phase. This advantage becomes the more effective the smaller the absorption in the magnetic medium, because then the contributions from different depths in bulk material may even differ in sign, leading to very weak overall bulk signals. For the highly transparent garnets, for example, no domain observation truly based on the Kerr effect is known as already mentioned in Sect. 2.4 (domains in garnets are observed in transmission by the Faraday effect). The contrast in ultrathin magnetic films can be further enhanced by interference. Equations (2.102a-2.102c) are equally valid for arbitrary thin film systems if the corresponding transmission or reflection coefficients are inserted. To achieve maximum Kerr signals, the magnetic film is first deposited onto a mirror, with a dielectric spacer layer of appropriate thickness. The system is then covered with an anti-reflection system as discussed at the end of Sect. 2.4.3. Such a mirror system can theoretically yield large improvements although its practical implementation may be difficult. Thin film mirror systems can in principle even overcome the disadvantage of longitudinal versus polar magnetization [177, 186, 193]: In an optimized mirror system all energy is eventually absorbed in the magnetic medium just as in a bulk sample with an ideal anti-reflection coating. The essential point of magneto-optics in ultrathin films is that the Kerr signal depends essentially on the optical properties of the adjacent layers, rather than on those of the magnetic film even in the general case of arbitrary magnetization direction and angle of incidence. This property was first demonstrated for the special case of polar magnetization and perpendicular incidence by S. Bader [124]. Later it was generalized by extending the multiple beam analysis outlined in this Section [185, 193].

In [185, 186, 205] this theoretical approach was further extended to the cases of optically anisotropic films and to layer systems with an arbitrary, non-uniform magnetization distribution. The former may be important for mechanically stressed thin films or for films with growth-induced anisotropy. Such deviations from bulk material symmetry may lead to anisotropy in the optical and magneto-optical material parameters. This may cause optical birefringence effects that interact with the linear magneto-optical effects. Non-uniform magnetization distributions can lead to diffraction phenomena, if the characteristic length of the magnetic structure is comparable with the wavelength of light. In magneto-optics such structures may be domain walls. The sensitivity function concept can be also extended to magneto-optical diffraction phenomena, including the gradient effect. For details we refer to the mentioned articles.

# 3.2.5 Depth Sensitivity in Magnetic Multilayers

The multiple beam approach presented in Sect. 3.2.4 for a single film can easily be extended to multilayers consisting of an arbitrary system of magnetic and non-magnetic thin films. The total magneto-optical effect of the film system is obtained by addition of the magneto-optical contributions of all the individual layers, which are calculated under the assumption that all the other layers are present but non-magnetic.

- (0) Air
- (1) Ferromagnetic layer
- (2) Non-magnetic layer
- (3) Ferromagnetic layer
- (4) Substrate

Fig. 3.13 Typical magnetic sandwich system, consisting of two ferromagnetic films that are interspaced by a non-magnetic layer

The problem of an arbitrary multilayer structure is then reduced to the problem of just *one* magnetic layer that is embedded in arbitrary non-magnetic cover- and substrate layers. Instead of considering simple interfaces like in Fig. 3.9b, the interfaces of the examined magnetic layer have now to be seen as complex in the sense that they physically consist of multilayers between the magnetic film (index 1) and incidence medium (index 0) or emergence medium (index 2). Such complex interfaces can be described by *effective* amplitude transmission- and reflection coefficients  $t_{\sigma\sigma}^{ij}$  and  $t_{\sigma\sigma}^{ij}$ , because in these layers the *s*- and *p*-polarized eigenmodes remain decoupled for the primary light so that the polarization states can still be treated independently [185]. The remaining layers (magnetic or spacer layers) are thus included in the transmission and reflection coefficients, which are obtained in the usual way from the Fresnel relations and from a recursive application of Airy's formulae (3.14) in the same sense as explicitly given for a two-layer system in (3.15).

Consider, as an example, a magnetic trilayer system, consisting of two ferromagnetic films that are interspaced by a non-magnetic layer (Fig. 3.13). The whole system is deposited on a thick buffer. The ferromagnets shall be homogeneously magnetized perpendicular to the film surface, and the incident light shall be polarized perpendicular to the plane of incidence (*s*-polarization). The sensitivity functions of the two ferromagnetic layers with indices (1) and (3), respectively, can be derived from (3.22a–3.22d). They are explicitly given by the following set of equations:

• For layer (1):

$$\begin{split} s_{\rm ps}^{\rm K,1} &= \\ &= -\frac{\pi n_1^2 Q_{\rm V,1} \gamma_1}{\lambda_0 n_0 \gamma_0} t_{\rm ss}^{01} t_{\rm pp}^{01} \frac{\left[\varphi(z) + r_{\rm ss}^{14} \varphi(2D_1 - z)\right] \left[\varphi(z) + r_{\rm pp}^{14} \varphi(2D_1 - z)\right]}{\left[1 - r_{\rm ss}^{10} r_{\rm ss}^{14} \varphi(2D_1)\right] \left[1 - r_{\rm pp}^{10} r_{\rm pp}^{14} \varphi(2D_1)\right]}; \\ \text{with} \quad r_{\rm ss,pp}^{14} &= \frac{r_{\rm ss,pp}^{12} + r_{\rm ss,pp}^{24} \varphi(2D_2)}{1 - r_{\rm ss,pp}^{21} r_{\rm ss,pp}^{24} \varphi(2D_2)}; \quad r_{\rm ss,pp}^{24} &= \frac{r_{\rm ss,pp}^{23} + r_{\rm ss,pp}^{34} \varphi(2D_3)}{1 - r_{\rm ss,pp}^{32} r_{\rm ss,pp}^{34} \varphi(2D_3)}. \end{split}$$
(3.26)

• For layer (3):

$$\begin{split} s_{\rm ps}^{\rm K,3} &= \\ &= -\frac{\pi n_3^2 \, Q_{\rm V,3} \gamma_3}{\lambda_0 n_2 \gamma_2} t_{\rm ss}^{03} t_{\rm pp}^{03} \frac{\left[\varphi(z) + r_{\rm ss}^{34} \varphi(2D_3 - z)\right] \left[\varphi(z) + r_{\rm pp}^{34} \varphi(2D_3 - z)\right]}{\left[1 - r_{\rm ss}^{30} r_{\rm ss}^{34} \varphi(2D_3)\right] \left[1 - r_{\rm pp}^{30} r_{\rm pp}^{34} \varphi(2D_3)\right]}; \\ \text{with } r_{\rm ss,pp}^{30} &= \frac{r_{\rm ss,pp}^{32} + r_{\rm ss,pp}^{20} \varphi(2D_2)}{1 - r_{\rm ss,pp}^{23} r_{\rm ss,pp}^{20} \varphi(2D_2)}; \quad r_{\rm ss,pp}^{20} &= \frac{r_{\rm ss,pp}^{21} + r_{\rm ss,pp}^{10} \varphi(2D_1)}{1 - r_{\rm ss,pp}^{12} r_{\rm ss,pp}^{13} \varphi(2D_1)}; \\ t_{\rm ss,pp}^{03} &= \frac{t_{\rm ss,pp}^{01} t_{\rm ss,pp}^{13} \varphi(D_1)}{1 - r_{\rm ss,pp}^{10} r_{\rm ss,pp}^{13} \varphi(D_1)}; \quad t_{\rm ss,pp}^{13} &= \frac{t_{\rm ss,pp}^{12} t_{\rm ss,pp}^{23} \varphi(D_2)}{1 - r_{\rm ss,pp}^{21} r_{\rm ss,pp}^{23} \varphi(2D_2)}; \\ r_{\rm ss,pp}^{13} &= \frac{r_{\rm ss,pp}^{12} + r_{\rm ss,pp}^{23} \varphi(2D_2)}{1 - r_{\rm ss,pp}^{21} r_{\rm ss,pp}^{23} \varphi(2D_2)}. \end{split} \tag{3.27}$$

The direct coefficients  $(r_{\rm ss,pp}^{12}, r_{\rm ss,pp}^{23}, t_{\rm ss,pp}^{01}, t_{\rm ss,pp}^{01})$  are immediately obtained from Fresnel's equations (2.52, 2.53). For the non-magnetic layers (2) and (4) the Kerr coefficients are set to zero.

Two examples of such simulations are presented in Fig. 3.14. In (a) the polar Kerr amplitude is plotted for two perpendicularly magnetized cobalt films that are interspaced by a copper layer. The signal of the lower cobalt film is strongly reduced as compared to that of the upper film due to absorption. In Fig. 3.14b the lower

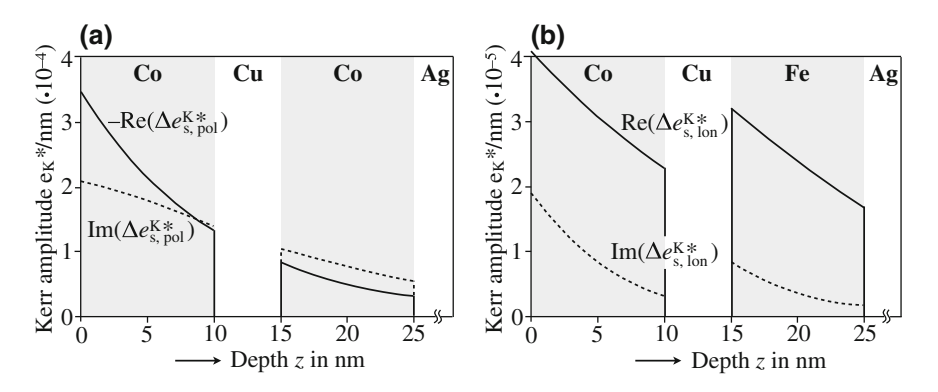


Fig. 3.14 Sensitivity functions of magnetic trilayer systems. **a** Two cobalt films of equal thickness are separated by a nonmagnetic copper spacer layer and deposited on a silver substrate. The film thickness are  $Co(10 \text{ nm})/Cu(5 \text{ nm})/Co(10 \text{ nm})/Ag(\infty)$ . Perpendicular incidence and perpendicular magnetization  $m_z = 1$  (polar Kerr effect are assumed. **b** Simulation of a mixed system  $Co(10 \text{ nm})/Cu(5 \text{ nm})/Fe(10 \text{ nm})/Ag(\infty)$  under the conditions of in-plane magnetization  $m_y = 1$ , (ps)-configuration and an incidence angle  $\vartheta_0 = 30^\circ$  (longitudinal Kerr effect. The simulations were performed with the optical parameters of bulk materials (Co: n = 2.214 + i 4.171,  $Q_V = 0.0195 + i 0.0051$ , Fe: n = 2.893 + i 3.069,  $Q_V = 0.042 + i 0.012$ , Cu: n = 0.239 + i 3.417, Ag: n = 0.135 + i 3.985 [193]) at a wavelength  $\lambda_0 = 633$  nm and under the assumption of p-polarized incident light. Like in Fig. 3.10 the conjugate complex of the Kerr amplitude is plotted

ferromagnet film is made of iron and the longitudinal Kerr effect (oblique incidence and in-plane magnetization) was assumed. As iron has a stronger intrinsic Kerr effect than cobalt, the signal of the bottom layer is reduced compared to that of the upper layer, but not as strong as in (a). The overall signal of the longitudinal Kerr effect in (b) is by about an order of magnitude smaller than that of the polar effect in (a), as expected.

# 3.2.6 Depth Selectivity in Magnetic Multilayers

In Sects. 3.2.3–3.2.5 it was shown that the total Kerr signal of any magnetic sample can be seen as a superposition of contributions from different depths, which differ in phase according to a complex amplitude penetration function like that in (3.16). The different phases of contributions from different depths can be exploited in Kerr microscopy and magnetometry to obtain *depth-selective* information on the magnetization, especially in magnetic multilayers. The possibilities of such experiments can be extended by using different light wavelengths, as also the wavelength enters the penetration function. In this section we will introduce both, the phase and wavelength concepts of depth selectivity. The information depth profile also depends on the angle of incidence. In metallic systems, however, this dependence is weak as shown at the end of Sect. 3.2.3. A variation of the incidence angle can therefore hardly be used for depth selectivity.

In the context of Fig. 3.10 we have discussed that in a Kerr experiment a contrast is generated by interference of the regularly reflected light amplitude and the Kerr amplitude (remember Fig. 2.14b). Only light components that are in phase can interfere and generate a detectable plane-polarized wave. With a rotatable compensator the phases angle between regular and Kerr amplitude can be selected freely so that either the magnetization at the surface is detected optimally or the "focus" is on subsurface magnetization components, meaning that the regular component is allowed to interfere with the Kerr component generated at the respective locations. The sensitivity curves in Fig. 3.10b show a number of such choices for bulk iron. So with proper phase selection, the "zero" of the information depth can be shifted over a wide range within the penetration depth of light. In this way light from selected depth zones can be made invisible if their Kerr amplitude is adjusted out of phase with respect to the regular light. This phase adjustment is the basis for the phase concept of depth-selective Kerr microscopy.

Consider a magnetic sandwich system, in which two ferromagnetic films are interspaced by a non-magnetic layer (Fig. 3.15). By adequate phase selection with the compensator<sup>5</sup> the zero of the information depth curve can be put somewhere in the middle of one of the two layers so that the sum of all differential Kerr contributions from this layer cancels. Then only the magnetization from the other layer can be seen. By proper phase selection the magnetization of both layers can thus be imaged

<sup>&</sup>lt;sup>5</sup> In practice, compensator and analyser are rotated "simultaneously" until the desired sensitivity is obtained.

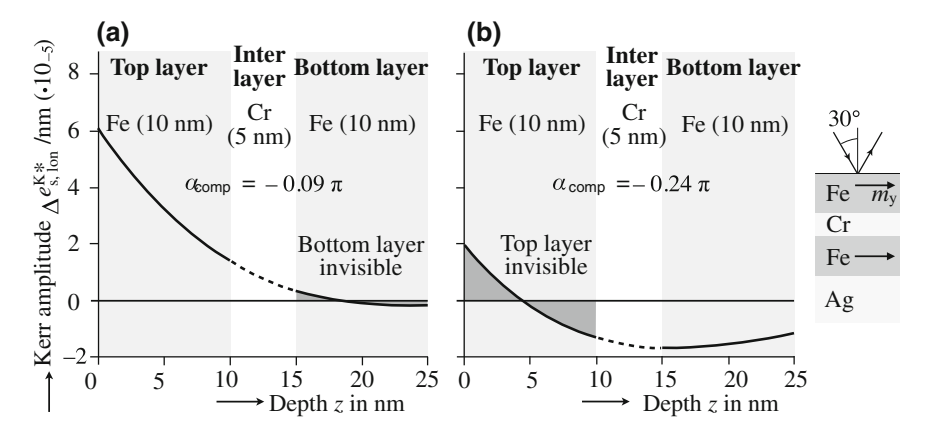


Fig. 3.15 Thickness dependence of the Kerr amplitude of an Fe/Cr/Fe sandwich film system as indicated. By proper adjustment of the relative phase between Kerr amplitude and regularly reflected light the zero crossing of the penetration function can be shifted either into the middle of the bottom (a) or top ferromagnetic layer (b), so that the integral Kerr contribution of the corresponding layer cancels. The Kerr amplitudes were calculated with the formula derived in Sect. 3.2.4. An incidence angle  $\vartheta_0=30^\circ$ , p-polarized incident light, and in-plane magnetization in the longitudinal Kerr configuration were assumed. The compensator is a quarter wave plate with setting as indicated in Fig. 2.7b. For the material parameters see the captions of Figs. 3.10 and 3.14

separately. From Fig. 3.15 it is obvious that the bottom film contributes less signal than the upper film due to absorption. This kind of depth-selection was first applied for layer-selective Kerr microscopy in [151, 278], where the two iron films of an Fe/Cr/Fe sandwich sample have been imaged separately. We will reproduce these results in Sect. 3.3 together with further examples.

An elegant interpretation of depth selectivity, which applies to *ultrathin* ferromagnetic films (thickness in the nanometer range) in a multilayer stack, was presented by Hamrle et al. [245]. The authors start with the Kerr rotation  $\theta_K$  and ellipticity  $\xi_K$ as given in (2.87, 2.88) and suggest to visualize the Kerr amplitude as a vector in the complex  $\theta_K \xi_K$ -plane (Fig. 3.16a). The projection of the Kerr vector on the real axis gives the Kerr rotation, and that on the imaginary axis the Kerr ellipticity. The length of the Kerr vector corresponds to the Kerr amplitude  $K_0$  and its orientation to the Kerr phase  $\delta_{\rm K}$ . For a mutilayer structure as sketched in Fig. 3.16b, the total Kerr amplitude is given by the sum over all the Kerr amplitudes of the individual magnetic layers. In Fig. 3.16b the additivity of the amplitudes is represented by the summation of the individual Kerr vectors. In the most general case, an experimental setup measures a Kerr signal  $S_K$ , which is the projection of the complex Kerr vector onto a projection axis P that makes an angle  $\psi$  with the real axis. If the projection axis is parallel to the real axis, the Kerr rotation is measured, and for an angle of 90° the Kerr ellipticity is obtained. With the compensator the projection angle can be arbitrarily adjusted.

Layer selectivity can now be conveniently discussed with this "projection"-concept: Let's again assume a magnetic sandwich system consisting of two (ultrathin)

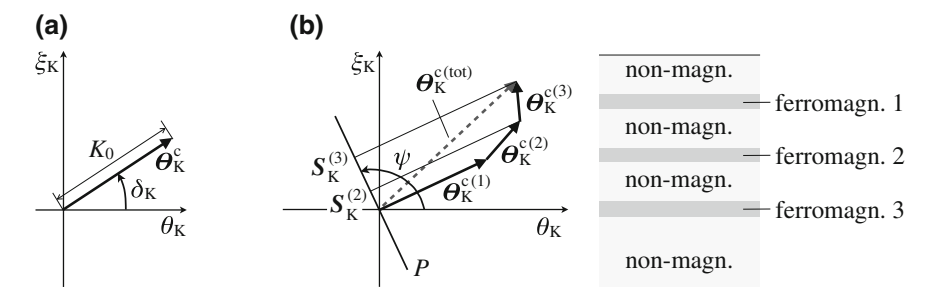
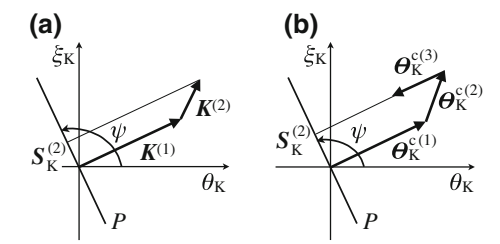


Fig. 3.16 Visualisation of the Kerr effect in the  $\theta_K \xi_K$ -plane. a The Kerr vector  $\boldsymbol{\theta}_K^c$  can be either described by the Kerr rotation  $\theta_K$  and ellipticity  $\xi_K$  (2.87) or by the Kerr amplitude  $K_0$  and phase  $\delta_K$  (2.88). b In a multilayer (consisting of ultrathin ferromagnetic layers that are interspaced by thicker non-magnetic layers), the measured Kerr signal  $S_K^{(i)}$  for each magnetic layer (i) is obtained from the projection of the Kerr vector  $\boldsymbol{\theta}_K^{(i)}$  on the projection axis P, the orientation of which is determined by the projection angle  $\psi$ . After Hamrle et al. [245]

ferromagnetic films that are separated by a nonmagnetic spacer layer. By phase selection with the compensator proper projection angles can be chosen so that the Kerr vector from the first ( $\theta_K^{c(1)}$ ) or second ( $\theta_K^{c(2)}$ ) magnetic layer is perpendicular to the projection axis. Then the magnetization of this layer is invisible and only the other shows up with a Kerr signal. This situation is depicted in Fig. 3.17a for canceling of the Kerr component of the first layer. In systems with more than two magnetic layers this concept in principle also works if one succeeds to set the Kerr vectors of all but one layer parallel to each other and perpendiciular to the projection axis. In Fig. 3.17b this situation is shown for three magnetic layers, where the Kerr signals from the first and third layer are canceled simultaneously and, consequently, only a signal from the second layer is obtained. Hamrle et al. [245] called this the "parallel Kerr vector" method.

So far the Kerr vectors were assumed to be fixed in the  $\theta_K \xi_K$ -plane (i.e. the wavelength of light and the angle of incidence were taken as constant) and the projection angle  $\psi$  was tuned with the compensator. Alternatively also the wavelength can be changed to obtain depth selectivity. In the projection concept this means that the projection angle is fixed and the orientation of the Kerr vectors is modified by varying the light wavelength or, though much less effective, the angle of incidence.

Fig. 3.17 Kerr vectors and projection axis in the  $\theta_K \xi_K$ -plane for a system consisting of two **a** and three magnetic layers **b** that are interspaced by non-magnetic layers. In both cases a Kerr signal is only obtained from layer (2). After [245]



The "parallel Kerr vector" method can then be applied as discussed. In [245] this elegant method was experimentally verified on a (TbFe/Si $_3$ N $_4$ ) $_4$  multilayer system for magneto-optical recording, where the hysteresis curves of all four magnetic layers could be obtained individually by changing the photon energy in an optical magnetometer. Further depth-sensitive hysteresis measurements by using different wavelengths were presented in [279, 280].

# 3.3 Depth-Selective Kerr Microscopy

In bulk metallic materials the depth sensitivity of the magneto-optical effects can hardly be used. If a surface is ideally oriented (meaning that it contains one or more easy axes of magnetic anisotropy), the domains do not significantly change beneath the surface. In the other extreme case of strongly misoriented surfaces, the phenomenon of domain branching [111] connects fine surface domains with wide basic domains by a system of intermediate domain generations, the complexity of which depends on the sample thickness. These subsurface domains would in fact be interesting for depth-sensitive analysis. However, the finest closure domains right at the surface, e.g. in iron, have a lateral extension of about 1 µm. Towards the depth, an extension of the closure domains in the same range is expected, which is already orders of magnitude deeper than the magneto-optical information depth of 20 nm—the interesting subsurface domains will thus be not accessible. Examples, where the spin structure changes within the information depth, are domain walls in low-anisotropy materials or dense stripe domains in thick films with weak out-ofplane anisotropy. Both micromagnetic objects develop a vortex spin configuration to avoid (or at least reduce) magnetic charges [111]. For a vortex wall, however, the lateral extension of the (surface-) vortex is of the order of some 10 to some 100 nm, depending on anisotropy and sample thickness. This is below or at the limit of optical resolution. Although some diffraction-broadened images of such walls can be readily obtained by Kerr microscopy (allowing to identify "Néel caps" and the location of internal Bloch lines [111]), a depth-selective analysis appears questionable. The same applies to stripe domains, which have a width (at nucleation) equal to the film thickness. A reasonable magneto-optical investigation of these objects requires film thicknesses of at least 1 µm [111]. Stripe domains of that width do not have a significant change of spin structure within 20 nm below the surface. In any case, the magnetization structure of both, vortex walls and stripe domains, can be precisely predicted by micromagnetic calculations so that experimental detection is not necessary.

To exploit the depth sensitivity of magneto-optical microscopy, a significant change of the magnetic microstructure within the information depth is required, while at the same time the micromagnetic objects need to have lateral extensions wider than the resolution limit of optics. These conditions can be met in sufficiently-extended magnetic multilayer systems. If two or more ferromagnetic layers are present within the information depth, their individual magnetizations might be distinguished or

even be imaged separately. Depth *selectivity* in multilayers requires, however, that the contrast can be selectively adjusted to the individual layers. Several examples of film systems, where this is possible, are presented in the following. They are based on the phase concept of depth selectivity, which so far is the only method that has been applied for *microscopy*. For layer-selective *magnetometry* studies we refer to the literature mentioned at the end of Sect. 3.2.6.

In practice, layer selectivity is readily possible if the magnetic films of a stack have different hysteresis properties. An example is presented in Fig. 3.18. Here the magnetization curve of a Co/Cu/Ni<sub>81</sub>Fe<sub>19</sub> sandwich film was measured magneto-optically by integrating the image contrast in a Kerr microscope. The thicknesses of cobalt and copper add up to 10 nm so that also the nickel-iron (permalloy) layer contributes to the Kerr signal. Both films are exchange-decoupled and have different coercivities, leading to a double-step magnetization curve when the field is swept along the easy anisotropy axis. For general settings of polarizer, analyzer, and compensator (aiming at maximum overall Kerr contrast), the two steps appear within the same loop (Fig. 3.18a). From the corresponding domain images it is evident that the permalloy film is magnetized by the motion of a 180° wall. When it sweeps along, the stray field of this Néel wall acts on the cobalt film and creates an irregular, partial reversal there with patch domains left. The magnetization of both, NiFe and

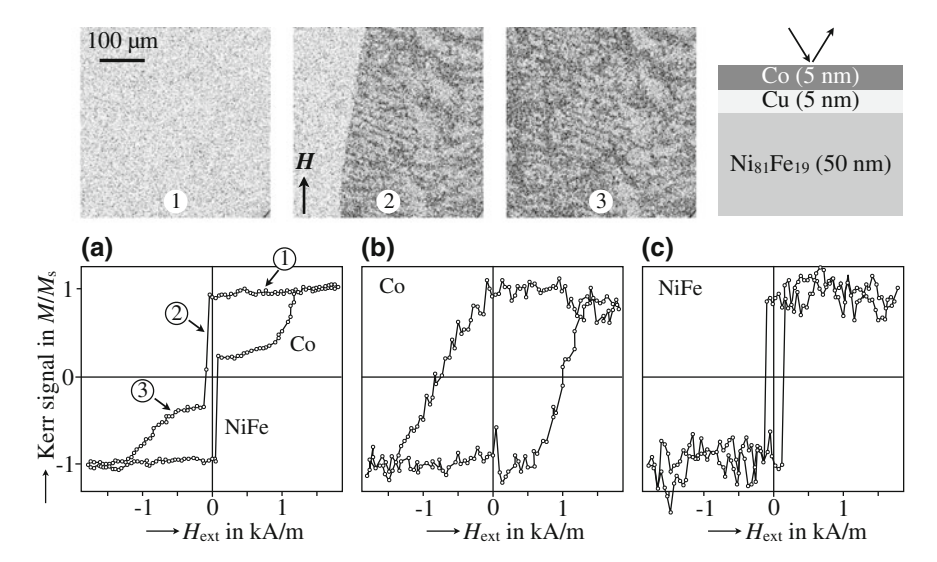


**Fig. 3.18** Magnetization curves on an extended Co/Cu/Permalloy trilayer, measured magneto-optically at different settings of analyser and compensator. In **a** the magnetization of both ferromagnetic films add to the detected Kerr signal, while in **b** and **c** only the cobalt and Permalloy layers, respectively, contribute. The domain images, obtained under "mixed" conditions, show the switching behavior along the curve (**a**) as indicted by numbers. An LED light source with a wavelength around 520 nm was used for this experiment. Sample courtesy *A. Svalov* and *G. Kurlyandskaya* (Ekaterinburg), imaging and magnetometry together with *L. Lokamani* (Dresden)

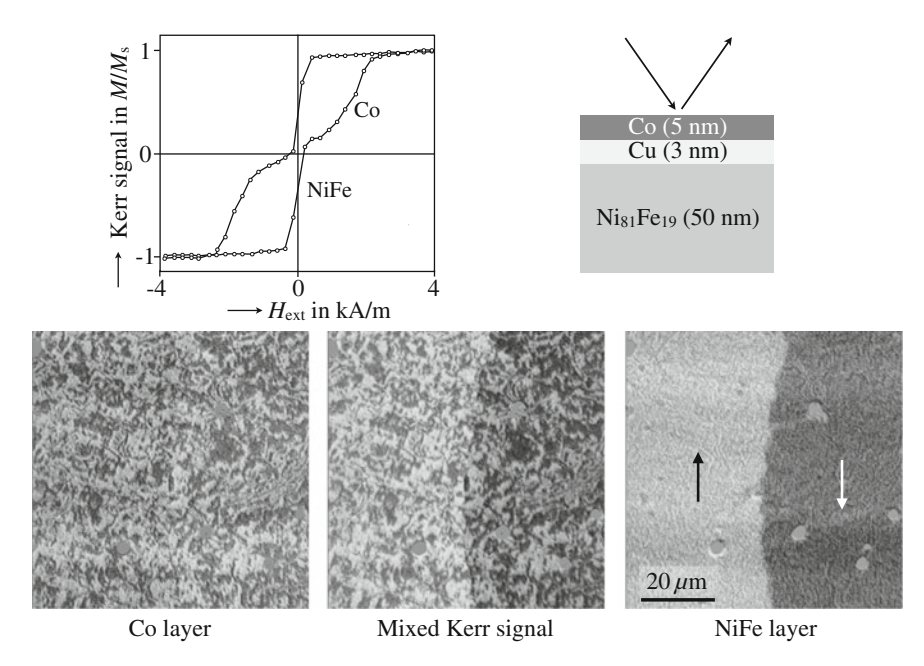


**Fig. 3.19** Depth-selective Kerr microscopy on Co/Cu/Permalloy trilayer. By proper phase selection with a compensator an identical domain pattern was imaged under mixed and layer-selective conditions as indicated. The magnetization curve, measured magneto-optically under mixed sensitivity conditions, shows the switching of both films. Rather than monochromatic light, the spectrum of a xenon arc lamp was used for this experiment. Sample courtesy *D. Bürgler* (Jülich), imaging and magnetometry courtesy *J. McCord* (Dresden)

Co, is seen in these images according to the hysteresis curve in Fig. 3.18a. Analyser and compensator settings can then be systematically varied till either of the steps is solely left in the magnetization curve as shown in Fig. 3.18b, c. The experiment is now selectively sensitive to the corresponding layers and layer-selective domain imaging can be performed with the respective optical settings. Note that the noise in layer-selective curves is stronger than in the mixed curve. This is related to the low thickness of the upper cobalt layer in Fig. 3.18a and to the significant damping of the signal that emerges from the lower permalloy layer in case of Fig. 3.18b. For the mixed curve the overall thickness of magnetic material, in which the light can interact with the magnetization, is larger.

<sup>&</sup>lt;sup>6</sup> A feasible alternative method was found by *L. Lokamani* (IFW Dresden): instead of using a compensator, Lokamani obtained layer selectivity by rotating polarizer and analyser relative to each other. If the polarizer is out of the (standard) *s*- or *p*-direction, elliptical light is generated by reflection on any metal (see Sect. 2.2.5). The degree and sign of ellipticity depends on the polarizer angle. So instead of shifting the phase between regular- and Kerr component in the reflected light with a compensator, a suitable phase shift between these two light components can as well be obtained by making use of the "natural" phase shift between *s*- and *p*-component that occurs under off-axis polarization conditions.

In Fig. 3.19 this procedure was applied to a similar sample. Like for the previous figure, the proper analyser and compensator settings for layer selectivity were determined by making use of the different coercivities of cobalt and permalloy. These settings are now applied to finally obtained layer-selective domain contrast. Three images of an identical domain pattern, obtained after demagnetization in an alternating easy-axis field, are shown. In the mixed Kerr image, the contrast of both ferromagnetic layers is superimposed. It can be separated into a simple 180° domain state in the permalloy film and a complex mixture of patch domains and 360° walls that are obviously present in the cobalt layer. The magnetic charges at the patch boundaries and 360° walls cause charge-compensating structures (like "zero-degree walls", see [111]) in the NiFe-film by magneto-static interaction. They are faintly visible within the otherwise wide NiFe domains.

A further example of layer-selective microscopy and magnetometry is presented in Fig. 3.20. The Co/Si/GdCo trilayer is characterized by a peculiar magnetization curve if measured magneto-optically (Fig. 3.20a). In this figure both, the GdCo

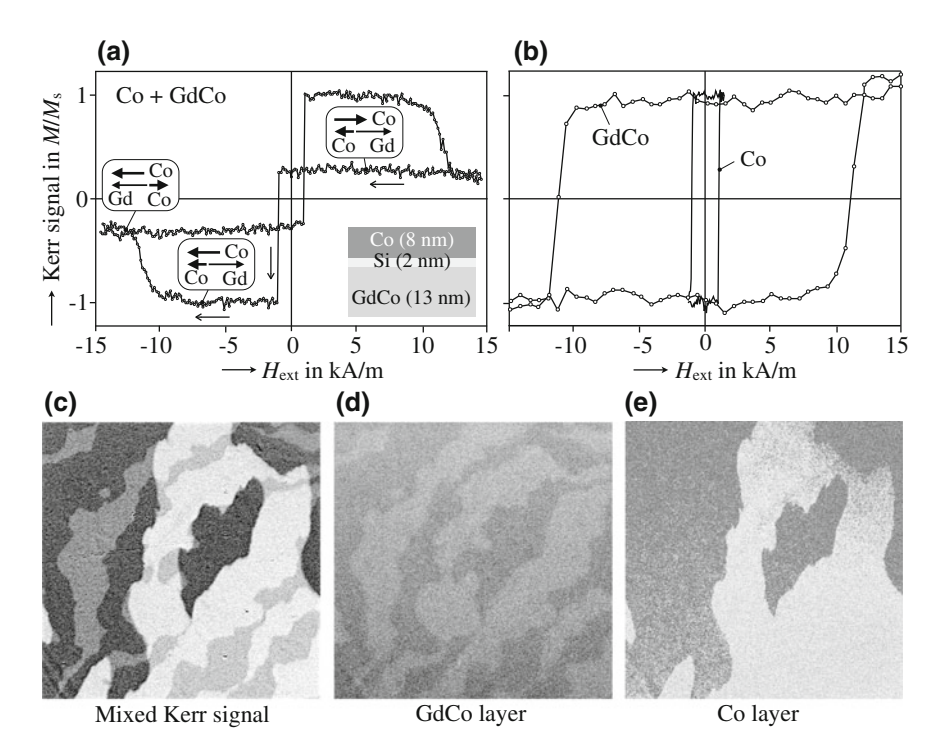


**Fig. 3.20** Depth-selective Kerr microscopy and magnetometry on a Co/Si/GdCo trilayer. The mixed Kerr signal in **a** was separated into signals of the indvidual layers in **b** by phase adjustment, here by rotating polarizer and analyser. Under the same conditions the Kerr domain images **c**-**e** of an identical domain state were obtained. The same light source as in Fig. 3.18 was used. Sample courtesy *A. Svalov* and *G. Kurlyandskaya* (Ekaterinburg), imaging and magnetometry together with *L. Lokamani* (Dresden)

and Co layers contribute to the Kerr signal. The chosen GdCo alloy [281, 282] has two ferrimagnetically coupled (i.e. antiparallel magnetized) sublattices, in which the magnetic moment of the Gd-sublattice dominates over that of the Co-sublattice. The direction of the Gd-sublattice moment is thus in the same direction as the total moment of the GdCo-film. When we follow the hysteresis curve along the indicated arrows, the following order of macrospin configuration is observed: (i) In positive field the magnetic moments of the Gd-sublattice and that of the Co-layer are parallel to the external field. Consequently, the cobalt moments in the Co-layer and GdColayer are opposite so that the sum of the cobalt moments is small. As the Kerr signal is generated solely by the cobalt moment (not gadolinium), a weak overall signal is measured. (ii) At a small negative field of about 1 kA/m the Co-film is remagnetized abruptly. The cobalt moments are now parallel, leading to a strong Kerr signal. (iii) In stronger negative field the total moment of the GdCo-layer finally also follows the external field direction. This leads to a reversal of both, the Co- and Gd-sublattices in the GdCo-film. The cobalt moments are then antiparallel again, resulting in a weak Kerr signal. On the way back the process is analogous. The Si-spacer layer more or less interrupts the coupling, so that both films are remagnetized independently. Figure 3.20b shows the separated hysteresis curves of the two individual layers. Like in the previous experiments, the two characteristic switching fields of the trilayer can conveniently be used to find proper microscope settings for layer selection. With the same settings the domain images (c-d) were obtained. A domain state is shown that was obtained after ac-demagnetization along the (vertical) easy axis. No attempt is made to draw magnetization vectors in these images.

A first experimental verification of this kind of depth-selective Kerr microscopy was achieved by *Rührig* [278] on an Fe/Al/Fe trilayer. Figure 3.21 shows a similar example, observed on an Fe(10 nm)/Cr(wedge)/Fe(10 nm) sandwich. In this film system the coupling between the iron layers oscillates between ferromagnetic (parallel alignment of magnetization), biquadratic (90° alignment) and antiferro-

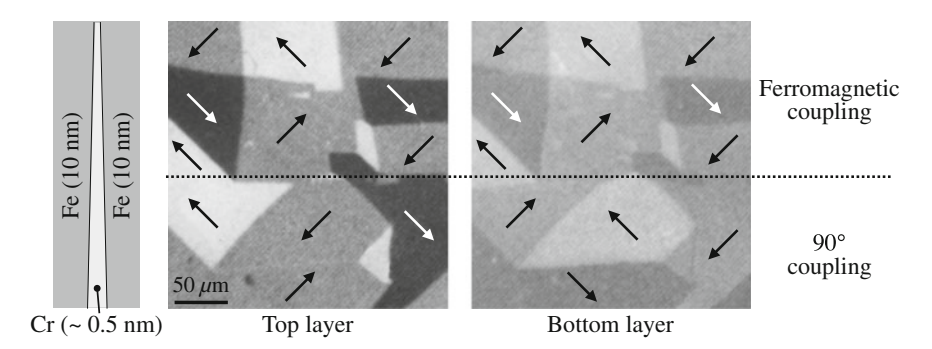


Fig. 3.21 Depth-selective Kerr microscopy on an FeCrFe sandwich film with wedge-shaped Crinterlayer. The coupling changes from ferromagnetic to biquadratic  $(90^{\circ})$  coupling within the image. The bottom layer contrast is weaker due to absorption. The yellow-green spectral lines of a mercury arc lamp were used for imaging. After [151]

magnetic (antiparallel alignment) with increasing chromium thickness—this type of oscillatory interlayer coupling has actually been discovered on such films [32, 283], together with the giant magnetoresistance effect [32, 34, 35]. The film for Fig. 3.21 has a wedge-shaped interlayer, so that all types of coupling can be observed on the same sample. Such wedge-specimens are ideally suited for domain studies as the influence of coupling on the domains can be readily identified by direct comparison. The domain pattern in Fig. 3.21 was imaged around a interlayer thickness of about 0.5 nm where the coupling changes from ferromagnetic to biquadratic. The typical domain patterns of both coupling types are visible within the same image. The trilayer has been epitaxially grown in (100)-orientation, so that the ferromagnetic layers have two orthogonal in-plane easy axes of magnetization, which are occupied for all coupling types. The Kerr contrast was carefully adjusted so that antiparallel domains along one easy axis appear black and white, while those along the other axis are equally gray. In the left image the compensator was rotated in such a way that only the magnetization of the top iron layer becomes visible, while in the right image only the bottom layer shows up. In the regime of ferromagnetic coupling, identical domains have the same color in both layers due to the parallel magnetization. In the regime of biquadratic coupling, all domains imaged in white or black in the upper layer are grey in the bottom layer, and vice versa. Of course the intensity of the bottom layer is lower than of the top layer due to absorption. Thus the 90° alignment of the magnetization vectors can be nicely confirmed by depth-selective experiments. The contrast separation in the FeCr/Fe trilayer was experimentally achieved by simultaneously rotating analyser and compensator until the "desired" contrast of each iron layer was achieved. This was possible in this case because the domain magnetization of each individual layer could be easily anticipated based on the cubic anisotropy and defined orientation of domain walls. More details on the domains in this multilayer system are presented in Sect. 3.4 in connection with Voigt- and Gradient microscopy.

In the example presented in Fig. 3.22 the separation of contrasts was again easily possible as the ferromagnetic materials have extremely different properties. Here an ultrathin iron film is epitaxially deposited on a (100)-oriented iron whisker, interspaced by a MgO layer. The whisker domain structure typically consists of 180° domains along the whisker axis that may be interrupted by 90° diamond domains. The contrast of the diamond domain in the whisker can easily be separated from the film domain contrast as shown in Fig. 3.22a. The contrast sensitivity was along the vertical in-plane axis in all pictures, which corresponds to one of the two surfaceparallel easy axes. According to crystal anisotropy, only three levels of gray are seen: black and white for domains magnetized along the sensitivity axis, and gray for both kinds of transverse domains. This is true for whisker and film, because the film is grown in the same orientation as the whisker surface and thus has the same orientation of crystallographic axes. The pattern in Fig. 3.22a was observed at low magnification. As compared to the simple diamond domain present in the whisker, the film domains (right image in Fig. 3.22a) appear highly complex with no clear relation between film and whisker magnetization directions. This indicates the absence of significant exchange or orange peel coupling between film and whisker. Nevertheless, the diamond of the whisker is still somehow reflected in the orientation of the film domain walls. In [284] it was demonstrated that this correlation is due to magnetostatic interaction, caused by the residual stray fields emerging from the whisker domain walls. In Fig. 3.22a these are the 90° walls of the diamond, which were wiggling during ac demagnetization and which thereby wrote the film domains.

In Fig. 3.22b a similar correlation is shown for a 180° wall running along the whisker axis. The whisker wall, which is imaged separately in the left picture of the figure, was moving up and down during demagnetization, and by doing so, a checkerboard domain pattern was written in the film, transferred by stray field coupling. The presence of the 180° whisker wall is also visible in the film by a straight horizontal domain boundary line that separates head-on film domains. Interesting is the correlation between whisker wall fine structure and film domains. Those points along the straight domain boundary in the film where the checkerboard domains change contrast are obviously directly related to the presence of Bloch lines in the whisker (indicated by arrows in the whisker image of Fig. 3.22b), whereas pure capswitch transitions, also present in the whisker wall, have no influence. The weak areal contrast in the whisker image is most likely due to an imperfect depth selectivity in the experiment. This can also be true for the residual wall contrasts (besides that of the 180° wall). Note, however, that the Néel walls in the iron film (which surround the checkerboard domains) could also induce some charge-compensating structures in the whisker surface that could be responsible for the line contrasts in the whisker image of Fig. 3.22b. For more information on this micromagnetically interesting system we refer to [284].

If the films in a multilayer stack do not significantly differ in their hysteresis properties, it might be difficult to find the proper microscope settings for layer selectivity (exceptions of this "rule" were presented in Figs. 3.21, 3.22). A solution to this problem, which works for ultrathin magnetic films in a multilayer with non-magnetic spacer layers, was presented by *Hamrle et al.* [245] under the heading "cascade numerical projection method". In this method, the total Kerr signal is measured under different experimental conditions, i.e., different wavelengths of light, different incidence angles or different projection angles  $\psi$  (compare Fig. 3.16). So a set of independent measurements is obtained from which the Kerr signal, which originates from each individual magnetic layer, can be separated by means of well-chosen linear combinations of the different Kerr hysteresis loops. In [245] this method was demonstrated for magnetometric measurements on a gold/cobalt multilayer, in which three cobalt layers (0.6 nm thick each) were interspaced by 5 nm thick gold layers. For microscopic imaging, however, this possibility has not yet been applied so far.

<sup>&</sup>lt;sup>7</sup> Note that different hysteresis properties are not required for layer selective imaging based on the X ray dichroism methods presented in Chaps. 4 and 5. As these effects exhibit an inherent elemental specificity, layer selectivity can be readily achieved if the individual layers of a multilayer stack differ in their elemental composition. On the other hand, if the individual layers are of the same composition, layer selectivity can only be obtained with the interference-based approaches presented in this chapter.

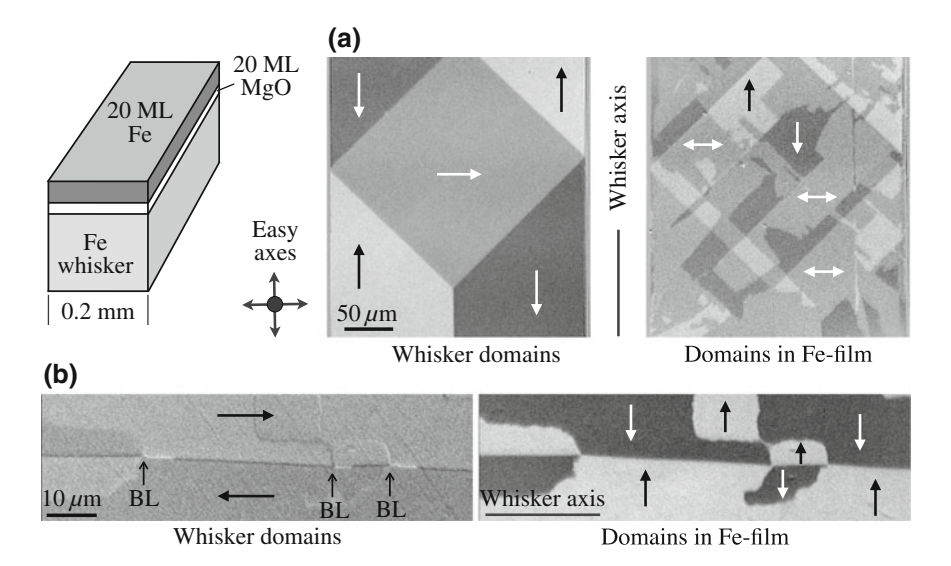


**Fig. 3.22** Depth-selective Kerr microscopy on a bulky iron whisker that is covered by an epitaxial iron layer of 20 monolayers (ML) thickness with a MgO spacer layer of the same thickness. Both, whisker surface and iron film are in (100)-orientation with two in-plane anisotropy axes. All images have been obtained after ac-demagnetization, at low-resolution in (a) and high-resolution in (b). Identical domain states are shown in each case, imaged selectively on the whisker (*left*) and film (*right*). After [284]

## 3.4 Voigt- and Gradient Microscopy

The information depth of the Voigt- and Gradient effects, which in metallic materials is of the same order as that of the Kerr effect, can also be applied for domain analysis, especially in case of *in-plane* magnetized multilayers. For such films the Kerr effect disappears at perpendicular incidence of light, whereas both, the Voigt and gradient effect show up simultaneously (compare Fig. 2.1). The typical domain- and domain boundary contrast of the Voigt effect and Gradient effect, respectively, can then be evaluated by following the symmetry rules of the two effects, which were introduced in Sects. 2.5 and 2.6.

The favorable application of Voigt and Gradient microscopy, together with their depth sensitivity, can best be demonstrated on the epitaxially grown sandwich structures that have been introduced already in Fig. 3.21. The Fe/Cr/Fe system is the prototype of such trilayers. As mentioned in the previous section, the coupling between the ferromagnetic films oscillates between ferromagnetic (FM), biquadratic (90°) and antiferromagnetic (AFM) as a function of interlayer thickness. A Kerr micrograph of such a sample is shown in Fig. 3.23a. Due to the wedge-shaped chromium spacer,

<sup>&</sup>lt;sup>8</sup> In [183] empirical information depth profiles for the Voigt effects (intrinsic and gyroelectric) were derived by similar analysis as shown for the Kerr effect in Sect. 3.2.4. For details we refer to this paper.

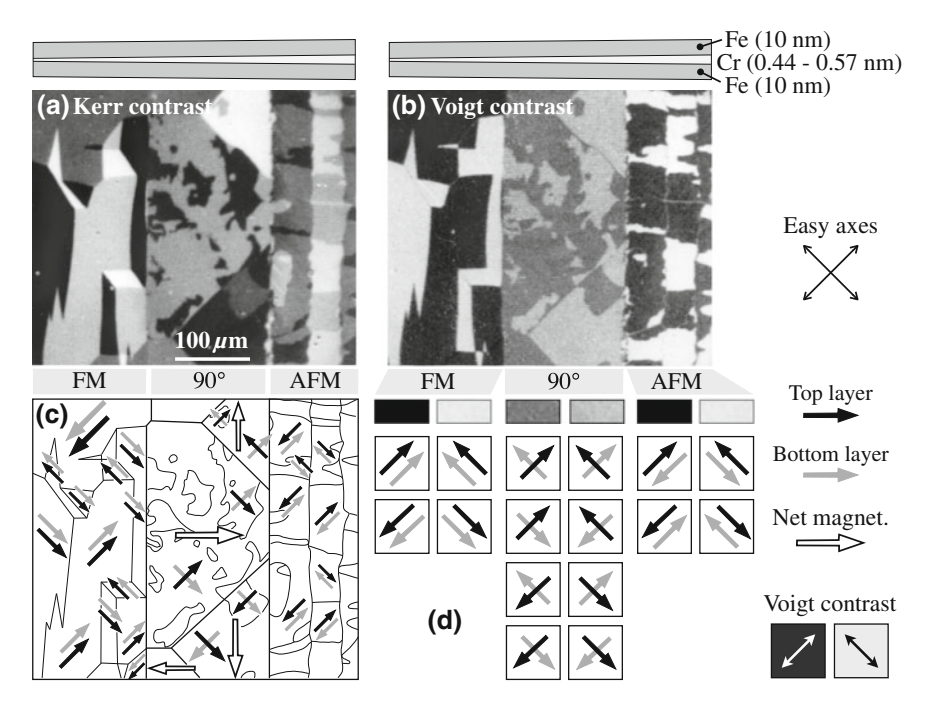


**Fig. 3.23** Comparison of Kerr (a) and Voigt (b) contrast on the same Fe/Cr/Fe sandwich as in Fig. 3.21. Here the coupling varies from ferro- to antiferromagnetic with a biquadratic  $(90^\circ)$  coupling zone in between. The vector diagram  $\mathbf{c}$  was derived by taking the Kerr and Voigt contrast into account. In  $\mathbf{d}$  the 16 possible magnetization alignments in the top and bottom layers are indicated, together with the Voigt intensities. (After [151])

the typical domain patterns of the three types of coupling appear within the same image. The magnetization of the iron films follows the two in-plane easy (100) axes, independent of the coupling type as indicated in the interpretation map (Fig. 3.23c). The different areas can be distinguished by the domain character, especially the orientation of the domain walls. For ferromagnetic coupling, regularly-oriented 90° and 180° walls are observed. They follow the principle of flux continuity<sup>9</sup> so that net magnetic charges on the walls are avoided as far as possible. Consequently, 90° walls are aligned at 45° relative to the easy axes and the 180° walls are oriented along the axes. Compared with the ferromagnetic domains, the domains observed for antiferromagnetic coupling look rather irregular. The reason is obvious: since the magnetization vectors in both iron layers are aligned antiparallel, they cancel each other locally and there is no net magnetization, which would enforce a specific orientation of the domain walls. Often the irregular domains have a patch-like character [283]. For biquadratic coupling, the magnetization vectors are aligned at 90° in both Fe layers. There are eight possibilities of doing so in a biaxial material (see Fig. 3.23d). Two at a time, where the vectors in the top and bottom layers are

<sup>&</sup>lt;sup>9</sup> A domain wall is free of magnetic charge ("pole-free") if the normal components of magnetization on both sides of a wall are the same [111].

exchanged, result in the same net magnetization, which points along a diagonal hard direction. Since the net magnetization is the same for two corresponding subphases, the orientation of the walls separating them may be arbitrary, while the net phase walls have to follow the rules of flux continuity. So the coexistence of regular and irregular domain walls is characteristic of biquadratic coupling.

By relying just on the Kerr image, the quantitative assignment of magnetization vectors in the individual domains, as shown in Fig. 3.23c, is only possible in the regime of ferromagnetic coupling. Here both iron layers add up in the Kerr contrast due to the parallel magnetization. By considering the mentioned continuity law for the wall orientation, together with the four gray levels of Kerr contrast, the magnetization vectors can easily be determined. For biquadratic and antiferromagnetic coupling, however, this is not possible. Here the bottom layer modifies the top layer contrast according to the 90° or antiparallel alignment, respectively. For general microscope settings (i.e. if no effort is taken to choose proper analyser and compensator settings to allow depth-selective imaging as was done in Fig. 3.21), up to eight levels of Kerr contrast can be expected for biquadratic coupling, and up to four levels for antiferromagnetic coupling—all different from the four levels appearing for ferromagnetic coupling. So the depth sensitivity of magneto-optic information can make the interpretation of Kerr contrasts rather difficult if a compensator is not applied or if the depth sensitivity is not adjusted carefully. Some of the possible 16 contrast levels are visible in Fig. 3.23a.

In such confusing situations, Voigt microscopy [151, 285] offers an elegant alternative to conventional Kerr microscopy, again by considering its depth sensitivity. A Voigt image of the same domain pattern as in Fig. 3.23a is shown in (b). A strong black/white contrast is observed in the FM and AFM areas, and a weaker two-level grey contrast in the biquadratic zone. The sketch in Fig. 3.23d helps to interpret those contrasts under consideration of the partial contributions from the two iron layers. The sensitivity function was adjusted so that the top layer contribution of the Voigt effect is stronger, but there is still some contrast also from the bottom layer. For FM and AFM coupling there are four possible magnetization arrangements in each case, two of them with the net magnetization along the black Voigt axis and the other two along the white axis. Since the sign of the (quadratic) Voigt contrast is the same in both iron layers it adds up to a strong black and white contrast. In the 90° zone there are eight possible magnetization arrangements. In four of them the top layer is magnetized along the black axis, but this black is weakened by the opposite Voigt contrast from the bottom layer. Correspondingly, the white from the top layer is darkened by the orthogonally magnetized bottom layer for the other four possibilities. So we end up with a weak black/white contrast in the 90° zone and a strong black and white Voigt contrast in the FM and AFM regions. Obviously the three different areas of coupling can very easily be distinguished in the Voigt image, much easier than in the multicontrast Kerr image of Fig. 3.23a. The Voigt contrast allows to determine the anisotropy axes that are occupied. Together with the Kerr image, which allows to determine the directions of magnetization, it is possible to come up with the quantitative mapping shown in Fig. 3.23c.

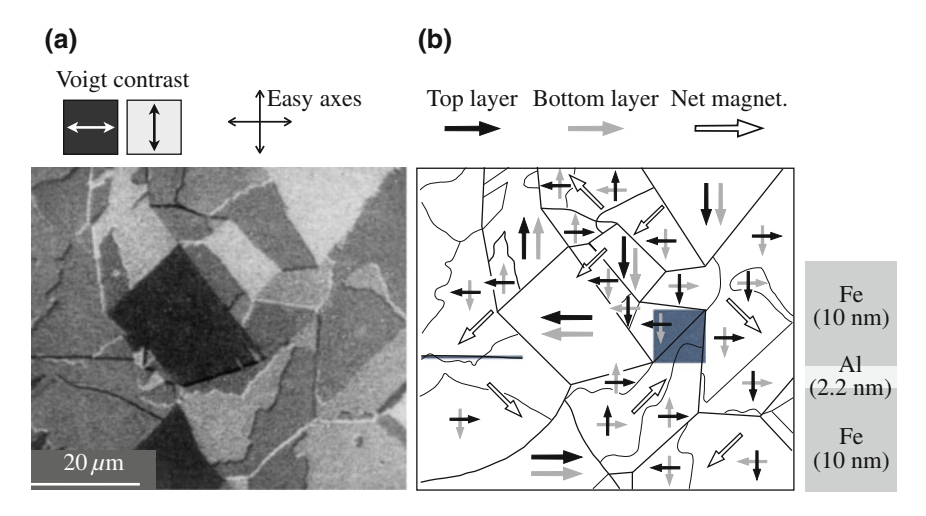


Fig. 3.24 a Voigt- and Gradient microscopy on a decoupled Fe/Al/Fe sandwich. The vector diagram  ${\bf b}$  was determined from the domain and domain boundary contrasts in (a) by considering the symmetry laws of the two effects. The coexistence of parallel and  $90^{\circ}$  relative magnetization alignment indicates the decoupling of the two iron layers. (After [151])

This knowledge can now be applied to more complicated domain patterns like that in Fig. 3.24a. Again the Voigt contrast immediately tells us how to interpret them. The domains show four Voigt grey levels. From the previous discussion we know that black and white indicates collinear (parallel or antiparallel) alignment, while weak and strong grey indicates 90° alignment. Since all four colors coexist and are mixed together, and because the colors can be arranged differently by applying an external field, we can conclude that this must be uncoupled behavior, or more precisely, a behavior where a weak coupling is dominated by coercivity effects. It is hard to distinguish uncoupled from FM-coupled layers in hysteresis measurements. In Voigt microscopy, however, this is immediately possible. Moreover, a domain model like in Fig. 3.24b can easily be constructed by just studying the contrasts in the image which in addition to the Voigt contrast also reveals the gradient contrast at the domain boundaries. To do this we first decide from the intensity of the Voigt contrast whether the vectors are aligned collinearly or orthogonally. Then we determine the axis of magnetization from the Voigt color (according to the sketch in Fig. 3.23d, under the assumption of a stronger contribution of the top layer). Finally, the gradient contrast can be analyzed. It is determined by the orientation of the domain boundary, together with the orientation of the magnetization difference vector (net difference vector in the case of biquadratic coupling) of its neighboring domains, both relative to the given polarization axis of light (Sect. 2.6). So a definite determination of the direction of the domain magnetization vectors becomes possible. In constructing a magnetization map one should of course never forget the rules of micromagnetics, that is, the orientation of the domain walls. Only if a model is fully compatible with both the wall orientations and the contrasts, can we be sure about it.

# **Chapter 4 Depth-Sensitive Photoelectron Emission Microscopy**

## 4.1 Photoelectron Emission Microscopy

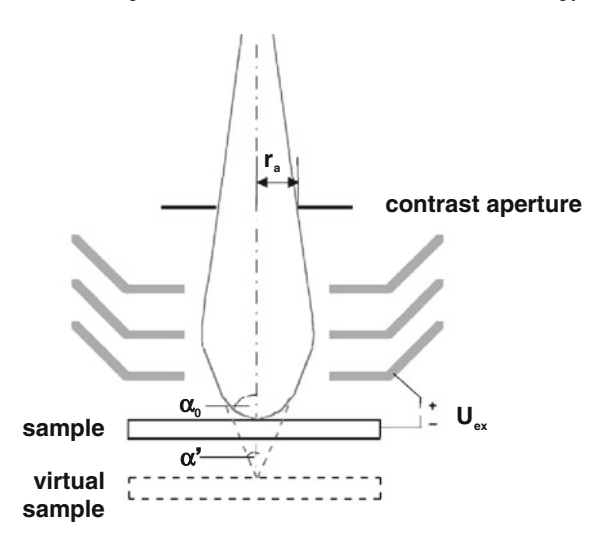
The very first PEEM instruments were realized already in the thirties of the previous century [286,287], which puts them among the oldest electron microscopes. In an electron emission microscope, the electrons that are used to image the sample do not come from a separate electron source like in conventional electron microscopy, but are emitted from the specimen. The basic principle is the electron-optical analogon to a light-optical microscope. To accept a large solid angle, immersion-lens objectives are used in which a strong electrostatic field accelerates the emitted electrons into the microscope. Figure 4.1 schematically shows an electrostatic tetrode lens like it is used for electron emission microscopy. A high voltage  $U_{\rm ex}$  is applied to the front lens, the so-called extractor lens, and creates a field of typically around 10 keV/mm between sample and microscope. The sample is thus part of the optical system. As a consequence, electrons emitted under the real starting angle  $\alpha_0$  reach the instrument under the virtual starting angle  $\alpha'$ , and appear to originate from a larger distance, the virtual object plane.  $\alpha_0$  and  $\alpha'$  are related by

$$\frac{\alpha_0}{\alpha'} \approx \sqrt{\frac{eU_{\rm ex}}{\mathcal{E}_0}},$$
 (4.1)

where  $\mathcal{E}_0$  is the starting energy of the emitted electrons. Unlike in light optics, no simple diverging electron optical lenses exist. Apart from sophisticated aberration-correction schemes [288], the standard means to reduce spherical and chromatic aberrations is to limit the maximum starting angle by a contrast aperture located in the diffraction plane of the electron optics.

From (4.1) follows that the accepted solid angle of electron emission is inversely proportional to the starting energy  $\mathcal{E}_0$ . Slow secondary electrons are thus transmitted by much higher numbers compared to photoelectrons of higher kinetic energy. Since the spectrum of emitted electrons is usually also dominated by secondary electrons, in instruments without explicit energy filtering the image is essentially

Fig. 4.1 Sketch of an electrostatic tetrode lens used for electron emission microscopy. The electric field created by the voltage  $U_{\rm ex}$ accelerates the emitted electrons into the objective lens.  $\alpha_0$  and  $\alpha'$  denote their real and virtual starting angles, respectively. The maximum starting angle is limited by a contrast aperture with radius  $r_a$ . The thin gray lines indicate electron trajectories with that maximum starting angle



created exclusively by low-energy secondary electrons. The term "photoelectron" in the name of PEEM is therefore somehow misleading. Its origin dates back to the time when PEEM was mainly used in threshold photoemission, where excitation is by 4.9 eV photons from mercury lamps. In that case there are no inelastically scattered secondary electrons. Applications of PEEM in connection with synchrotron radiation usually exploit the proportionality between X-ray absorption and secondary electron yield in a sample. The resulting images yield X-ray-absorption spectroscopic contrast.

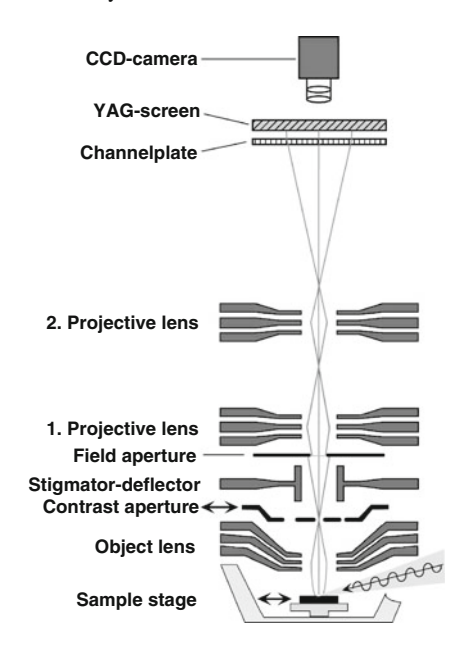
Besides electrostatic tetrode lenses, also magnetostatic triode lenses are frequently used in commercially available PEEM instruments. Due to the lower aberrations of magnetic lenses, their lateral resolution can be higher [289]; a disadvantage for the study of magnetic materials may be the non-vanishing magnetic field at the sample.

The rest of the PEEM consists of a number of additional lenses and stigmator–deflector elements, which project the image from the image plane of the objective lens onto an imaging unit. In the latter, the electron signal is amplified by one or several multi-channel plate amplifiers, and converted into visible light by a fluorescence screen, from where it can be recorded by a video camera. Figure 4.2 shows a sketch of a complete electrostatic PEEM. A more detailed description of technical aspects and the different contrast mechanisms of PEEM can be found in [290].

## 4.2 Electron Yield Detection of Absorption from Buried Layers

The detection of X-ray absorption by electron yield, as it is used in XMCD-PEEM, is an inherently surface-sensitive method because of the mean free path length of the electrons that are used for the imaging. The low-energy secondary electrons that make

Fig. 4.2 Sketch of a typical electrostatic PEEM with integrated sample stage. A field aperture in the image plane of the objective lens can be used to limit the field of view and to exclude unwanted stray electrons. Two projective lenses and an octupole stigmator-deflector project the image onto the imaging unit consisting of a microchannelplate and a fluorescent screen, from where the image is recorded by a charge-coupled device camera



up for nearly the entire intensity in a PEEM image are created in inelastic scattering events following the Auger decay of the core hole generated by the primary photon absorption process. For the design of suitable samples for layer-resolved magnetic imaging by XMCD-PEEM it is vital to know which kind of signal can be expected from a layer that is buried by overlayers. In this section we will discuss the secondary electron yield detection of X-ray absorption from buried layers, and show how the influence of overlayers can be estimated.

The electron yield absorption signal from a sample, which could be either an ultrathin layer as well as a semi-infinite substrate, is affected in two ways by the presence of overlayers. For simplicity we will assume here that none of the overlayers contains the same element as the one used to measure the sample. First, the electron yield signal of the sample is attenuated upon transmission through the overlayers. This can be described by an attenuation length  $\lambda$ , which depends on the inelastic electron scattering cross section of each of the overlayers. Second, depending on the shape of the element-specific absorption spectra of the overlayers, they can contribute a background at the position of the absorption peak of the sample. These two effects are illustrated by an example in Fig. 4.3. It shows the absorption spectrum measured by total electron yield of a trilayer consisting of 6 atomic monolayers (ML) Co on top of 5 ML Cu/15 ML Ni, deposited epitaxially on a Cu(001) single crystal surface. The displayed spectrum was obtained as the average of absorption spectra for positive and negative helicity. The  $L_{2,3}$  absorption peaks of Co and Ni are clearly recognized, as labeled in Fig. 4.3. The presence of the Cu and Co overlayers first leads to an attenuated electron yield signal  $Y_{\rm Ni}$  of the Ni  $L_3$  peak. This is due to electron scattering in the overlayers, and in a continuum model can be described by

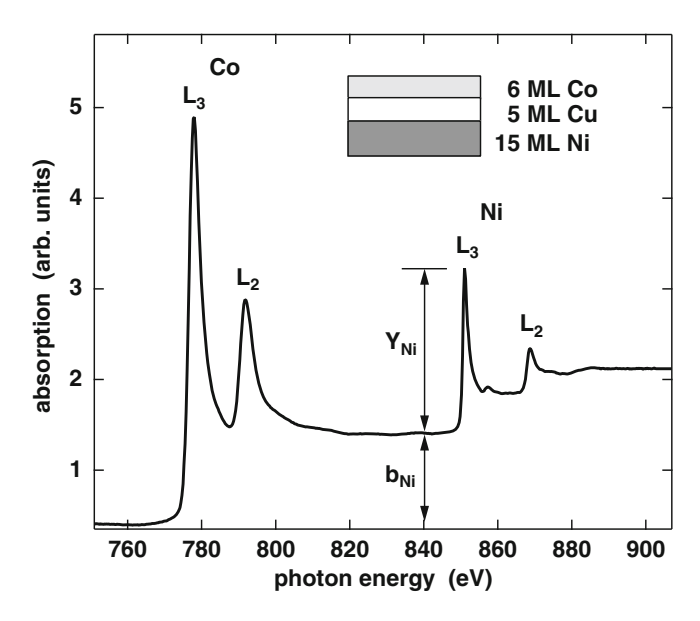


Fig. 4.3 Helicity-averaged absorption spectrum of a 6 ML Co/5 ML Cu/15 ML Ni trilayer on Cu(001), measured by total electron yield. The *inset* shows a sketch of the trilayer.  $L_2$  and  $L_3$  absorption peaks of Co and Ni are labeled. The presence of the Co overlayer leads to an attenuated Ni  $L_3$  absorption signal  $Y_{\rm Ni}$  because of inelastic scattering in the Co layer, and at the same time adds a background  $b_{\rm Ni}$  due to Co  $2p \rightarrow 4s$  transitions

exponential attenuation lengths  $\lambda_{\mathrm{Cu}}$  and  $\lambda_{\mathrm{Co}}$ . The signal from the Ni bottom layer is attenuated by a factor  $\exp(-d_{\mathrm{Cu}}/\lambda_{\mathrm{Cu}})$  by the Cu layer, and again by a factor  $\exp(-d_{\mathrm{Co}}/\lambda_{\mathrm{Co}})$  by the Co layer.  $d_{\mathrm{Cu}}$  and  $d_{\mathrm{Co}}$  are the thicknesses of the Cu and Co overlayer, respectively. More generally we can write for the attenuation of the electron yield signal  $Y_1^0(\hbar\omega_1)$  of layer 1 by overlayers  $i=2,3,\ldots$ 

$$Y_1(\hbar\omega_1) = Y_1^0(\hbar\omega_1) \prod_{i>1} e^{-d_i/\lambda_i(\hbar\omega_1)}.$$
 (4.2)

Here  $Y_1(\hbar\omega_1)$  is the measured signal of layer 1 at its peak position  $\hbar\omega_1$ . The unattenuated signal  $Y_1^0(\hbar\omega_1)$  of layer 1 can be obtained from its absorption coefficient  $\alpha_1(\hbar\omega_1)$ , a photon-energy-dependent secondary electron production factor  $c_1(\hbar\omega_1)$ , and the attenuation length  $\lambda_1$  of layer 1 as

$$Y_1^0(\hbar\omega_1) = c_1(\hbar\omega_1)\alpha_1(\hbar\omega_1) \left(1 - e^{-d_1/\lambda_1(\hbar\omega_1)}\right). \tag{4.3}$$

The photon energy dependence of the secondary electron conversion factor  $c_i(\hbar\omega)$  can be approximated to be proportional to the photon energy [291], where the proportionality constant  $c_i$  is material-dependent. It has been shown that this proportionality is not strictly valid over an extended range of photon energies [292]. Deviations of

about 30 % were observed in the energy range from 40 to 1,500 eV [292]. For the present estimation, taking into account our more limited photon energy range, we will nevertheless use  $c_i(\hbar\omega) \propto \hbar\omega$ . We will furthermore assume that  $c_i=c$  is the same for all layers in a given multilayered stack, since the dependence on surface properties as work function and surface morphology has a major influence on the secondary electron emission compared to different inelastic scattering behavior within the individual layers.

The attenuation lengths  $\lambda_i$  can be measured by increasing the thickness of overlayers in a controlled way while monitoring the signal from a capped layer underneath. Experimental values have been determined by Nakajima et al. for Fe, Co and Ni [293]. They obtained  $\lambda_{\text{Fe}} = 1.7$  nm, and  $\lambda_{\text{Co}} = \lambda_{\text{Ni}} = 2.5$  nm. Attenuation lengths for Cu and Au have been measured by Henneken et al. [294]. They found values of  $\lambda_{\text{Cu}} = 2.3$  nm, and  $\lambda_{\text{Au}} = 2.0$  nm.

A second effect that has to be considered, in addition to the attenuation of the electron yield signal by overlayers, is the overlayer-related enhancement of background. In the present example a background  $b_{\rm Ni}$  at the energetic position of the Ni  $L_3$  peak is due to the presence of the overlayers. It is related mainly to the Co and less to the Cu layer, because the Co 2p binding energy is lower than the one of Ni 2p. This leads to intensity from Co  $2p \rightarrow 4s$  transitions (which makes up for the step-like shape of the 2p edges) at the energy of the Ni  $L_3$  absorption peak. It can be described by  $b_{\rm Ni} = Y_{\rm Co}(\hbar\omega_{\rm Ni})$ , where  $\hbar\omega_{\rm Ni}$  means the Ni  $L_3$  photon energy, and  $Y_{\rm Co}(\hbar\omega_{\rm Ni}) = Y_{\rm Co}^0(\hbar\omega_{\rm Ni})$  is the electron yield intensity of the absorption of the Co layer at that energy. The Cu 2p binding energy is higher (about 933 eV), so that the Cu layer does not contribute significant background  $b_{\rm Ni}$  at  $\hbar\omega_{\rm Ni} \approx 853$  eV.

In a more general way we can write for the background  $b(\hbar\omega_1)$  at the photon energy corresponding to the absorption peak of layer 1

$$b(\hbar\omega_1) = \sum_{i \neq 1} \left( Y_i^0(\hbar\omega_1) \prod_{j>i} e^{-d_j/\lambda_j(\hbar\omega_1)} \right). \tag{4.4}$$

Here we have also considered the attenuation of the background from layer i by overlayers j > i on top of layer i. The background contribution  $Y_i^0(\hbar\omega_1)$  of layer i can be obtained in analogy to (4.3) as

$$Y_i^0(\hbar\omega_1) = \hbar\omega_1 c\alpha_i(\hbar\omega_1) \left(1 - e^{-d_i/\lambda_i(\hbar\omega_1)}\right). \tag{4.5}$$

To get a feeling for the deterioration of image quality we will now estimate the change of  $L_3$  absorption image statistics by the Cu and Co overlayers. Since the detection relies on counting local intensity, the image noise can be described by a Poisson statistics in which the square of the relative noise  $\sigma_{\text{Ni}}^2$  of a Ni  $L_3$  absorption image is

$$\sigma_{\text{Ni}}^2 \propto \frac{Y_{\text{Ni}} + b_{\text{Ni}}}{Y_{\text{Ni}}^2}.\tag{4.6}$$

The relative noise in the uncapped Ni layer is

$$\sigma_{\text{Ni},0}^2 \propto \frac{1}{Y_{\text{Ni}}^0}.\tag{4.7}$$

As a measure of the image deterioration we can define a factor *x* by which the exposure time of an image has to be multiplied to get the same relative noise as in the uncapped Ni layer. The comparison of the squared noise of the capped and uncapped Ni layer leads to

$$\frac{1}{x} \frac{Y_{\text{Ni}} + b_{\text{Ni}}}{Y_{\text{Ni}}^2} = \frac{1}{Y_{\text{Ni}}^0},\tag{4.8}$$

from which follows that

$$x = \frac{Y_{\text{Ni}}^0}{Y_{\text{Ni}}} \left( 1 + \frac{b_{\text{Ni}}}{Y_{\text{Ni}}} \right). \tag{4.9}$$

The first term in (4.9) is just the increase of measuring time needed to compensate the signal attenuation by the overlayers. In the present example it is equal to  $\exp(d_{\text{Cu}}/\lambda_{\text{Cu}} + d_{\text{Co}}/\lambda_{\text{Co}})$  (cf. (4.2)). The second term describes the influence of the enhanced background from overlayers. If we consider only the contribution of the Co layer to the background, we can use (4.2)–(4.5) and express

$$\frac{b_{\text{Ni}}}{Y_{\text{Ni}}} = \frac{Y_{\text{Co}}^{0}(\hbar\omega_{\text{Ni}})}{Y_{\text{Ni}}^{0}(\hbar\omega_{\text{Ni}})e^{-(d_{\text{Co}}/\lambda_{\text{Co}} + d_{\text{Cu}}/\lambda_{\text{Cu}})}}$$

$$= \frac{\alpha_{\text{Co}}(\hbar\omega_{\text{Ni}})}{\alpha_{\text{Ni}}(\hbar\omega_{\text{Ni}})} \frac{\left(e^{d_{\text{Co}}/\lambda_{\text{Co}}} - 1\right)e^{d_{\text{Cu}}/\lambda_{\text{Cu}}}}{1 - e^{-d_{\text{Ni}}/\lambda_{\text{Ni}}}}.$$
(4.10)

Here we have used  $c_i(\hbar\omega_{\rm Ni})=\hbar\omega_{\rm Ni}c$ , and neglected a possible photon energy dependence of the attenuation lengths, i.e.,  $\lambda_i(\hbar\omega)=\lambda_i$ . For the estimate of the necessary exposure time, tabulated values of  $\alpha_i(\hbar\omega)$  can be used. A convenient way is to use the web interface of the Berkeley server [295]. The values found there are based on tabulated atomic scattering factors by Henke et al. [296]. They describe the absorption quite well in the photon energy region outside the main absorption edges, as for example  $\alpha_{\rm Co}(\hbar\omega_{\rm Ni})$ , which is obtained as 11.3  $\mu$ m<sup>-1</sup>, but fail at the strong  $L_{2,3}$  resonances, as  $\alpha_{\rm Ni}(\hbar\omega_{\rm Ni})$ . The absorption coefficients at these resonances, however, can be obtained by scaling the experimental absorption curve below the  $L_3$  and above the  $L_2$  edge to the Henke data, and then taking the scaled values at the peak maxima. In the present example the tabulated data yield  $\alpha_{\rm Ni}(840~{\rm eV})=1.6~\mu{\rm m}^{-1}$  below the Ni  $L_3$  edge, and  $\alpha_{\rm Ni}$  (890 eV) = 11.6  $\mu$ m<sup>-1</sup> above the Ni  $L_2$  edge. From the Ni absorption spectrum shown in Fig. 4.3, an  $L_3$  peak height of 2.5 times the Ni  $L_{2,3}$  edge jump is obtained. The absorption coefficient at the Ni  $L_3$  maximum is thus approximated as  $[1.6+2.5\times(11.6-1.6)]~\mu{\rm m}^{-1}=26.6~\mu{\rm m}^{-1}$ .

The absorption coefficients of some of the 3d transition metals at the photon energies of the Fe, Co, and Ni  $L_3$  absorption maxima from [295] are reproduced

		Cr	Mn	Fe	Co	Ni	Cu
Fe $L_3$	(707 eV)	11.4	11.7	1.7 (59)	2.1	2.5	2.8
Co $L_3$	(778 eV)	9.8	10.4	11.3	1.7 (47)	1.9	2.3
Ni L <sub>3</sub>	(853 eV)	8.0	8.4	10.2	11.3	1.6 (27)	1.9

**Table 4.1** Absorption coefficients in  $\mu$ m<sup>-1</sup> of some of the 3d metals at the Fe, Co, and Ni  $L_3$  edges, from [295]

For the  $L_3$  resonances, the numbers before the brackets are for the pre-edge absorption coefficient, while the numbers in brackets indicate the value at the peak maximum, as calculated from the absorption edge jump and a peak to edge jump ratio of 5.0, 4.2, and 2.5, for Fe, Co, and Ni, respectively

in Table 4.1. For the  $L_3$  resonances, both the tabulated pre-edge absorption coefficient and the absorption maximum are given as numbers without and inside brackets, respectively. The latter has been estimated from the scaled edge jump ratio, as described above.

To estimate the value of x in the example of Fig. 4.3, we can use the already mentioned literature values for the attenuation lengths  $\lambda_{\text{Co}} = \lambda_{\text{Ni}} = 2.5$  nm [293], and  $\lambda_{\text{Cu}} = 2.3$  nm [294]. For the conversion of the layer thicknesses from atomic monolayers (ML) to nanometers we will use vertical interatomic layer distances of 0.170 nm/ML for Ni [297], 0.173 nm/ML for Co [298], and one half of the Cu bulk lattice constant for Cu (0.181 nm/ML). With these values,  $b_{\text{Ni}}/Y_{\text{Ni}}$  in (4.10) becomes 0.51. This Ni  $L_3$  background to signal ratio is close to the experimental value of 0.58 taken from Fig. 4.3. Using the calculated value and (4.9), we finally arrive at x = 3.4. A 3.4-fold increase of exposure time is thus sufficient to compensate the signal attenuation of Co and Cu overlayers of about 1 nm thickness each on the Ni absorption signal, and to result in the same signal-to-noise ratio in the final domain image as it would be for the uncapped Ni layer.

In the general case of detecting the absorption signal of layer k inside a stack of n layers, one has to replace (4.9) by

$$x = \frac{Y_k^0}{Y_k} \left( 1 + \frac{b_k}{Y_k} \right),\tag{4.11}$$

where now

$$\frac{Y_k^0}{Y_k} = \prod_{i>k} e^{d_i/\lambda_i(\hbar\omega_k)} \tag{4.12}$$

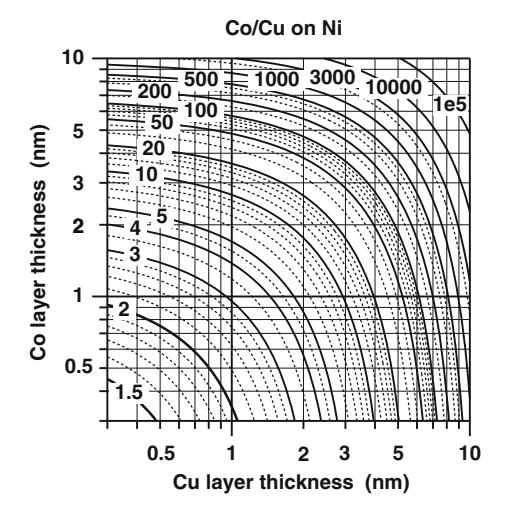
is the attenuation of the signal of layer k, and

$$\frac{b_k}{Y_k} = \frac{\sum_{i \neq k} \left( \alpha_i(\hbar \omega_k) (1 - e^{-d_i/\lambda_i(\hbar \omega_k)}) \prod_{j > i} e^{-d_j/\lambda_j(\hbar \omega_k)} \right)}{\alpha_k(\hbar \omega_k) (1 - e^{-d_k/\lambda_k(\hbar \omega_k)}) \prod_{i > k} e^{-d_i/\lambda_i(\hbar \omega_k)}}.$$
(4.13)

The numerator describes the background contributed by all other layers  $i \neq k$ . The background of each of these layers is attenuated by higher-lying layers j > i; this is expressed by the product. Note that this includes also layer k itself in cases i < k. In practice, however, the background from layers below layer k may be neglected, except for very thin  $d_k$ . The summed background  $b_k$  is relative to the signal  $Y_k$  from layer k, attenuated by all higher layers i > k. This is expressed in the denominator of (4.13).

Using (4.11)–(4.13), the feasibility of layer-resolved XMCD-PEEM for any layered system can be estimated on the basis of the absorption coefficients  $\alpha_i$  and attenuation lengths  $\lambda_i$  of the different layers i. In the following we will present some typical layered systems containing 3d ferromagnetic layers. The first example is Co/Cu/Ni, the same system as discussed before. To reduce the number of parameters, Ni is now considered as semi-infinite sample. Figure 4.4 shows the measuring time elongation factor x that is needed to compensate for the presence of the Co/Cu overlayers when detecting the Ni  $L_3$  absorption signal. It is presented by contour lines as a function of both, Cu layer thickness  $d_{\text{Cu}}$  displayed on the bottom axis, and Co layer thickness  $d_{\text{Co}}$  displayed on the left axis. It is seen that, as long as the overlayer thicknesses are of the order of 1 nm as in the example of Fig. 4.3, correction factors are well below 10. Of course it will depend on the particular experiment and spatial resolution which value for x can be considered "feasible". As a rough rule of thumb, keeping in mind that magnetic domains from a semi-infinite sample can be

Fig. 4.4 Overlayer compensation factor *x* needed for Ni *L*<sub>3</sub> electron yield measurement of a semi-infinite Ni sample buried by Co/Cu overlayers as a function of Cu and Co overlayer thicknesses. *x* describes the increase in data acquisition time required to obtain the same signal-to-noise ratio as without the Co and Cu overlayers



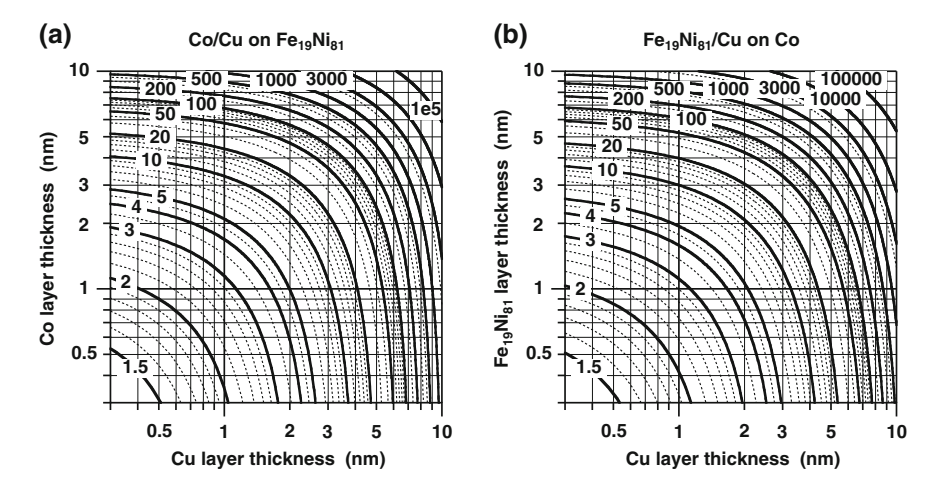


**Fig. 4.5** Overlayer compensation factor x needed for Co  $L_3$  electron yield measurement of  $\mathbf{a}$  a semi-infinite Ni<sub>81</sub>Fe<sub>19</sub> sample buried by Co/Cu overlayers as a function of Cu and Co overlayer thicknesses,  $\mathbf{b}$  a semi-infinite Co sample buried by Ni<sub>81</sub>Fe<sub>19</sub>/Cu overlayers as a function of Cu and Ni<sub>81</sub>Fe<sub>19</sub> overlayer thicknesses. x describes the increase in data acquisition time required to obtain the same signal-to-noise ratio as without the Co and Cu overlayers, and is presented as contour lines

imaged with reasonable resolution by exposure times less than 10 s, an increase by a factor of 1,000 could still be tolerable if a few domain images of the buried layer are sufficient, but would be too long if a whole series of images needs to be acquired.

Figure 4.5 shows the same plot for the combination of cobalt and permalloy (Ni<sub>81</sub>Fe<sub>19</sub>) as magnetic materials. Panel (a) shows the necessary correction factor for Fe  $L_3$  detection of a Ni<sub>81</sub>Fe<sub>19</sub> sample as a function of Co and Cu overlayer thicknesses, whereas in panel (b) Co represents the sample, and is covered by Cu and Ni<sub>81</sub>Fe<sub>19</sub> layers. While the order of magnitude of overlayer thicknesses leading to a certain x is the same as in Fig. 4.4, both cases displayed in Fig. 4.5 are slightly more favorable. This is due to the higher Fe and Co  $L_3$  absorption cross sections compared to Ni  $L_3$ , cf. Table 4.1. Overlayer thicknesses in Fig. 4.5b are about 10–15 % higher than in Fig. 4.5a; this is mainly a consequence of the higher background contribution of the Fe atoms in the permalloy overlayer at the Co  $L_3$  photon energy compared to the case when the Fe edge is measured and Co and Cu are overlayers. In the latter case both overlayers have a higher 2p binding energy than Fe, and contribute only little to the background, as seen also from Table 4.1.

When the thickness of the bottom layer is reduced, the relative weight of the background contributed by the overlayers, i.e., the second term in (4.11), increases. This means that in addition to having a smaller signal from that layer, also the influence of the overlayers on the measuring time increases. Figure 4.6 shows as an example the dependence of the compensation factor x on the bottom layer thickness for fixed thicknesses of spacer and top layer of 2 nm each. The two curves correspond to the two trilayer systems considered in Fig. 4.5a, b. As the bottom layer thickness

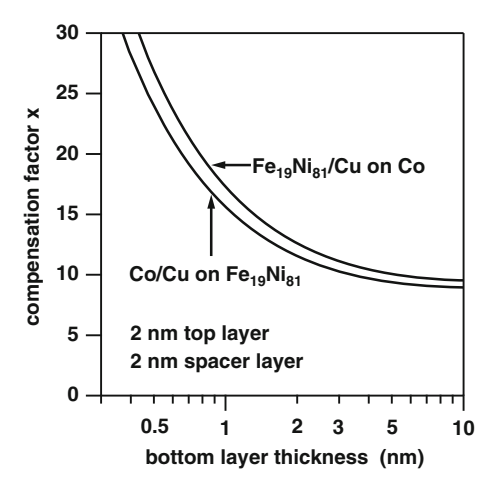


Fig. 4.6 Dependence of overlayer compensation factor x needed for electron yield measurement of the bottom layer in a magnetic trilayer on the bottom layer thickness. Shown are the two systems considered in Fig. 4.5 for fixed thicknesses of the top ferromagnetic layer and the nonmagnetic Cu spacer layer of 2 nm each. x describes the increase in data acquisition time required to obtain the same signal-to-noise ratio as without overlayers

is reduced, the relative measurement time increases from  $x \approx 9$ , the value found in Fig. 4.5 for an infinitely thick bottom layer, in particular for bottom layer thicknesses below the attenuation length of about 2 nm.

## 4.3 Imaging Ferromagnetic Materials by X-ray Magnetic Circular Dichroism

In this section we will present some recent applications of layer-resolved magnetic domain imaging by XMCD-PEEM. Microscopic layer-resolved imaging is mandatory for the investigation of local or microscopic properties of a multilayered magnetic system. Besides, a microscopic view of the sample has also several advantages for the investigation of coupling phenomena in magnetic multilayered systems. The thickness dependence of the interlayer coupling, for instance, may be conveniently investigated by imaging wedge-shaped samples. We will present examples that illustrate the capabilities of layer-resolved magnetic imaging by XMCD-PEEM. An important issue of high relevance also for technological applications is the local magnetic interaction between two magnetic layers by the magnetostatic stray fields from domain boundaries. Its investigation requires a microscopic layer-resolved view into the magnetic domain patterns of the individual magnetic layers. An example has been already presented in Fig. 3.22 in the previous chapter. At the end of the following section, the investigation of this interaction by XMCD-PEEM will be discussed.

### 4.3.1 NiFe/Cu/Co Trilayers

A first example of layer-resolved magnetic domain images is shown in Fig. 4.7. The magnetic part of the sample was a trilayer of 5 ML ferromagnetic NiFe at the top, separated by 5 ML nonmagnetic Cu from 15 ML ferromagnetic Co at the bottom. To pin the magnetization of the Co layer, the trilayer was deposited on top of a 15 ML FeMn antiferromagnetic layer, and annealed to 450 K after deposition of the Co layer in order to increase the size of the as-grown Co domains [299]. The multilayer was grown epitaxially on a Cu(001) single crystal surface. All domain images in the following are presented as gray-scale coded asymmetry images for opposite light helicity, i.e., the difference of absorption images acquired for both helicities of circularly polarized light is divided by the sum. In this way all topographic features that may be present in the images cancel out, since they do not depend on the helicity of the exciting X rays. The resulting asymmetry images represent thus pure element-resolved magnetic information. Different projections of the local magnetization direction on the direction of light incidence result in different values of the asymmetry, and are represented by different shades of gray. In Fig. 4.7 the light was incident from bottom to top, impinging upon the sample surface under an angle of 30°.

Figure 4.7a shows the as-grown domain image of the ferromagnetic Co bottom layer, as seen through the NiFe/Cu overlayers from the asymmetry at the Co  $L_3$  absorption maximum. No external magnetic fields have been applied. Most of the image is covered by two different shades of gray. The bright gray areas correspond to domains in which the magnetization direction is pointing within the film plane to the

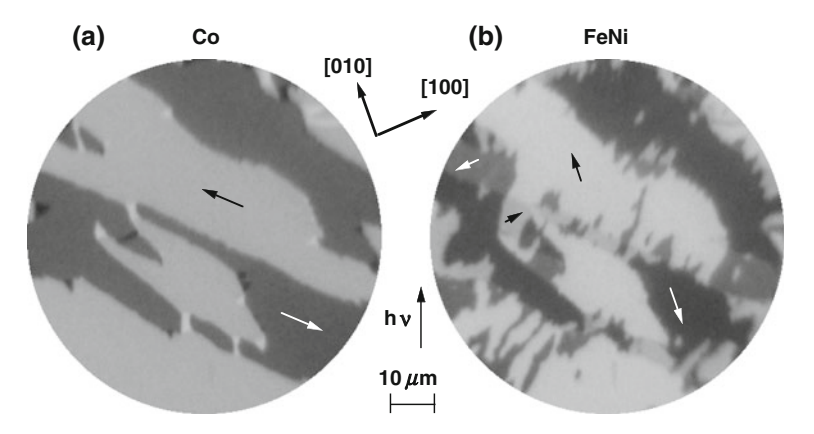


**Fig. 4.7** Layer-resolved magnetic domain images of 5 ML NiFe/5 ML Cu/15 ML Co/15 ML FeMn/Cu(001). **a** Magnetic domain image of the Co layer, **b** magnetic domain image of the NiFe layer. Crystallographic directions, direction of light incidence, and magnetization directions of some of the domains are indicated by *arrows*. The magnetization directions of the two magnetic layers form an angle of 45°, with the magnetization pointing along (110) crystallographic directions in the Co domains, and along (100) directions in the NiFe domains

upper left of the image, along the  $[\bar{1}10]$  crystallographic direction, as indicated by an arrow. In the surrounding dark gray areas the magnetization is oppositely oriented, and points along  $[1\bar{1}0]$ . The azimuthal orientation of the crystal with respect to the light incidence direction is indicated in the center of the figure. In addition to the  $[\bar{1}10]$  and  $[1\bar{1}0]$  oriented domains, also a few small domains are recognized which display a brighter white and darker black contrast: Some white areas are seen connecting the bright gray domains, and two small black domains can be found inside the dark gray area at the left of the image. They correspond to magnetization directions along [110] and  $[\bar{1}\bar{1}0]$ , respectively,  $90^\circ$  to the magnetization of the larger domains. Because of the azimuthal orientation of the sample, they are more aligned with the light incidence and thus exhibit a stronger dichroic asymmetry.

Figure 4.7b displays the magnetic domain pattern of the NiFe top layer, obtained from the XMCD asymmetry at the Fe  $L_3$  absorption maximum. Although a first view tells us that domains in the two layers are correlated, there are significant differences in the details. Most part of the NiFe domain image is covered by domains of two different shades of gray. They are somehow correlated to the large bright gray and dark gray domains of the Co image, although the exact boundaries are different. Besides these two types of domains, also smaller domains with a different shade of gray are seen in Fig. 4.7b. Their contrast differs only little from that of the larger domains, being slightly less bright and slightly less dark, respectively. The magnetization directions in the NiFe domains can thus not be identical to the direction of the corresponding Co domains of panel (a). There, the contrast of the small domains was higher compared to the contrast of the large predominant domains. Analysis of the asymmetry shows that in the NiFe layer the domains are magnetized along (100) in-plane crystallographic directions, 45° different from the (110) magnetization directions of the Co layer. The large bright and dark domains in Fig. 4.7b are thus magnetized along [010] and [ $0\overline{1}0$ ], respectively, as indicated by arrows. The smaller domains with slightly lower contrast are identified as domains with [100] and [100] magnetization direction, respectively, as also indicated by arrows in some of the domains. The latter have a slightly smaller projection on the light incidence direction, leading to the slightly lower contrast compared to the  $\pm [010]$  directions.

The advantage of layer-resolved magnetic domain imaging is that by comparing the two images taken under identical conditions, conclusions about the local magnetic coupling between the two layers can be drawn. Detailed comparison of panels (a) and (b) of Fig. 4.7 shows that nearly everywhere within the field of view locally the magnetization directions of the NiFe and Co layer form an angle of 45°. On top of the large bright domains of the Co layer, for example, mostly bright NiFe domains along [010] are recognized, but also some dark [100] oriented domains, as at the very right and left edges of the image, as well as at the bottom. On top of the large dark Co domains the NiFe magnetization is predominantly along the dark [010] direction, but also, as at the left edge of the image, along [100]. The explanation for this behavior comes from a consideration of the magnetic anisotropy energies of the individual magnetic layers and the magnetic interlayer coupling energy. The magnetic anisotropy energy is the difference in free energy for different magnetization directions with respect to the crystallographic

lattice, and defines the preferred magnetization axes [2, 30]. Its angular dependence follows the crystal symmetry of the system. In the fourfold symmetric single crystalline films of Fig. 4.7, the magnetic anisotropy energy in the film plane must assume a fourfold symmetric form, with minima along either the four (100), or the four (110) directions. The magnetic interlayer coupling energy depends only on the relative angle between the magnetization directions of two ferromagnetic layers that are separated by a nonmagnetic spacer layer, and exhibit a minimum for either 0°, 90°, or 180° [31, 283, 300–303]. The images of Fig. 4.7 can be explained by assuming (110) easy axes of magnetization in the Co layer, (100) easy axes of magnetization in the NiFe layer, and a 0° preferential coupling between the two layers. If the coupling energy is much lower than the anisotropy energies of the two layers, the total energy will have a minimum if the magnetization directions are close to the individual easy axes, and locally enclose an angle of 45°, as is observed in Fig. 4.7. The interlayer coupling energy is felt by the growing NiFe layer on top of the Cu/Co bilayer as an effective field at the interface, pointing locally into the directions of the Co magnetization. Even if the coupling energy is much lower compared to the anisotropy energy, it is sufficient to determine the as-grown domain pattern of the NiFe layer. In fact it is found to be nearly exclusively oriented by 45° to the Co magnetization. The only exceptions are found close to the domain walls in the Co layer; this can be the consequence of an additional, local coupling energy mediated by the magnetostatic stray fields from the Co domain walls, as will be discussed later in the following section.

## 4.3.2 Co/Cu/Ni Trilayers

## **4.3.2.1** Canting of Magnetization Direction as a Consequence of Competing Anisotropy and Coupling Energies

Another example for competing anisotropy and interlayer coupling energies are epitaxial Co/Cu/Ni trilayers on Cu(001). The magnetic anisotropy energy of epitaxial Ni films on Cu(001) favors magnetization directions perpendicular to the film plane ("out-of-plane") in a certain thickness range [24, 304, 305]. Co films on Cu(001), as already seen from the previous example (Sect. 4.3.1), are preferentially magnetized along  $\langle 110 \rangle$  directions within the film plane ("in-plane") [306, 307]. The competition between the anisotropy energies of the individual magnetic layers and the magnetic interlayer coupling energy in Co/Cu/Ni trilayers is expected to lead to several interesting collinear and noncollinear magnetic configurations. While the anisotropy energy favors a noncollinear alignment of the magnetization directions along the individual easy axes, the magnetic coupling energy is lowest when the magnetization of the two magnetic layers is collinear.

Layer-resolved magnetic domain images of a Co/Cu/Ni trilayer on Cu(001) are shown in Fig. 4.8. Here, the Co magnetic layer and the Cu nonmagnetic spacer layer have been prepared as small crossed wedges [308], in which the thickness increases

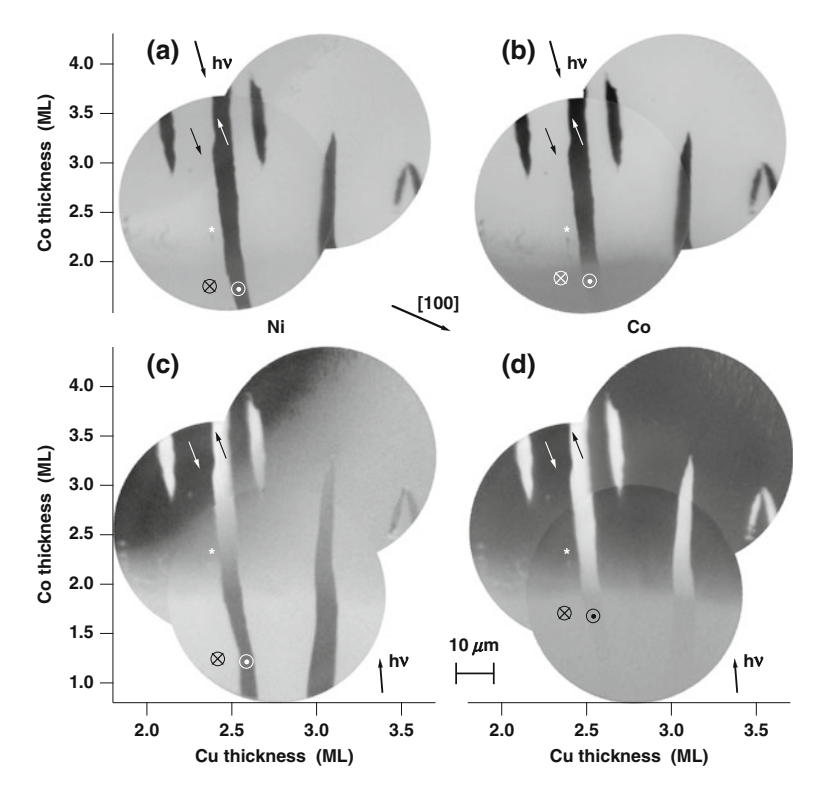


**Fig. 4.8** Layer-resolved magnetic domain images of Co/Cu/16 ML Ni/Cu(001). Co and Cu layers have been deposited as crossed wedges; thicknesses are given at the *bottom* and *left axes*, respectively. (**a**, **c**) Magnetic domain images of the Ni layer, (**b**, **d**) magnetic domain images of the Co layer. Images (**a**, **b**) and images (**c**, **d**) have been taken for different azimuthal orientation of the incident X rays, as indicated by *arrows* labelled "hv". Crystallographic direction and magnetization directions in some of the domains are indicated. Different transitions between collinear and non-collinear magnetization configurations are observed as a function of Co and Cu thicknesses

laterally along orthogonal directions. The thickness dependence of the layer-resolved domain patterns on both, the thicknesses of the Co and Cu layers, is such converted into a lateral dependence, which can be imaged in parallel. This results in general in tremendous savings of measurement time. Within the field of view of Fig. 4.8, the Co thickness increases from bottom to top, as labelled at the left axes, while the Cu thickness increases from left to right, as labelled at the bottom axes. The left images (a) and (c) show the magnetic domain pattern of the bottom Ni layer, the right images (b) and (d) the domain pattern of the top Co layer. The top and bottom row of images correspond to different azimuthal directions of X-ray incidence, as indicated by small arrows labelled " $h\nu$ ". Acquiring images at the same sample position under different light incidence angles is a convenient way of vectorial characterization of local magnetization directions. In particular in a system in which the magnetization direction may point out of the film plane under oblique angles, which we will see is the

case in the present system, it is necessary to determine not only the projection of the magnetization direction onto the X-ray incidence direction, but to obtain information about the local magnetization directions of both magnetic layers in space. In practice, because of the immobile set-up of a synchrotron beamline, the sample has to be rotated azimuthally, keeping or re-finding the same field of view.

Two measurements performed under different azimuthal angles constitute two linearly independent measurements of the magnetization vector at each position of the images. Under the assumption that the absolute value of magnetization stays constant, this is sufficient to determine the two degrees of freedom of the orientation of magnetization in space, for example azimuthal and polar angle. For a near 180° change of incidence azimuth, as in Fig. 4.8, the two special cases of pure out-of-plane magnetization (magnetization direction collinear to the surface normal) and pure inplane magnetization can be easily recognized by their behavior of the contrast upon variation of the light incidence azimuth: For pure out-of-plane magnetization, the magnetic contrast does not change, because the projection of the incident X rays onto the surface normal does not depend on the azimuth angle. Identical magnetic contrast upon 180° rotation of the sample means consequently that the magnetization direction is aligned along the surface normal. For pure in-plane magnetization, on the other hand, the projection of the incident X rays on the magnetization direction will be just opposite for a 180° change of the incidence azimuth, so that a reversal in grayscale contrast is expected in that case.

Long stripe-like domains of about  $5{\text -}10~\mu m$  width are recognized in Fig. 4.8. In the Co domain images, the contrast decreases significantly below about 2.0 ML Co layer thickness. If one had only the information of the upper two images, panels (a) and (b), available, one could be lead to the conclusion that above that Co thickness Ni and Co magnetization directions are identical, because the grayscale contrast in this part of the images appears to be identical. From the bottom row of images, however, it becomes immediately clear that this conclusion is entirely wrong. The stripes on the right hand side, for example, obviously show quite different contrast in the Ni and Co domain images. If it is not a priori clear that the magnetization direction is confined to a certain plane or axis, it is thus advisable to have some kind of vectorial characterization available in order to draw the right conclusions.

Comparison of the images obtained under different X-ray incidence angles reveals regions of nearly complete perpendicular magnetization at the very bottom of the Ni domain images, i.e., for the lowest Co thicknesses. No change of contrast between Fig. 4.8a, c is observed there. The behavior in the upper left part of the images, in the region of higher Co and lower Cu thickness, is completely different. Here the contrast reverses completely between panels (a) and (c). According to the above discussion the magnetization direction in the Ni domains is out-of-plane at the bottom of the images. A darker contrast corresponds here to domains with magnetization pointing out of the surface, which thus exhibit an antiparallel projection onto the light incidence, while brighter domains correspond to a magnetization direction pointing into the surface, as indicated in the images. The magnetization direction in the domains in the upper left part of the images is along opposite (110) crystallographic directions in the film plane, as indicated by arrows. Here the brighter contrast corresponds to

a more parallel alignment of magnetization direction and in-plane projection of the light incidence, which means  $[1\bar{1}0]$  in Fig. 4.8a, and  $[\bar{1}10]$  in Fig. 4.8c, as indicated by arrows.

In between the regions of pure out-of-plane and pure in-plane Ni magnetization direction, a gradual change of contrast is observed in Fig. 4.8c. This corresponds to a gradual change of the Ni magnetization direction between out-of-plane and in-plane as a function of both Co and Cu thicknesses. Following the left stripe in panel (c) that starts with a dark contrast at the bottom and is marked as pointing out of the sample surface, corresponding to [001] magnetization, its grayscale representation continuously changes to brighter when going to higher Co thicknesses, while the surrounding bright area becomes continuously darker. Close to the position marked by a small white asterisk in Fig. 4.8, this domain and the surrounding domain exhibit identical shades of gray in panel (c). This continuous change of grayscale corresponds to a continuous canting of the Ni magnetization direction from [001] to  $[\bar{1}10]$  in the stripe, and from  $[00\bar{1}]$  to  $[1\bar{1}0]$  in the surrounding domain. It is well recognized in Fig. 4.8c, where the light incidence azimuth is such that its projection onto the [001] and  $[\bar{1}10]$  directions results in opposite sign, while it is nearly not recognizable in Fig. 4.8a, where these two directions result in similar projections.

This continuous canting of the Ni magnetization direction is the consequence of the competition between the magnetic anisotropy of the Ni layer favoring perpendicular magnetization, and the magnetic interlayer coupling energy, favoring collinear alignment with the Co magnetization direction [309]. The Co magnetization direction is obtained from panels (b) and (d) of Fig. 4.8. Comparing these two domain images, it is obvious that the contrast reverses upon azimuth rotation in all the region at Co thicknesses above about 2.0 ML. From this a near-in-plane magnetization direction of the Co layer can be concluded, as indicated by arrows. The coupling of the Ni magnetization direction to that Co magnetization leads to the observed magnetization canting in the Ni domain images [309]. A corresponding canting should be also present in the Co layer, but is expected to be much smaller because of the size of the magnetic anisotropies of the two magnetic layers: The absolute value of the Co in-plane anisotropy is nearly an order of magnitude larger than the Ni out-of-plane anisotropy [310].

Below 2 ML Co thickness the contrast from the Co layer decreases strongly. This can be explained by the coalescence of the Co layer at that thickness. At lower thicknesses isolated Co islands may be formed that exhibit superparamagnetic behavior at room temperature [311]. Interestingly, some faint contrast is still observed just below 2 ML Co thickness. It shows identical grayscale contrast in Fig. 4.8b, d, meaning that it corresponds to an out-of-plane magnetization, as indicated in the figures. At these small Co thicknesses the Co anisotropy is obviously strongly reduced, leading to the observed out-of-plane orientation of Co moments [312]. In this thickness range the observed ferromagnetic signal of the Co layer at room temperature may be just due to induced ordering by the interaction with the Ni layer [313].

Summarizing the findings from Fig. 4.8, three qualitatively different phases with respect to the magnetic ordering are observed in the Co/Cu/Ni trilayers as a function of Co and Cu thicknesses: A collinear out-of-plane phase at low Co thicknesses, a

collinear in-plane phase at low Cu thicknesses, and a noncollinear phase at higher Cu thicknesses, in which the magnetization of the Ni layer points along obliquely canted angles out of the film plane, while the Co magnetization is nearly in the film plane. Analysis of the canting angle as a function of Co and Cu thickness provides information on the relative strength of the competing anisotropy and coupling energy contributions to the free energy of the system [309]. Magnetic domain imaging on wedged samples is seen to be an extremely effective way to obtain this information. Because the two-dimensional Co and Cu thickness space is sampled in parallel, it results in significantly shorter acquisition times compared to laterally averaging techniques. The present example shows that using imaging techniques can be quite advantageous even if only macroscopic properties, like the magnetization directions of the two magnetic layers in the present example, are to be investigated.

#### 4.3.2.2 Local Magnetic Interlayer Coupling by Domain Wall Interaction

If the thickness of the Cu spacer layer in Co/Cu/Ni trilayers is increased beyond the thicknesses studied in the previous example, the magnetic interlayer coupling that tries to align the Co and Ni magnetization directions into a collinear configuration gets strongly reduced. This coupling is caused by confined electronic states in the spacer layer [31, 300, 301], and by magnetostatic interaction between the magnetic layers from correlated roughness at the interfaces with the spacer layer [314]. Both mechanisms decrease rapidly when increasing the nonmagnetic spacer layer thickness. A weak interlayer coupling offers the opportunity to study other, local coupling mechanisms by layer-resolved magnetic microscopy, as will be shown below and in Chap. 3.

Figure 4.9 shows layer-resolved magnetic domain images of a Co/Cu/Ni trilayer with 6 ML thickness of the nonmagnetic Cu spacer layer. The thicknesses of the Co and Ni layers are 4 and 15.5 ML, respectively. Shown is the layer-resolved domain structure after application of a 240 Oe external field. This domain pattern is qualitatively identical to the as-grown domain pattern, which can be found in [315], but shows the effect we want to discuss here in a more pronounced way. No canting of the magnetization directions of neither of the magnetic layers is observed at 6 ML Cu layer thickness [315, 316], confirming the reduced interlayer coupling compared to the previous example of Fig. 4.8. The domain image of the Ni layer, shown in panel (a), exhibits a stripe domain pattern typical for out-of-plane magnetized samples. Bright and dark stripes correspond to domains with magnetization pointing into the film plane and out of the film plane, respectively, as indicated in the figure. The magnetic domain pattern of the Co layer, shown in panel (b), exhibits a similar stripe domain pattern, however with in-plane magnetization. Here, bright and dark areas correspond to domains with magnetization along [110] and [110] in-plane directions, respectively, as indicated by arrows. The direction of light incidence and crystallographic orientation of the sample are also given in the figure.

Although the magnetization directions in the two magnetic layers are oriented at 90° to each other everywhere in the images, conforming with the orthogonal

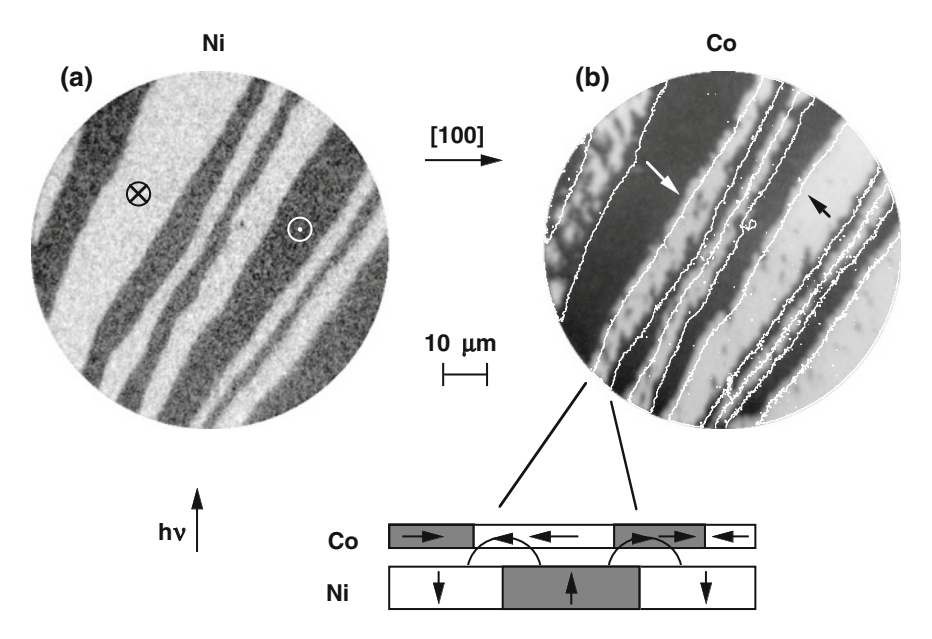


**Fig. 4.9** Layer-resolved domain images of 4 ML Co/6 ML Cu/15.5 ML Ni/Cu(001). **a** Magnetic domain image of the Ni layer, **b** magnetic domain image of the Co layer. *White lines* indicate the positions of Ni domain walls, obtained from a contour plot of panel **a**. Direction of light incidence, crystallographic direction, and magnetization directions in some of the domains are indicated. Comparison of the Ni and Co domain patterns reveals the presence of a local coupling mechanism mediated by magnetic stray fields from the Ni domain boundaries, as explained in the sketch at the *bottom* of the figure

arrangement of the individual easy axes of the Ni and Co layers, a certain correlation between the two domain patterns is evident. Dark, [110]-oriented domains in the Co layer are predominantly found at the positions of bright,  $[00\bar{1}]$ -oriented domains in the Ni. The same holds for domains with the respective opposite magnetization directions. Looking at the layer-resolved domain patterns in more detail, however, yields important deviations from that correlation, close to the domain boundaries. For a more accurate comparison of the domain positions, the domain walls of the Ni layer have been redrawn as white lines into the Co domain image. The lines have been obtained from a contour plot as the contour lines corresponding to 50 % asymmetry change between bright and dark domains of the Ni image. A systematic shift of the Co domain pattern to the upper left with respect to the Ni domain pattern is evident, which amounts on average to 1.5 µm. It is the consequence of a local magnetic coupling mechanism, mediated by magnetic stray fields emanating from domain walls. The sketch at the bottom of Fig. 4.9 explains the situation. It shows a schematic view of the trilayer, in which dark and bright sections represent domains with magnetization directions indicated by the straight arrows inside the layers. At the domain walls between the dark and bright domains of the Ni layer, a magnetic stray field is present outside the Ni layer, as indicated by the curved arrows. Its component along the surface normal changes sign at the domain wall. In addition, there is also a component of the stray field along the film plane. Interaction of that component with the Co magnetization leads to an additional Zeeman energy, which is minimized for a parallel alignment of the Co magnetization direction and the in-plane component of the stray field from the Ni domain boundaries. At the domain walls at which a bright ("down") domain in Ni on the left is separated from a dark ("up") domain on the right, this is the case if the Co magnetization points from right to left, i.e., has a bright contrast. Such a configuration is illustrated in the left part of the sketch. The right part represents the opposite arrangement of Ni domains: A dark ("up") domain on the left is separated from a bright ("down") domain at the right. In this case the direction of the in-plane component of the stray field, pointing to the right, coincides with the magnetization direction of the dark domains in Co. The observed shift to the upper and left of the Co domain pattern reduces thus the Zeeman energy of these stray fields.

A micromagnetic simulation [315] reveals that the strength of the in-plane component of the stray field from the perpendicularly magnetized Ni layer at the vertical position of the Co layer amounts to nearly 500 Oe at the center of the Ni domain wall, but decreases rapidly as a function of lateral distance. At only 50 nm distance from the domain wall center, much less than the shift of the Co domains observed in Fig. 4.9, it has already decayed to below 10 Oe. The effect of such a sharp lateral field spike on the Co layer is found to be more spread out by the exchange energy of the Co layer, which is proportional to the square of the gradient of the magnetization, and tries to avoid sharp deviations in magnetization direction in space. The effect on the Co layer was found from the micromagnetic simulations to be about comparable to a field of 200 Oe, with a width at half maximum of about 100 nm. One can imagine this exchange-averaging effect like a tip pressing on a membrane, or on the surface of a soap bubble. The value of 200 Oe is close to the experimentally determined effect (250 Oe, [315]). The remaining discrepancy between 200 and 250 Oe has been attributed to the neglect of the fourfold magnetocrystalline anisotropy of the Co layer in the simulation [315].

The total energy is minimized, strictly speaking, only for a configuration in which the Co stripe domains are shifted by half the period of the Ni stripe pattern, so that the Co domain walls are located at the centers of the Ni domains, and vice versa. At some of the narrower stripes of Fig. 4.9 this configuration is indeed approximately realized. The energy differences for a different location of the Co domains, however, are quite small once the "correct" Co domain is located in the closer vicinity of the Ni domain walls, the only region where the stray fields are sizeable. Other mechanisms, such as pinning of the Co domain walls by structural or morphological features, may become comparable in energy, leading to the domain pattern as observed in Fig. 4.9b, where the wider stripes in Co are not located centric to the Ni domain walls.

Another example, in which  $90^{\circ}$  domain walls interact across a non-magnetic spacer layer, is shown in Fig. 4.10 [317]. In square-shaped microstructures of a 4 nm Ni<sub>81</sub>Fe<sub>19</sub>/3 nm Cu/15 nm Co trilayer, elongated stripe-like domains with triangular edge domains at the two sides of the structure are formed. Figure 4.10 shows layer-resolved XMCD-PEEM magnetic domain images of such a microstucture. Panel (a)

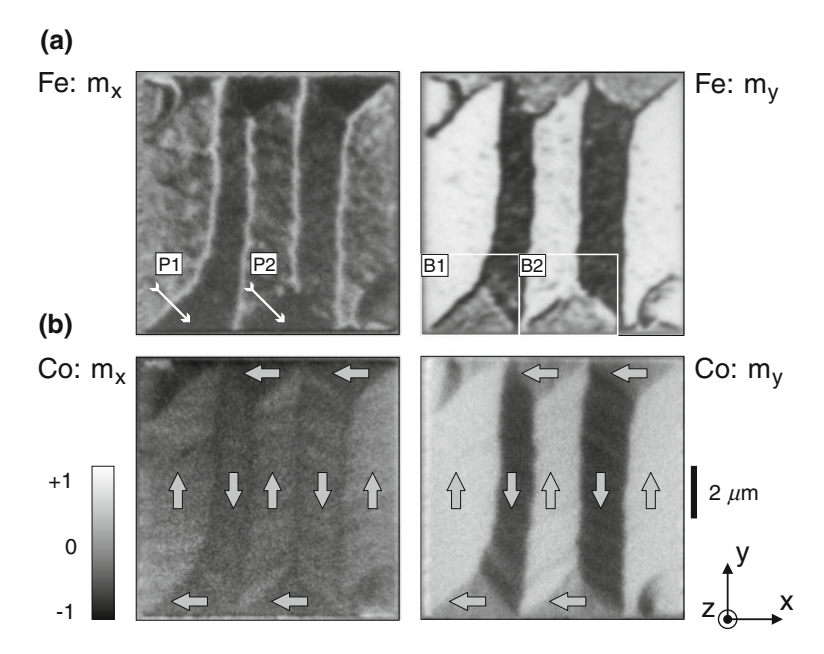


Fig. 4.10 Layer-resolved XMCD-PEEM magnetic domain images of a  $10 \times 10 \,\mu\text{m}^2$  microstructure consisting of a 4 nm Ni<sub>81</sub>Fe<sub>19</sub>/3 nm Cu/15 nm Co trilayer. a Magnetic domain images of the NiFe layer, acquired at the Fe  $L_3$  edge, **b** magnetic domain images of the Co layer, acquired at the Co  $L_3$  edge. Images have been taken for two X-ray incidence directions differing by 90°. The *left images* display the magnetic contrast sensitive along the horizontal, the *right* along the vertical direction. *Arrows* in **b** indicate the local magnetization direction. Within the two squares labeled "B1" and "B2" in (a), different types of domain walls develop in the NiFe layer at the positions of 90° domain walls of the Co layer: A 270° wall at the position labeled "P1", and a 90° wall with overshoot at the position labeled "P2". From [317] (Copyright IOP Publishing & Deutsche Physikalische Gesellschaft. CC BY-NC-SA)

at the top shows the magnetic domain pattern of the NiFe layer, panel (b) at the bottom the corresponding domain pattern of the Co layer. Images have been taken for two X-ray incidence directions differing by 90°, resulting in vectorial information about the local magnetization directions in each of the layers. The left images display the magnetic contrast sensitive along the horizontal, the right along the vertical direction. Within the domains, the magnetization of the two ferromagnetic layers is aligned along identical directions. This is a consequence of ferromagnetic interlayer coupling due to interface roughness-induced magnetic stray fields.

Deviations from that ferromagnetic alignment are seen at the domain walls. The layer-resolved XMCD-PEEM images allow to identify details of the magnetic configuration at the domain walls. The domain walls separating the elongated domains appear dark in the image of the Co layer, but show up with a bright contrast in the NiFe layer image (left images). These domain walls are of the 180° Néel-type, with magnetization in the domain walls pointing to the left in the Co image and to the right in the NiFe image. The antiparallel coupling in the domain wall, different

from the overall parallel interlayer coupling in the rest of the sample, is due to the magnetostatic interaction between two 180° domain walls, which favors antiparallel alignment. In this case, in both layers regular 180° Néel domain walls can be formed to minimize the stray field energy, with opposite magnetization direction within the walls.

A special case occurs at the boundaries between domains with 90° different magnetization direction, like the edge domains at the top and bottom part of the images of Fig. 4.10. Here, the situation is not symmetric any more, since the sense of rotation of magnetization in 90° domain walls is fixed. An antiparallel magnetization orientation at the domain boundaries in the two layers, which would reduce the magnetostatic coupling energy, is only possible if the domain walls in at least one layer assume a configuration other than a regular 90° domain wall. In the example of Fig. 4.10, two different domain wall configurations in the magnetically softer NiFe layer are observed: One in which the magnetization between two domains rotates by 270° instead of 90°, seen at the position labeled by "P1", and one in which the magnetization first makes an outward turn into the wrong direction, followed by a correspondingly larger rotation back in order to complete in total of 90° rotation. The latter is, for example, observed at the position labeled by "P2". Both cases lead to a partially antiparallel alignment of the magnetization in the domain walls, and lower the magnetostatic energy. Both configurations are energetically prohibited in a single magnetic layer, but appear in the coupled trilayer system because here the total free energy, including also the magnetostatic coupling energy, can be lower.

A local coupling mechanism by domain wall stray fields, as presented in these examples of layer-resolved microscopic domain imaging, is of highest technological and fundamental importance. It had been proposed to explain the high degree of antiferromagnetic order found in as-grown weakly coupled multilayers [318], which is irreversibly lost upon magnetization in an external field. The creeping loss of remanent magnetization of the magnetically hard layer in hard–soft spin valves after repeated magnetization cycles of the soft layer [319] has been also attributed to a stray field domain wall interaction [320].

## 4.3.3 NiFe/Al<sub>2</sub>O<sub>3</sub>/Co Trilayers

Local magnetic coupling by domain wall stray fields can also be important in tunnel junction-like trilayers, in which two metallic ferromagnetic layers are separated by an insulating oxide barrier. Figure 4.11 shows layer-resolved magnetic domain images of a Ni<sub>80</sub>Fe<sub>20</sub>/Al<sub>2</sub>O<sub>3</sub>/Co trilayer [321]. The thicknesses of the NiFe and Co layer were 4 and 7 nm, respectively, while the alumina barrier was 2.6 nm thick. The films were deposited on a step-bunched Si(111) substrate with 8° miscut, which was first covered with 3 nm of CoO in order to make the Co layer magnetically harder. The whole film structure was capped with 3 nm Al as protection layer. The presence of the step bunches leads to an in-plane anisotropy of the ferromagnetic layers. After demagnetization with an AC magnetic field of decreasing amplitude,

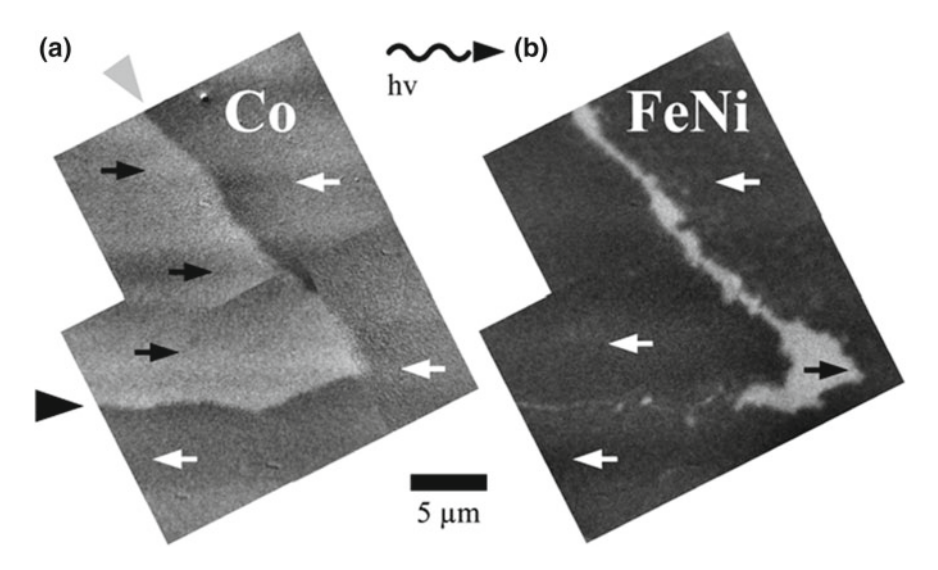


**Fig. 4.11** Layer-resolved magnetic domain images of a 4 nm Ni<sub>80</sub>Fe<sub>20</sub>/2.6 nm Al<sub>2</sub>O<sub>3</sub>/7 nm Co trilayer. **a** Magnetic domain image of the Co layer, **b** magnetic domain image of the NiFe layer. The direction of light incidence as well as magnetization directions in some of the domains are indicated. *Black* and *gray arrowheads* in **a** indicate parallel and partly charged domain walls in the Co layer, respectively. Comparison of the Co and NiFe domain patterns reveals the local coupling mediated by magnetic stray fields from the Co domain boundaries, evident by the presence of quasi walls in the magnetically softer NiFe layer. Reproduced from [321] with permission. Copyright IOP Publishing. All rights reserved

the magnetically soft NiFe layer was saturated along the easy axis by a field of 3 mT, higher than the NiFe coercivity, but lower than the Co coercivity.

Figure 4.11a shows the resulting domain image of the magnetically harder Co layer. A domain structure typical for a magnetic layer with an in-plane anisotropy is observed, with one pointed white domain and a surrounding black domain. Local magnetization directions are indicated by arrows. Contrast variations inside the domains are due to inhomogeneous intensity of the X-ray beam. Two main domain wall orientations between the two domains are present: One parallel to the easy axis of magnetization at the bottom of the white domain, indicated by a black arrowhead, and another one tilted with respect to this axis by about 45°, indicated by a gray arrowhead. In the former no magnetic charges are present from the adjacent domains, while the latter represents a charged situation in which the magnetization directions of the adjacent domains partly point towards each other. We call these configurations "parallel" and "head-on" domain walls, respectively.

Figure 4.11b shows the magnetic domain image of the magnetically soft NiFe layer at the same position of the sample. Macroscopically, this layer is saturated with magnetization pointing to the left. Around the positions of the domain walls in the Co layer, however, significant deviations from this macroscopic magnetization direction are observed. While at the position of the parallel domain wall of the Co layer a faint

bright line is recognized, a relatively broad region with opposite magnetization is observed close to the positions of the head-on domain wall in the Co layer.

It is clear that the unsaturated bright regions in the domain image of the NiFe layer are a consequence of the local magnetostatic interaction between the two ferromagnetic layers by the stray fields of the Co layer at the position of the domain walls. The distinct behavior observed for parallel and head-on domain walls can be explained as follows [321]: For the layer thicknesses of this example, domain walls in both Co and NiFe layers are expected to be of the Néel type [111]. For the parallel wall, the domains do not contribute to the domain wall stray field. The stray field of the Néel wall itself has a component perpendicular to the wall. This stray field leads to a tilt away from the easy axis of the NiFe magnetization [322], which is visible in Fig. 4.11 as the faint bright line. For the head-on wall, the main contribution to the stray field outside the Co layer comes from the domains, similar to the example in the previous section. It is firstly stronger than that of the Néel wall, and secondly pointing in the direction opposite to the macroscopic NiFe magnetization direction, hence along the easy axis of the films. The effect on the NiFe layer is consequently stronger, and the bright region is more extended than the one above the parallel wall. At the tip of the Co domain the magnetization directions of the domains in the Co layer are entirely head-on, and thus the largest effect on the NiFe layer is observed with an opposite domain of nearly 5 µm size induced by the stray field of the Co laver.

These examples demonstrate the relevance of the local magnetostatic coupling at domain boundaries. Despite its obvious importance, surprisingly little work has focused on this interaction up to now. The reason may be the lack of adequate techniques. To detect and investigate this interaction, which in contrast to the well-studied globally observable magnetic interlayer coupling acts only locally, a microscopic technique is needed. In addition, layer-resolution is an important prerequisite to investigate these coupling mechanisms. XMCD-PEEM is thus one method that is ideally suited for such kinds of experiments. Another example of a study of local interlayer coupling by domain wall stray fields has been already presented in Chap. 3. There, the effect of domains in an iron single crystal on the magnetization reversal of an ultrathin Fe film is studied using layer-resolved magnetic domain imaging by magneto-optical Kerr effect microscopy with depth-selectivity, another method capable of investigating such mechanisms.

## 4.3.4 Ni/Fe/Co Trilayers

Near-two-dimensional ultrathin films, epitaxially deposited on suitable substrates, may exhibit structural phases that would not be stable in volume materials. Ultrathin epitaxial Fe films are a famous example. If Fe is grown on a Cu(001) single crystal surface, or on a substrate with a comparable surface lattice spacing, different structural and magnetic phases occur, depending on thickness. For Fe thicknesses below approximately 4 ML, a ferromagnetic phase (phase 1) is observed, which

was characterized as a strained fcc-like [323] or strained bcc-like phase [324]. Even more interesting is the phase that occurs in the subsequent thickness range between about 4 and 11 ML (phase 2). It exhibits an fcc-like structure and a strongly reduced magnetic moment [325–327], which had been attributed to a paramagnetic or antiferromagnetic phase of fcc Fe. For Fe thicknesses above 11 ML the film structure turns into the ferromagnetic bcc phase [328], which is also the stable volume phase at ambient conditions. Numerous studies on ultrathin Fe films on Cu(001) and similar substrates have been conducted, since this system may reveal details of the interplay between structure and magnetism.

Layer-resolved magnetic imaging using XMCD-PEEM has also made its contribution by studying the magnetic interlayer coupling across ultrathin fcc Fe films. Measurements at Fe/Ni<sub>81</sub>Fe<sub>19</sub> multilayers [329] and observations by Kerr effect at Co/Fe/Co trilayers on Cu(001) [330, 331] had already indicated that fcc Fe films of phase 2 could possibly mediate an antiparallel coupling between adjacent ferromagnetic layers. This could then be indeed confirmed by layer-resolved XMCD-PEEM magnetic domain imaging [308, 332, 333]. Figure 4.12 shows large-scale  $(180 \times 290 \,\mu\text{m}^2)$  as-grown magnetic PEEM images of a crossed double microwedge of Ni and Fe on 6 ML Co/Cu(001) from [308]. Here an Fe layer was sandwiched between Co and Ni magnetic layers. Its thickness increases from right to left, as indicated at the upper axis. The Ni top layer was deposited as a wedge that starts at the position labelled by "0" at the right axis, and increases in thickness towards the bottom of the images. Comparing the Co (left) and Ni images (right), it is clearly observed that the magnetization directions of the Ni and Co layers are opposite around Fe thicknesses of 5 ML, where the Co image shows a uniform white contrast, while a dark vertical stripe is recognized in the Ni image. Linescans of the XMCD asymmetry at the maximum of the respective  $L_3$  absorption maxima are shown by white bullets superimposed to the images. The black line at 4 ML Ni thickness indicates the position at which the linescans have been taken, and at the same time serves as zero line for the linescans. A negative Ni XMCD asymmetry is thus present at about 5 ML Fe thickness, opposite in sign compared to the Co XMCD.

A second, less pronounced dark stripe is observed around 11 ML Fe thickness. At this position also the Co image exhibits some darker contrast, indicating imperfect saturation. The linescan reveals, however, that the contrast in the Ni image drops down to about zero, while in the Co image the XMCD signal is still positive. This has been interpreted as indication for an oscillatory interlayer coupling with a period of about 6 ML, consistent with the period in the oscillatory interlayer coupling observed in most non-magnetic fcc transition metals [31]. The Fe thickness of the second antiparallel coupling region coincides with the transition between phases 2 and 3 of the Fe, and became observable only for higher residual gas pressures during Fe layer deposition [308], which extends the thickness range in which the non-ferromagnetic phase 2 of Fe is observed [334, 335].

In addition to the information about the Co and Ni magnetic layers, layer-resolved magnetic imaging by XMCD-PEEM provides also information about the Fe layer. From the linescan of the Fe image of Fig. 4.12, beginning and end of phase 2 can be clearly recognized by the different level of XMCD asymmetry. The drop at about

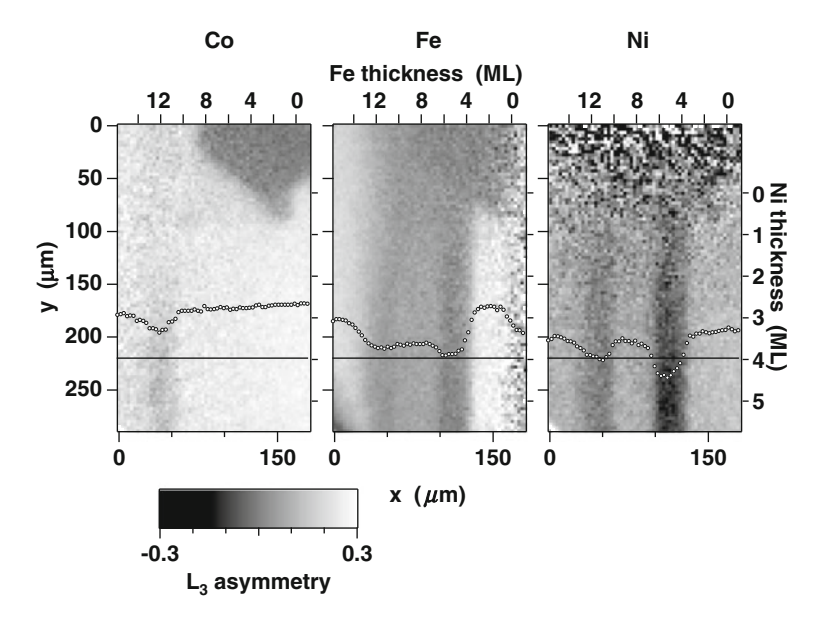


**Fig. 4.12** Layer-resolved magnetic images of a trilayer of 0–5.7 ML Ni/0–15.5 ML Fe/6 ML Co/Cu(001), prepared as a crossed double wedge. Images from left to right show the magnetic domain images of the Co, Fe, and Ni layer, respectively. *Two dark stripes* in the Ni image at about 5 and 11 ML Fe thickness point towards regions of antiparallel magnetic interlayer coupling across the fcc Fe layer. Reprinted from [308], Copyright (2000), with permission from Elsevier

4 ML Fe thickness and the increase at about 13 ML are related to the transitions from phases 1 to 2 and from 2 to 3, respectively. The lower XMCD signal in phase 2 is related to the presence of non-ferromagnetic Fe, enabling non-parallel interlayer coupling across the Fe layer. The Fe XMCD in phase 2 qualitatively follows that of the Ni, but is offset to positive values. This indicates that probably some Fe at both interfaces exhibits ferromagnetism, leading to the observation of a weighted average of the Co and Ni XMCD in the Fe signal [308].

A clearer sign of an oscillatory magnetic interlayer coupling across an Fe layer was reported later on in [332]. Figure 4.13 shows layer-resolved magnetic domain images of a Ni/Fe/Co trilayer on Cu(001) for different Fe thicknesses. The different images correspond to different positions on the sample, in which the Fe layer was deposited as a wedge of 2 mm width. In each of the images, the Fe thickness increases from left to right by 0.24 ML around the value cited below the images. Comparison of the Co (top) and Ni (bottom) as-grown domain images reveals antiparallel coupling in the image for 5.3 ML and in the left half of the image for 6.2 ML Fe thickness, as well as in the image for 11.8 ML and in the right half of the image for 8.7 ML Fe thickness. Between 6.2 and 8.7 ML Fe thickness only domain patterns with identical contrast in the Co and Ni images, indicating parallel coupling, are observed. From that study using layer-resolved magnetic domain imaging, the oscillatory interlayer coupling across fcc Fe, a nominally magnetic material, was thus confirmed. Similar investigations revealed also an influence of the strength of the interlayer coupling

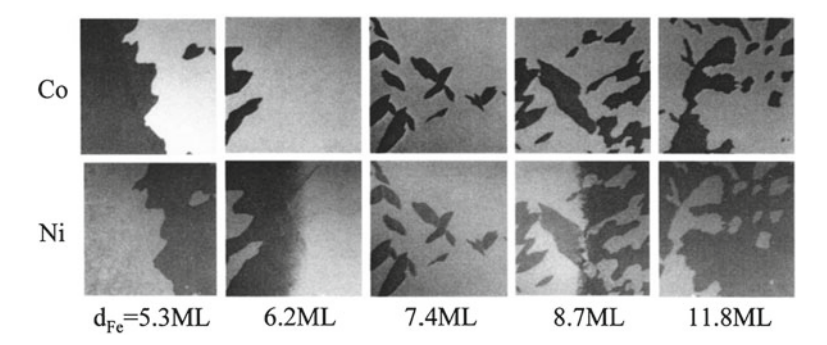


**Fig. 4.13** Layer-resolved domain images of 11 ML Cu/8.8 ML Ni/5.3–11.8 ML Fe/8 ML Co/Cu(001). *Top row* Magnetic domain images of the Co layer, *bottom row* magnetic domain images of the Ni layer. The images show a  $40 \times 40 \ \mu\text{m}^2$  region of the sample. The Fe thickness increases by 0.24 ML from left to right within each image. Reprinted with permission from [332]. Copyright (2003) by the American Physical Society

across fcc Fe on the onset of ferromagnetic order in very thin Ni layers [333, 336], and on the spin reorientation transition in thicker Ni films [332].

### 4.3.5 Ni/FeMn/Co Trilayers

Besides ferromagnetic ultrathin films, also antiferromagnetic materials have increasingly moved into the focus of interest. This is on the one hand motivated by fundamental curiosity, since much less is known about the properties of antiferromagnetic thin films compared to ferromagnetic films. While techniques like neutron scattering or Mössbauer spectroscopy have been used already in the sixties for the investigation of bulk antiferromagnetic materials, the properties of ultrathin antiferromagnetic films have mainly remained concealed due to experimental constraints of these techniques, which in general require thick samples to obtain sufficient signal. On the other hand, technological interest in antiferromagnetic thin layers has rapidly increased during the last decade. As outlined in Sect. 1.1, antiferromagnetic films are increasingly used as a means of pinning and manipulating the magnetization of adjacent ferromagnetic layers, which is an important issue for all kinds of magnetoresistive devices that rely on the independent switching of one out of several different ferromagnetic layers in a multilayered stack. The presence of the antiferromagnetic layer on the magnetization reversal of the ferromagnetic layer in such a bilayer usually manifests itself in two typical phenomena: The first is the exchange bias effect, as introduced in Sect. 1.1.3, a horizontal shift of the magnetization loop away from zero field after cooling the sample in a magnetic field through the antiferromagnetic ordering temperature. The second is a significant increase of the coercivity of the ferromagnetic layer.

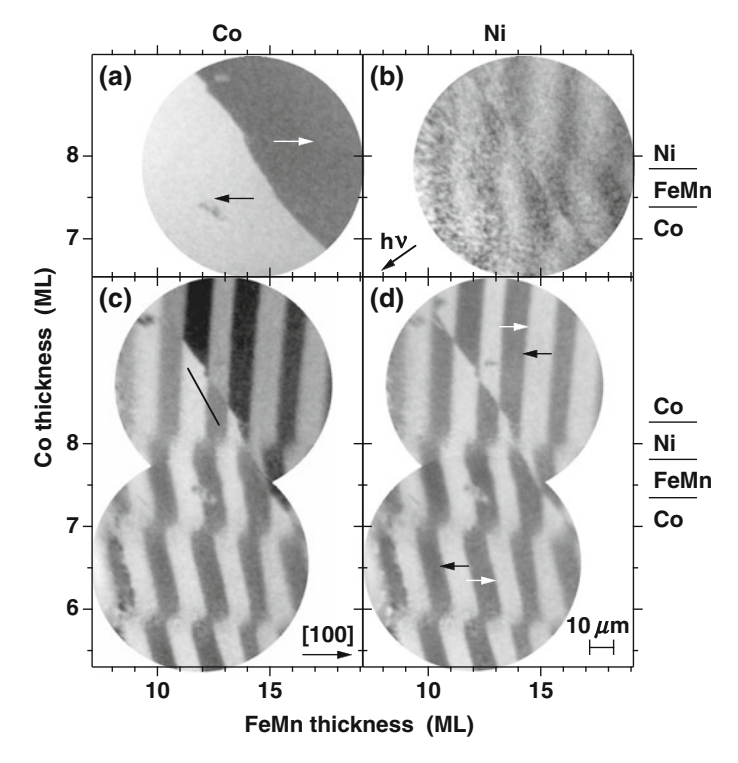


Fig. 4.14 a, b Layer-resolved domain images of a 15 ML Ni/FeMn/Co trilayer on Cu(001). The FeMn and Co layers were deposited as crossed micro-wedges with Co and FeMn thicknesses increasing from bottom to top and from left to right, respectively, as indicated at the left and bottom axes.  $\mathbf{c}$ ,  $\mathbf{d}$  The same sample after deposition of an additional Co layer of 3 ML thickness on top. This layer induces a spin reorientation transition of the top Ni layer from a canted out-of-plane magnetization direction to an in-plane direction. *Left images*  $\mathbf{a}$ ,  $\mathbf{c}$  show the XMCD contrast obtained at the Co  $L_3$  edge, the *right images*  $\mathbf{b}$ ,  $\mathbf{d}$  the contrast obtained at the Ni  $L_3$  edge. From [337]

In this paragraph we present results of a layer-resolved magnetic domain imaging study by XMCD-PEEM of a trilayer in which two ferromagnetic layers are separated by an ultrathin antiferromagnetic layer. Different from that, layer-resolved imaging can also be used to obtain directly information about the domains in the antiferromagnetic layer simultaneously to information about the domains of the ferromagnetic film if magnetic linear dichroism is used as contrast mechanism for the imaging of antiferromagnetic domains. This will be discussed in Sect. 4.4.

Figure 4.14 shows as-grown layer-resolved magnetic domain images of a trilayer in which two ferromagnetic layers are separated by a single-crystalline FeMn antiferromagnetic spacer layer. In the top row, panels (a) and (b), the two ferromagnetic layers were Co as bottom layer and 15 ML Ni as the top layer. The trilayers were grown epitaxially on a Cu(001) single crystal substrate. Similar to the sample presented in Fig. 4.8 in Sect. 4.3.2, the Co layer exhibits a preferred magnetization

direction in the film plane, while the Ni layer has its magnetic easy axis perpendicular to the film plane. Panel (a) shows the magnetic domain image of the Co layer, panel (b) the domain image of the Ni layer at the same position. The Co ferromagnetic bottom layer and FeMn antiferromagnetic spacer layer were deposited as crossed micro-wedges, with thicknesses increasing from bottom to top for Co and from left to right for FeMn, as indicated at the respective axes. The Co layer has mainly two large domains with bright and dark contrast corresponding to magnetization directions pointing to the left and right, respectively. The direction of the incoming X rays is indicated in panel (b). The Ni domain image is more complicated: It shows a superposition of faint vertical stripes on a domain pattern of many small domains. The contrast of the stripes changes at the position of the domain boundary of the Co layer. It is interpreted as a canted magnetization direction in the Ni layer due to the competition between out-of-plane anisotropy and interlayer coupling to the in-plane magnetized Co layer, analogous to the situation described in Sec. 4.3.2. The small domains are domains of the out-of-plane component of the Ni magnetization [337], and are explained by a laterally fluctuating random pinning of the perpendicular spin component of the Ni layer during growth on the surface of the antiferromagnetic FeMn layer [309]. The stripes that are additionally recognized are due to a canting of the Ni magnetization in these small domains. The in-plane component of the canting oscillates as a function of FeMn thickness between parallel and antiparallel to the Co magnetization direction with a period of 2 ML [337]. Such an oscillatory interlayer coupling across an antiferromagnetic spacer layer is expected for any commensurate antiferromagnetic spin structure, provided the interface roughness is sufficiently low.

This interpretation is confirmed after inducing a spin-reorientation transition in the top Ni layer. This can be done by deposition of a thin Co overlayer on top of the Ni layer. Because of the stronger anisotropy of the Co layer compared to Ni, this will turn the easy axis of the top layer into the film plane [310]. Figure 4.14c, d show layer-resolved magnetic domain images of the same sample as in panels (a) and (b) at about the same position after deposition of additional 3 ML Co on top. Now the preferred magnetization direction of both the bottom and top ferromagnetic layers is in the film plane. Panel (c) shows the domain image obtained at the Co  $L_3$  edge, panel (d) the image obtained at the Ni  $L_3$  edge. Note that now both the bottom and top ferromagnetic layers contain Co, so that the information obtained at the Co  $L_3$  absorption edge is a weighted average of both layers. The Ni image (d), however, represents solely the domain image of the top layer. From comparison of images (c) and (d), the domain image of the bottom Co layer can be reconstructed; it is the same as in panel (a), with a dark domain in the upper right part, and a large bright domain everywhere else.

Since the magnetization of the top ferromagnetic layer is now fully in the film plane, the small domains with opposite out-of-plane magnetization component have vanished. The vertical stripes of the in-plane component, related to regions of alternating parallel and antiparallel alignment of top and bottom magnetic layers as a function of FeMn spacer layer thickness, are now clearly recognized. At the position of the domain boundary of the bottom Co layer they consequently reverse contrast. Interestingly these stripes are not straight, but show some kinks in the bottom half of

images (c) and (d). This is the region of the Co wedge. The Co bottom layer thickness increases up to 8 ML, as indicated at the left axis, and then stays constant at a thickness of 8 ML in the region above. The kinks observed in the stripes of alternating coupling across the FeMn layer are periodic as a function of Co thickness, and disappear once the Co thickness is constant. From the period of these kinks, 1 ML, it has to be concluded that their origin is related to the roughness at the Co–FeMn interface. Because of the layer-by-layer growth of Co on Cu(001), the roughness at the surface of the Co layer oscillates as a function of Co thickness with a period of 1 ML: Films of integer atomic layer thickness are smoother than films with a half-filled surface layer. The roughness of the Co–FeMn interface obviously modulates the phase of the coupling oscillation. Interesting is the saw-tooth-like shape of this modulation, which allows to draw additional conclusions about the interface coupling between Co and antiferromagnetic FeMn [338].

From the experiments presented here and other, similar, layer-resolved imaging experiments on trilayers with FeMn as spacer layer and non-collinear easy axes of the two ferromagnetic layers, it could be concluded that ultrathin FeMn films exhibit a three-dimensional non-collinear antiferromagnetic spin structure [337]. While either the component parallel to the film plane or the component perpendicular to it are set by the magnetization of the bottom ferromagnetic layer, the other component is also present, and free to act as if there were no bottom layer. In addition, the absence of linear magnetic dichroism at the Fe  $L_3$  edge points towards a non-collinear spin structure also within the film plane [337]. Neutron diffraction [339, 340] and Mössbauer spectroscopy experiments [341] had already revealed a three-dimensional non-collinear spin structure in bulk FeMn samples. The presented XMCD-PEEM layer-resolved magnetic images could also confirm the presence of such a noncollinear spin structure in ultrathin films [337]. This has important implications on theoretical models of the interaction between ferromagnetic and antiferromagnetic layers, and for understanding the exchange bias effect along different magnetization components [342, 343].

## 4.4 Imaging Antiferromagnetic Materials by X-ray Magnetic Linear Dichroism

Layer-resolved magnetic imaging of heterostructures containing antiferromagnetic layers using XMCD as contrast mechanism can already contribute substantially to the understanding of the magnetic interaction at the AF–FM interface, as could be seen from the example of Sect. 4.3.5. Even more information is obtained if not only the ferromagnetic layers and the induced ferromagnetic moments in the AF layer are imaged, but if linear magnetic dichroism in soft X-ray absorption spectroscopy is used to image also the antiferromagnetic domains. Since the magnetization of antiferromagnets is zero, and there is thus no defined magnetization direction, circular magnetic dichroism can not be used to image antiferromagnetic materials. However,

X-ray magnetic linear dichroism (XMLD), as presented in Sect. 2.7.1, is sensitive on the orientation of the local spin axis, not the spin direction. XMLD may therefore be used to image antiferromagnetic domains with collinear antiferromagnetic spin structure.

# 4.4.1 Magnetic Linear Dichroism as Contrast Mechanism for Layer-Resolved Magnetic Imaging Using PEEM

Magnetic imaging employing XMLD as magnetic contrast mechanism has been mainly used to visualize antiferromagnetic domains in oxidic antiferromagnets, as will be presented in the following sections. However, the XMLD effect, although much weaker than in oxides, is also present in metallic samples. As an introductory example, Fig. 4.15 shows a comparison of layer-resolved magnetic imaging with XMCD and XMLD [224]. The sample was a bilayer consisting of a ferromagnetic Co film and an antiferromagnetic FeMn film. The left images show layer-resolved magnetic domain images obtained with circularly polarized X rays at the same spot of the sample. Here the contrast was obtained, as explained previously, by calculating the asymmetry images between raw images taken with opposite helicity of the circularly polarized X rays. Figure 4.15a shows the magnetic domains in the Co layer, panels (c) and (e) below represent the XMCD signal from the FeMn layer, measured at the Fe and Mn  $L_3$  edges, respectively. It can be seen that the Fe moments follow the magnetic domain pattern of the Co layer, while the Mn moments are oriented oppositely. One has to keep in mind that the XMCD asymmetry represents only the ferromagnetically aligned portion of the respective atomic species.

It has to be mentioned that the crystallographic magnetization directions in the Co/FeMn bilayer change by  $45^{\circ}$  between the upper and lower parts of the images. This is due to the thickness dependence of the antiferromagnetic ordering temperature of FeMn in contact with in-plane-magnetized Co films, which equals room temperature at a thickness of about 10 ML [344]. In the sample shown in Fig. 4.15 the FeMn film was shaped into a micrometer-sized wedge, with thickness increasing from top to bottom, as labeled at the left axes. Consequently, in the upper parts of the images with thicknesses below 10 ML the FeMn layer is paramagnetic at room temperature, while in the lower parts it is antiferromagnetic. The interaction with the Co layer forces its magnetization direction from  $\langle 110 \rangle$  to  $\langle 100 \rangle$  in the bottom part [299].

Figure 4.15b shows an image of the XMLD signal of the Co layer, measured for constant linear polarization of the X rays as the asymmetry between images taken with different photon energy close to the Co  $L_3$  edge [224]. Because of the higher symmetry of the set up using linear polarization, domains with opposite magnetization direction can not be distinguished any more. Comparing panels (a) and (b) one can see very nicely how domains that appear black and white in the lower part of Fig. 4.15a exhibit the same gray contrast in Fig. 4.15b.

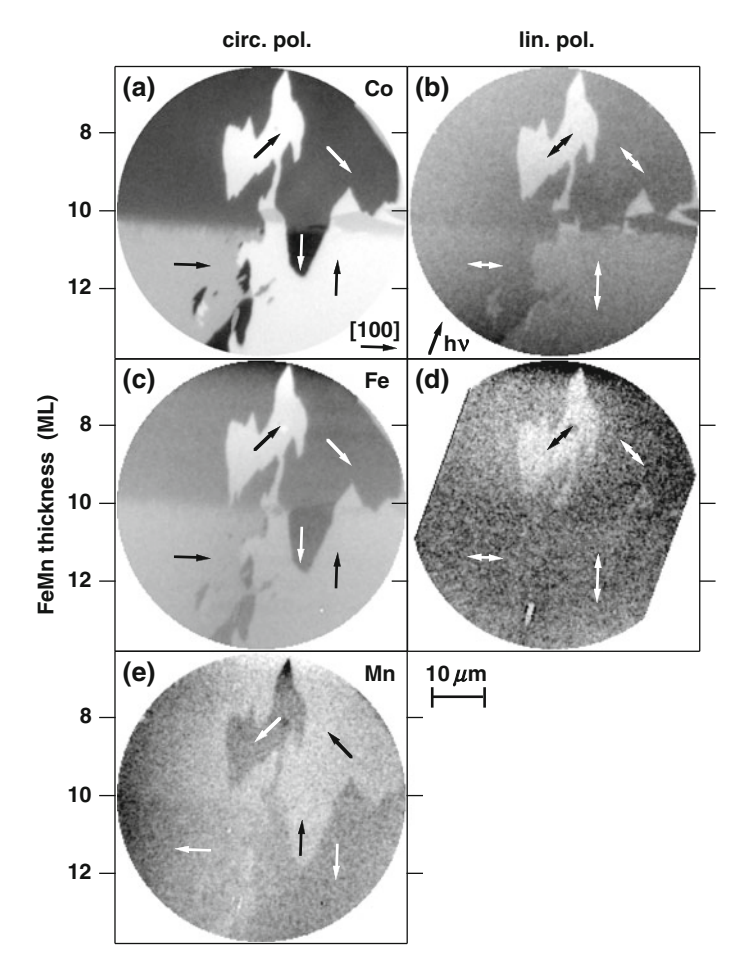
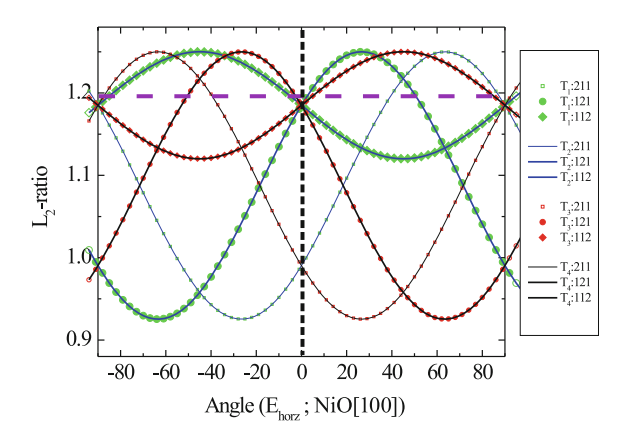


Fig. 4.15 Magnetic domain images of a FeMn/Co/Cu(001) structure obtained at the  $L_3$  edges of **a**, **b** Co, **c**, **d** Fe, and **e** Mn. The thickness of the FeMn layer, increasing from the top to the bottom of each image, is shown on the vertical axis, the thickness of the Co layer was 12 ML. Crystallographic orientation of the Cu substrate and azimuthal angle of incidence are shown in panels **a** and **b**, respectively. The *left* and *right columns* represent the XMCD and XMLD contrast, respectively. *Arrows* indicate the domain magnetization. From [224]

As mentioned in Sect. 4.3.5, the spin structure in FeMn films is non-collinear, therefore no XMLD signal can be detected from the antiferromagnetically ordered part of the film. However, the small number of ferromagnetically aligned Fe moments that lead to the domain image shown in Fig. 4.15c, also gives rise to a magnetic linear dichroism. It can indeed be detected by XMLD-PEEM, as shown in Fig. 4.15d, if sufficient signal-to-noise statistics is accumulated.

The images of Fig. 4.15 are presented on quite different grayscale ranges: While the full image contrast between saturated white and saturated black is 20 % in the Co

Fig. 4.16 The expected XMLD intensities for the twelve bulk-terminated NiO S-domains depending on the azimuthal angle  $\phi$  for s-polarized X rays. The curves show a cos<sup>2</sup> dependence with different amplitudes and vertical as well as horizontal offsets. The broken horizontal line indicates the experimentally determined XMLD intensity at angle  $\phi = 0$ , as indicated by the vertical line. From [347]



XMCD image (a), it has been amplified to 8 % for the Fe (c) and 1.5 % for Mn (e) XMCD images, and amounts to 3 % in the Co XMLD image (b), and only 0.7 % in the Fe XMLD image (d). The total acquisition time for image (d) was about 170 min, during which the relative position between PEEM and sample was sufficiently stable.

The real power of combining XMCD and XMLD domain imaging in layered structures lies in the investigation of layered samples containing antiferromagnetic layers with collinear spin structure. This will be discussed in the following for a number of oxidic antiferromagnetic samples.

# 4.4.2 Exchange Coupling at the Interface of NiO and a Ferromagnetic Metal

One of the first antiferromagnetic materials that were studied by XMLD and by XMLD-PEEM are NiO single crystals and thin layers. Layer-resolved magnetic domain imaging has been used to investigate the interaction between AF NiO and a ferromagnet. PEEM studies were performed on thin ferromagnetic layers deposited onto NiO single crystal surfaces. To be able to distinguish between the two layers, one makes again use of the chemical selectivity of the signal which is inherent in the imaging by exciting electrons from core levels. The properties of Co layers on NiO were investigated in a number of studies [345–348].

Figure 4.17 shows domain images for 8 ML Co deposited on a freshly cleaved NiO(100) surface. The AF domains of the NiO substrate are revealed as shown above by exploiting the linear dichroism occurring at the Ni  $L_2$  edge, and presented in the left column. The images show the well-known stripes running parallel to the [010] direction in the surface. Using s-polarized light for excitation, only the in-plane components of the magnetic moment are imaged. Switching to circularly polarized light and tuning to the Co  $L_3$  edge, the ferromagnetic domains in the Co overlayer are exposed, as shown in the right column. At first sight the domain pattern

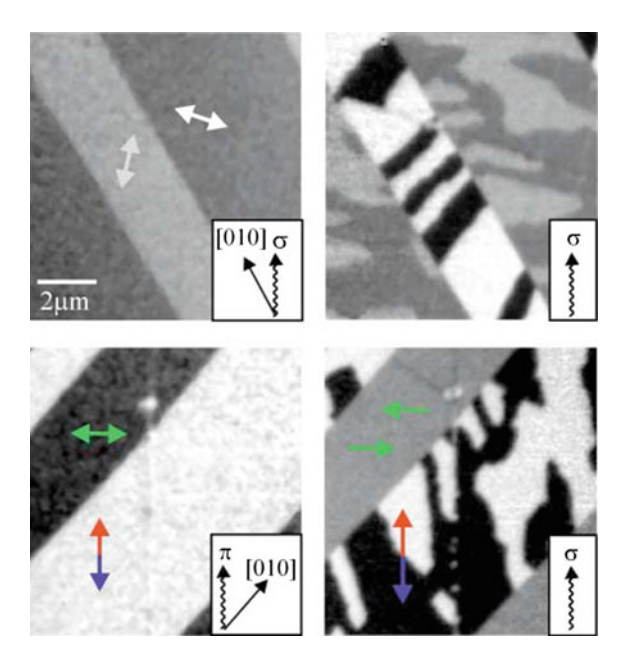


**Fig. 4.17** Comparison of antiferromagnetic (*left column*) and ferromagnetic (*right column*) domain patterns for 8 ML of Co on NiO(001) and two different azimuthal geometries. *Arrows* and *wavy lines* indicate the directions of the magnetic axes and photon wave vectors, respectively. Linear polarization is labeled *p*, circular and plane polarization *s*. Each NiO domain has two corresponding Co domains with antiparallel spin alignment. *Bottom panel* The sample is rotated so that the polarization vector is along [110]. The contrast from one subgroup of ferromagnetic domains vanishes. Reprinted with permission from [345]. Copyright (2001) by the American Physical Society

appears much more complicated, as there are more contrast levels than in the NiO images, and also the domain shapes appear more complicated. However, the domain topology is related to the one of the underlying NiO, as some domain walls in the Co layer coincide with walls in the NiO. One recognizes in the bottom images that in the NiO domains appearing with bright contrast, the Co shows bright and dark regions. On the other hand, for the NiO domains appearing with dark contrast, a uniform intermediate contrast level is observed for Co. The high and low contrast level in the Co layer arises from ferromagnetic domains the magnetization direction of which is collinear, either (nearly) parallel or antiparallel to the light helicity. The uniform contrast in the remaining regions shows that the magnetization direction in these domains is perpendicular to the light helicity. This is confirmed by imaging under a different azimuthal orientation of the sample, shown in the top images, where one finds that also those regions which appear uniform in the middle image are composed of oppositely magnetized domains. The experiment reveals a uniaxial anisotropy whose direction is governed by the underlying antiferromagnetic order.

The next step is to derive the relative orientation of the magnetic moments in the FM and AF layers. The circular dichroism is maximum if the magnetization is either

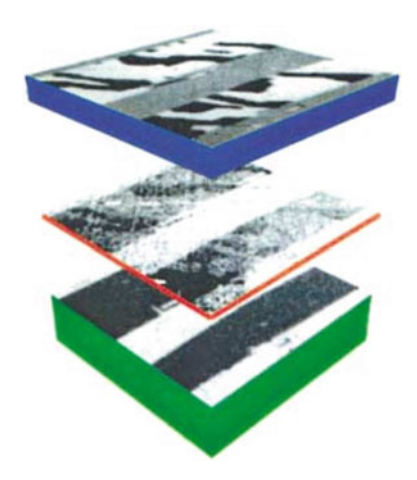


**Fig. 4.18** Circular (XMCD) and linear (XMLD) X-ray dichroism images of a cleaved NiO(100) sample covered by 8 ML of Co as grown. The images on the *top* and *middle slices* show FM XMCD images recorded with handed circular polarization at the Co (top) and Ni (middle)  $L_3$  absorption edges. The *bottom slice* shows an AFM XMLD image of NiO recorded with linear polarization at the Ni  $L_2$  edge. Reprinted with permission from [346]. Copyright (2001) by the American Physical Society

parallel or antiparallel to the light helicity. This allows determination of the direction of the magnetization in the ferromagnetic layer. The direction of the magnetic moments in the antiferromagnet had originally been inferred from a comparison of the experimental spectra to theoretical modelling [214]. From atomic multiplet calculations performed for  $\langle 100 \rangle$  spin orientation it followed that the lower energy feature of the Ni  $L_2$  absorption edge is stronger when the electric field of the linearly polarized radiation is perpendicular to the magnetic moments. This led to the conclusion that the moments in the bright domains are parallel to the direction of light incidence, as indicated by arrows, and that therefore the moments in the ferromagnetic and antiferromagnetic layers are collinear. As already mentioned in Sect. 2.7.1, it had been recognized later that XMLD strongly depends on the crystallographic orientation of the spins, and that for a  $\langle 110 \rangle$  spin orientation the dichroism at the Ni  $L_2$  edge even exhibits opposite sign compared to (100) orientation [221]. Reinterpreting the results of [345], the Ni spins therefore are not, as depicted in Fig. 4.17, collinear to the Co ones, but perpendicular. This revised finding is less surprising than the original interpretation, since for a compensated AF interface one may expect spin-flop coupling, i.e., the moments in the AF and the FM layer should form an angle close to 90° [349].

To address the issue of exchange bias, one would like to know whether the antiferromagnet develops uncompensated magnetic moments at the interface to the ferromagnet. If there were such uncompensated moments the orientation of which is linked to that of the ferromagnet, they should be detectable by circular magnetic dichroism at the Ni edge. The result of such an experiment is shown in Fig. 4.18.

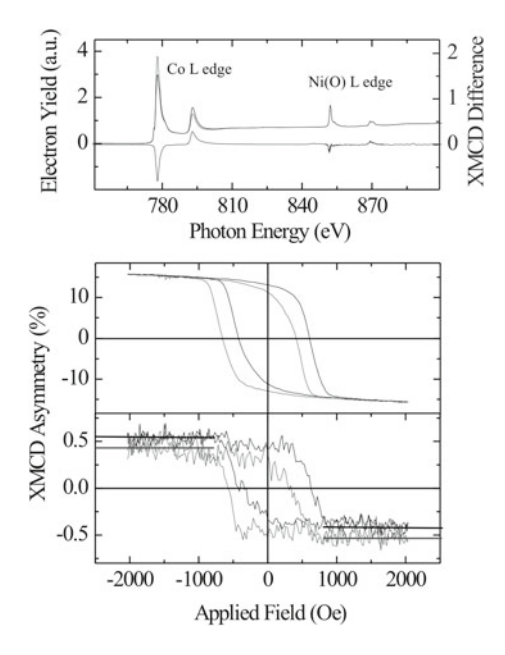


Fig. 4.19 Top XAS and XMCD spectra of Co and NiO. The XMCD difference shows the same behavior for both species (negative values at the  $L_3$  and positive values at the  $L_2$  edge), indicating the parallel alignment of Co and Ni spins. Bottom Hysteresis loops of Co and Ni acquired in two different geometries. The saturation magnetizations of the two Co loops are identical, while the Ni loops exhibit a small vertical loop shift, originating from pinned interfacial spins. Horizontal lines serve as a guide to the eye. The horizontal symmetry of the two loops is identical. Co and Ni loops show a distinct horizontal loop shift and coercivity which is identical for both species, indicating again the parallel interfacial exchange coupling between "free" interfacial moments and the ferromagnetic Co layer. From [347]

One indeed observes a small contrast by using circularly polarized light tuned to the Ni edge [346]. This contrast shows a domain pattern identical to that of the ferromagnetic Co domains. The magnitude of the dichroic signal is of course small, since uncompensated moments may occur only at the interface. From the line shapes of the Ni and Co absorption edges one can see that there is some intermixing at the interface, which results in partially reduced NiO and partially oxidized Co. The partial reduction of NiO at the interface is the cause for the occurrence of uncompensated spins. A detailed characterization of the chemical state of the uncompensated spins may be derived from the line shape of the circular dichroism spectrum. As far as the statistical quality of the data allows, one can conclude that the majority of the Ni moments is in fact in a state similar to the metallic one, however, because of the small ferromagnetic signal one cannot rule out oxide species completely. From an analysis of the non-dichroic line shape details one finds that for the Co/NiO system there is an intermixed region with a thickness of about two layers at the interface.

To which extent these spins are related to exchange bias may be determined from measurements of element-specific hysteresis loops. If the ferromagnetic layer was

affected by the interaction with the antiferromagnetic layer across the interlayer, its hysteresis loop should be shifted horizontally, parallel to the external field axis. As shown in Fig. 4.19, the Co loop of a field-cooled Co/NiO sandwich sample shows such a shift, amounting to about 120 Oe [347]. In addition, the coercive field is rather large, about 500 Oe. If in such a sample some of the spins of the antiferromagnet are pinned due to the interaction with the ferromagnet, they always point in the same direction, irrespective of the external field. This should manifest itself in a shift of the hysteresis loop vertically, i.e., like a different saturation magnetization for up and down. The Ni loop is much more noisy than the Co one since only the uncompensated spins at the interlayer contribute. Nevertheless, the loop exhibits a horizontal shift in the same direction as the Co loop. Furthermore, the saturation magnetizations show a small difference between the two magnetization directions. The total range of the hysteresis loop is one, and the difference is about 0.1, i.e., one tenth of the uncompensated spins at the interface are pinned by the coupling to the underlying antiferromagnetic layer. The coercive field is larger for magnetization in the direction in which the saturation is smaller. This shows that there is a ferromagnetic coupling between the pinned uncompensated interface spins of the antiferromagnet and the ferromagnetic Co film.

The XMCD spectrum shows dichroism of the same sign at the Co and Ni edges. This is consistent with the previously determined collinear coupling. Furthermore, it shows that the coupling between the Co moments and the uncompensated Ni moments is ferromagnetic.

Further experiments of this type have been carried out on other FM/AF systems [348]. On the whole, the results are analogous to those presented here. However, with metallic antiferromagnets like IrMn, imaging of the antiferromagnetic domains by linear magnetic dichroism is not possible due to the small contrast.

#### 4.4.3 CoO/NiO Heterostructures

Measurements on CoO have been attempted, however, because of the Néel temperature of 291 K, one has to cool the sample to ensure a sufficiently high degree of magnetic order. Since intrinsically the oxides are semiconductors or insulators, this leads to a strongly reduced conductivity, such that imaging by total electron yield is not possible. To overcome this problem, ultra-thin films grown on NiO may be used as samples. From investigations of NiO/CoO super-lattices by neutron scattering it is known that for short-period superlattices the Néel temperature is the average of the Néel temperatures of the constituent oxides, weighted by the content of the respective oxides [350]. Therefore, one may expect that an ultra-thin film of CoO on NiO will show the same ordering temperature as the substrate. This behavior is also found for ultra-thin transition-metal films on ferromagnetic substrates. CoO can be prepared by deposition of Co in an atmosphere of oxygen. Figure 4.20 shows the absorption spectrum of such a film, which is in agreement with that of bulk CoO. By tuning to the Ni edge, the antiferromagnetic domains in the underlying NiO are imaged. Now

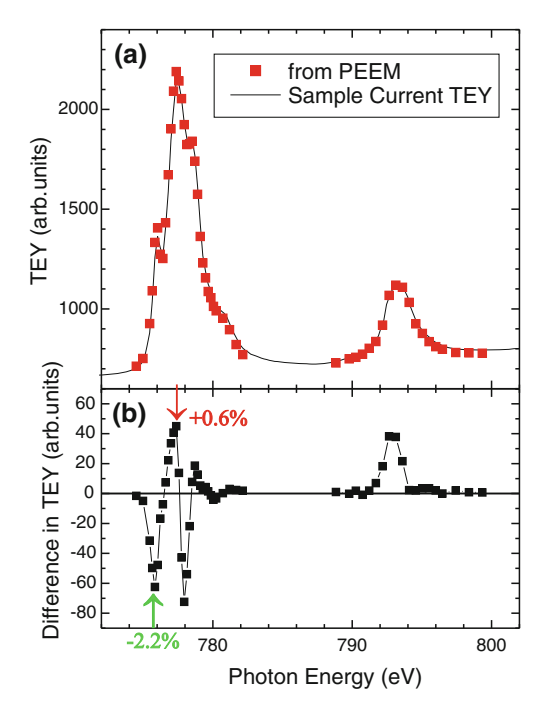


**Fig. 4.20** XAS spectrum (a) and magnetic linear dichroism (b) of CoO grown as ultrathin film on NiO. *Squares* show the spectrum derived from PEEM images, the *line* is obtained from a total electron yield measurement. From [215]

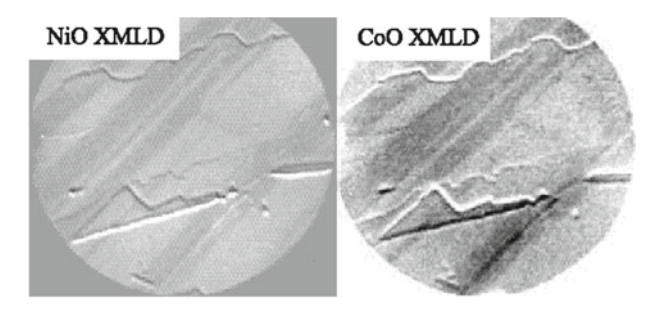


Fig. 4.21 PEEM images of the NiO/CoO surface antiferomagnetic domain structure, obtained by X-ray magnetic linear dichroism. Left Image obtained at the Ni  $L_2$  edge, right image obtained at the Co  $L_3$  edge. From [347]

Co  $L_{2,3}$  absorption spectra were taken from regions which belong to different NiO domains. These spectra are also found to differ, as shown by the dichroism spectrum in the lower portion of Fig. 4.20. This spectrum is in good agreement with other experimental spectra as well as with a calculated spectrum for CoO.

In the next step, images were acquired with the photon energy tuned to the different features in the dichroism spectrum. Figure 4.21 shows on the left the antiferromagnetic domains of the NiO substrate, acquired in the same way as described before. The right panel of Fig. 4.21 shows the image obtained by calculating the asymmetry of the local intensities of the Co  $L_{2.3}$  XMLD spectrum in a pointwise fashion. It shows exactly the same pattern as observed for the NiO substrate. Therefore the pattern can be interpreted in terms of antiferromagnetic domains in the CoO thin film. This shows that in the CoO film the Néel temperature is significantly higher than in bulk CoO, as expected from the above argument. One may expect that for a film of 8 ML thickness the Néel temperature will be that of the substrate. With increasing thickness the Néel temperature of bulk CoO should prevail. An interesting issue is the type of magnetic order present at the surface, and to what extent it is modified by the substrate. As will be shown below, the surface magnetic order of NiO is influenced by a ferromagnetic metal deposited on the surface, therefore it is likely that there will also be a mutual influence between the NiO substrate and the CoO film. However, to date no experiments have been carried out to address these issues.

#### 4.4.4 Co/LaFeO<sub>3</sub> Heterostructures

Another system in which layer-resolved magnetic imaging has revealed important insight into the interface interaction between antiferromagnetic and ferromagnetic layers is Co layers on LaFeO<sub>3</sub> films. The latter can be grown epitaxially on SrTiO<sub>3</sub>(001) single crystals, because the lattice constant of SrTiO<sub>3</sub>(001) matches both, half the LaFeO<sub>3</sub> unit cell along the c direction as well as along the a-b diagonal with only about 0.5 % mismatch [351]. The antiferromagnetic spin axis in thin films deviates from the one of bulk LaFeO<sub>3</sub>. In LaFeO<sub>3</sub>/SrTiO<sub>3</sub>(001) it was found to be inclined with respect to the film plane, with its in-plane projection pointing along the c direction [351].

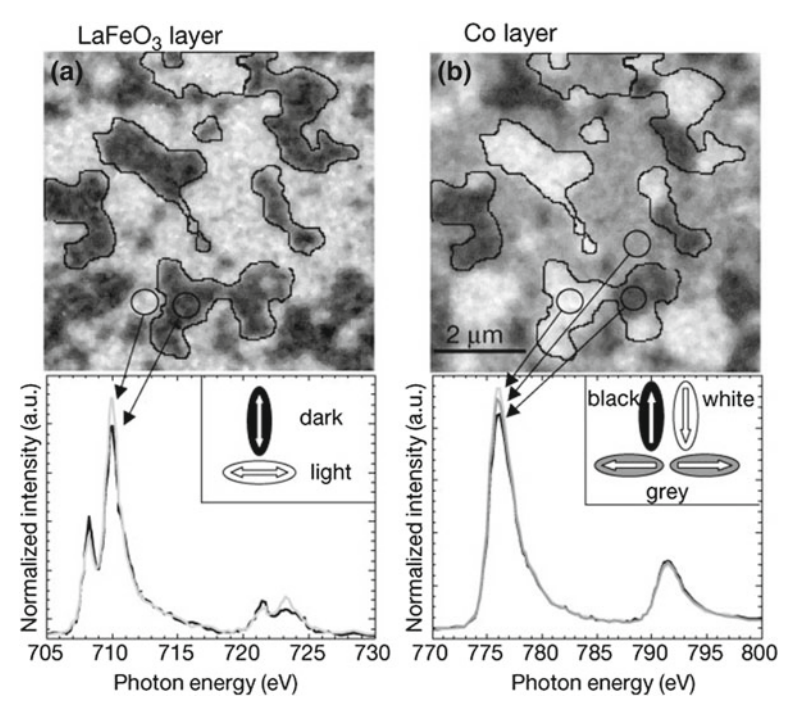
LaFeO<sub>3</sub>, like NiO, is an oxidic antiferromagnet, and exhibits a large XMLD effect at the Fe  $L_{2,3}$  edges. Its use for magnetic imaging [230] yielded antiferromagnetic domain patterns that reproduce the crystal orientation of the twinned orientations in which LaFeO<sub>3</sub> can grow on the fourfold symmetric SrTiO<sub>3</sub>(001) substrate.

Figure 4.22 shows layer-resolved magnetic domain images of a 1.2 nm ferromagnetic Co layer on top of a 40 nm LaFeO<sub>3</sub> film [352]. The left image shows the contrast obtained at the Fe  $L_3$  edge using linearly polarized X rays, and thus represents the local directions of spin axes in the buried antiferromagnetic LaFeO<sub>3</sub> film. Bright and dark contrast corresponds to high and low intensity at the second peak of the crystal field-split Fe  $L_3$  absorption maximum, as shown in the local absorption spectra below the image. The X-ray incidence direction is along the vertical of Fig. 4.22. The electric field vector E of the linearly polarized X rays of panel (a) is parallel to the surface, and thus horizontal with respect to Fig. 4.22. Comparison to calculations and experiments on  $\alpha$ -Fe<sub>2</sub>O<sub>3</sub> [209] allows to assign higher intensity at that peak to a more parallel spin direction with respect to the X-ray electric field

vector, i.e., the spins in the brighter areas are pointing along right-left directions, while it is up-down in the darker areas. This is sketched in the inset of the bottom panel of Fig. 4.22a.

Tuning the X-ray photon energy to the maximum of the Co  $L_3$  absorption maximum, and using circularly polarized excitation results in the magnetic domain image of the ferromagnetic Co layer at the very same position. This is reproduced in Fig. 4.22b. Here, three different levels of grayscale contrast can be recognized. They can be attributed to four different magnetization directions of domains, as shown below, two of which lead to the same intermediate gray contrast.

The mutual orientation of Fe spins in the antiferromagnetic LaFeO<sub>3</sub> layer and the Co spins in the ferromagnetic Co layer can be directly extracted by comparing images (a) and (b) of Fig. 4.22. Black lines help to overlap identical areas. It is seen that in this system the preferred orientation of Co magnetization is along the spin axis of the antiferromagnet, i.e., along its c axis. Dark areas in panel (a) appear either black or white in panel (b); they correspond to a spin direction parallel to the light



**Fig. 4.22** Layer-resolved magnetic domain images and local X-ray absorption spectra from the antiferromagnetic and ferromagnetic layers of 1.2 nm Co/40 nm LaFeO<sub>3</sub>/SrTiO<sub>3</sub>(001). **a** Fe *L* edge XMLD image, showing the antiferromagnetic domains in the LaFeO<sub>3</sub> layer; **b** Co *L* edge XMCD image, showing the ferromagnetic domains in the Co layer. The in-plane orientations of the antiferromagnetic axis and ferromagnetic spins are indicated below the images. The spectra shown underneath were recorded in the indicated areas and illustrate the origin of the intensity contrast. Reprinted from Ref. [352] by permission from Macmillan Publishers Ltd, Copyright (2000)

incidence azimuth. Medium gray contrast is found in panel (b) at the positions of bright areas of panel (a). Both correspond to a spin axis along the horizontal of the images.

Important information about the coupling between ferromagnetic and antiferromagnetic spins at the interface is deduced from such layer-resolved images. The images shown in Fig. 4.22 are from as-grown samples that had not been subject to external magnetic fields before imaging. Additional insight into the magnetic coupling mechanism can be obtained if the sample's reaction on magnetic fields is monitored by layer-resolved magnetic domain imaging. In PEEM it is not possible to record images under applied magnetic fields, but images of the remanent state of the sample after application of magnetic fields of different directions can be acquired. An example is shown in Fig. 4.23. It shows layer-resolved magnetic domain images of the same Co/LaFeO<sub>3</sub> sample as Fig. 4.22. The top four images show the ferromagnetic domains in the Co layer after application of an external magnetic field along the [100] direction of strength as labeled in the images. Since the detection direction was also along this axis, bright and dark areas correspond to domains of magnetization direction in negative and positive field direction, respectively, while gray domains have their magnetization perpendicular to the field. The bottom right panel shows the antiferromagnetic domains of the underlying LaFeO<sub>3</sub> layer, imaged with linearly polarized photons at the Fe  $L_3$  edge.

It is seen that by the external field mainly white domains of the Co are switched into black ones, while the gray domains remain nearly unaffected. Following the evolution of the contrast at specific positions as a function of external magnetic field allows to extract local remanent magnetization curves. Two of them are shown in the bottom left panel for the positions labeled "1" and "2". These two loops are shifted to the right and left, respectively, with respect to zero field. This means that the Co layer is locally exchange biased by the antiferromagnetic LaFeO<sub>3</sub> layer, with opposite sign at the two positions.

The authors of [353] performed a statistical analysis of more than thousand Co domains and found a correlation between the domain size and the statistical distribution of the local exchange bias field. Smaller domains had a wider distribution of bias fields than larger domains, such that the highest exchange bias fields were observed in small domains. This finding allows to verify theoretical predictions about the origin of the exchange bias effect; in particular it is in agreement with the random field model put forward by Malozemoff [354].

# **4.5 Time- and Layer-Resolved Magnetic Imaging** by XMCD-PEEM

The pulsed nature of synchrotron radiation allows for the straightforward extension of layer-resolved magnetic microscopy with synchrotron radiation towards time-resolved pump-probe experiments. Typical pulse widths of the X-ray pulses in

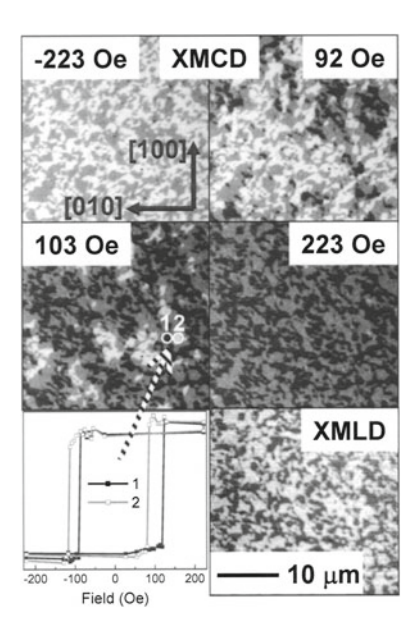


**Fig. 4.23** Layer-resolved magnetic domain images and local magnetization loops from the antiferromagnetic and ferromagnetic layers of 1.2 nm Co/40 nm LaFeO<sub>3</sub>/SrTiO<sub>3</sub>(001). *Top* and *middle row* Co XMCD domain images in remanence, sensitive to the [100] magnetization direction, after applying fields between  $\pm 223$  Oe along [100]. *Bottom right*: LaFeO<sub>3</sub> XMLD image using linear polarization along [010]. *Bottom left* Local remanent hysteresis loops of two domains labeled "1" and "2" and marked by circles in one of the domain images, showing oppositely oriented local exchange bias fields. Reprinted with permission from [353]. Copyright [2004], AIP Publishing LLC

standard operation of a synchrotron light source are around 50–100 ps. These pulses act like flashes to acquire snapshots of the sample at a certain time, for example, after the excitation by a magnetic field pulse. Since the intensity of a single X-ray pulse is by far not enough to obtain a magnetic domain image, such an experiment has to be performed repeatedly in a stroboscopic way, in which the sample is periodically excited, and periodic snapshots of the magnetic domain configuration are acquired at certain fixed phase correlations between the excitation (pump) and the X-ray pulses (probe). For this, the excitation to the sample has to be synchronized to the X-ray pulses from the synchrotron light source. First time-resolved pump–probe XMCD experiments, still without lateral resolution, have been presented in 2001 by Bonfim et al. [355]. In these experiments, fluorescence yield detection was used to extract the layer-resolved stroboscopic magnetic response of Co/Al<sub>2</sub>O<sub>3</sub>/NiFe trilayers on magnetic field pulses that were periodically applied by a microcoil close to the sample.

Vogel et al. combined two years later the same method with magnetic imaging using a PEEM in order to obtain in addition lateral resolution [357]. Figure 4.24 shows the schematic set-up of such an experiment. The objective lens of the PEEM is depicted at the top. Below, a 12.5  $\mu m$  thick Cu foil isolated by capton sheets is

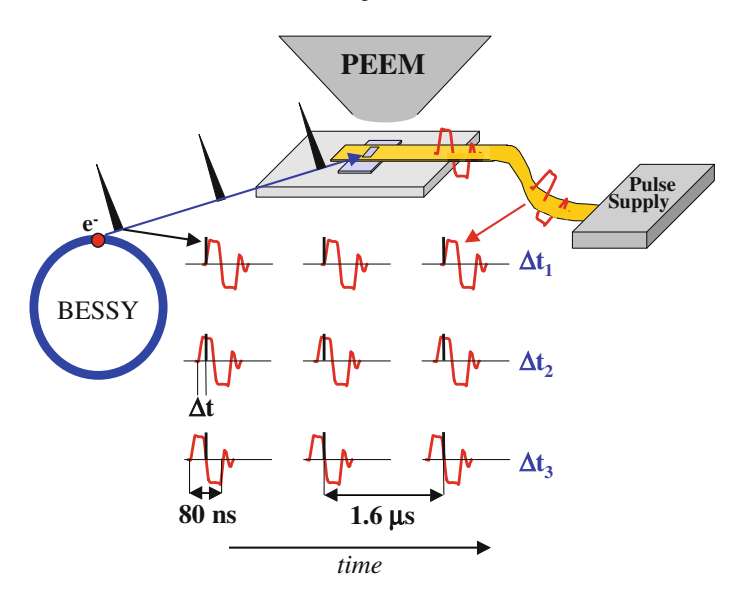


**Fig. 4.24** Principle of a time-resolved pump–probe experiment for layer-resolved magnetic domain imaging by XMCD-PEEM. Current pulses from a pulse generator, synchronized to the synchrotron X-ray pulses, create field pulses at the sample position in a microcoil. Images are taken for various time delays  $\Delta t$  between field pulses (pump) and the exposing synchrotron X-ray pulses (probe). From [356]

wrapped once around the sample. A window of  $2 \times 3 \text{ mm}^2$  is cut out from the top layer of the Cu foil in order to expose the sample surface to the X-ray pulses from the synchrotron source. A pulse power supply is triggered by the clock signal from the electron storage ring, and sends periodic current pulses every 1.6 µs through the Cu foil. In the example sketched in Fig. 4.24 these current pulses exhibit a bipolar temporal shape of 80 ns overall length, i.e., they consist of a positive followed by a negative current pulse. This has the advantage of leaving the sample periodically in the same magnetic state, without the need for an external restoring bias field. The three rows of graphs at the bottom of Fig. 4.24 symbolize the experiment performed for three different phase relations between the current or field pulses (bipolar 80 ns wide curves) and the X-ray pulses (vertical bars). They represent the periodic field or X-ray intensity plotted as a function of time. The phase relation between field and X-ray pulses can be characterized by the delay time  $\Delta t$  between the start of the field pulse and the synchrotron radiation pulse. Repeating the experiment for different delay times allows to image the response of the sample to the field at a certain time during the pulses. The three rows of graphs correspond to three different values of  $\Delta t$ . In a typical experiment, about  $10^8$  pulses are accumulated for an image. Since the repetition frequency of X-ray pulses at BESSY in the single bunch mode of operation is 800 ns, the electrons emitted by every second X-ray pulse, which does not correspond to a magnetic field pulse, has to be blanked out in order to match

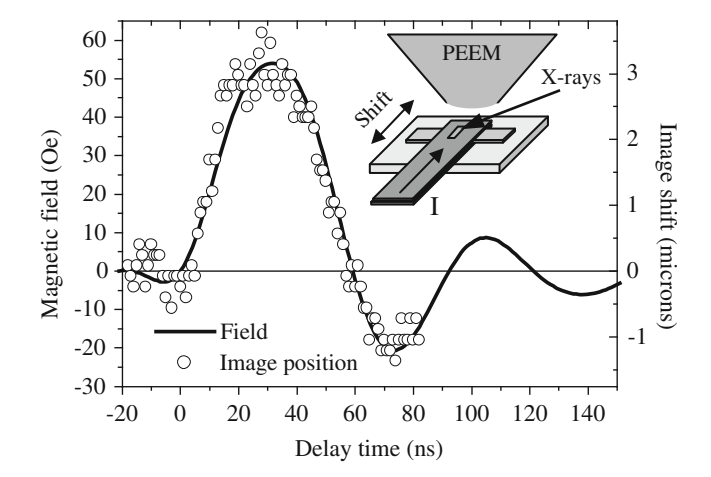


**Fig. 4.25** The *inset* shows a sketch of the experimental set-up in which a microcoil is used to apply short magnetic field pulses to a sample in front of the objective lens of a PEEM. The graph shows as a continuous line the temporal shape of the current pulse through the microcoil, converted into magnetic field strength at the sample position (*left axis*), the symbols give the lateral apparent displacement of the PEEM image exerted by the Lorentz force on the electrons leaving the sample surface (*right axis*). Reprinted with permission from [358]. Copyright [2004], AIP Publishing LLC

the pulse separation of 1.6  $\mu$ s. This was achieved by applying a periodic negative voltage to a retarding grid electron energy analyzer in the PEEM [357].

It is important to know the exact shape of the applied field pulse. This can be obtained by monitoring the current as a function of time by a fast oscilloscope. However, depending on the impedance of coil and cable, the current measured at the oscilloscope may not follow exactly the current at the position of the sample. Another possibility is to monitor the influence of the magnetic field on the trajectories of the emitted secondary electrons by the Lorentz force. This is recognized as a shift of the image of the sample. Figure 4.25 shows as open circles the image shift, evaluated as the position of a certain characteristic detail of the sample in stroboscopic images, as a function of the delay time  $\Delta t$  between current pulse and X-ray pulse (right ordinate). The continuous line represents the oscilloscope trace of the current of the pulse power supply, given in units of the magnetic field at the sample position (left ordinate). A current of about 7.5 A is necessary to create a field of 50 Oe. It is seen that in this example with moderate rise times of the field pulses both graphs correspond quite well to each other. A field of 50 Oe leads to an image displacement of about 3  $\mu$ m.

Using this method for studying the magnetization reversal dynamics in extended trilayers, in which two ferromagnetic layers are separated by a nonmagnetic spacer layer, it could be shown that the domain wall energy, that is the energy that is needed to create new segments of domain borders, is playing an important role for the speed of domain wall motion if the domains are small [359]. It may even lead to a significant delay in the initial expansion of newly nucleated reversed domains [360].

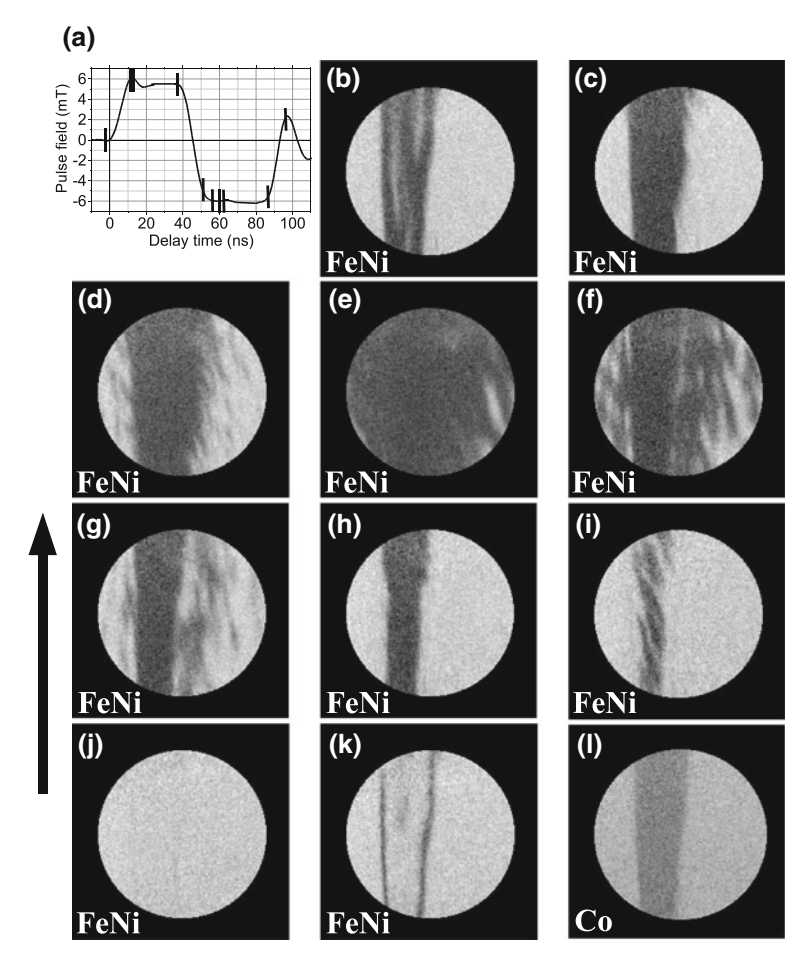


**Fig. 4.26** Time- and layer-resolved XMCD-PEEM images of the magnetization state of the NiFe (b–k) and Co layers (l) of a 4 nm Ni $_{80}$ Fe $_{20}$ /2.6 nm Al $_{2}$ O $_{3}$ /7 nm Co/3 nm CoO/Si(111) sample. The field of view in these images is about 100  $\mu$ m and the spatial resolution 1  $\mu$ m. The projection of the X-ray incidence direction on the sample surface is pointing up in the images (parallel to the *arrow*) and is parallel (antiparallel) to the direction of the field for positive (negative) pulses. The magnetization direction is in the plane of the layers and points up (parallel to the *arrow*) for black domains, and down for white domains. The NiFe images were taken for delays between photon and magnetic pulses of -3, 11, 13, 37, 51, 56, 60, 62, 87, and 97 ns, as indicated in (a). The Co image was taken for a delay of 60 ns. From [322]

Another example of time- and layer-resolved magnetic imaging by XMCD-PEEM is presented in Fig. 4.26. It shows stroboscopic domain images of a trilayer consisting of 4 nm Ni<sub>80</sub>Fe<sub>20</sub>, 2.6 nm Al<sub>2</sub>O<sub>3</sub>, and 7 nm Co on top of 3 nm CoO/Si(111). The nonmagnetic Al<sub>2</sub>O<sub>3</sub> layer separates the ferromagnetic NiFe and Co layers. Such structures are used, for example, in devices utilizing the tunnel magnetoresistance effect (cf. Fig. 1.1b). The temporal shape of the magnetic field pulses is plotted in

Fig. 4.26a as a function of time. It consists of a positive and a negative plateau of about 6 mT field amplitude and lengths of 40 ns each, with rise and fall times of about 6 ns [322]. At the end of the negative pulse, at about 100 ns delay time, a small positive overshoot followed by some ringing terminates the pulse sequence.

Figure 4.26b–k show layer-resolved magnetic domain images of the Ni<sub>80</sub>Fe<sub>20</sub> (permalloy) layer at the delay times listed in the figure caption and marked in panel (a) by small vertical bars. White and black regions correspond to domains with an inplane magnetization direction pointing parallel and anti-parallel to the black arrow, respectively. Figure 4.26l shows a layer-resolved image of the domains in the Co layer at a delay time of 60 ns. The amplitude of the field pulses was chosen such that it affected the magnetization of the magnetically softer permalloy layer, but had no effect on the magnetically harder Co layer, which was in addition coupled to the underlying CoO layer [322].

Figure 4.26b represents the domain pattern in the NiFe layer before the pulse. The domain pattern resembles the one of the Co layer (Fig. 4.261). This is attributed to the rather strong magnetostatic roughness-induced coupling that tends to align the magnetization directions in the two magnetic layers. Some residual white domains at places where the Co layer is magnetized in the black direction are probably created during the ringing of the previous magnetic field pulse. When the field increases into the positive direction, first a propagation of the domain walls in the permalloy layer takes place (Fig. 4.26c). At the maximum of the positive pulse also some newly nucleated reversed domains become visible (Fig. 4.26d). At the end of the positive pulse, the permalloy layer is almost saturated except for some remaining white domains at the right and left bottom (panel (e)). When the field is reversed, new white domains appear during the rising flank of the pulse (Fig. 4.26f). These domains are located in the region where the Co layer has a white domain, but also show up with a quite high probability at the positions of the domain boundaries, the domain walls. At the end of the negative pulse (Fig. 4.26g), the permalloy layer seems to be completely saturated in the white direction. Closer inspection actually shows that faint gray lines are still present at the position where domain walls are present in the Co layer. These lines grow wider during the positive overshoot at 97 ns delay time (Fig. 4.26k). From this series of images it is seen that the probability for domain nucleation during the fast magnetization reversal of the Ni<sub>80</sub>Fe<sub>20</sub> layer of a Ni<sub>80</sub>Fe<sub>20</sub>/Al<sub>2</sub>O<sub>3</sub>/Co tunnel junction is enhanced at the positions of domain walls in the underlying Co layer. These measurements reveal thus a local magnetic coupling between the two ferromagnetic layers at domain walls. Micromagnetic simulations confirmed this coupling, which is due to local magnetic stray fields emanating from domain walls [322]. A similar local magnetic coupling mediated by the stray fields of domain walls has been already presented in Sect. 4.3.2. During the magnetization reversal, this local coupling to the domain walls acts as an additional effective field transverse to the field from the current pulses, and induces locally a small transverse magnetization component in the soft permalloy layer. These regions, in which the magnetization is not exactly opposite to the external field, experience a higher torque and are hence subject to a faster switching and thus to a faster nucleation of reversed domains shortly after the external field is applied. It should be noted that the observation of the dynamic effect of such a local coupling mechanism requires all three features of time-resolved imaging by XMCD-PEEM, namely the lateral resolution, the layer sensitivity, and the time resolution.

The magnetic field at the sample position in the example described above is basically determined by the current flow in the bottom turn of the microcoil. The geometry is thus similar to that of a so-called strip line, in which a current is run through a flat strip of conducting material on top of which the samples resides. For a given current the magnetic field decreases with increasing distance from the strip. The minimum distance between the magnetic film at the sample surface and the bottom part of the microcoil is limited by the thickness of the substrate. Because of that relatively large distance high currents are needed to generate sizeable fields, in the above example 7.5 A for 5 mT. This limits the accessible pulse widths or rise times to a few nanoseconds. Pulse power supplies for such currents are based on CMOS technology, which at present does not allow the creation of faster pulses in the current regime of ten amperes. At lower currents, however, there are several ways of creating faster pulses such as power supplies based on burst diodes or photoconductive switches. In order to use such faster pulses for time-resolved magnetic imaging, one has to give up on the advantage of inserting standard samples into the time-resolved experimental set-up, as it is possible with the microcoil approach. This is because larger fields at lower currents can only be achieved if the sample surface is approached to the strip line. In the limit of close to zero distance of the sample to the strip line, the induced field H can be approximated by the current I through the strip line divided by two times the width w of the strip line:

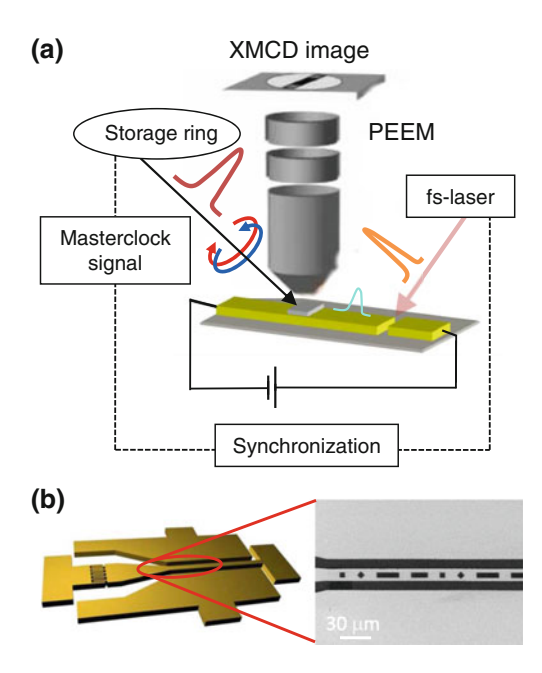
$$H \approx \frac{I}{2w}.\tag{4.14}$$

Sufficiently close contact between sample and strip line, however, can only be achieved if the sample is lithographically defined on top of the strip line.

The know-how for the use of such set-ups comes from time-resolved experiments using the magneto-optical Kerr effect, or magnetic imaging by Kerr microscopy. In those cases the laser probe pulse in the visible light range can be as short as a few hundred femtoseconds. Transfer of such experiments to XMCD-PEEM imaging has been already successfully demonstrated. To revert to a reversible starting configuration before each pulse, only micro-structured single-layered films have been studied up to now, in which a flux-closure vortex domain pattern has the lowest magnetostatic energy and thus works as a reversible ground state. Schneider and coworkers used a strip-line set-up and a fast pulse power supply to study the magnetization reversal of permalloy elements [362–364]. Pulse widths down to about 1 ns full width at half maximum were achieved in that way.

Figure 4.27 schematically shows a set-up in which a photoconductive switch is used for the excitation of current pulses in the strip line. A femtosecond laser is shone on a region that contains a lithographic gold structure patterned into a finger-like structure. The laser pulses excite charge carriers in the underlying semiconducting substrate, which are subsequently carried away through the strip line by the electric

Fig. 4.27 a Schematics of a time-resolved XMCD-PEEM experiment using laser excitation of a photoconductive switch connected to a stripline. Laser pulses from a femtosecond laser are synchronized to the masterclock signal of the storage ring of the synchrotron radiation source. and can be shifted by a fixed time delay with respect to each other. b Sketch of the lithographic switch-stripline assembly and a scanning electron microscopy image of magnetic microstructures on the stripline. Reprinted with permission from [361]. Copyright [2008], AIP Publishing LLC

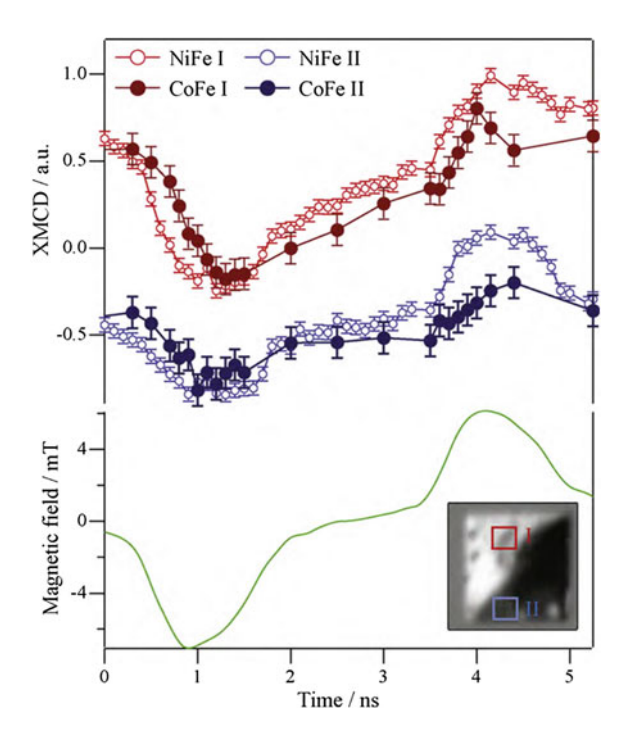


field of an externally applied voltage. For time-resolved imaging with synchrotron radiation, the laser pulses have to be synchronized to the X-ray pulses from the synchrotron light source, as sketched in Fig. 4.27a. Fig. 4.27b shows how the switch part of the gold structure connects to the stripline, and includes a scanning electron microscope image of the stripline with magnetic microstructures on top. With such a set-up, current pulses as short as 70 ps full width at half maximum could be achieved [361].

With a similar experiment, Choe et al. could image the gyrotropic motion of the vortex core in the center of a flux-closure domain pattern as a function of time [365]. No such gyrotropic motion was observed in another experiment by Raabe et al., who used a synchronized laser and a fast photodiode for the pulse generation [366]. This apparent contradiction was later explained by Cheng et al., who concluded that the free motion of a magnetic vortex always corresponds to a circular core trajectory, but that for core displacements above a certain threshold due to nonlinear dynamical effects transient distortions of the vortex core occur, which give the appearance of a linear core trajectory in pump–probe experiments [367].

An example of the layer-selective application of time-resolved PEEM is presented in Fig. 4.28. It shows the result of a time-resolved PEEM experiment on an  $8\times 8~\mu\text{m}^2$  FeCo/Cr/NiFe trilayer element with 2.5 nm Cr spacer layer thickness, corresponding to weak ferromagnetic interlayer coupling between the two ferromagnetic layers. The structure was excited by bipolar magnetic field pulses, created by current pulses in an underlying 25  $~\mu\text{m}$  wide strip line [368]. The magnetic microstructure of the element under study is shown in the inset in the bottom right of Fig. 4.28. The bottom curve

Fig. 4.28 Temporal evolution of layer-resolved magnetic contrast in an  $8 \times 8 \,\mu\text{m}^2$  ferromagnetically coupled FeCo/Cr/NiFe trilayer element in response to bipolar magnetic field pulses, as depicted in the bottom panel. Solid symbols represent the domain contrast of the CoFe bottom laver. measured at the photon energy of the Co  $L_3$  edge, open symbols the domain contrast of the NiFe top layer, measured at the photon energy of the Ni  $L_3$  edge. The top and middle panels are the results from evaluations of the XMCD contrast in regions of the bright and dark domain, respectively, as shown in the inset. Reprinted from [368], Copyright (2010), with permission from Elsevier



of the figure displays the shape of the bipolar field pulses of about 7 mT, which were applied at 1.25 MHz repetition rate. Stroboscopic pump–probe imaging at the Co and Ni  $L_3$  edges yields time-resolved information about the response of the magnetic system in the two ferromagnetic layers. Figure 4.28 shows time traces of the magnetic XMCD contrast at two positions of the structure, as indicated in the inset. The top panel corresponds to a position in the domain with the bright contrast, the middle panel to a region from the dark domain. Overall, the XMCD contrast follows roughly the time evolution of the magnetic field. A closer inspection, however, reveals distinct differences in the responses of the different ferromagnetic layers: The XMCD signal of the bottom CoFe layer, depicted by solid symbols, always lags behind that of the top NiFe layer, represented by open symbols, by about 250 ps [368]. This can be explained by the different coercivities of the two layers, which lead to different switching times for domain wall motion and rotational processes [369].

The presented examples demonstrate how time resolution can be implemented to layer-resolved magnetic imaging. The further development of such advanced time-resolved magnetic imaging techniques and its application for the time- and layer-resolved magnetic imaging of multilayered structures will no doubt be one of the most promising future directions in the investigation of ultrafast magnetization reversal in technologically relevant magnetic systems.

# **Chapter 5 Magnetic Transmission Soft X-Ray Microscopy**

The final chapter deals with transmission soft X-ray microscopy (TXM). Similar to the optical microscopes described in previous chapters, M-TXM is a pure photon-based technique, but harnesses the specific properties of X-rays, which provides higher spatial resolution, larger penetration depth, quantifiable and element-specific magnetic information, and a temporal resolution which is set by the time structure of the X-ray sources in use. TXMs are becoming now even commercially available products, and are available at most current synchrotron facilities worldwide. This chapter describes the basic instrument components of TXMs and will exemplify their use for layer-resolved (and time-resolved) magnetic microscopies by a few selected examples.

#### 5.1 Introduction

This chapter describes the basic features of magnetic transmission soft X-ray microscopy (M-TXM). It uses the same magnetic contrast mechanism as the PEEM technique, however, as it is a purely photon in/photon out-based technique, M-TXM is insensitive to external magnetic fields which can be applied during the image recording. M-TXM is complementary to PEEM in terms of probing depth. Whereas PEEM relies on detecting electrons which can escape only more or less from the surface region, M-TXM probes the volume of the specimen. The upper limit is set by the penetration depth of soft X-rays to about 200 nm, and the lower limit depends on the signal/noise ratio. Domains from layers as thin as about 1 nm have been recorded with M-TXM. The spatial resolution that can be obtained is largely determined by the optical performance of the Fresnel zone plate optical elements, and the time resolution is limited to the time structure of the X-ray source similar as it is for PEEM.

The basic concept of M-TXM is to combine the element-selective magnetic information of XMCD with the imaging capabilities of a high resolution transmission X-ray microscope [233, 370–373]. The idea is to image magnetic domain structures in ferromagnetic thin films, layered systems, and nanostructured elements by

recording with high spatial resolution the local transmission coefficient of circularly polarized X rays after their passage through a ferromagnetic sample.

The major differences between M-TXM and PEEM are that M-TXM is

- sensitive to the bulk properties of the sample and
- a purely photon-based technique.

The former property, which reflects the high penetrability of soft X rays in matter up to about 200 nm, allows to study even deeply buried layers. This is of particular importance since in technological applications layered magnetic systems are often composed of stacks of multiple different layers the thickness of which may exceed the escape depth of low-energy secondary electrons. To study the magnetic properties of each individual layer and its coupling to the other layers in the stack, which determines the general functionality of the device, layer-resolved magnetic imaging of deeply buried layers may be required.

The latter property is a major advantage that allows to study the response of magnetic domain structures in individual layers upon applying external magnetic fields. Thus fundamental details in magnetization reversal processes can be addressed. As we shall see later, these studies can be performed with a spatial resolution that approaches fundamental length scales such as exchange lengths and grain sizes.

This chapter is organized as follows. First we present some basic considerations for the absorption of circularly polarized photons in matter. Second, the experimental technique of M-TXM will be explained in detail with emphasis on the optical components as they provide the spatial resolution. After discussing specific requirements to prepare X-ray-transparent samples, the main part deals with the characteristic features of M-TXM, thereby demonstrating the strengths and the limitations of this technique with regard to layer-resolved magnetic microscopy at high spatial and temporal resolution. The chapter closes with some remarks on future perspectives of M-TXM such as to push the spatial resolution to below 10 nm and the time resolution into the femtosecond regime.

## 5.2 Absorption of X Rays in Transmission Experiments

In contrast to the detection of secondary electrons created in the X-ray absorption process, as discussed in the preceding section, we now describe the detection of photons which transmit the sample. While the previous detection method provides an inherent surface sensitivity, the transmission method is inherently bulk sensitive. In other words, while there is a maximum probing depth for electrons, the signal in a transmission experiment has a lower limit with respect to the thickness of suited samples. It turns out that both techniques complement each other in that respect. In fact, there is an overlap in the accesible thickness of magnetic films (see Sect. 5.3.4)

In the photon energy range below about  $50 \,\mathrm{keV}$  the dominant absorption process of X rays in matter is the photoelectric effect. A beam of photons passing through a thickness of matter d is not degraded in energy  $\mathcal{E}$ , but only attenuated in intensity I.

The attenuation suffered by a photon beam can be shown to follow an exponential law with respect to d (Beer's law, see also 2.22)

$$I_t(\mathcal{E}, Z, d) = I_0(\mathcal{E}) \cdot e^{-\alpha(\mathcal{E}, Z) \cdot d}$$
(5.1)

with  $I_0(\mathcal{E})$  being the incident and  $I_t(\mathcal{E}, Z, d)$  the transmitted beam intensity. The absorption coefficient  $\alpha(\mathcal{E}, Z)$  is the characteristic quantity describing the absorbing material (atomic number Z) and it is directly related to the total internal cross section. It shows a strong dependence both on the atomic number ( $\propto Z^5$ ) and the photon energy ( $\propto \mathcal{E}^{-7/2}$ ). Approximate helicity-averaged values for the absorption coefficients of the 3d ferromagnets have been given in Table 4.1.

From the experimental point of view the most straightforward determination of  $\alpha(\mathcal{E}, Z)$  is to measure the incoming and transmitted photon intensities  $(I_0(\mathcal{E}), I_t(\mathcal{E}, Z, d))$  and applying (5.1) to give

$$\alpha(\mathcal{E}, Z) = \frac{1}{d} \ln \frac{I_1(\mathcal{E}, Z, d)}{I_0(\mathcal{E})}.$$
 (5.2)

The quantity  $\alpha$  includes the magnetization-dependent part from the XMCD effect, see Sect. 2.7.3. We will write  $\alpha^+$  for the absorption coefficient for X rays of positive helicity, and  $\alpha^-$  for the absorption coefficient for negative helicity. For imaging purposes often the asymmetry A is presented, defined as

$$A = \frac{\alpha^+ - \alpha^-}{\alpha^+ + \alpha^-} = \frac{\alpha^+ - \alpha^-}{2\alpha} \tag{5.3}$$

with

$$\alpha = \frac{1}{2}(\alpha^+ + \alpha^-) \tag{5.4}$$

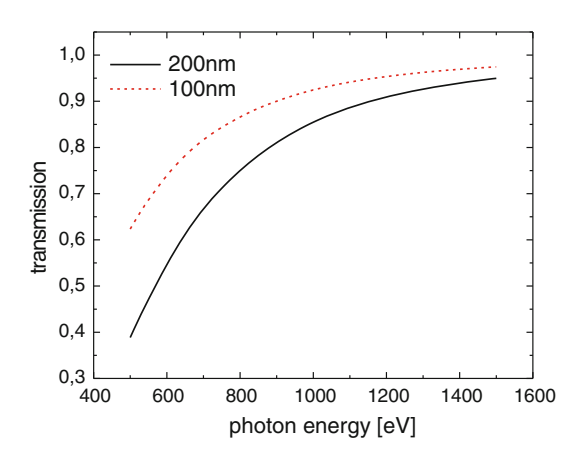
being the helicity-averaged absorption coefficient.

The asymmetry A defines the magnetic contrast in experiments where the absorption coefficient is measured, for example in total electron yield measurements as described in the preceding section. Typical values for this asymmetry are around 27% for metallic Fe and Co [240], and about 15% for Ni [242], assuming 100% circular polarization.

For transmission experiments, the sample has to be supported by a suitable substrate to account for the limited penetration depth of soft X rays. In most cases  $Si_3N_4$  is used because of its low absorption coefficient. The transmission  $I_t/I_0$  of  $Si_3N_4$  membranes with 100 and 200 nm thicknesses, typically used as substrates for transmission experiments, is depicted in Fig. 5.1. Around the L edges of transition metals, such as Fe, Co or Ni, more than 70% of the photon intensity is transmitted.

<sup>&</sup>lt;sup>1</sup> These substrates are also commonly used in transmission electron microscopy (TEM).

Fig. 5.1 Transmission of soft X rays through Si<sub>3</sub>N<sub>4</sub> membranes of 100 and 200 nm thicknesses



Before we move to the case of transmission through a multilayered magnetic structure, let us first consider a single magnetic film of thickness  $d_1$  on top of a substrate of thickness  $d_S$ . The helicity-averaged absorption coefficient of the film is  $\alpha_1 = (\alpha_1^+ + \alpha_1^-)/2$ , and the absorption coefficient of the substrate  $\alpha_S$ . The transmitted intensity, including the effect of magnetic circular dichroism of the film, is then for positive helicity

$$I_{\rm t}^+ = I_0 \cdot e^{-(\alpha_1^+ d_1 + \alpha_{\rm S} d_{\rm S})},$$
 (5.5)

and for negative helicity

$$I_{\rm t}^- = I_0 \cdot {\rm e}^{-(\alpha_1^- d_1 + \alpha_S d_S)}.$$
 (5.6)

If the resulting asymmetry of the transmitted intensity, defined as

$$A_{t} = \frac{I_{t}^{+} - I_{t}^{-}}{I_{t}^{+} + I_{t}^{-}},\tag{5.7}$$

is calculated, the attenuation of the transmitted X-ray beam due to the supporting substrate,  $\exp(-\alpha_S t_S)$ , as well as the incident intensity  $I_0$  cancel out and one arrives at

$$A_{t} = \frac{e^{-\alpha_{1}^{+}d_{1}} - e^{-\alpha_{1}^{-}d_{1}}}{e^{-\alpha_{1}^{+}d_{1}} + e^{-\alpha_{1}^{-}d_{1}}}.$$
(5.8)

For small  $d_1$  compared to the absorption length  $1/\alpha_1$  this simplifies to

$$A_{\rm t} \approx -\frac{\alpha_1^+ - \alpha_1^-}{2} \cdot d_1. \tag{5.9}$$

From this equation, one immediately recognizes the important difference between the asymmetry A of the absorption coefficient (5.3) and the asymmetry of the transmitted photon intensity  $A_t$  (5.9). Firstly, the sign of  $A_t$  is opposite to that of A; this follows directly from the respective definitions (5.3) and (5.7), since A includes the absorption coefficient, while for  $A_t$  the transmitted intensity, which is smaller for larger absorption, is the relevant measure. Secondly, for small thicknesses  $d_1$  the absolute value of  $A_t$  is small and proportional to  $d_1$ . At a thickness  $d_1 = 1/\alpha_0$  we find  $A_t \approx -A$ . For larger thicknesses the absolute value of the asymmetry of the transmitted intensity exceeds that of the absorption asymmetry, and finally approaches asymptotically -1 for very thick layers (cf. 5.8).

The signal-to-noise level in magnetic imaging experiments is governed by the figure of merit, in this case

$$F = A_t^2 \cdot I_t, \tag{5.10}$$

where we approximate  $I_t$  by the helicity-averaged transmitted intensity  $I_0 \cdot \exp(-\alpha_1 d_1)$ . In other words, the exposure time has to be extended if the asymmetry is reduced in order to reach the same noise level in a magnetic image. A reduction in transmitted intensity has also to be compensated by a longer exposure time. The factor by which the measuring time increases scales inversely to the figure of merit F.

The graph in Fig. 5.2 shows the figure of merit F as a function of film thickness for these three 3d metals. Using typical values for metallic Fe and Co, the thickness with the highest signal-to-noise ratio for magnetic imaging in transmission is 29 nm

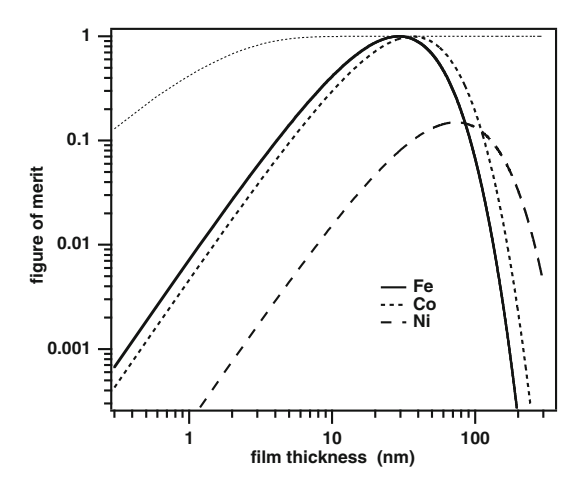


Fig. 5.2 Relative figures of merit as a function of film thickness for single films of metallic Fe, Co, and Ni as indicated in the legend for magnetic imaging using XMCD at the  $L_3$  absorption maximum in transmission. Values used for the calculation of the *curves* were A=27% for Fe and Co, A=15% for Ni, and absorption coefficients for the  $L_3$  maximum from Table 4.1. For comparison, the *dotted line* represents the relative figure of merit for total electron yield detection, scaled to one at the maximum

for Fe, about 37 nm for Co, and 73 nm for Ni. For small thicknesses  $I_t \approx I_0$ , and the behavior of F is dominated by the square of  $a_t$ . In that regime F follows roughly a quadratic behavior as

$$F \approx \left(\frac{\alpha_1^+ - \alpha_1^-}{2}\right)^2 \cdot d_1^2. \tag{5.11}$$

This means that a reduction of the magnetic layer thickness by a factor of two has to be compensated by a four times longer exposure time to achieve the same signal-to-noise ratio. At 1 nm thickness, F is about or below 1% of that at  $d_{1,\max}$ . Note that the transmission of the substrate enters only as an additional factor in F; the shape of the curves and the relative height are preserved if the same substrate is used.

To compare to the thickness dependence of total electron yield detection, the thin dotted line in Fig. 5.2 depicts the relative figure of merit of the  $L_3$  edge XMCD of an Fe film on a Cu substrate detected by total electron yield. For the electron escape depth and the absorption coefficients the values of the preceding chapter were used. Note that the figures of merit of different detection schemes can not be compared on an absolute basis, as the intensity of the source, the transmission of the instruments as well as the efficiency of the detectors enters. The curve is therefore scaled to the same maximum as the curve for Fe measured in transmission in order to enable a relative comparison. One has also to keep in mind that in electron yield detection a weighted average emphasizing the contribution of the surface-near region is obtained, while transmission results in an unweighted average of the entire film.

We will now consider transmission through a multilayered structure in which the layers  $i = 1, 2, \ldots$  have thicknesses  $t_i$  and absorption coefficients  $\alpha_i$ . The transmitted intensity can then be expressed by

$$I_t = I_0 \cdot e^{-\alpha_S d_S} \cdot \prod_i e^{-\alpha_i d_i}, \qquad (5.12)$$

where  $\alpha_S$  and  $d_S$  denote the absorption coefficient and thickness of the substrate, respectively. From (5.12) and (5.7) it is seen that, unlike the case of total electron yield detection, the asymmetry in transmission  $a_t$  at fixed photon energy caused by the XMCD effect of a certain layer does not change if other layers are added as long as these layers do not contribute an XMCD effect at that photon energy. Equation 5.12 also tells us that in a transmission experiment the sequence of the layers does not play any role. Measuring the XMCD effect of layer A in an A/B/C stacking sequence gives the same intensity and asymmetry as, e.g., in a C/A/B stacking sequence.

In analogy to the treatment in Sect. 4.2 and to be able to compare to total electron yield detection we can now examine the overlayer compensation factor x. x is defined as the prolongation factor for the measuring time needed after adding overlayers to a magnetic film in order to obtain a magnetic image with the same statistics as before. From the above discussion it follows that  $x = F_0/F$ , where  $F_0$  and F are the figures of merit for the uncapped and capped film, respectively. x is thus simply

$$x = \left(\prod_{i \ge 2} e^{-\alpha_i d_i}\right)^{-1}.$$
 (5.13)

For better comparison with Sect. 4.2 we present in Fig. 5.3 two-dimensional plots of x as a function of the thicknesses of two overlayers. Like in Fig. 4.5 we present x for two examples, a Ni<sub>81</sub>Fe<sub>19</sub> film covered by Co/Cu (a), and a Co film covered by Ni<sub>81</sub>Fe<sub>19</sub>/Cu (b). Note that in the case of transmission the influence of the thicknesses of the two different overlayers acts independently on x, thus one could have used also another way of representation. However, the comparison between Figs. 4.5 and 5.3 is very instructive, and reveals the major difference between the two approaches to XMCD magnetic imaging. Note the different numbers on the axes and at the contour lines in Figs. 4.5 and 5.3. While adding 5 nm of Co and 5 nm of Cu on top of a Ni<sub>81</sub>Fe<sub>19</sub> sample requires a more than 500-fold increase in acquisition time for equal image statistics in total electron yield imaging, putting the same overlayers on an Ni<sub>81</sub>Fe<sub>19</sub> film in a transmission experiment hardly influences the image quality; the required increase in measuring time is less than 3%.

While in total electron yield measurements the sample is probed from the top, hence there is a strong dependence on the sequence of the layers in a multilayered structure, this does not play any role in transmission. The two ways of detection are thus highly complementary. Depending on the questions one wants to address, and on the samples, one may find one or the other approach more appropriate. In total electron yield the escape length of the electrons limits the detected volume to

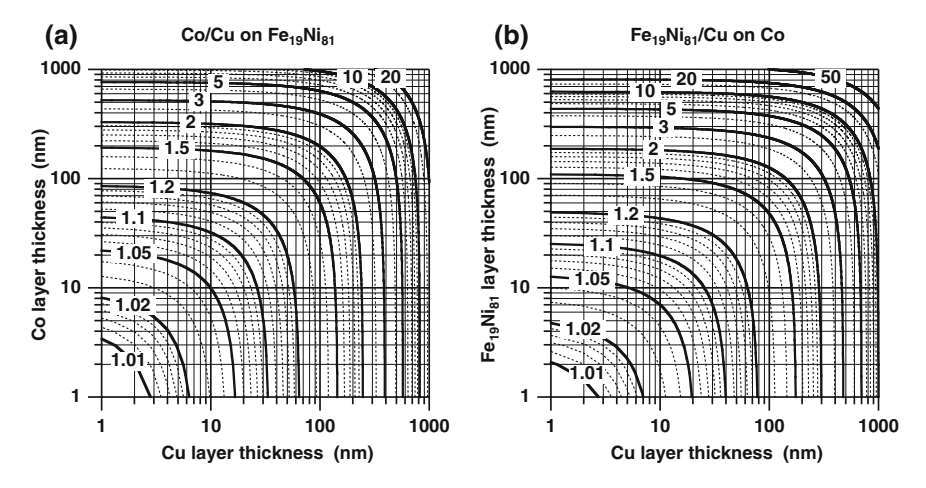


Fig. 5.3 Overlayer compensation factor x due to overlayers needed for the  $L_3$  XMCD measurement of a an Ni $_{81}$ Fe $_{19}$  film with Co/Cu overlayers as a function of Cu and Co overlayer thicknesses, b a Co film with Ni $_{81}$ Fe $_{19}$ /Cu overlayers as a function of Cu and Ni $_{81}$ Fe $_{19}$  overlayer thicknesses. x describes the increase in data acquisition time required to obtain the same signal-to-noise ratio as without the Co and Cu overlayers, and is presented by *contour lines* as a function of Cu and Ni $_{81}$ Fe $_{19}$  overlayer thicknesses

the near-surface region of the sample. This can be an advantage if, for example, the layered system under investigation is a magnetic trilayer or spin-valve sample sitting on top of a pinning structure, synthetic antiferromagnet, or other underlayers that contain similar elements. It may be a disadvantage if the layers of interest are buried under relatively thick capping or protecting layers, or if the layered magnetic structures themselves are too thick for total electron yield detection. In general the absorption of thinner layers is easier to image by total electron yield detection than in transmission, as seen from the thin dotted line in Fig. 5.2. Detecting the signal from layers in a depth of more than a couple of nanometers, on the contrary, is only possible in transmission.

In addition to the depth-probing behavior, other aspects may need to be considered. One is the sample structure. While in total electron yield the type of sample underneath the structure one wants to investigate does not matter as long as the surface can be made conductive and reasonably flat, samples for transmission have to be prepared on suitable membranes. Studies of samples on single crystal substrates, as they are presented in Chap. 4, are thus easier for total electron yield imaging by photoelectron emission microscopy (PEEM). However, the advantages of photononly based microspectroscopy has recently triggered intense efforts to grow epitaxial films on X-ray transparent substrates. One example is the technique of ion beam-assisted deposition on MgO (IBAD MgO) [374].

Another important aspect is the demand for recording magnetic images in varying external magnetic fields. While total electron yield detection of X-ray absorption without spatial resolution works well also under quite strong applied magnetic fields, the fact that magnetic imaging with secondary electrons in a PEEM relies on the capability to exactly localize where the electrons are generated prevents in general the application of even weak magnetic fields. Some efforts have been reported with specially designed microgap electromagnets which can be used to a limited extent for PEEM imaging in magnetic field. It has been demonstrated that in this way up to 33 mT magnetic field could be applied locally to the sample without significant distortion or reduction of lateral resolution [375]. In transmission experiments the application of arbitrarily high magnetic fields is much easier, since the detected photons do not interact with magnetic fields. Therefore, investigations of quasistatic magnetization reversal behavior by layer-resolved magnetic imaging under applied magnetic field is thus readily achieved with transmission soft X-ray microscopy (TXM).

With regard to spatial resolution both PEEM and TXM are working to approach the 10 nm regime. So far, TXM is leading the field with a better than 15 nm spatial resolution [376]. With the availability of state-of-the-art imaging electron energy filters the resolution available in XMCD-PEEM imaging has improved and in the future, better zone-plate production schemes for TXM on the one hand, and sophisticated aberration-correction schemes for PEEM on the other hand will push the available resolution in both techniques further into the low nanometer regime.<sup>2</sup>

<sup>&</sup>lt;sup>2</sup> A completely different approach of X-ray based imaging is the current development of lensless imaging. Although in principle these techniques should be only limited by the wavelength, so far the spatial resolution obtained for magnetic imaging is far away from that limit [377, 378].

# 5.3 Basic Elements in Magnetic Transmission Soft X-Ray Microscopy

Magnetic transmission soft X-ray microscopy combines a high-resolution transmission X-ray microscope with XMCD as magnetic contrast mechanism. This was successfully demonstrated for the first time in 1996 with a full-field microscope at BESSY I in Berlin/Germany, where the magnetic domain structure in an amorphous GdFe alloy was recorded at the  $L_{2,3}$  edges of Fe [233]. Currently, the full-field transmission soft X-ray microscope (XM-1) jointly operated by the Center for X-ray Optics and the Advanced Light Source in Berkeley, CA, is the only operational system worldwide used for magnetic full-field X-ray imaging.<sup>3</sup>

Instead of using an X-ray optical imaging system, a corresponding scanning transmission X-ray microscope (STXM) to record magnetic microstructures can also be used [381]. With the help of an interferometric control of the sample stage, a significant improvement in spatial resolution has been achieved for STXM [382]. Since first STXM systems have become commercially available, their number at various synchrotrons is increasing rapidly. Magnetic STXM imaging has been reported, for example, at the Advanced Light Source in Berkeley [383–386], the Swiss Light Source [387, 388], the Canadian Light Source [389] and at BESSY II [390, 391].

#### 5.3.1 Fresnel Zone Plates as Optical Elements

The fact that the refractive index of soft X rays is close to unity has prevented the development of X-ray microscopy for a long time. However, it is now well accepted that Fresnel zone plates can be used as diffractive optical elements to build an X-ray microscope [371].

Fresnel zone plates are circular gratings with a radially increasing line density. Positive interference of the diffracted radiation of a particular wavelength from such elements occurs at a well-defined downstream position, which is the focal length. Fresnel zone plates can be fabricated involving state-of-the-art nanofabrication technologies [392, 393], and their X-ray optical performance is determined by the number of zones N and the outermost zone width  $\Delta r$  [371].

One easily derives for the diameter D, the focal length f and the numerical aperture NA of a Fresnel zone plate the following expressions

<sup>&</sup>lt;sup>3</sup> The latest generation of a full-field TXM has been recently installed at BESSY [379, 380]. This instrument provides high spectral resolution, which makes it unique for spectro-microscopy studies, with a clear advantage particularly for multi-dimensional imaging. However, the current undulator source does not provide polarized light and therefore magnetic imaging is not (yet) implemented.

$$D = 4N\Delta r,\tag{5.14}$$

$$f = \frac{4N(\Delta r)^2}{\lambda},\tag{5.15}$$

$$NA = \frac{\lambda}{2\Delta r},\tag{5.16}$$

with  $\lambda$  being the wavelength of the photons ( $E[\text{keV}] = 1.24/\lambda[\text{nm}]$ ). The spatial resolution  $\Delta x$  that can be obtained with a Fresnel zone plate is largely determined by the outermost zone width  $\Delta r$  and is given by

$$\Delta x = \frac{k_1 \lambda}{NA} \tag{5.17}$$

where  $k_1$  is an illumination-dependent constant ranging from 0.3 to 0.61 [394]. For partially coherent illumination, e.g., for the soft X-ray microscope XM-1 located at a bending magnet,  $k_1 \approx 0.4$  and therefore the theoretical resolution is

$$\Delta x = 0.8 \Delta r,\tag{5.18}$$

which means that for a Fresnel zone plate with  $\Delta r = 15 \,\text{nm}$  [131] the spatial resolution is 12 nm. The shift of the Rayleigh criterion towards smaller half periods in a binary pattern with partially incoherent light is shown in Fig. 5.4.

Recent advances in the nanofabrication of Fresnel zone plates have demonstrated that a spatial resolution approaching 10 nm can be achieved [131, 395–397]. Since isolated lines can be written easily down to the sub-10 nm regime, one of the concepts

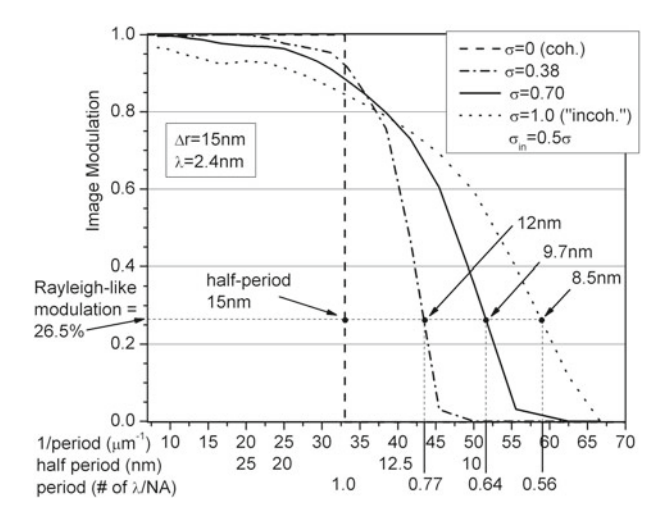


**Fig. 5.4** Calculated modulation of a dense line binary pattern for a 15 nm zone plate and the dependence on partial coherence showing the shift of the Rayleigh criterion towards smaller half periods, i.e., better spatial resolution can be obtained with partially incoherent light. From [370]

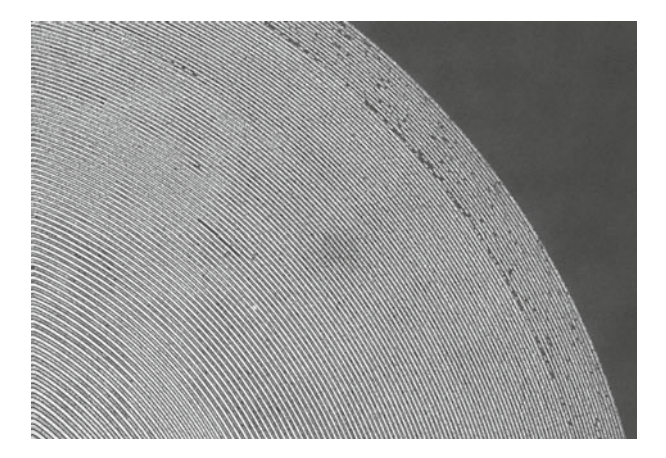


**Fig. 5.5** Scanning electron microscopy micrograph of a Fresnel zone plate with a 15 nm outermost zone width. From [131]. Reprinted by permission of Macmillan

to achieve high density line patterns for high-resolution Fresnel zone plates consists of an overlay technique where in the first step only half of the line patterns are written by electron-beam lithographic techniques, and then in a subsequent step the remaining lines are positioned in between these lines [131]. Consequently, this is only possible if the electron-beam system allows for a high accuracy placement of the second line pattern, which has to be typically one third of the generated features, i.e., for 15 nm features this requires a 5 nm accuracy. Figure 5.5 shows a scanning electron micrograph of a zone plate with 15 nm outermost zone width fabricated by the Center for X-ray Optics in Berkeley, CA.

## 5.3.2 Experimental Set-Up

The principle of the optical set up in a full-field soft X-ray microscope is similar to a conventional microscope. It consists of a light source, a condenser, an objective lense, and a detector. The major difference is that condenser and objective lense are Fresnel zone plates. The X-ray optical set-up of the endstation XM-1 at the Advanced Light Source is shown in Fig. 5.6.

It follows the pioneering X-ray microscope design developed by Schmahl et al. [372]. XM-1 uses soft X rays emitted from a bending magnet. After passing a plane mirror, which is coated, e.g., with Ni to reject higher energies, the photons illuminate a condenser zone plate (CZP) that has a central stop. The CZP provides both a partially coherent hollow cone illumination of the sample and, in combination with a pinhole located close to the sample, serves as linear monochromator with a typical monochromaticity of about  $\lambda/\Delta\lambda=500$ . Thus, at a photon energy of 700 eV the spectral resolution is about 1.3 eV. The photon energy range at XM-1 is between 500 and 1,300 eV, thereby covering the water window around a photon wavelength of

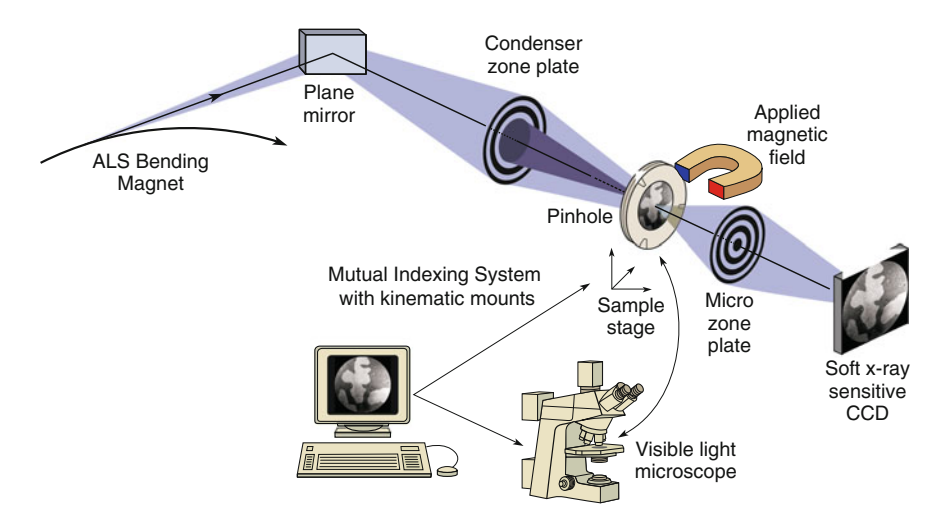


**Fig. 5.6** Schematics of the optical set up for the soft X-ray microscope XM-1. A visible light microscope, which is mutually indexed to the sample stage, serves for prealignment of the sample. From [370]

2.4 nm, most of the L edges of 3d transition metals, and the M edges of rare earth systems. After the photons have transmitted the specimen, a second Fresnel zone plate, the microzone plate (MZP), projects a full-field image onto an X-ray-sensitive two-dimensional charge-coupled device (CCD) detector. It is a backside-illuminated thinned CCD. The current CCD chip has  $2,048 \times 2,048$  pixels, with a pixel size of  $13.5 \times 13.5 \,\mu\text{m}^2$ . Typical values for the magnification are between 1,500 and 2,000, yielding a field of view of about  $10\,\mu\text{m}$  per image. Depending on the flux of available photons the illumination time per image is about  $1-2\,\text{s}$  for samples with a strong contrast (see discussion in Sect. 5.2).

To obtain magnetic contrast through XMCD, circularly polarized X rays emitted off orbit are selected by an aperture in front of the CZP masking either the top or bottom half of the incoming radiation. Figure 5.7 displays the magnetic domain structure observed in an amorphous GdFe system recorded at the Fe  $L_3$  edge at 706 eV with radiation 2.5 mm above and below the storage ring's orbital plane. As can be clearly seen, the magnetic contrast is reversed upon reversal of the sense of circular polarization. Dividing such two images by each other allows to eliminate the non-magnetic background and to enhance the magnetic contrast.

One of the major advantages of magnetic soft X-ray microscopy is that as a pure photon-in/photon-out technique external magnetic fields can be applied to the sample during image acquisition, with in principle any strength and any direction. Thus magnetization reversal processes, such as the evolution of the domains in complete magnetization switching cycles, can be studied in detail [398]. So far, at XM-1 solenoids with specially shaped pole pieces provide magnetic fields up to several hundred mT pointing both parallel to the photon beam as well as parallel to the sample plane.

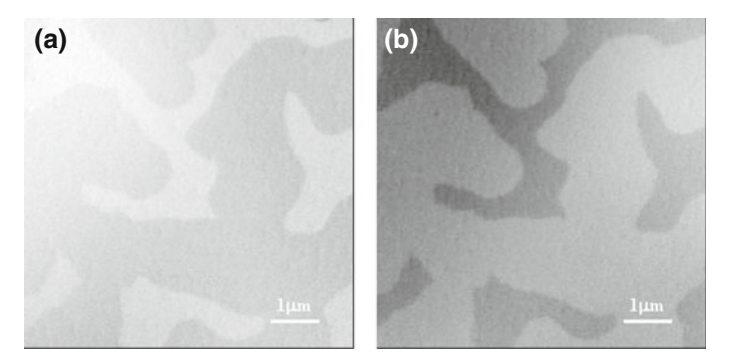
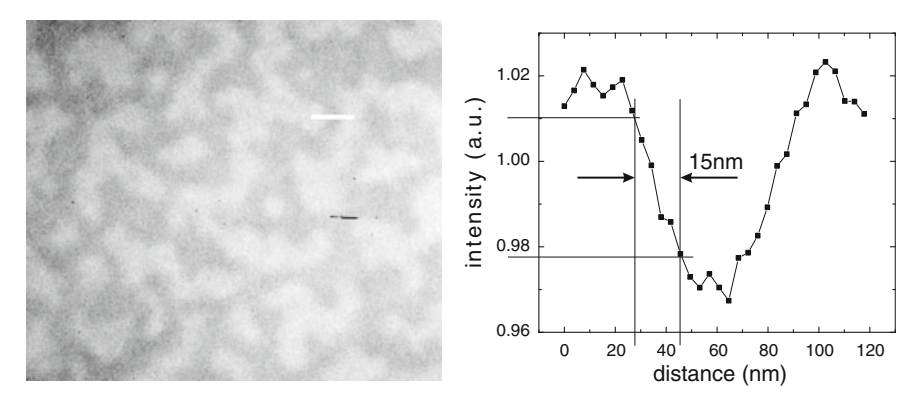


Fig. 5.7 Magnetic domain structure of an amorphous GdFe sample observed with circular polarization above and below the orbital plane at the Fe  $L_3$  edge showing the reversal of magnetic contrast. From [227]. Reprinted by permission of AIP



**Fig. 5.8** M-TXM magnetic domain image and intensity profile across the boundary of a magnetic domain in a  $(Co_{83}Cr_{17})_{87}Pt_{13}$  alloy film showing a lateral resolution of better than 15 nm. From [376]. Reprinted by permission of AIP

A typical example for high-resolution magnetic imaging with M-TXM is shown in Fig. 5.8, where the magnetic domain structure in a 50 nm thin nanogranular  $(Co_{84}Cr_{16})_{87}Pt_{13}$  layer with a pronounced perpendicular magnetic anisotropy has been recorded at the Co  $L_3$  edge. A common knife-edge analysis of the intensity profile covering the 10–90% values reveals a 15 nm spatial resolution [376]. The grain-size distribution of that sample, which was determined from a TEM analysis [399], peaks at around 20 nm, which allows to conclude that from M-TXM images it is possible to study the magnetic domain structure on the grain-size level, i.e., on a magnetically fundamental length scale in that system.

Since the dichroic contrast is given by the projection of the magnetization onto the photon propagation direction, both out-of-plane- and in-plane-magnetized domains can be imaged by illuminating the sample at tilted angles with respect to the photon beam direction (see Fig. 5.9). Currently, at the XM-1 microscope, the samples can be

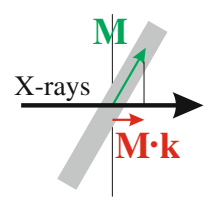


Fig. 5.9 The in-plane magnetization M, which is the dominant orientation in thin films, can be imaged with M-TXM by tilting the sample surface at an angle relative to the photon propagation direction k in order to obtain a non-vanishing component of M along k

tilted up to 30° thereby decreasing the contrast by a factor of two [400]. Comparing the domain structure taken under various angles, the M-TXM technique allows to distinguish between in-plane and out-of-plane contributions. A specific example are magnetic vortex structures, where there are both in-plane spin structures, the chirality, as well as out-of-plane spins in the center, the polarity. M-TXM can image both and is therefore a valuable tool to investigate the physics of magnetic vortex structures, in particular also their spin dynamics [401–403].

#### 5.3.3 Sample Properties

In order to prepare suitable samples for soft X-ray transmission microscopy, the limited penetration depth of soft X rays has to be taken into account so as to choose proper substrates and design the specimen itself (see Sect. 5.2). However, similar considerations apply to samples for transmission electron microscopy, and therefore the expertise that has been built up by this community over decades can be transferred into M-TXM easily.<sup>4</sup>

According to the strong dependence on the atomic number, substrate materials with a low Z are preferred and, in principle, any substrate that can be fabricated at a thickness that is transparent to soft X rays can be used. So far, the most commonly used substrates are  $\mathrm{Si_3N_4}$  membrane windows, even more since they are commercially available in a wide range of frame and membrane sizes and thicknesses. The attenuation for typical  $\mathrm{Si_3N_4}$  thicknesses of  $100-200\,\mathrm{nm}$  in the soft X-ray regime is shown in Fig. 5.1. Typical substrates have frame sizes up to a few mm with a typical frame thickness of  $200-500\,\mu\mathrm{m}$ , which makes these substrates easy to handle.

Whereas the polycrystalline Si<sub>3</sub>N<sub>4</sub> substrates work very well for many specimens in soft X-ray microscopy, there are numerous specimens which require epitaxial growth, and large efforts are currently undertaken to address this challenge. Amongst

<sup>&</sup>lt;sup>4</sup> The complementarity of Lorentz TEM and M-TXM with regard to in-plane versus out-of-plane sensitivity of the magnetization allows for interesting studies of various aspects in identical systems.

other techniques, ion-beam-assisted deposition of biaxially oriented MgO layers has been developed recently and was used for nanocalorimetry of FeRh thin films [404].<sup>5</sup>

Concerning the low-dimensional magnetic systems of interest, which are generally thinner than 100 nm, the upper limit of the penetration depth of soft X rays is in general no limit for M-TXM samples. In fact, such systems match in a perfect way the penetrability of soft X rays in matter and are the major advantage to study layered magnetic systems with M-TXM. Regarding the signal-to-noise ratio the challenge to M-TXM is how thin a layer can be detected.

#### 5.3.4 Sensitivity to Thin Layers

The sensitivity of M-TXM to thin layers shall be illustrated by two examples. Coupled antiferromagnet/ferromagnet systems exhibit an exchange bias effect, as mentioned in Sect. 1.1.3, the microscopic origin of which is not yet fully understood. Figure 5.10a displays the results obtained at the Fe  $L_3$  edge (707 eV) of an array of squared 20 nm MnIr/10 nm permalloy (Ni<sub>80</sub>Fe<sub>20</sub>, Py) elements showing a four-domain Landau domain configuration for all sizes, with various senses of rotation. Since the nominal thickness of Fe in 10 nm Py is only about 2 nm, these results demonstrate the sensitivity of M-TXM to detect small signals in in-plane configuration [406]. The observed domain structure is consistent with magnetic force microscopy (MFM) results, however, M-TXM shows the local Fe magnetization directly rather than the stray fields, which the MFM technique is probing.

Another example demonstrating the sensitivity limits of M-TXM are ultrathin ferromagnetic films with perpendicular anisotropy, which are of interest for novel

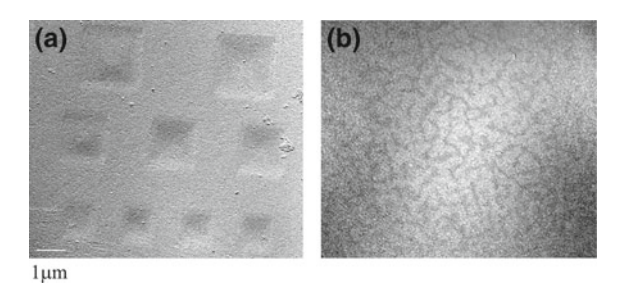


Fig. 5.10 a Magnetic domain pattern in  $1\times1~\mu\text{m}^2$  20 nm MnIr/10 nm Py (Ni<sub>80</sub>Fe<sub>20</sub>) square elements recorded at the Fe  $L_3$  edge (707 eV). The bar corresponds to 1  $\mu$ m. From [406]. Reprinted by permission of Elsevier. b Magnetic domain pattern of a 3 nm Ta/50 nm Cu/3 nm Ta/10 nm Py/10 nm Cu/[0.2 nm Co/0.6 nm Ni]<sub>4</sub>/0.2 nm Co/5 nm Pt ferromagnetic multilayer film recorded at the Co  $L_3$  edge (778 eV). The total Co thickness is about 1 nm. From [407]. Reprinted by permission of Elsevier

 $<sup>^5</sup>$  Nanoheater devices on  $\rm Si_3N_4$  membranes, which have been developed for nanocalorimetry of thin films [405], provide a reliable platform for TXM measurements at elevated temperatures up to several 100 °C.

spin-based devices, such as spin-transfer torque magnetic random access memories and spin-torque nano-oscillators [408]. In many cases, layer stacks that consist of magnetic layers with different easy axis directions can improve spin-transfer device performance and are therefore the focus of current device physics studies [64]. Practical devices need low current for magnetization switching as well as stability against thermal noise; devices with perpendicular magnetic anisotropy combine both. Multilayers of [Co/Ni] have perpendicular magnetic anisotropy and high spin polarization and are thus promising candidates for spin current devices. Of particular interest is the determination of the magnetic properties of individual magnetic layers in the composite layer stack in order to understand the interplay between magnetic interactions, such as magnetic anisotropies, the magnetic response and the underlying magnetic microstructure.

For M-TXM studies, [Co/Ni] multilayers, capped with Pt, were deposited onto a permalloy (Py)/Cu base layer by evaporation in an ultra high vacuum chamber. The samples, with a complete layer stack 3 Ta/50 Cu/3 Ta/10 Py/10 Cu/[0.2 Co/0.6 Ni] $_n$ /0.2 Co/5 Pt (thicknesses in nanometers) were deposited on silicon nitride (Si $_3$ N $_4$ ) membranes supported by Si substrate frames to allow for sufficient X-ray transmission. The thickness of the Cu spacer layer, 10 nm, was chosen to magnetically decouple the in-plane magnetized Py layer from the out-of-plane magnetized [Co/Ni] multilayer. A Co/Pt capping layer was used to further enhance the interface-induced perpendicular magnetic anisotropy of the [Co/Ni] multilayer. To address the influence of the number of bilayers, samples with varying repeats n=4, 6, and 8, were studied. The challenge for M-TXM is to achieve sufficiently high signal-to-noise ratio to resolve the magnetic domain structure in the ultrathin films. Figure 5.10b shows the domain structure in the n=4 repeat [Co/Ni] multilayer sample. Evidently, the XMCD contrast is sufficiently strong to resolve domains with a width of about 100–200 nm in a Co layer thickness of about 1 nm.

## **5.4** Imaging Layered Magnetic Microstructures

### 5.4.1 Elemental Specificity

The magnetic contrast in M-TXM, i.e., the XMCD effect, provides an inherent elemental specificity, which allows imaging of an individual element in multi-component systems. Thus information on the chemical morphology, which influences drastically the behavior of the global magnetization in the presence of external fields, can be obtained.

Figure 5.11 shows M-TXM studies of an amorphous  $Gd_{25}Fe_{75}$  system prepared by magnetron sputtering onto a 350 nm polyimide membrane. The X-ray images were obtained both at the Fe  $L_3$  (707 eV) (a) and  $L_2$  (720 eV) (b) edges as well as at the Gd  $M_5$  (1,190 eV) (c) and  $M_4$  (1,222 eV) (d) edges [409]. With an on-line contrast of more than 25 % given by the maximum dichroic absorption close to the absorption

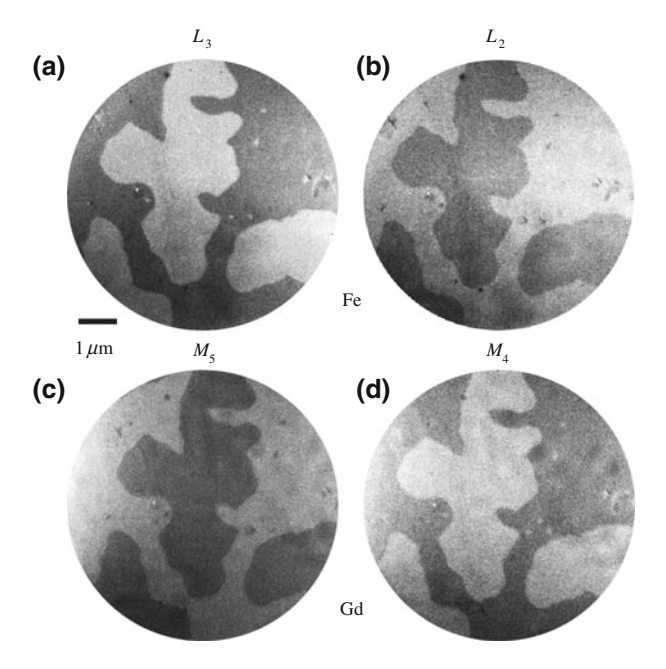


Fig. 5.11 M-TXM images of an amorphous  $Gd_{25}Fe_{75}$  layer recorded at the spin-orbit-coupled Fe  $L_3$  (a) and  $L_2$  (b) as well as at the Gd  $M_5$  (c) and  $M_4$  (d) absorption edges. Reprinted from [409] with kind permission from Springer Science and Business Media

edge, dark and light areas can be clearly identified. Hence, they can be attributed to magnetic domains, where the direction of the local Fe magnetization points in and out of the paper plane, respectively. With a spectral resolution of about 500, as shown above, the signals at the  $L_3$  and the  $L_2$  edges in Fe, separated by about 13 eV by spin—orbit coupling, can be easily resolved. The different spin—orbit coupling for the respective  $p_{1/2}$  and  $p_{3/2}$  core levels is reflected by the expected change in contrast between the  $L_3$  and the  $L_2$  edge. This reversal is furthermore an unambiguous proof of the magnetic character of the features observed. An identical domain pattern is found for the images taken at the corresponding spin—orbit-coupled  $M_{5,4}$  edges of Gd (Fig. 5.11c, d), which is to be expected for such an amorphous system. However, the contrast change from parallel  $(d_{5/2})$  to  $(d_{3/2})$  spin—orbit interaction at the relevant  $M_{5,4}$  edges occurs in reverse direction than at the Fe  $L_{3,2}$  edges. One can conclude that the atomic magnetic moments of the rare earth (Gd) and the transition metal (Fe) atoms couple antiparallel.

## 5.4.2 Magnetization Reversal Processes in Nanostructured Elements

Due to a modified energetic balancing between stray field, exchange, and anisotropy energies the magnetic domain patterns will be drastically modified if they are confined

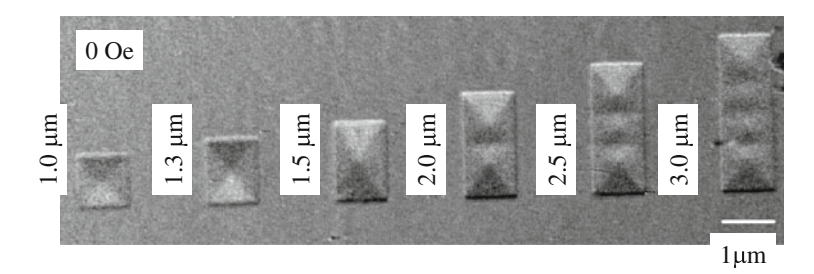


Fig. 5.12 M-TXM image of a series of rectangular  $Ni_{80}Fe_{20}$  elements showing the variation of the domain structure with the geometrical aspect ratio of the elements. Reproduced from [409] with kind permission from Springer Science and Business Media

inside structures of various shape and dimensions. Artificially structured elements, like magnetic nanostructures, are of specific use for such studies.

A prototype system to study the impact of geometry and shape on the magnetic domain configuration are thin permalloy ( $Ni_{80}Fe_{20}$ , Py) elements such as squares, rectangles, or dots. Permalloy is a soft magnetic material with a magnetic permeability around 2,000–3,000 and a coercivity at the order of only 100 A/m. Its magnetostatic energy is usually two to three orders of magnitude larger than the anisotropy energy. Since the most favorable configuration of the magnetization in such elements is oriented in the plane of the film, such systems need to be studied with M-TXM in tilted geometry (see Fig. 5.9). Due to the competition of stray field and exchange energies, the multidomain state is more favorable for specimens with dimensions larger than the exchange lengths, while small particles form a single domain state to achieve the magnetic ground state. The question which specific configuration is formed, and, in particular, the investigation of their characteristic switching behavior, is of large scientific interest.

The M-TXM image displayed in Fig. 5.12 [409] was obtained at the Ni  $L_3$  edge (852 eV) showing the magnetic domain configuration in a series of rectangular elements of 50 nm thick Py with an aspect ratio (width/length) varying from 1 to 1/3. At remanence a symmetric four-domain pattern is observed up to an aspect ratio of 1/2. The known sign of circular polarization allows the unambiguous assignment of the sense of rotation of the magnetization inside the closed domain structure. For example, the rotation sense of the magnetization in the square is oriented in counterclockwise direction, as sketched in Fig. 5.13.

The switching mechanisms of each element can be followed from M-TXM images taken in various external fields (Fig. 5.14 [410]). The direction of the magnetic field was in the plane of the system and along the short edge (the width) of the elements. Due to the large field of view in the XM-1 instrument, the whole series could be recorded within one image and the unambiguity of the magnetic contrast compared to magnetic force microscopy, which detects stray fields, provides valuable information. Applying the field along the long side in a rectangular permalloy element changes the observed domain pattern drastically. A typical flux closure Landau pattern obtained in a rectangular element, where the magnetic field is applied along the long axis, is shown in Fig. 5.15a with increasing field strength from top to bot-

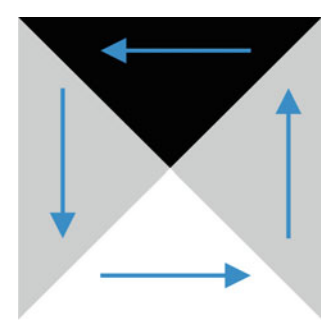
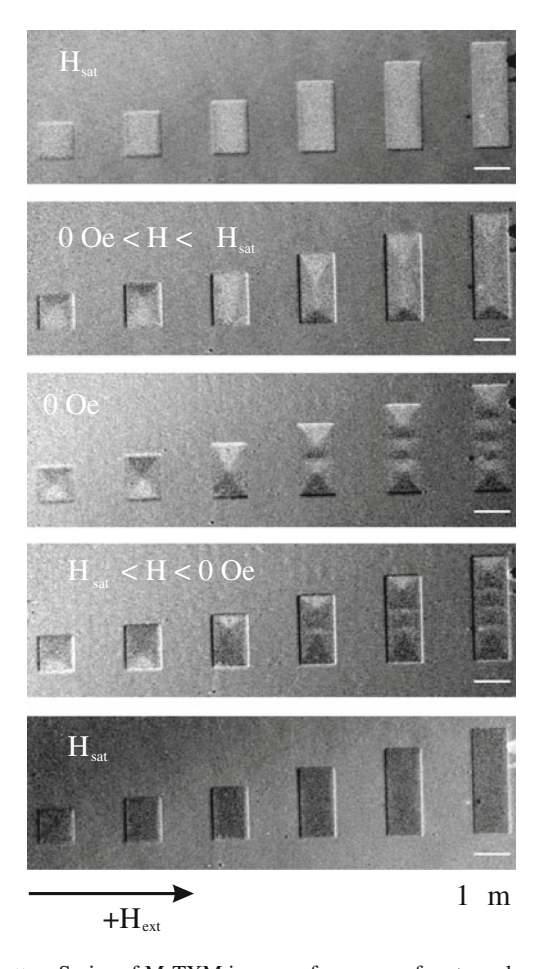


Fig. 5.13 Direction of the magnetization in the closure domains in a Landau pattern as observed in the *square* in Fig. 5.12



**Fig. 5.14** Top to bottom Series of M-TXM images of an array of rectangular permalloy elements in various applied magnetic fields with the field direction along the short edge, showing the different magnetization reversal processes in each element. From [409]. Reprinted by permission of IOP Publishing

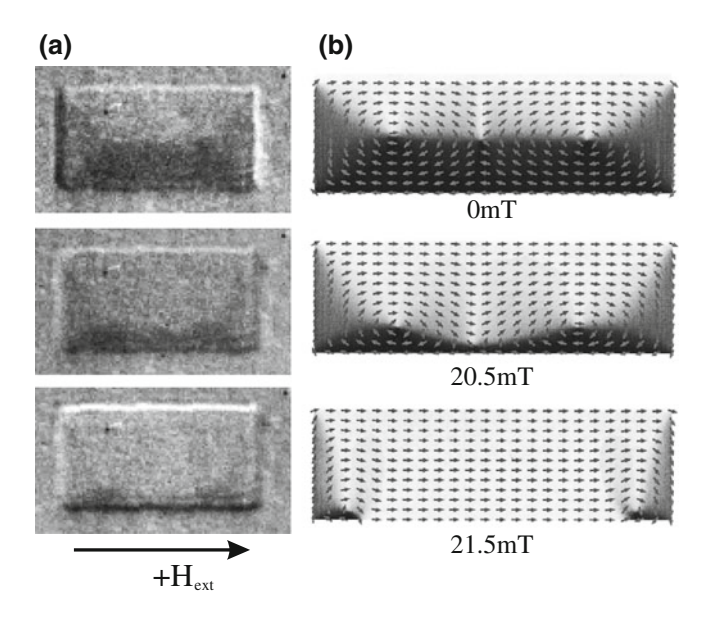


Fig. 5.15 a Variation of the static domain pattern in a  $1 \mu m \times 2 \mu m$  rectangular and 50 nm thin permalloy (Ni<sub>80</sub>Fe<sub>20</sub>) element in various external fields, as given on the *right*. **b** Comparison with micromagnetic simulations. From [411]. Reprinted by permission of Elsevier

tom. The circulation of the magnetization in the flux-closure domain pattern inside the element is clockwise, as can be seen from the fact that with increasing external field the white domain enlarges. This is in accordance with the projection of the magnetization derived from the sense of circular polarization.

The domain patterns observed with M-TXM can also be compared to micromagnetic simulations. In Fig. 5.15b [411] the development of the Landau pattern, starting from a symmetric pattern at 0 mT, can be followed. The external field applied along the long edge moves the two vortices down, thereby enlarging the white domain at higher fields. This demonstrates that the micromagnetic model describes perfectly the experimental results.

While patterned magnetic thin film elements are widely studied, antidot arrays, which consist of a continuous film containing a regular array of non-magnetic inclusions or holes, are not so widely studied. However, they are of particular interest because of the complementary and novel domain configurations, additional magnetic anisotropies and modification of the magnetization reversal, which in turn affects the switching fields and the magnetoresistive behavior. Basic configurations for square antidot arrays with the antidot size greater or equal to the antidot separation exhibit a periodic checkerboard domain pattern [412, 413].

M-TXM offers the advantage to image fine details of the reversal behavior of the magnetic spin configurations in antidot arrays. To fabricate antidot arrays on silicon nitride membranes, one has to avoid regular lift-off techniques [414]. We will

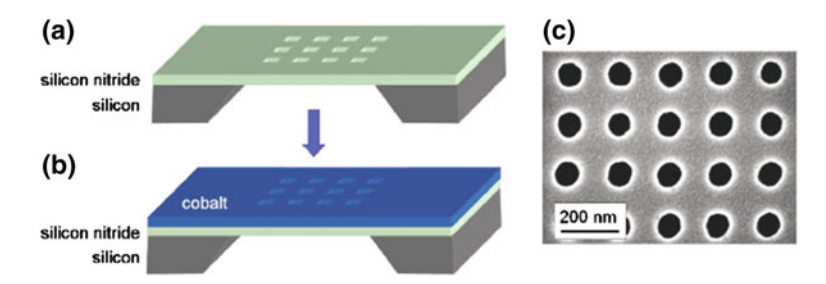


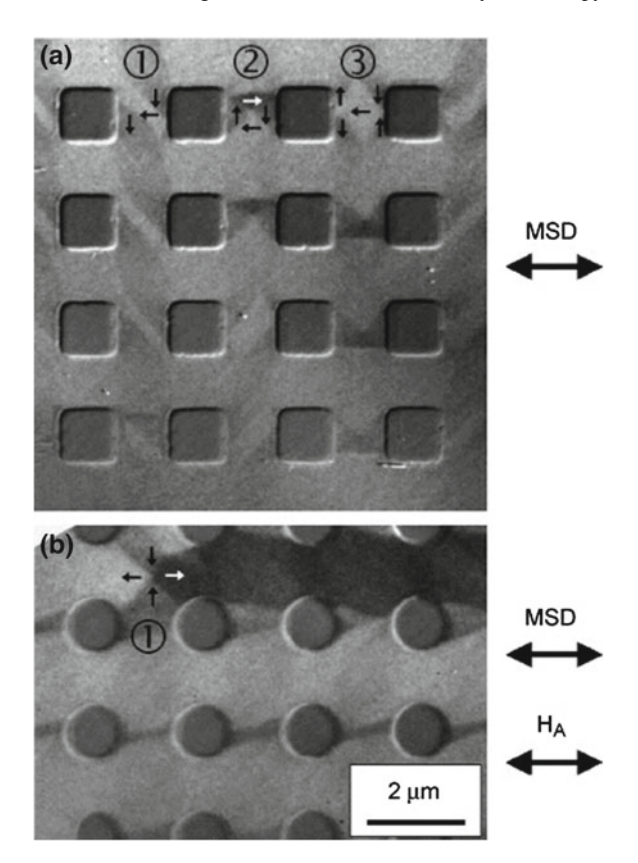
**Fig. 5.16** Schematic diagram showing the fabrication of antidot arrays on silicon nitride membranes: **a** First *hole arrays* are fabricated in the membrane by electron-beam lithography, and **b** a 40 nm-thick cobalt layer is deposited onto the membrane substrate. **c** SEM image of a 200 nm period antidot array. From [414]. Reprinted by permission of Elsevier

now briefly present some results on a Co antidot array obtained by M-TXM. In a first step the antidot pattern was written by an electron-beam writer in a polymethylmethacrylate (PMMA) resist, which was spin-coated onto a silicon nitride membrane substrate coated with a 20 nm thick chromium film. Using reactive ion etching (RIE) this antidot pattern in the PMMA resist was transferred into the chromium thin film, which was subsequently used as a mask to etch holes into the silicon nitride membrane (100 nm thick) by RIE (see Fig. 5.16a). Finally, a 40 nm thin cobalt film, which was the ferromagnetic layer, was deposited on the membrane with the holes (see Fig. 5.16b) by DC-magnetron sputtering and capped with a 1 nm thick aluminium layer to prevent oxidation.

Antidot arrays covering a square area with side length of 10– $20~\mu m$ , and antidot periods p ranging from  $2~\mu m$  down to 200~nm can thus be fabricated and observed with M-TXM. A scanning electron microscope (SEM) image of a typical array is shown in Fig. 5.16~c.

M-TXM results from a study of the spin configuration in Co antidot arrays at the Co  $L_3$  absorption edge are shown in Fig. 5.17. The direction of the applied field,  $H_A$ , is horizontal in the paper plane, which is parallel to the magnetization sensitivity direction (MSD). In the as-grown state, flux closure patterns, reminiscent of those in square elements, are present between the antidots (Fig. 5.17a) and include S states associated with diagonal domains (position 1), Landau states (position 2), and the flower states associated with whisker (or spike) domains (position 3). The first and last states have been predicted for antidot arrays by micromagnetic simulations [415]. After application of an in-plane field, chains of domains appear and interesting spin configurations occur at the chain ends. For example, at the chain ends in the antidot arrays with circular holes (position 1 in Fig. 5.17b), a spin configuration with four  $90^{\circ}$  walls is seen.

**Fig. 5.17** Antidot arrays with 2 μm period: **a** As-grown flux closure states in an array with *square holes* S state at position 1, Landau state at position 2, flower state at position 3, and **b** A domain chain forms upon application of a magnetic field in an array with *circular holes* with the end of the chain comprising of four 90° walls. From [414]. Reprinted by permission of Elsevier



### 5.4.3 Domain Structures in Multilayered Systems

So far, we have demonstrated the capabilities of M-TXM with regard to high-spatial-resolution imaging of magnetic domains upon applying external magnetic fields, and elemental specificity in multicomponent alloy thin films. We now turn to layered magnetic structures. A microscopic understanding of the magnetic coupling of individual layers in multilayered systems is of fundamental interest, but is also at the forefront of current technological developments for magnetic storage and sensor devices. To design a certain functionality, the development of the magnetic microstructure during a full magnetization reversal process in such systems needs to be explored for each individual layer in-situ. The high penetrability of soft X rays, the chemical sensitivity, and the purely photon-based approach of M-TXM makes it the ideal tool for such studies.

As a first example and to demonstrate the capabilities of M-TXM for layer-resolved magnetic domain imaging, we discuss results obtained in a technologically relevant PtCo/TbFe system. Its layer sequence is Pt/[0.75 nm Pt/0.25 nm



Fig. 5.18 Schematic of the layer structure and the antiparallel orientation of the magnetization of each layer in a  $Pt/[0.75 \text{ nm } Pt/0.25 \text{ nm } Co]_{50}/3 \text{ nm } Pt/25 \text{ nm } Tb_{30}Fe_{70}/5 \text{ nm } Pt$  system. From [416]

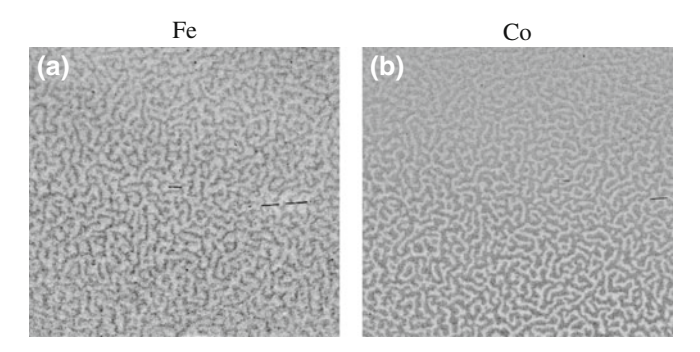


**Fig. 5.19** M-TXM images of a Pt/[0.75 nm Pt/0.25 nm Co] $_{50}$ /3 nm Pt/25 nm Tb $_{30}$ Fe $_{70}$ /5 nm Pt system recorded at -3.0 kOe at the **a** Fe  $L_3$  edge and **b** the Co  $L_3$  edge showing an antiparallel alignment of the magnetization in the two magnetic layers

Co]<sub>50</sub>/3 nm Pt/25 nm Tb<sub>30</sub>Fe<sub>70</sub>/5 nm Pt. This system exhibits a pronounced perpendicular anisotropy. It is expected that the magnetization of the PtCo and the TbFe sublayers couple antiparallel. The schematic design is displayed in Fig. 5.18.

Given the different elemental composition in that system, the elemental sensitivity of M-TXM can be utilized to image at high spatial resolution and in varying applied magnetic fields the magnetic microstructure in the individual layers. Figure 5.19 displays two M-TXM images recorded at remanence, where Fig. 5.19a was taken at the Fe  $L_3$  edge, thereby being sensitive to the magnetic microstructure of the TbFe sublayer only. While maintaining the same magnetic ordering, Fig. 5.19b was recorded by tuning the photon energy to the Co  $L_3$  edge, yielding magnetic information about the [Pt/Co] multilayer. One can easily see that both images exhibit an irregular domain pattern with the smallest features having sizes below 100 nm. By overlaying the two patterns onto each other, one realizes that the patterns obtained at the Co and the Fe absorption edges exhibit a reversed contrast. This is an unambiguous proof that the magnetic moments of the Fe and the Co atoms are antiparallel to each other, since the sense of circular polarization of the X rays was identical in both images.

Complementary to magnetic X-ray microscopy, which images at high spatial resolution the local magnetic spin configuration, X-ray resonant magnetic scattering (XRMS) is another powerful tool that utilizes XMCD as contrast mechanism to obtain, however, information about the averaged magnetic microstructure in ferromagnetic specimens [417–419]. Utilizing *s* linearly polarized incident radiation,

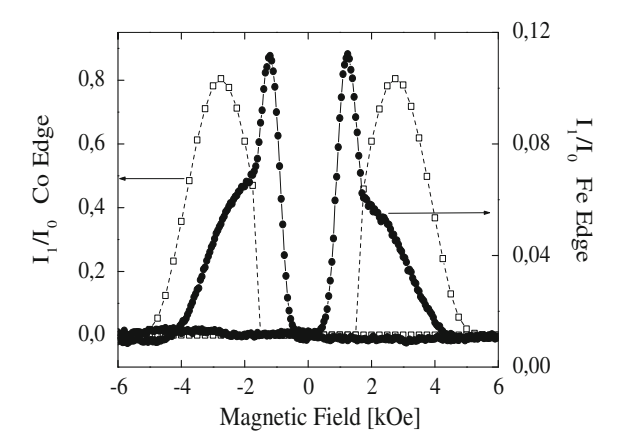


Fig. 5.20 XRMS data of the Pt/ $[0.75 \text{ nm Pt}/0.25 \text{ nm Co}]_{50}/3 \text{ nm Pt}/25 \text{ nm Tb}_{30}\text{Fe}_{70}/5 \text{ nm Pt}$  system recorded at the Fe and Co  $L_3$  absorption edges as a function of magnetic field perpendicular to the sample plane swept from 7 kOe to -7 kOe and back to 7 kOe. The open symbols correspond to the Co results (intensity displayed on the *left axis*), while the solid circles represent the respective Fe signal (*right axis*). Note the weaker signal at the Fe edge compared to the Co edge. From [416]

the scattered intensity then contains contributions from magnetic-magnetic and charge-charge correlations [420]. In the symmetric small-angle scattering geometry, where the scattering vector is contained to the film plane, there would be no magnetic scattering intensity for a uniformly magnetized sample, while it is maximum if a regular domain pattern is present. Fig. 5.20 displays XRMS results for the identical sample as has been used for the X-ray microscopy studies shown in Fig. 5.19. Again, the XRMS spectra were obtained at the Fe and Co  $L_3$  edges to investigate in a layer-sensitive manner the magnetization reversal of each individual layer. The XRMS spectra indicate that upon increasing the external magnetic field a domain pattern develops firstly in the Tb<sub>30</sub>Fe<sub>70</sub> layer, while the [Pt/Co] multilayer is still saturated. At a somewhat higher external field there are both, domains emerging in the [Pt/Co] layer and a reduced number of domains in the Tb<sub>30</sub>Fe<sub>70</sub> layer. The largely reduced scattering intensity at the Fe edge at higher fields either indicates a small magnetization perpendicular to the surface, i.e., a not fully magnetized film as a consequence of the competition between Zeeman and coupling energies, or a small number of magnetic inhomogeneities, such as domains.

It is both, the spatially averaging information of XRMS and the locally resolving magnetic domain structure of M-TXM which provide a complete and coherent microscopic picture of magnetization processes in such layered structures. Whereas Fig. 5.19 was taken at remanence, where the individual Fe and Co magnetizations are coupled antiparallel but with the identical magnetic domain structures, Fig. 5.21 now shows the magnetic microstructure in the [PtCo]/TbFe bilayer system for two different applied external magnetic fields. The top row clearly shows that at 1.6 kOe the Co magnetization is still in the saturated state, i.e., no domain formation has yet occurred, while the Fe-containing layer exhibits already a clear domain structure.

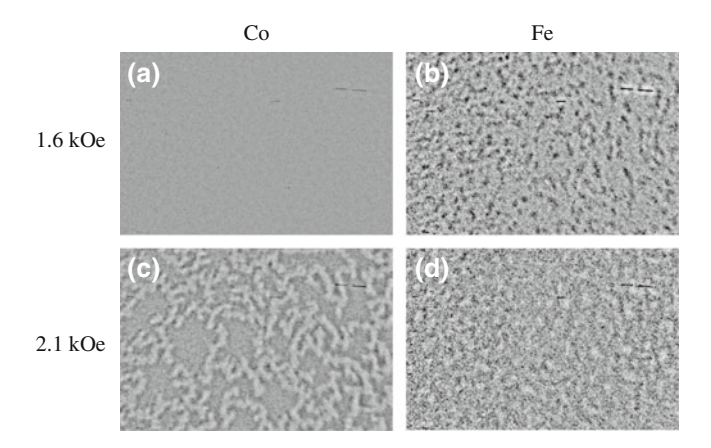


Fig. 5.21 Layer-resolved M-TXM images of a Pt/[0.75 nm Pt/0.25 nm Co] $_{50}$ /3 nm Pt/25 nm Tb $_{30}$ Fe $_{70}$ /5 nm Pt system taken at two different applied magnetic fields as indicated at the *left* (compare Fig. 5.20), revealing the domain configuration in each of the layers individually. The field of view is about 6  $\mu$ m in the horizontal direction. *Left* XMCD contrast at the Co  $L_3$  edge, *right* XMCD contrast at the Fe  $L_3$  edge

The observed magnetic contrast is rather weak, but in agreement with the XRMS data, where the weak signal suggests that the domains formed in the TbFe layers are either not fully magnetized normal to the film or small in number. At a somewhat higher magnetic field (panels (c) and (d) of Fig. 5.21), both layers exhibit a magnetic domain structure, however there is no correlation observable between the two patterns. The antiparallel alignment between the domain patterns of the [PtCo] and the TbFe layers, as shown in Fig. 5.19, develops only at higher magnetic fields around 3 kOe. This is important information since it shows the magnetic coupling on a microscopic length scale. M-TXM is the most suited microscopic technique that provides these results without ambiguity in such a relatively thick sample.

Utilizing dipolar interactions between various adjacent layers in magnetic multilayers is very attractive from a technological point of view. Some examples of dipolar interaction mediated by the magnetostatic stray fields from domain walls have been already presented in Sect. 4.3. To improve the reliability of magnetoelectronic devices and for applications in multilevel magnetic recording, systems with perpendicular anisotropy are considered as potential candidates. Of particular interest are spin valve systems, where the different size of the coercive fields in two layers is utilized. As an example we consider a double layer consisting of 5 nm Ta/20 nm  $Co_{74}$ Tb<sub>26</sub>/3.5 nm Cu/20 nm  $Co_{88}$ Tb<sub>12</sub>/2 nm Cu/2 nm Pt.

The macroscopic characterization of its magnetic behavior is shown in Fig. 5.22 by its M(H) profile obtained by vibrating sample magnetometry (VSM) measurements. There are two steps in the hysteresis loop indicative of the switching of the two magnetic layers at different magnetic fields.

Although, other than in the previous example on the PtCo/TbFe system, both magnetically relevant layers contain the same elements, namely Tb and Co, albeit

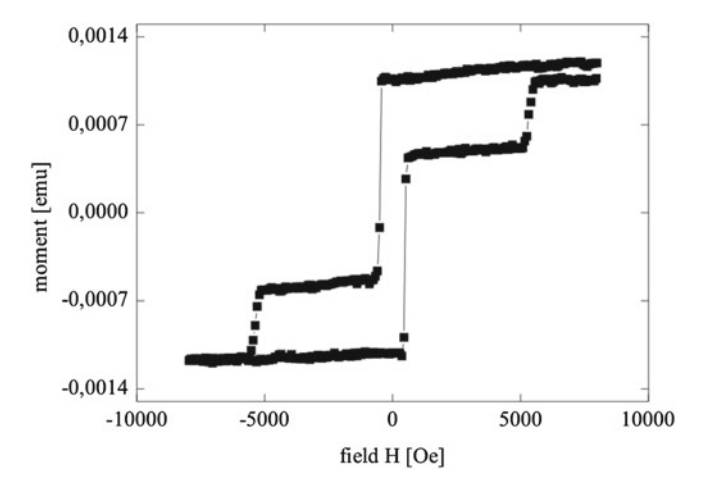


Fig. 5.22 VSM measurement of the spin valve system  $5 \text{ nm Ta}/20 \text{ nm Co}_{74}\text{Tb}_{26}/3.5 \text{ nm Cu}/20 \text{ nm Co}_{88}\text{Tb}_{12}/2 \text{ nm Cu}/2 \text{ nm Pt}$  indicating the switching of the individual magnetic layers at different magnetic fields. From [421]

at different compositions, magnetic X-ray images recorded at the Co  $L_3$  absorption edge still allow to study the development of the domain structure in each layer separately. This is because the hysteretic behavior of the two separate layers with different composition is different, e.g. they switch at different external magnetic fields. Furthermore, the dipolar coupling between each layer has a strong impact on the observed domain structures, if compared to the domain structure and behavior in uncoupled layers of the same composition. Fig. 5.23 shows a sequence of X-ray images taken around the coercive field of the soft layer at about 480 Oe. The shrinking of the magnetic domains in the soft layer in Fig. 5.23a—c can be clearly seen, until at 490 Oe only the domain pattern of the hard magnetic layer remains, indicating that the soft layer has now fully saturated. The boundaries of the remaining domains of the soft layer in Fig. 5.22a—c close to saturation are mostly positioned at domain walls of the hard layer. This indicates that indeed a magnetostatic interaction between the domain walls in the two layers is present.

Another feature related to dipolar interactions in trilayers is the stray field-induced replication of domains or bit patterns, which is a subject of great interest.

As an example we show experimental results of the domain replication in an all-perpendicular anisotropy system. Again, combining a soft/Pd/hard multilayer system, such as 3 nm Pd/[0.2 nm Co $_{30}$ Ni $_{70}$ /1.5 nm Pd] $_{30}$ /10 nm Pd/[0.3 nm Co/0.8 nm Pd] $_{20}$ /1.2 nm Pd, the magnetic configuration of the hard and soft layers can be independently investigated during external magnetic field cycles with M-TXM at the Co and Ni edges, respectively. Field cycles lead to the formation of a soft layer magnetic domain state which is identical to the domain configuration previously trapped in the hard layer.

Hysteresis loops for this system measured at 300 K with the field perpendicular to the sample plane are displayed in Fig. 5.24a. These data indicate already the different

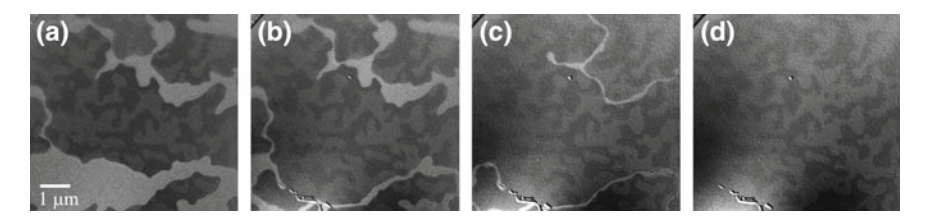


Fig. 5.23 M-TXM images of a spin valve system 5 nm Ta/20 nm Co<sub>74</sub>Tb<sub>26</sub>/3.5 nm Cu/20 nm Co<sub>88</sub>Tb<sub>12</sub>/2 nm Cu/2 nm Pt recorded at the Co  $L_3$  edge in various fields **a** 315 Oe, **b** 343 Oe, **c** 455 Oe, and **d** 490 Oe within the hysteresis loop. The magnetically hard Co<sub>74</sub>Tb<sub>26</sub> layer does not change its domain configuration in this field range, while the soft Co<sub>88</sub>Tb<sub>12</sub> layer switches completely into a fully saturated state at 490 Oe in agreement with the M(H) curve obtained from VSM (Fig. 5.22)

switching in the individual layers. Starting from positive saturation, the major loop reveals two distinct steps corresponding to the independent reversal of the soft layer at  $H_N^0=350$  Oe followed by the switching of the hard layer at H=4 kOe. The minor field cycles for saturated hard layer (dotted line) and for half-reversed hard-layer magnetization (open symbols) are distinctly different. Sweeping the external perpendicular magnetic field from +8 to -4.2 kOe, where the hard layer has reversed half of its magnetization, a domain state is created in the hard layer with about 50% up and 50% down domains. These domains interact via their stray field with the soft layer, which leads to the different behavior. Fig. 5.24b points out this difference. It displays the derivative dM/dH of the descending branch of the magnetization loop during the reversal of the soft layer starts at lower fields  $H_N^d$  compared to the saturated hard layer. This is attributed to the magnetostatic interaction between the two layers [422].

This interpretation of hysteresis data can be directly visualized by layer-resolved M-TXM. Tuning the photon energy to the Co  $L_3$  absorption edge and recording the domain structures in external magnetic fields perpendicular to the sample plane, Fig. 5.24c indeed confirms that after reversing half of the hard layer magnetization, an equal amount of up and down labyrinth domain patterns are visible. Since the soft layer magnetization is already saturated for the field applied in Fig. 5.24c, the domain configuration measured at the Co  $L_3$  edge reflects the hard layer state only. The reversal of the soft layer can be visualized by tuning the photon energy to the Ni  $L_3$  edge (Fig. 5.24d, e). Starting from positive soft layer saturation, one observes the domain nucleation around 0 Oe in the soft layer (Fig. 5.24d), in perfect agreement with the magnetization data in Fig. 5.24a. Reducing the field further to about -300 Oe (Fig. 5.24e) leads to a domain pattern in the soft layer that very much resembles the one of the hard layer (Fig. 5.24c). This indicates that the changes in the soft layer reversal originate from the influence of dipolar fields induced by the hard layer domains on the soft layer. At about -300 Oe, the domain state of the hard layer has been completely copied (replicated) into the soft layer. It is interesting to note that,

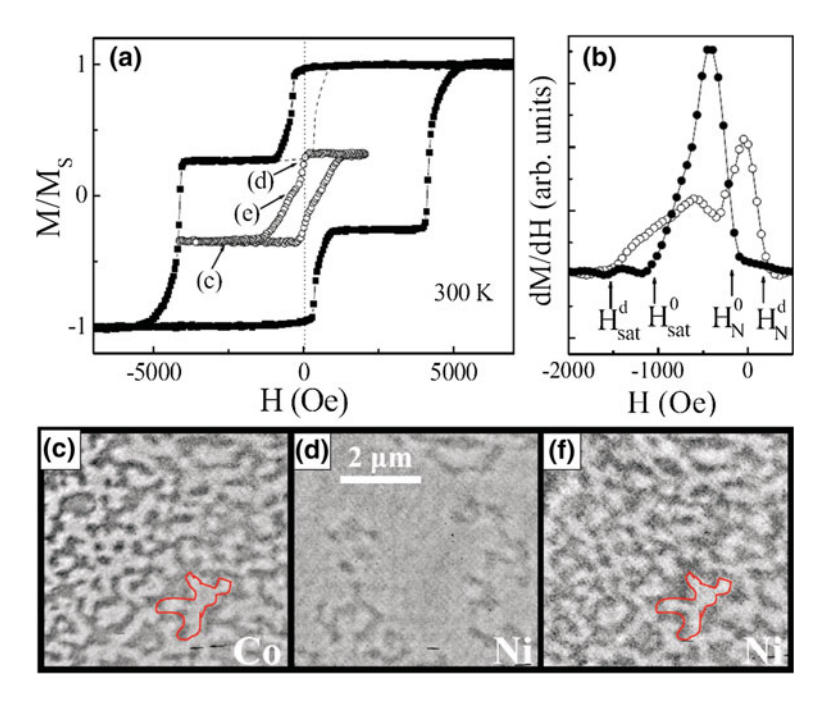


Fig. 5.24 a Normalized hysteresis loops of a [CoNi/Pd]<sub>30</sub>/Pd/[Co/Pd]<sub>20</sub> soft/Pd/hard multilayer system measured at 300 K. *Square solid* symbols show the major loop, while the *dashed line* and *open circles* correspond to minor loops with the hard layer in a uniform and a domain state, respectively. **b** Derivative of the descending major and minor (*solid* and *open* symbols) hysteresis loop branches. **c**-**e** M-TXM images, each  $6 \times 6 \mu m^2$ , showing the magnetic domain configuration as observed for the three states marked in (**a**), respectively. Image **c** is collected at the Co  $L_3$  edge (778 eV), while images **d** and **e** are obtained at the Ni  $L_3$  edge (854 eV). *Lines* mark a particular magnetic domain in order to facilitate comparison of the images. From [422]

although the same replicated domain state is observed during several successive field loops, there is no evidence for an identical nucleation sequence.

## 5.5 Time and Layer-Resolved Magnetic Imaging by M-TXM

The results presented so far in this chapter utilized the elemental specificity of XMCD and the high spatial resolution of soft X-ray microscopy to study layer-resolved static domain structures in multilayered and nanostructured ferromagnetic systems. Like the methods presented in the previous chapters, M-TXM allows to implement time resolution in order to study, in addition, the spin dynamics in the sub-nanosecond regime. Time-resolved M-TXM is performed a stroboscopic pump-probe experiment, where the time resolution is given by the inherent time structure of the X-ray

source. As for time-resolved magnetic imaging using PEEM (Sect. 4.5), this concept has two fundamental limitations that one should be aware of:

- The time resolution is dictated by the shortest X-ray pulse one can achieve with current synchrotron sources. This is typically in the sub-nanosecond regime. There are techniques available to pursue synchrotron experiments with a femtosecond time resolution, e.g., slicing a part from the electron bunch or to sweep the detector signal very fast laterally (streak camera). However, due to the massive reduction in photon intensity, this approach is not a viable way for two-dimensional high-resolution imaging.
- The limited number of photons per X-ray pulse is even at today's high-brilliance synchrotron sources very limited and therefore only a stroboscopic scheme is feasible. Consequently, this implies that only the reproducible component of spin dynamic processes can be addressed. The scientifically fascinating and technologically challenging areas of non-reproducable, e.g., fluctuating fast and ultrafast spin dynamics, can only be approached in single-shot imaging experiments. Upcoming facilities for highly intense and ultrashort X-ray pulses such as X-ray free electron laser sources or other femtosecond sources, including high harmonic generation lab based X-ray sources, hold the promise to close this gap.

We will in the following present some examples of time-resolved M-TXM studies. The first example deals with the excitation of a single layer microstructured square permalloy element with an out-of-plane magnetic field pulse [423]. To excite the spin dynamics, a pump pulse generating a short magnetic field pulse with a rise time of 100 ps was generated by a voltage pulse launched into a 50 Ohm-matched micro coil, as schematically shown in Fig. 5.25. The probe is the X-ray flash of the synchrotron, which is delayed with respect to the pump pulse in steps of less than 20 ps to study the temporal evolution of the magnetization. Due to the limited photon flux in a single burst, the typical accumulation time per image is about 3–5 s, and about 500

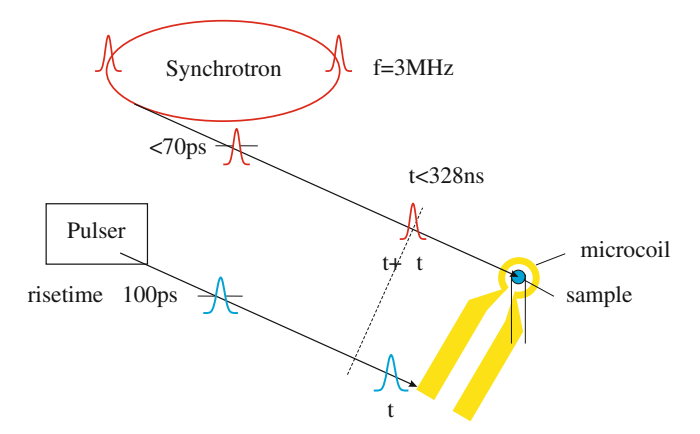


Fig. 5.25 Experimental set-up for stroboscopic imaging with a pump-and-probe scheme at the ALS running in two-bunch mode

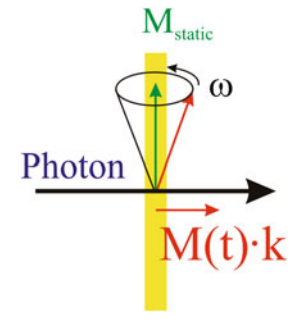
images need to be integrated for each time step. Taking into account the 3 MHz repetition rate of the synchrotron, the sample has undergone for one single image about  $10^8-10^9$  pump–probe cycles. To further increase the signal-to-background ratio, in this study images with the magnetic field pulse applied in forward  $(I^+)$  and backward  $(I^-)$  direction were recorded to obtain a normalized signal  $(I^+ - I^-)/(I^+ + I^-)$ . Generally, as is done with static images, a saturated magnetic image is subtracted from each image taken for each time step to remove non-magnetic contributions.

Upon excitation with the pump pulse the magnetization starts a precession and accordingly changes its direction with time. As a function of the delay time between the pump and the probe pulse one therefore expects a time-varying projection of the magnetization onto the photon propagation direction, i.e., a time-dependent XMCD signal as can be seen in the schematic of Fig. 5.26.

The bottom row of Fig. 5.27 [423] shows time-resolved M-TXM results for a  $4\,\mu m \times 4\,\mu m \times 50\,nm$  Py element. Both the coil and the sample were prepared by electron-beam lithography onto a  $Si_3N_4$  membrane. Field pulses of 100 ps rise time and a maximum field strength of about 50 Oe are generated by an electronic pulser. The sample is viewed at normal incidence to the photon beam and thus the static in-plane domain structure (c.f. Fig. 5.13) is invisible, while the field pulse applied normal to the sample plane creates a time-dependent z component of the magnetization that can be recorded.

If the probe pulse arrives at the sample before the pump pulse, the magnetization is still in its ground state, and therefore no magnetic contrast is observed. However, right after the pump pulse the magnetization starts to precess, and the result clearly shows two different precession frequencies at different locations in the sample. While the first mode refers to the square as a whole, which can be seen by the overall change of contrast across the whole square being maximum at  $+400\,\mathrm{ps}$ , a second mode is located only at the diagonals in the square, i.e., at the region of the domain walls. The contrast at the domain walls appears only at later times, visible in the image for  $\Delta t = +600\,\mathrm{ps}$ . This implies a lower precession frequency at the positions of the domain walls compared to the regions within the domains. The top row in Fig. 5.27 shows corresponding micromagnetic simulations based on the Landau-Lifshitz-Gilbert equation (1.1). The agreement between modeling and experimental

Fig. 5.26 Schematics of the precessional motion of the magnetization upon excitation with a short field pulse. As a function of the delay time between pump and probe pulse the magnetization exhibits a varying projection along the photon beam direction



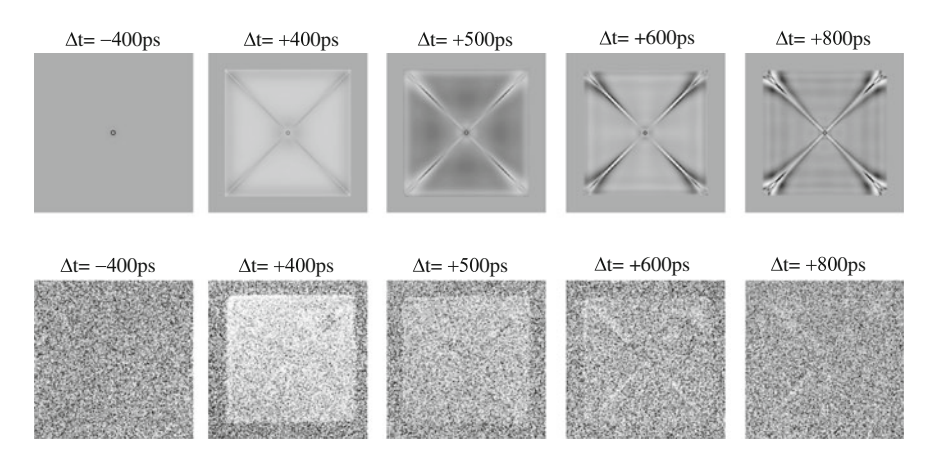


Fig. 5.27  $\it Top$  Simulation and  $\it bottom$  Experimental data of the local distribution of magnetization dynamics in a  $4 \, \mu m \times 4 \, \mu m \times 50 \, nm$  Py element. Different columns show the differential change in contrast, i.e., the difference between images taken at different delay times, as a function of delay time between magnetic field pulse and X-ray probe pulse. From [423]. Reprinted by permission of AIP

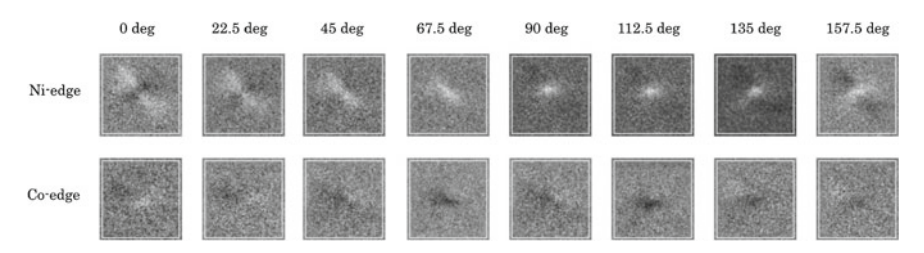


Fig. 5.28 Spatially resolved differential images of a  $1 \times 1 \,\mu\text{m}^2$  Ni<sub>80</sub>Fe<sub>20</sub>/Cu/Co trilayer element, taken at the  $L_3$  Ni (top row) and Co edges (bottom row). The images are recorded at different delay times of the 250 MHz excitation with respect to the probing X-ray flashes. The time delay steps correspond to specific phase changes of the sinusoidally alternating excitation field. The image contrast represents the difference in XMCD intensity of two images taken for 180° different phases. From [424]. Reprinted by permission of AIP

data is excellent, which indicates that the spin dynamics at sub-ns time scales can be adequately described by this model.

Such time-resolved studies can also be performed on layered magnetic materials, playing up the advantage of layer-selective magnetic imaging. Figure 5.28 shows an example of a scanning transmission X-ray microscopy study on a  $1 \times 1~\mu\text{m}^2$  element of a trilayer composed of a ferromagnetic permalloy (Ni<sub>80</sub>Fe<sub>20</sub>) layer and a Co layer, 20 nm in thickness each, separated by 10 nm of nonmagnetic Cu [424]. In static conditions, the two ferromagnetic layers exhibit identical Landau flux-closure domain patterns, similar to the one shown in Fig. 5.13. For the dynamic measurements, the structure was subject to an in-plane sinusoidal magnetic field of 250 MHz and an amplitude of 8,000 A/m. To enhance the very weak magnetic contrast, Fig. 5.28, like

Fig. 5.27, shows the differential XMCD contrast, i.e., the difference between XMCD images recorded at the eight different phase angles during a field cycle, as labeled at the top of the images, and the corresponding XMCD images recorded at 180° different phase. The upper row shows images taken at the photon energy of the Ni  $L_3$  edge, corresponding to the magnetic domain configuration in the Ni<sub>80</sub>Fe<sub>20</sub> layer, the bottom row shows images acquired at the Co  $L_3$  edge, representing the Co layer. It is evident that the dynamic response to the AC magnetic field is different in the two layers. Whereas the contrast change in the center of the magnetically softer Ni<sub>80</sub>Fe<sub>20</sub> layer is positive (bright contrast) at phases around 90°, the magnetically harder Co layer exhibits dark contrast. The contrast patterns of the Ni<sub>80</sub>Fe<sub>20</sub> layer at 0 and 157.5° point towards a displacement of the vortex core in the center of the Landau domain pattern to the left and right, respectively, and indicate thus a circular-like vortex core motion in the Ni<sub>80</sub>Fe<sub>20</sub> layer [424]. The motion of the domain pattern in the Co layer is not so easily identified from the images shown in Fig. 5.28, but is clearly different from that of the Ni<sub>80</sub>Fe<sub>20</sub> layer, suggesting a magnetostatic repulsion between the two vortex cores in dynamic conditions.

#### **5.6 Future Perspectives**

Magnetic transmission X-ray microscopy is a powerful technique that allows to investigate the static and dynamic character of magnetic structures in a variety of nanoscale, multicomponent, and multilayered magnetic materials. The diffraction limit of soft X rays is far below the spatial resolution that can be addressed with current Fresnel zone plates used as optical element, which leaves therefore a lot of room for further improvements. Fundamental length scales such as magnetic exchange lengths are within reach with the current strategy to fabricate zone plates with an outermost zone width down to 10 nm and below.

The time resolution so far is limited by the available sources. However, the emerging X-ray free electron laser sources will provide soft X-ray pulses with a time structure in the femtosecond regime and more than enough peak brilliance to allow for single-shot experiments. This will grant access to fundamental time scales in nanomagnetism.

Together with XMCD as element-specific contrast mechanism and the huge magnetic cross section, the magnetization dynamics in complex heterostructures that can be investigated with magnetic transmission X-ray microscopy will provide detailed insight into fundamental principles of magnetism in layered devices.

- 1. A. Yelon, Interactions in multilayer magnetic films, in *Physics of thin films*, vol. 6, ed. by G. Hass, R.E. Tun (Academic Press, New York, London, 1971), pp. 205–300
- 2. U. Gradmann. Magnetism in ultrathin transition metal films. In: K. H. J. Buschow (Ed.), Handbook of Magnetic Materials, vol. 7, 1. Elsevier (1993)
- 3. E. Bauer. Growth of thin films. J. Phys.: Cond. Matt. 11, 9365 (1999)
- 4. J. Thomassen, F. May, B. Feldmann, M. Wuttig, H. Ibach, Magnetic live surface layers in Fe/Cu(100). Phys. Rev. Lett. **69**, 3831 (1992)
- 5. S. Müller, P. Bayer, C. Reischl, K. Heinz, B. Feldmann, H. Zillgen, M. Wuttig, Structural instability of ferromagnetic fcc Fe films on Cu(100). Phys. Rev. Lett. **74**, 765 (1995)
- W.L. O'Brien, B.P. Tonner, Room-temperature magnetic phases of Fe on fcc Co(001) and Ni(001). Phys. Rev. B 52, 15332 (1995)
- 7. W. Kuch, S.S.P. Parkin, Fe structural and magnetic phases in Fe/Ni $_{81}$ Fe $_{19}$ (001) multilayers. Europhys. Lett. **37**, 465 (1997)
- S. Sundar Manoharan, M. Klaua, J. Shen, J. Barthel, H. Jenniches, J. Kirschner. Artificially ordered Fe-Cu alloy superlattices on Cu(001). I. Studies on the structural and magnetic properties. Phys. Rev. B 58, 8549 (1998)
- 9. M. Wuttig, X. Liu, *Ultrathin metal films* (Springer, Berlin, 1994)
- D. Sander, The correlation between mechanical stress and magnetic anisotropy in ultrathin films. Rep. Prog. Phys. 62, 809 (1999)
- C.M. Schneider, P. Bressler, P. Schuster, J. Kirschner, J.J. de Miguel, R. Miranda, Curie temperature of ultrathin films of fcc cobalt epitaxially grown on atomically flat Cu(100) surfaces. Phys. Rev. Lett. 64, 1059 (1990)
- J. Kohlhepp, H.J. Elmers, S. Cordes, U. Gradmann, Power laws of magnetization in ferromagnetic monolayers and the two-dimensional Ising model. Phys. Rev. B 45, 12287 (1992)
- 13. Y. Li, K. Baberschke, Dimensional crossover in ultrathin Ni(111) films on W(110). Phys. Rev. Lett. 68, 1208 (1992)
- H.J. Elmers, J. Hauschild, U. Gradmann, Critical behavior of the uniaxial ferromagnetic monolayer Fe(110) on W(110). Phys. Rev. B 54, 15224 (1996)
- 15. J.A.C. Bland, C. Daboo, B. Heinrich, Z. Celinski, R.D. Bateson, Enhanced magnetic moments in bcc Fe films. Phys. Rev. B **51**, 258 (1995)
- J. Hunter Dunn, D. Arvanitis, N. Mårtensson. Magnetism of thin Fe films on Cu(100). Phys. Rev. B 54, R11157 (1996)
- 17. G. Rangelov, H.D. Kang, J. Reinmuth, M. Donath, Surface magnetic properties of ultrathin Fe films on W(110) studied by spin-resolved appearance potential spectroscopy. Phys. Rev. B **61**, 549 (2000)
- D. Weller, J. Stöhr, R. Nakajima, A. Carl, M.G. Samant, C. Chappert, R. Mégy, P. Beauvillain,
   P. Veillet, G.A. Held, Microscopic origin of magnetic anisotropy in Au/Co/Au probed with
   x-ray magnetic circular dichroism. Phys. Rev. Lett. 75, 3752 (1995)

M. Tischer, O. Hjortstam, D. Arvanitis, J. Hunter, Dunn, F. May, K. Baberschke, J. Trygg, J. M. Wills, B. Johansson, O. Eriksson. Enhancement of orbital magnetism at surfaces: Co on Cu(100). Phys. Rev. Lett. 75, 1602 (1995)

- W. Kuch, M. Salvietti, X. Gao, M.-T. Lin, M. Klaua, J. Barthel, C.V. Mohan, J. Kirschner, Artificially ordered FeCu alloy superlattices on Cu(001). II. Spin-resolved electronic properties and magnetic dichroism. Phys. Rev. B 58, 8556 (1998)
- P. Ryan, R.P. Winarski, D.J. Keavney, J.W. Freeland, R.A. Rosenberg, S. Park, C.M. Falco, Enhanced magnetic orbital moment of ultrathin Co films on Ge(100). Phys. Rev. B 69, 054416 (2004)
- 22. D.P. Pappas, K.-P. Kämper, H. Hopster, Reversible transition between perpendicular and inplane magnetization in ultrathin films. Phys. Rev. Lett. **64**, 3179 (1990)
- M. Albrecht, T. Furubayashi, M. Przybylski, J. Korecki, U. Gradman, Magnetic step anisotropies. J. Magn. Magn. Mater. 113, 207 (1992)
- M. Farle, B. Mirwald-Schulz, A.N. Anisimov, W. Platow, K. Baberschke, Higher-order magnetic anisotropies and the nature of the spin-reorientation transition in face-centered-tetragonal Ni(001)/Cu(001). Phys. Rev. B 55, 3708 (1997)
- M. Farle, Ferromagnetic resonance of ultrathin metallic layers. Rep. Prog. Phys. 61, 755 (1998)
- S. Rusponi, T. Cren, N. Weiss, M. Epple, P. Buluschek, L. Claude, H. Brune, The remarkable difference between surface and step atoms in the magnetic anisotropy of two-dimensional nanostructures. Nat. Mater. 2, 546 (2003)
- I.M. Miron, K. Garello, G. Gaudin, P.-J. Zermatten, M.V. Costache, S. Auffret, S. Bandiera,
   B. Rodmacq, A. Schuhl, P. Gambardella, Perpendicular switching of a single ferromagnetic layer induced by in-plane current injection. Nature 476, 189 (2011)
- 28. A. Hoffmann, Spin Hall Effects in Metals. IEEE Trans. Mag. 49, 5172 (2013)
- I.M. Miron, G. Gaudin, S. Auffret, B. Rodmacq, A. Schuhl, S. Pizzini, J. Vogel, P. Gambardella, Current-driven spin torque induced by the Rashba effect in a ferromagnetic metal layer. Nat. Mater. 9, 230 (2010)
- J.A.C. Bland, B. Heinrich, *Ultrathin magnetic structures*, vol. 1 (Springer, Berlin Heidelberg New York, 2004)
- B. Heinrich, J.A.C. Bland, *Ultrathin magnetic structures*, vol. 2 (Springer, Berlin Heidelberg New York, 1994)
- 32. P. Grünberg, R. Schreiber, Y. Pang, M.B. Brodsky, H. Sowers, Layered Magnetic Structures: Evidence for Antiferromagnetic Coupling of Fe Layers across Cr Interlayers. Phys. Rev. Lett. **57**, 2442 (1986)
- 33. S.S.P. Parkin, N. More, K.P. Roche, Oscillations in exchange coupling and magnetoresistance in metallic superlattice structures: Co/Ru, Co/Cr, and Fe/Cr. Phys. Rev. Lett. **64**, 2304 (1990)
- 34. M.N. Baibich, J.M. Broto, A. Fert, F. Nguyen Van Dau, F. Petroff, P. Etienne, G. Creuzet, A. Friederich, J. Chazelas, Giant magnetoresistance of (001)Fe/(001)Cr magnetic superlattices. Phys. Rev. Lett. **61**, 2472 (1988)
- G. Binasch, P. Grünberg, F. Saurenbach, W. Zinn, Enhanced magnetoresistance in layered magnetic structures with antiferromagnetic interlayer exchange. Phys. Rev. B 39, 4828 (1989)
- R.L. White, Giant magnetoresistance materials and their potential as read head sensors. IEEE Trans. Magn. 30, 346 (1994)
- C.H. Tsang, R.E. Fontana Jr, T. Lin, D. Heim, B.A. Gurney, M.L. Williams, Design, fabrication, and performance of spin-valve read heads for magnetic recording applications. IBM J. Res. Develop. 42, 103 (1998)
- B. Dieny, V.S. Speriosu, S.S.P. Parkin, B.A. Gurney, D.R. Wilhoit, D. Mauri, Giant magnetoresistance in soft ferromagnetic multilayers. Phys. Rev. B 43, 1297 (1991)
- 39. S.S.P. Parkin, Origin of enhanced magnetoresistance of magnetic multilayers: Spin-dependent scattering from magnetic interface states. Phys. Rev. Lett. **71**, 1641 (1993)
- S.S.P. Parkin, Systematic variation of the strength and oscillation period of indirect magnetic exchange coupling through the 3d, 4d, and 5d transition metals. Phys. Rev. Lett. 67, 3598 (1991)

41. S.S.P. Parkin, R. Bhadra, K.P. Roche, Oscillatory magnetic exchange coupling through thin copper layers. Phys. Rev. Lett. **66**, 2152 (1991)

- A. Cebollada, R. Miranda, C.M. Schneider, P. Schuster, J. Kirschner, Experimental evidence of an oscillatory magnetic coupling in Co/Cu/Co epitaxial layers. J. Magn. Magn. Mater. 102, 25 (1991)
- 43. M. Julliere, Tunneling between ferromagnetic films. Phys. Lett. A 54, 225 (1975)
- 44. S.S.P. Parkin, K.P. Roche, M.G. Samant, P.M. Rice, R.B. Beyers, R.E. Scheuerlein, E.J. O'Sullivan, S.L. Brown, J. Bucchigano, D.W. Abraham, Y. Lu, M. Rooks, P.L. Trouilloud, R.A. Wanner, W.J. Gallagher, Exchange-biased magnetic tunnel junctions and application to nonvolatile magnetic random access memory. J. Appl. Phys. 85, 5828 (1999)
- 45. S. Tehrani, J. Slaughter, E. Chen, M. Durlam, J. Shi, M. DeHerren, Progress and outlook for MRAM technology. IEEE Trans. Magn. 35, 2814 (1999)
- 46. J.C. Slonczewski, Conductance and exchange coupling of two ferromagnets separated by a tunneling barrier. Phys. Rev. B **39**, 6995 (1989)
- 47. R. Meservey, P.M. Tedrow, Spin-polarized electron tunneling. Phys. Rep. 238, 173 (1994)
- 48. J.S. Moodera, G. Mathon, Spin polarized tunneling in ferromagnetic junctions. J. Magn. Magn. Mater. **200**, 248 (1999)
- J.S. Moodera, L.R. Kinder, T.M. Wong, R. Meservey, Large Magnetoresistance at Room Temperature in Ferromagnetic Thin Film Tunnel Junctions. Phys. Rev. Lett. 74, 3273 (1995)
- J.S. Moodera, J. Nowak, R.J.M. van de Veerdonk, Interface Magnetism and Spin Wave Scattering in Ferromagnet-Insulator-Ferromagnet Tunnel Junctions. Phys. Rev. Lett. 80, 2941 (1998)
- P. LeClair, H.J.M. Swagten, J.T. Kohlhepp, R.J.M. van de Veerdonk, W.J.M. de Jonge, Apparent Spin Polarization Decay in Cu-Dusted Co/Al<sub>2</sub>O<sub>3</sub>/Co Tunnel Junctions. Phys. Rev. Lett. 84, 2933 (2000)
- 52. P. LeClair, J.T. Kohlhepp, H.J.M. Swagten, W.J.M. de Jonge, Interfacial density of states in magnetic tunnel junctions. Phys. Rev. Lett. **86**, 1066 (2001)
- P. LeClair, J.T. Kohlhepp, C.H. van de Vin, H. Wieldraaijer, H.J.M. Swagten, W.J.M. de Jonge,
   A.H. Davis, J.M. MacLaren, J.S. Moodera, R. Jansen, Band Structure and Density of States
   Effects in Co-Based Magnetic Tunnel Junctions. Phys. Rev. Lett. 88, 107201 (2002)
- S. Yuasa, T. Nagahama, Y. Suzuki, Spin-polarized resonant tunneling in magnetic tunnel junctions. Science 297, 234 (2002)
- S.S.P. Parkin, C. Kaiser, A. Panchula, P.M. Rice, B. Hughes, M. Samant, S.-H. Yang, Giant tunnelling magnetoresistance at room temperature with MgO (100) tunnel barriers. Nat. Mater. 3, 862 (2004)
- K. Nagasaka, CPP-GMR technology for magnetic read heads of future high-density recording systems. J. Magn. Magn. Mater. 321, 508 (2009)
- B.N. Engel, J. Åkerman, B. Butcher, R. Dave, M. DeHerrera, M. Durlam, G. Grynkewich, J. Janesky, S. Pietambaram, N. Rizzo, J. Slaughter, K. Smith, J.J. Sun, S. Tehrani, A 4-Mb toggle MRAM based on a novel bit and switching method. IEEE Trans. Magn. 41, 132 (2005)
- 58. J.-G. Zhu, Y. Zheng, G.A. Prinz, Ultrahigh density vertical magnetoresistive random access memory. J. Appl. Phys. **87**, 6668 (2000)
- S. Tehrani, J.M. Slaughter, M. DeHerrera, B. Engel, N. Rizzo, J. Salter, M. Durlam, R. Dave, J. Janesky, B. Butcher, K. Smith, G. Grynkewich, Magnetoresistive random access memory using magnetic tunnel junctions. Proceedings of the IEEE 91, 703 (2005)
- J.C. Slonczewski, Current-driven excitation of magnetic multilayers. J. Magn. Magn. Mater. 159, L1 (1996)
- E.B. Myers, D.C. Ralph, J.A. Katine, R.N. Louie, R.A. Buhrman, Current-induced switching of domains in magnetic multilayer devices. Science 285, 867 (1999)
- J.-E. Wegrowe, D. Kelly, Y. Jaccard, P. Guittienne, J.-P. Ansermet, Current-induced magnetization reversal in magnetic nanowires. Europhys. Lett. 45, 626 (1999)
- 63. J.A. Katine, F.J. Albert, R.A. Buhrman, E.B. Myers, D.C. Ralph, Current-driven magnetization reversal and spin-wave excitations in Co/Cu/Co pillars. Phys. Rev. Lett. **84**, 3149 (2000)

 S. Mangin, D. Ravelosona, J.A. Katine, M.J. Carey, B.D. Terris, E.E. Fullerton, Currentinduced magnetization reversal in nanopillars with perpendicular anisotropy. Nat. Mater. 5, 210 (2006)

- S. Ikeda, K. Miura, H. Yamamoto, K. Mizunuma, H.D. Gan, M. Endo, S. Kanai, J. Hayakawa, F. Matsukura, H. Ohno, A perpendicular-anisotropy CoFeBMgO magnetic tunnel junction. Nat. Mater. 9, 721 (2010)
- D.C. Worledge, G. Hu, D.W. Abraham, J.Z. Sun, P.L. Trouilloud, J. Nowak, S. Brown, M.C. Gaidis, E.J. O'Sullivan, R.P. Robertazzi, Spin torque switching of perpendicular Ta-CoFeB-MgO-based magnetic tunnel junctions. Appl. Phys. Lett. 98, 022501 (2011)
- 67. G.A. Prinz, Magnetoelectronics. Science 282, 1660 (1998)
- 68. G.A. Prinz, Magnetoelectronics applications. J. Magn. Magn. Mater. 200, 57 (1999)
- S.A. Wolf, D.D. Awschalom, R.A. Buhrman, J.M. Daughton, S. von Molnár, M.L. Roukes, A.Y. Chtchelkanova, D.M. Treger, Spintronics: A Spin-Based Electronics Vision for the Future. Science 294, 1488 (2001)
- 70. S.D. Bader, S.S.P. Parkin, Spintronics. Annu. Rev. Condens. Matter Phys. 1, 71 (2010)
- 71. T. Shinjo (ed.), Nanomagnetism and Spintronics (Elsevier, Oxford, 2009)
- G. E. W. Bauer, A. H. MacDonald, and S. Maekawa (Eds.). Spin Caloritronics, Special issue of Solid State Commun. vol. 150, 459–552 Elsevier (2010)
- R. Jansen, P.S. Anil, Kumar, O. M. J. van't Erve, R. Vlutters, P. de Haan, and J. C. Lodder. Thermal spin-wave scattering in hot-electron magnetotransport across a spin valve. Phys. Rev. Lett. 85, 3277 (2000)
- 74. P.A. Kumar, R. Jansen, O. van't Erve, R. Vlutters, S. Kim, and J. Lodder. 300% magnetocurrent in a room temperature operating spin-valve transistor. Physica C: Superconductivity **350**, 166 (2001)
- S. van Dijken, X. Jiang, S.S.P. Parkin, Comparison of magnetocurrent and transfer ratio in magnetic tunnel transistors with spin-valve bases containing Cu and Au spacer layers. Appl. Phys. Lett. 82, 775 (2003)
- 76. S. van Dijken, X. Jiang, S.S.P. Parkin, Giant magnetocurrent exceeding 3400% in magnetic tunnel transistors with spin-valve base layers. Appl. Phys. Lett. 83, 951 (2003)
- O. M. J. van't Erve, R. Vlutters, P. S. Anil Kumar, S. D. Kim, F. M. Postma, R. Jansen, J. C. Lodder. Transfer ratio of the spin-valve transistor, Appl. Phys. Lett. 80, 3787 (2002)
- 78. P.R. Hammar, B.R. Bennett, M.J. Yang, M. Johnson, Observation of spin injection at a ferromagnet-semiconductor interface. Phys. Rev. Lett. **83**, 203 (1999)
- 79. Y. Ohno, D.K. Young, B. Beschoten, F. Matsukura, H. Ohno, D.D. Awschalom, Electrical spin injection in a ferromagnetic semiconductor heterostructure. Nature **402**, 790 (1999)
- G. Schmidt, D. Ferrand, L.W. Molenkamp, A.T. Filip, B.J. van Wees, Fundamental obstacle for electrical spin injection from a ferromagnetic metal into a diffusive semiconductor. Phys. Rev. B 62, R4790 (2000)
- G. Schmidt, G. Richter, P. Grabs, C. Gould, D. Ferrand, L.W. Molenkamp, Large Magnetoresistance Effect Due to Spin Injection into a Nonmagnetic Semiconductor. Phys. Rev. Lett. 87, 227203 (2001)
- V.P. LaBella, D.W. Bullock, Z. Ding, C. Emery, A. Venkatesan, W.F. Oliver, G.J. Salamo, P.M. Thibado, M. Mortazavi, Spatially resolved spin-injection probability for gallium arsenide. Science 292, 1518 (2001)
- 83. G.A. de Wijs, R.A. de Groot, Towards 100% spin-polarized charge-injection: The half-metallic NiMnSb/CdS interface. Phys. Rev. B **64**, 020402 (2001)
- 84. G. Schmidt, Concepts for spin injection into semiconductors-a review. J. Phys. D: Appl. Phys. 38, R107 (2005)
- A. Schmehl, V. Vaithyanathan, A. Herrnberger, S. Thiel, C. Richter, M. Liberati, T. Heeg, M. Röckerath, L.F. Kourkoutis, S. Mühlbauer, P. Böni, D.A. Muller, Y. Barash, J. Schubert, Y. Idzerda, J. Mannhart, D.G. Schlom, Epitaxial integration of the highly spin-polarized ferromagnetic semiconductor EuO with silicon and GaN. Nat. Mater. 6, 882 (2007)
- B.T. Jonker, G. Kioseoglou, A.T. Hanbicki, C.H. Li, P.E. Thompson, Electrical spin injection into silicon from a ferromagnetic metal/tunnel barrier contact. Nat. Phys. 3, 542 (2007)

J. Wang, J.B. Neaton, H. Zheng, V. Nagarajan, S.B. Ogale, B. Liu, D. Viehland,
 V. Vaithyanathan, D.G. Schlom, U.V. Waghmare, N.A. Spaldin, K.M. Rabe, M. Wuttig,
 R. Ramesh, Epitaxial BiFeO<sub>3</sub> Multiferroic Thin Film Heterostructures. Science 299, 1719 (2003)

- 88. M. Fiebig, T. Lottermoser, D. Fröhlich, A.V. Goltsev, R.V. Pisarev, Observation of coupled magnetic and electric domains. Nature **419**, 818 (2002)
- 89. M. Fiebig, Revival of the magnetoelectric effect. J. Phys. D: Appl. Phys. 38, R123 (2005)
- 90. N.A. Hill, Density functional studies of multiferroic magnetoelectrics. Ann. Rev. Mat. Res. **32**, 1 (2002)
- N. Spaldin, Analogies and Differences between Ferroelectrics and Ferromagnets, in Physics of Ferroelectrics: A modern perspective Topics in Applied Physics, ed. by K.M. Rabe, C.H. Ahn, J.M. Triscone (Springer, Berlin Heidelberg New York, 2007)
- N.A. Spaldin, M. Fiebig, The Renaissance of Magnetoelectric Multiferroics. Science 309, 391 (2005)
- 93. M. Gajek, M. Bibes, S. Fusil, K. Bouzehouane, J. Fontcuberta, A. Barthélémy, A. Fert, Tunnel junctions with multiferroic barriers. Nat. Mater. 6, 296 (2007)
- 94. C. Ederer, N.A. Spaldin, Magnetoelectrics: A new route to magnetic ferroelectrics. Nat. Mater. 3, 849 (2004)
- M.G. Samant, J. Stöhr, S.S.P. Parkin, G.A. Held, B.D. Hermsmeier, F. Herman, M. van Schilfgaarde, L.C. Duda, D.C. Mancini, N. Wassdahl, R. Nakajima, Induced spin polarization in Cu spacer layers in Co/Cu multilayers. Phys. Rev. Lett. 72, 1112 (1994)
- T. Emoto, N. Hosoito, T. Shinjo, Magnetic polarization in Au layers of Au/M (M=Fe Co, and Ni) multilayers with <sup>119</sup>Sn probes studied by Mössbauer spectroscopy. J. Magn. Magn. Mater. 189, L136 (1998)
- 97. A. Scherz, H. Wende, P. Poulopoulos, J. Lindner, K. Baberschke, P. Blomquist, R. Wäppling, F. Wilhelm, N.B. Brookes, Induced V and reduced Fe moments at the interface of Fe/V(001) superlattices. Phys. Rev. B **64**, 180407 (2001)
- 98. J.W. Freeland, R.H. Kodama, M. Vedpathak, S.C. Erwin, D.J. Keavney, R. Winarski, P. Ryan, R.A. Rosenberg, Induced Ge spin polarization at the Fe—Ge interface. Phys. Rev. B **70**, 033201 (2004)
- 99. N. Jaouen, F. Wilhelm, A. Rogalev, J.M. Tonnèrre, T. Johal, G. Van der Laan, Ag- and W-induced magnetic moment in 3d multilayer. IEEE Trans. Magn. 41, 3334 (2005)
- T. Ohkochi, N. Hosoito, K. Mibu, Depth-selective measurements of induced magnetic polarization in Cu layers of Gd/Cu multilayers by 119 Sn Mössbauer spectroscopy. J. Phys. Cond. Matt. 17, 4023 (2005)
- J. Unguris, R.J. Celotta, D.T. Pierce, Magnetism in Cr thin films on Fe(100). Phys. Rev. Lett. 69, 1125 (1992)
- 102. D. Knabben, T. Koop, H.A. Dürr, F.U. Hillebrecht, G. van der Laan, Cr magnetic moments in Fe-Cr layered structures. J. Electron Spectrosc. Relat. Phenom. **86**, 201 (1997)
- 103. W. Kuch, R. Frömter, J. Gilles, D. Hartmann, C. Ziethen, C.M. Schneider, G. Schönhense, W. Swiech, J. Kirschner, Element-selective magnetic imaging in exchange-coupled systems by magnetic photoemission microscopy. Surf. Rev. Lett. 5, 1241 (1998)
- 104. D. Schmitz, O. Rader, C. Carbone, W. Eberhardt, Temperature dependence of the magnetic circular dichroism of the c(2x2) Mn/Ni (100) surface alloy. Phys. Rev. B **54**, 15352 (1996)
- 105. K. Lenz, S. Zander, W. Kuch, Magnetic proximity effects in antiferromagnet/ferromagnet bilayers: The impact on the Néel temperature. Phys. Rev. Lett. 98, 237201 (2007)
- 106. W.H. Meiklejohn, C.P. Bean, New Magnetic Anisotropy. Phys. Rev. 102, 1413 (1956)
- V. Skrumryev, S. Stoyanov, Y. Zhang, G. Hadjipanayis, D. Givord, J. Nogués, Beating the superparamagnetic limit with exchange bias. Nature 423, 850 (2003)
- 108. W.H. Meiklejohn, Exchange Anisotropy-A Review. J. Appl. Phys. 33, 1328 (1962)
- J. McCord, R. Schäfer, R. Mattheis, K.-U. Barholz, Kerr observations of asymmetric magnetization reversal processes in CoFe/IrMn bilayer systems. J. Appl. Phys. 93, 5491 (2003)
- J. McCord, R. Schäfer, Domain wall asymmetries in Ni<sub>81</sub>Fe<sub>19</sub>/NiO: proof of variable anisotropies in exchange bias systems. New J. Phys. 11, 083016 (2009)

- 111. A. Hubert, R. Schäfer, Magnetic Domains (Springer, Berlin Heidelberg New York, 1998)
- 112. M. de Graef, Y. Zhu (eds.), Magnetic imaging and its applications to materials (Academic Press, San Diego, 2001)
- 113. H. Hopster, H. Oepen (eds.), *Magnetic Microscopy of Nanostructures* (Springer, Berlin Heidelberg New York, 2004)
- 114. W. Kuch, Magnetic imaging, in Magnetism: A Synchrotron Radiation Approach, ed. by E. Beaurepaire, H. Bulou, F. Scheurer, J.P. Kappler (Springer, Berlin Heidelberg New York, 2006)
- 115. A.V. Kimel, B.A. Ivanov, R.V. Pisarev, P.A. Usachev, A. Kirilyuk, T. Rasing, Inertia-driven spin switching in antiferromagnets. Nat. Phys. 5, 727 (2009)
- 116. I. Radu, K. Vahaplar, C. Stamm, T. Kachel, N. Pontius, H.A. Dürr, T.A. Ostler, J. Barker, R.F.L. Evans, R.W. Chantrell, A. Tsukamoto, A. Itoh, A. Kirilyuk, T. Rasing, A.V. Kimel, Transient ferromagnetic-like state mediating ultrafast reversal of antiferromagnetically coupled spins. Nature 472, 205 (2011)
- J.H. Mentink, J. Hellsvik, D.V. Afanasiev, B.A. Ivanov, A. Kirilyuk, A.V. Kimel, O. Eriksson, M.I. Katsnelson, T. Rasing, Ultrafast spin dynamics in multisublattice magnets. Phys. Rev. Lett. 108, 057202 (2012)
- 118. R. Schäfer. Investigation of domains and dynamics of domain walls by the magneto-optical Kerr effect. In: H. Kronmüller and S. S. P. Parkin (Eds.), Handbook of magnetism and advanced magnetic materials, vol. 3, 1513. Wiley. (2007)
- 119. F. Krausz, M. Ivanov, Attosecond physics. Rev. Mod. Phys. 81, 163 (2009)
- 120. C. La-O-Vorakiat, M. Siemens, M.M. Murnane, H.C. Kapteyn, S. Mathias, M. Aeschlimann, P. Grychtol, R. Adam, C.M. Schneider, J.M. Shaw, H. Nembach, T.J. Silva, Ultrafast Demagnetization Dynamics at the *M* Edges of Magnetic Elements Observed Using a Tabletop High-Harmonic Soft X-Ray Source. Phys. Rev. Lett. 103, 257402 (2009)
- 121. B. Vodungbo, A. Barszczak, Sardinha, J. Gautier, G. Lambert, M. Lozano, S. Sebban, E. Meltchakov, F. Delmotte, V. Lopez-Flores, J. Arabski, C. Boeglin, E. Beaurepaire, R. Delaunay, J. Lüning, and P. Zeitoun. Table-top resonant magnetic scattering with extreme ultraviolet light from high-order harmonic generation. Europhys. Lett. 94, 54003 (2011)
- 122. M. Abo-Bakr, J. Feikes, K. Holldack, P. Kuske, W.B. Peatman, U. Schade, G. Wüstefeld, H.-W. Hübers, Brilliant, Coherent Far-Infrared (THz) Synchrotron Radiation. Phys. Rev. Lett. 90, 094801 (2003)
- 123. E.R. Moog, S.D. Bader, SMOKE signals from ferromagnetic monolayers:  $p(1 \times 1)$  Fe/Au(100). Superlattices and Microstructures 1, 543 (1981)
- 124. S.D. Bader, SMOKE. J. Magn. Magn. Mater. 100, 440 (1991)
- 125. Z.Q. Qiu, S.D. Bader, Surface magneto-optic Kerr effect (SMOKE). J. Magn. Magn. Mater. **200**, 664 (1999)
- 126. S.-H. Yang, B. S. Mun, N. Mannella, S.-K. Kim, J. B. Kortright, J. Underwood, F. Salmassi, E. Arenholz, A. Young, Z. Hussain, M. A. V. Hove, C. S. Fadley. Probing buried interfaces with soft x-ray standing wave spectroscopy: application to the Fe/Cr interface. J. Phys. Cond. Matt. 14, L407 (2002)
- 127. S.-H. Yang, B.C. Sell, C.S. Fadley, Probing multilayer spintronic structures with photoelectron and x-ray emission spectroscopies excited by x-ray standing waves. J. Appl. Phys. **103**, 07C519 (2008)
- 128. S.-H. Yang, B. Balke, C. Papp, S. Döring, U. Berges, L. Plucinski, C. Westphal, C.M. Schneider, S.S.P. Parkin, C.S. Fadley, Determination of layer-resolved composition, magnetization, and electronic structure of an Fe/MgO tunnel junction by standing-wave core and valence photoemission. Phys. Rev. B 84, 184410 (2011)
- 129. F. Kronast, R. Ovsyannikov, A. Kaiser, C. Wiemann, S.-H. Yang, D.E. Bürgler, R. Schreiber, F. Salmassi, P. Fischer, H.A. Dürr, C.M. Schneider, W. Eberhardt, C.S. Fadley, Depth-resolved soft x-ray photoelectron emission microscopy in nanostructures via standing-wave excited photoemission. Appl. Phys. Lett. 93, 243116 (2008)

A.X. Gray, F. Kronast, C. Papp, S.-H. Yang, S. Cramm, I.P. Krug, F. Salmassi, E.M. Gullikson,
 D.L. Hilken, E.H. Anderson, P. Fischer, H.A. Dürr, C.M. Schneider, C.S. Fadley, Standing-wave excited soft x-ray photoemission microscopy: Application to Co microdot magnetic arrays. Appl. Phys. Lett. 97, 062503 (2010)

- 131. W. Chao, B.H. Harteneck, J.A. Liddle, E.H. Anderson, D.T. Attwood, Soft X-ray microscopy at a spatial resolution better than 15nm. Nature **435**, 1210 (2005)
- 132. R. P. Ferrier, S. McVitie. The depth sensitivity of type II magnetic contrast. In: 49th Annual Meeting Electron Microscopy Society of America, San Francisco Press. 766–767 (1991)
- 133. K. Kobayashi, Observation of magnetic domains in thin-film heads by electron microscopy. IEEE Transl. J. Magn. Japan **8**, 595 (1993)
- 134. M. Faraday. On the magnetization of light and the illumination of magnetic lines of force. Phil. Trans. Royal Soc. (London) 136, 1 (1846)
- 135. J. Kerr. On rotation of the plane of polarization by reflection from the pole of a magnet. Phil. Mag. 3 (5), 321 (1877)
- J. Kerr, On reflection of polarized light from the equatorial surface of a magnet. Phil. Mag. 5, 161 (1878)
- 137. P. Zeeman, Measurements concerning the influence of a magnetization, perpendicular to the plane of incidence on the light reflected from an iron mirror. Leiden Commun. 29, 3 (1896)
- 138. P. Zeeman, On the influence of Magnetism on the Nature of the Light emitted by a Substance. Phil. Mag. **43**, 226 (1897)
- H.A. Lorentz, Le phénomène découvert par Hall et la rotation électromagnétique du plan de polarisation de la lumière. Néerl. Arch. 19, 123 (1884)
- 140. W. Voigt. Doppelbrechung von im Magnetfeld befindlichem Natriumdampf in der Richtung normal zu den Kraftlinien (Birefringence of sodium vapour in a magnetic field along a direction perpendicular to the lines of force). Nachr. Kgl. Ges. Wiss. Göttingen, Math. Phys. Kl. 4, 355 (1898)
- 141. A. Cotton and H. Mouton. Sur les propriétés magnéto-optiques des colloides et des liqueurs hétérogénes (On magneto-optic properties of colloids and inhomogeneous liquids). Ann. Chim. Phys 11(8), 145 (1907)
- 142. H.J. Williams, F.G. Foster, E.A. Wood, Observation of Magnetic Domains by the Kerr Effect. Phys. Rev. **82**, 119 (1951)
- 143. C.A. Fowler, E.M. Fryer, Magnetic Domains on Silicon Iron by the Longitudinal Kerr Effect. Phys. Rev. **86**, 426 (1952)
- 144. J. Kranz, A. Hubert, Die Möglichkeiten der Kerr-Technik zur Beobachtung magnetischer Bereiche (The potential of the Kerr technique for the observation of magnetic domains). Z. Angew. Phys. 15, 220 (1963)
- F. Schmidt, W. Rave, A. Hubert, Enhancement of magneto-optical domain observation by digital image processing. IEEE Trans. Magn. 21, 307 (1986)
- B.E. Argyle, B. Petek, J.D.A. Herman, Optical imaging of magnetic domains in motion. J. Appl. Phys. 61, 4303 (1987)
- 147. C.A. Fowler, E.M. Fryer, Magnetic Domains in Thin Films by the Faraday Effect. Phys. Rev. **104**, 552 (1956)
- 148. A. Bobeck, R. Fischer, A. Perneski, J. Remeika, L. van Uiterit, Application of orthoferrites to domain-wall devices. IEEE Trans. Magn. **5**, 544 (1969)
- J.J.F. Dillon, Observation of Domains in the Ferrimagnetic Garnets by Transmitted Light. J. Appl. Phys. 29, 1286 (1958)
- 150. R. Schäfer and A. Hubert. A new magnetooptic effect related to non-uniform magnetization on the surface of a ferromagnet. Phys. Status Solidi A **118**, 271 (1990)
- R. Schäfer, Magneto-optical domain studies in coupled magnetic multilayers. J. Magn. Magn. Mater. 148, 226 (1995)
- H.-C. Mertins, S. Valencia, A. Gaupp, W. Gudat, P. Oppeneer, C. Schneider, Magneto-optical polarization spectroscopy with soft X-rays. Appl. Phys. A 80, 1011 (2005)
- D.P. Siddons, M. Hart, Y. Amemiya, J.B. Hastings, X-ray optical activity and the Faraday effect in cobalt and its compounds. Phys. Rev. Lett. 64, 1967 (1990)

154. H.-C. Mertins, F. Schäfers, X. Le Cann, A. Gaupp, W. Gudat, Faraday rotation at the 2p edges of Fe Co, and Ni. Phys. Rev. B 61, R874 (2000)

- H.-C. Mertins, F. Schäfers, A. Gaupp, Soft-x-ray magneto-optical Faraday effect on Fe and Co films. Europhys. Lett. 55, 125 (2001)
- O. Hellwig, J.B. Kortright, K. Takano, E.E. Fullerton, Switching behavior of Fe-Pt/Ni-Fe exchange-spring films studied by resonant soft-x-ray magneto-optical Kerr effect. Phys. Rev. B 62, 11694 (2000)
- 157. H.-C. Mertins, P.M. Oppeneer, J. Kuneš, A. Gaupp, D. Abramsohn, F. Schäfers, Observation of the x-ray magneto-optical Voigt effect. Phys. Rev. Lett. **87**, 047401 (2001)
- 158. S. Valencia, A. Kleibert, A. Gaupp, J. Rusz, D. Legut, J. Bansmann, W. Gudat, P.M. Oppeneer, Quadratic X-Ray Magneto-Optical Effect upon Reflection in a Near-Normal-Incidence Configuration at the *M* Edges of 3*d*-Transition Metals. Phys. Rev. Lett. **104**, 187401 (2010)
- F. Schäfers, H.-C. Mertins, A. Gaupp, W. Gudat, M. Mertin, I. Packe, F. Schmolla, S.D. Fonzo, G. Soullié, W. Jark, R. Walker, X.L. Cann, R. Nyholm, M. Eriksson, Soft-X-Ray Polarimeter with Multilayer Optics: Complete Analysis of the Polarization State of Light. Appl. Opt. 38, 4074 (1999)
- 160. J.B. Kortright, M. Rice, S.-K. Kim, C.C. Walton, T. Warwick, Optics for element-resolved soft x-ray magneto-optical studies. J. Magn. Magn. Mater. **191**, 79 (1999)
- 161. W. Kuch, F. Offi, L. I. Chelaru, J. Wang, M. Kotsugi, and K. Fukumoto. Unpublished results.
- R. Atkinson, P. Lissberger, Sign conventions in magneto-optical calculations and measurements. IEEE Trans. Magn. 31, 6076 (1992)
- 163. G.R. Fowles, *Introduction to modern optics*, 2nd edn. (Dower Publications, New York, 1975)
- 164. M. Born, E. Wolf, *Principles of Optics*, 62 (Pergamon Press, Oxford, 1980)
- 165. P. Yeh. Optical waves in layered media. In: W. Goodman (Ed.), Wiley series in pure and applied optics. Wiley. (1988)
- 166. E. Hecht, *Optics* (Addison Wesley, San Francisco, 2002)
- 167. P.S. Pershan, Magneto-Optical Effects. J. Appl. Phys. 38, 1482 (1967)
- L. D. Landau, E. M. Lifshitz, L. P. Pitaevskii. Electrodynamics of continuous media. Pergamon, 2nd edn. (1984)
- P. Bechthold. Magnetooptische Effekte: Phänomenologische Beschreibung und Anwendungen. In: 30. IFF-Ferienkurs, Chap. 8.1. Jülich (1999)
- 170. M.J. Freiser, A survey of magnetooptic effects. IEEE Trans. Magn. 4, 152 (1967)
- 171. W. Wettling, Magneto-optics of ferrites. J. Magn. Magn. Mater. 3, 147 (1976)
- 172. J. Stöhr, H.C. Siegmann, Magnetism: from Fundamentals to Nanoscale Dynamics (Springer, Berlin, Heidelberg, 2006)
- 173. R.M.A. Azzam, N.M. Bashara, *Ellipsometry and polarized light* (North-Holland, Amsterdam, 1987)
- 174. W. Rave, R. Schäfer, A. Hubert, Quantitative observation of magnetic domains with the magneto-optical Kerr effect. J. Magn. Magn. Mater. 65, 7 (1987)
- 175. J. M. Bennett and H. E. Bennett. Polarization. In: W. Driscoll and W. Vaughan (Eds.), Handbook of Optics, 10–102. McGraw-Hill (1978)
- 176. A.V. Sokolv, Optical properties of metals (Blackie and Son Ltd., London, Glasgow, 1967)
- 177. G. Traeger, L. Wenzel, and A. Hubert. Computer experiments on the information depth and the figure of merit in magnetooptics. Phys. Status Solidi A **131**, 201 (1992)
- 178. S. Višňovský, Optics in magnetic multilayers and nanostructures (Taylor & Francis, Boca Raton, 2006)
- J. Zak, E. Moog, C. Liu, S. Bader, Universal approach to magneto-optics. J. Magn. Magn. Mater. 89, 107 (1990)
- Š. Višňovský, R. Krishnan, M. Nýlt, V. Prosser, Optical behaviour of Fe in magnetic multilayers. J. Magn. Soc. Jpn. 20, 41 (1996)
- 181. R. Gamble, P.H. Lissberger, M.R. Parker, A simple analysis for the optimization of the normal polar magneto-optical Kerr effect in multilayer coatings containing a magnetic-film. IEEE Trans. Magn. 21, 1651 (1985)

 C.-Y. You, S.-C. Shin, Generalized analytic formulae for magneto-optical Kerr effects. J. Appl. Phys. 84, 541 (1998)

- 183. R.P. Hunt, Magneto-Optic Scattering from Thin Solid Films. J. Appl. Phys. 38, 1652 (1967)
- 184. Z.J. Yang, M.R. Scheinfein, Combined three-axis surface magneto-optical Kerr effects in the study of surface and ultrathin-film magnetism. J. Appl. Phys. 74, 6810 (1993)
- V. Kamberský, L. Wenzel, A. Hubert, Magneto-optical interference and diffraction in isotropic and uniaxial multilayers. J. Magn. Magn. Mater. 189, 149 (1998)
- L. Wenzel, V. Kamberský, and A. Hubert. A systematic first-order theory of magnetooptic diffraction in magnetic multilayers. phys. status solidi A 151, 449 (1995)
- L. Wenzel. Simulation magneto-optischer Abbildungen (Simulation of magneto-optical images). Ph.D. thesis, Universität Erlangen-Nürnberg (1998)
- M. Mansuripur, Figure of merit for magneto-optical media based on the dielectric tensor. Appl. Phys. Lett. 49, 19 (1986)
- W.A. Challener, Figures of merit for magneto-optic materials. J. Phys. Chem. Solids 56, 1499 (1995)
- P.H. Lissberger, Kerr magneto-optic effect in nickel-iron films. I. Experimental. J. Opt. Soc. Am. 51, 957 (1961)
- J. Hamrle. Magneto-optical determination of the in-depth magnetization profile in magnetic multilayers. Ph.D. thesis, University Paris XI, (Orsay and Charles University, Prague, 2003)
- P. Bruno, Y. Suzuki, C. Chappert, Magneto-optical Kerr effect in a paramagnetic overlayer on a ferromagnetic substrate: A spin-polarized quantum size effect. Phys. Rev. B 53, 9214 (1996)
- A. Hubert, G. Traeger, Magneto-optical sensitivity functions of thin-film systems. J. Magn. Magn. Mater. 124, 185 (1993)
- P.H. Lissberger, M.R. Parker, Theory of the Voigt effect in gyroelectric media. Intern. J. Magn. 1, 209 (1970)
- V. Kamberský, The Schäfer-Hubert magneto-optical effect and classical gyrotropy in lightwave equations. J. Magn. Magn. Mater. 104–107, 311 (1992)
- 196. V. Kamberský. Private communication. (2010)
- B.E. Argyle, E. Terrenzio, Magneto-optic observation of Bloch lines. J. Appl. Phys. 55, 2569 (1984)
- R. Schäfer, M. Rührig, A. Hubert, Exploration of a new magnetization-gradient related magnetooptical effect. IEEE Trans. Magn. 26, 1355 (1990)
- V. Kamberský. On Magnetooptical Effects Caused by the Gradient of Magnetization. Phys Status Solidi A 123, K71 (1991)
- V. Kamberský. A Further Contribution to the Magneto-Optical Effects Caused By a Gradient of Magnetization. Phys. Status Solidi A 125, K117 (1991)
- R. Schäfer, C. Hamann, J. McCord, L. Schultz, V. Kamberský, The magneto-optical gradient effect in an exchange-biased thin film: experimental evidence for classical diffraction theory. New J. Phys. 12, 053006 (2010)
- V. Kamberský, Linear magneto-optical gradient effects in a plane wave. J. Magn. Magn. Mater. 125, 239 (1993)
- 203. V. Kamberský, R. Schäfer, Magneto-optic gradient effect in domain-wall images: At the crossroads of magneto-optics and micromagnetics. Phys. Rev. A 84, 013815 (2011)
- G. Träger, L. Wenzel, A. Hubert, V. Kamberský, Magnetooptical effects in non-uniform magnetized media. IEEE Trans. Magn. 29, 3408 (1993)
- L. Wenzel, A. Hubert, V. Kamberský, Transparent simulation of magneto-optic diffraction from arbitrary magnetic multilayers. J. Magn. Magn. Mater. 175, 205 (1997)
- 206. G. van der Laan, B.T. Thole, G.A. Sawatzky, J.B. Goedkoop, J.C. Fuggle, J.-M. Esteva, R. Karnatak, J.P. Remeika, H.A. Dabkowska, Experimental proof of magnetic x-ray dichroism. Phys. Rev. B 34, 6529 (1986)
- B.T. Thole, G. van der Laan, G.A. Sawatzky, Strong Magnetic Dichroism Predicted in the M<sub>4,5</sub> X-Ray Absorption Spectra of Magnetic Rare-Earth Materials. Phys. Rev. Lett. 55, 2086 (1985)

- R. Kappert, M. Sacchi, J. Goedkoop, M. Grioni, J. Fuggle, X-ray dichroism of Dy overlayers on Ni(110). Surf. Sci. 248, L245 (1991)
- P. Kuiper, B.G. Searle, P. Rudolf, L.H. Tjeng, C.T. Chen, X-ray magnetic dichroism of antiferromagnet Fe<sub>2</sub>O<sub>3</sub>: The orientation of magnetic moments observed by Fe 2p x-ray absorption spectroscopy. Phys. Rev. Lett. 70, 1549 (1993)
- 210. F.J. Morin, Electrical Properties of αFe<sub>2</sub>O<sub>3</sub> Containing Titanium. Phys. Rev. **83**, 1005 (1951)
- 211. M.M. Schwickert, G.Y. Guo, M.A. Tomaz, W.L. O'Brien, G.R. Harp, X-ray magnetic linear dichroism in absorption at the L edge of metallic Co, Fe, Cr, and V. Phys. Rev. B 58, R4289 (1998)
- C. Kao, J.B. Hastings, E.D. Johnson, D.P. Siddons, G.C. Smith, G.A. Prinz, Magnetic-resonance exchange scattering at the iron L<sub>II</sub> and L<sub>III</sub> edges. Phys. Rev. Lett. 65, 373 (1990)
- J. Friedrich, I. Rozhko, J. Voss, F.U. Hillebrecht, E. Kisker, V. Wedemeier, Scanning microscopy of magnetic domains using the Fe 3p core level transverse magneto-optical Kerr effect. J. Appl. Phys. 85, 4610 (1999)
- D. Alders, L.H. Tjeng, F.C. Voogt, T. Hibma, G.A. Sawatzky, C.T. Chen, J. Vogel, M. Sacchi, S. Iacobucci, Temperature and thickness dependence of magnetic moments in NiO epitaxial films. Phys. Rev. B 57, 11623 (1998)
- 215. N. Weber. Untersuchung von Übergangsmetallen und Übergangsmetalloxiden mit Synchrotronstrahlung. Ph.D. thesis, University of Düsseldorf (2002). http://docserv.uniduesseldorf.de/servlets/DocumentServlet?id=2212
- M. Marynowski, W. Franzen, M. El-Batanouny, V. Staemmler, Observation of an extraordinary antiferromagnetic transition on the NiO(100) surface by metastable helium atom diffraction. Phys. Rev. B 60, 6053 (1999)
- 217. J. Kuneš, P.M. Oppeneer, Anisotropic x-ray magnetic linear dichroism at the L<sub>2,3</sub> edges of cubic Fe Co, and Ni: Ab initio calculations and model theory. Phys. Rev. B 67, 024431 (2003)
- 218. E. Arenholz, G. van der Laan, R.V. Chopdekar, Y. Suzuki, Anisotropic x-ray magnetic linear dichroism at the Fe L<sub>2,3</sub> edges in Fe<sub>3</sub>O<sub>4</sub>. Phys. Rev. B **74**, 094407 (2006)
- 219. A.A. Freeman, K.W. Edmonds, G. van der Laan, N.R.S. Farley, T.K. Johal, E. Arenholz, R.P. Campion, C.T. Foxon, B.L. Gallagher, Giant anisotropy in x-ray magnetic linear dichroism in (Ga, Mn)As. Phys. Rev. B 73, 233303 (2006)
- 220. S. Czekaj, F. Nolting, L.J. Heyderman, P.R. Willmott, G. van der Laan, Sign dependence of the x-ray magnetic linear dichroism on the antiferromagnetic spin axis in LaFeO<sub>3</sub> thin films. Phys. Rev. B **73**, 020401(R) (2006)
- E. Arenholz, G. van der Laan, R.V. Chopdekar, Y. Suzuki, Angle-dependent Ni<sup>2+</sup> x-ray magnetic linear dichroism: Interfacial coupling revisited. Phys. Rev. Lett. 98, 197201 (2007)
- 222. G. van der Laan, E. Arenholz, R.V. Chopdekar, Y. Suzuki, Influence of crystal field on anisotropic x-ray magnetic linear dichroism at the  $Co^{2+}L_{2,3}$  edges. Phys. Rev. B **77**, 064407 (2008)
- 223. F. Nolting, D. Legut, J. Rusz, P.M. Oppeneer, G. Woltersdorf, C.H. Back, Anisotropy of the L<sub>2,3</sub> x-ray magnetic linear dichroism of Fe films on GaAs: Experiment and ab initio theory. Phys. Rev. B 82, 184415 (2010)
- 224. W. Kuch, F. Offi, L.I. Chelaru, J. Wang, K. Fukumoto, M. Kotsugi, J. Kirschner, J. Kuneš, Huge magnetocrystalline anisotropy of x-ray linear dichroism observed on Co/FeMn bilayers. Phys. Rev. B **75**, 224406 (2007)
- 225. W.L. Roth, Multispin Axis Structures for Antiferromagnets. Phys. Rev. 111, 772 (1958)
- T. Wolfram, R. Dewames, W. Hall, P. Palmberg, Surface magnetization near the critical temperature and the temperature dependence of magnetic-electron scattering from NiO. Surf. Sci. 28, 45 (1971)
- B. Kang, D. Kim, E. Anderson, P. Fischer, G. Cho, Polarization-modulated magnetic soft-xray transmission microscopy. J. Appl Phys 98, 093907 (2005)
- 228. M.R. Weiss, R. Follath, K.J.S. Sawhney, F. Senf, J. Bahrdt, W. Frentrup, A. Gaupp, S. Sasaki, M. Scheer, H.-C. Mertins, D. Abramsohn, F. Schäfers, W. Kuch, W. Mahler, The elliptically polarized undulator beamlines at BESSY II. Nucl. Instr. and Meth. A 467–468, 449 (2001)

 A.T. Young, E. Arenholz, S. Marks, R. Schlueter, C. Steier, H.A. Padmore, A.P. Hitchcock, D.G. Castner, Variable linear polarization from an X-ray undulator. J. Synchrotron Radiat. 9, 270 (2002)

- A. Scholl, J. Stöhr, J. Lüning, J.W. Seo, J. Fompeyrine, H. Siegwart, J.-P. Locquet, F. Nolting, S. Anders, E.E. Fullerton, M.R. Scheinfein, H.A. Padmore, Observation of antiferromagnetic domains in epitaxial thin films. Science 287, 1014 (2000)
- G. Schütz, W. Wagner, W. Wilhelm, P. Kienle, R. Zeller, R. Frahm, G. Materlik, Absorption of circularly polarized x rays in iron. Phys. Rev. Lett. 58, 737 (1987)
- J. Stöhr, Y. Wu, B.D. Hermsmeier, M.G. Samant, G.R. Harp, S. Koranda, D. Dunham, B.P. Tonner, Element-specific magnetic microscopy with circularly polarized x-rays. Science 259, 658 (1993)
- P. Fischer, G. Schütz, G. Schmahl, P. Guttmann, D. Raasch, Imaging of magnetic domains with the X-ray microscope at BESSY using X-ray magnetic circular dichroism. Z. Phys. B: Cond. Matt. 101, 313 (1996)
- 234. H. Ebert, Magneto-optical effects in transition metal systems. Rep. Prog. Phys. **59**, 1665 (1996)
- B.T. Thole, P. Carra, F. Sette, G. van der Laan, X-ray circular dichroism as a probe of orbital magnetization. Phys. Rev. Lett. 68, 1943 (1992)
- P. Carra, B.T. Thole, M. Altarelli, X. Wang, X-ray circular dichroism and local magnetic fields. Phys. Rev. Lett. 70, 694 (1993)
- R. Wu, A.J. Freeman, Limitation of the magnetic-circular-dichroism spin sum rule for transition metals and importance of the magnetic dipole term. Phys. Rev. Lett. 73, 1994 (1994)
- W.L. O'Brien, B.P. Tonner, G.R. Harp, S.S.P. Parkin, Experimental investigation of dichroism sum rules for V, Cr, Mn, Fe Co, and Ni: influence of diffuse magnetism. J. Appl. Phys. 76, 6462 (1994)
- Y.U. Idzerda, C.T. Chen, H.-J. Lin, H. Tjeng, G. Meigs, Application of magnetic circular dichroism to magnetic thin films. Physica B 208–209, 746 (1995)
- C.T. Chen, Y.U. Idzerda, H.-J. Lin, N.V. Smith, G. Meigs, E. Chaban, G.H. Ho, E. Pellegrin, F. Sette, Experimental confirmation of the x-ray magnetic circular dichroism sum rules for iron and cobalt. Phys. Rev. Lett. 75, 152 (1995)
- 241. X. Le Cann, C. Boeglin, B. Carrière, K. Hricovini, Magnetic linear and circular dichroism in core-level photoemission and magnetic circular x-ray dichroism in absorption for ultrathin films Fe/Pd(100). Phys. Rev. B **54**, 373 (1996)
- J. Vogel, M. Sacchi, Polarization and angular dependence of the L<sub>2,3</sub> absorption edges in Ni(110). Phys. Rev. B 49, 3230 (1994)
- 243. J.B. Kortright, S.-K. Kim, Resonant magneto-optical properties of Fe near its 2p levels: Measurement and applications. Phys. Rev. B **62**, 12216 (2000)
- C. Chang, A. Sakdinawat, P. Fischer, E. Anderson, D. Attwood, Single-element objective lens for soft x-ray differential interference contrast microscopy. Optics Letters 31, 1564 (2006)
- J. Hamrle, J. Ferré, M. Nývlt, Š. Višňovský, In-depth resolution of the magneto-optical Kerr effect in ferromagnetic multilayers. Phys. Rev. B 66, 224423 (2002)
- F. Schmidt, A. Hubert, Domain observations on CoCr-layers with a digitally enhanced Kerrmicroscope. J. Magn. Magn. Mater. 61, 307 (1986)
- E. Nikulina, O. Idigoras, P. Vavassori, A. Chuvilin, A. Berger, Magneto-optical magnetometry of individual 30 nm cobalt nanowires grown by electron beam induced deposition. Appl. Phys. Lett. 100, 142401 (2012)
- 248. S. Inoué, K. Spring, *Video microscopy: The fundamentals* (Plenum Press, New York and London, 1997)
- B.E. Argyle, J.G. McCord, New laser illumination method for Kerr microscopy. J. Appl. Phys. 87, 6487 (2000)
- T. von Hofe, N.O. Urs, B. Mozooni, T. Jansen, C. Kirchhof, D.E. Brgler, E. Quandt, J. McCord, Dual wavelength magneto-optical imaging of magnetic thin films. Appl. Phys. Lett. 103, 142410 (2013)

 S. Egelkamp, L. Reimer, Imaging of magnetic domains by the Kerr effect using a scanning optical microscope. Measurement Science and Technology 1, 79 (1990)

- 252. W. Clegg, N. Heyes, E. Hill, C. Wright, Development of a scanning laser microscope for magneto-optic studies of thin magnetic films. J. Magn. Magn. Mater. **95**, 49 (1991)
- T.J. Silva, A.B. Kos, Nonreciprocal differential detection method for scanning Kerr-effect microscopy. J. Appl. Phys. 81, 5015 (1997)
- 254. T. Nagai, H. Sekiguchi, A. Ito, Magnetization vector measurement with wide-band high spatial resolution Kerr microscope. IEEE Trans. Magn. 39, 3441 (2003)
- C.D. Wright, N.A.E. Heyes, W.W. Clegg, E.W. Hill, Magneto-optic scanning laser microscopy. Microscopy and Analysis 46, 21 (1995)
- 256. M.R. Freeman, W.K. Hiebert, Stroboscopic microscopy of magnetic dynamics, in Spin Dynamics in Confined Magnetic Structures I, ed. by B. Hillebrands, K. Ounadjela (Springer, Berlin, 2002), pp. 93–126
- J.C. Suits, Magneto-optical rotation and ellipticity measurements with a spinning analyzer. Rev. Sci. Instrum. 42, 19 (1971)
- K. Sato, Measurement of magneto-optical Kerr effect using piezo-birefringent modulator. Jpn. J. Appl. Phys. 20, 2403 (1981)
- 259. M. Gomi, M. Abe, A new high-sensitivity magneto-optic readout technique and its application to Co-Cr film. IEEE Trans. Magn. 18, 1238 (1982)
- R.M. Osgood, B.M. Clemens, R.L. White, Asymmetric magneto-optic response in anisotropic thin films. Phys. Rev. B 55, 8990 (1997)
- K. Postava, H. Jaffres, A. Schuhl, F. Nguyen Van Dau, M. Goiran, A. Fert, Linear and quadratic magneto-optical measurements of the spin reorientation in epitaxial Fe films on MgO. J. Magn. Magn. Mater. 172, 199 (1997)
- 262. Z.Q. Qiu, S.D. Bader, Surface magneto-optic Kerr effect. Rev. Sci. Instrum. 71, 1243 (2000)
- R.M. Osgood, K.T. Riggs, A.E. Johnson, J.E. Mattson, C.H. Sowers, S.D. Bader, Magnetooptic constants of hcp and fcc Co films. Phys. Rev. B 56, 2627 (1997)
- D.S. Kliger, J.W. Lewis, C.E. Randall, *Polarized Light in Optics and Spectroscopy* (Academic, Boston, 1990)
- 265. G.S. Krinchik, V.A. Artemev, Mageto-optical properties of nickel, cobalt, and iron in the ultra-violet, visible, and infra-red parts of the spectrum. Sov. Phys. JETP 26, 1080 (1968)
- J. Schoenes, Electronic structure of uranium monochalcogenides and uranium monopnictides. Phys. Rep. 66, 187 (1980)
- R. Schäfer, D. Chumakov, O. deHaas, L. Schultz, W. Maass, K.-U. Barholz, and R. Mattheis. Magnetization processes in spin-valve meanders for sensor applications. IEEE Trans. Magn. 39, 2089 (2003)
- R. Schäfer, A. Hubert, S.S.P. Parkin, Domain and domain wall observations in sputtered exchange-biased wedges. IEEE Trans. Magn. 29, 2738 (1993)
- 269. P.H. Berning, Theory and calculation of optical thin films, in Physics of thin films, ed. by G. Hass (Academic Press, New York, 1963)
- 270. P. Yeh, Optics of anisotropic layered media: a new (4×4) matrix algebra. Surf. Sci. **96**, 41 (1980)
- D.O. Smith, Magneto-optical scattering from multi-layer magnetic and dielectric films. Optica Acta 12, 13 (1965)
- D. Keay, P. Lissberger, Longitudinal Kerr Magneto-optic Effect in Multilayer Structures of Dielectric and Magnetic Films. J. Mod. Optics 15, 373 (1968)
- 273. S. Višňovský, Magnetooptical ellipsometry. Czech. J. Phys. B 36, 625 (1986)
- 274. M. Mansuripur, Analysis of multilayer thin-film structures containing magneto-optic and anisotropic media at oblique incidence using 2 x 2 matrices. J. Appl. Phys. 67, 6466 (1990)
- J. McCord. Magneto-optische Untersuchungen an magnetoresistiven Schichten (Magneto-optical investigations on magneto-resistive films). Ph.D. thesis, Universität Erlangen-Nürnberg (1997)
- R. Atkinson, P. Lissberger, Correct formulation of first-order magneto-optical effects in multilayer thin films in terms of characteristic matrices and derivation of a related superposition principle. J. Magn. Magn. Mater. 118, 271 (1993)

 Š. Višňovský, M. Nývlt, V. Prosser, R. Lopušník, R. Urban, J. Ferré, G. Pénissard, D. Renard, R. Krishnan, Polar magneto-optics in simple ultrathin-magnetic-film structures. Phys. Rev. B 52, 1090 (1995)

- 278. M. Rührig. Mikromagnetische Untersuchungen an gekoppelten weichmagnetischen Schichten (Micromagnetic investigations on coupled soft magnetic films). Ph.D. thesis, Universität Erlangen-Nürnberg (1993)
- G. Pénissard, P. Meyer, J. Ferré, D. Renard, Magneto-optic depth sensitivity to local magnetization in a simple ultrathin film structure. J. Magn. Magn. Mater. 146, 55 (1995)
- J. Ferré, P. Meyer, M. Nyvlt, S. Visnovsky, D. Renard, Magnetooptic depth sensitivity in a simple ultrathin film structure. J. Magn. Magn. Mater. 165, 92 (1997)
- A. Svalov, A. Fernández, V. Vas'kovskiy, G. Kurlyandskaya, J. Barandiarán, R. Lopez, Anton, and M. Tejedor. MOKE study of Co/Ti/(Gd-Co) multilayers near the magnetic compensation state. J. Allovs Comp. 419, 25 (2006)
- A. Svalov, A. Fernández, J. Barandiarán, V. Vas'kovskiy, I. Orue, M. Tejedor, G. Kurlyandskaya, Magnetic transition in Co/(Gd-Co) multilayers. J. Magn. Magn. Mater. 320, e734 (2008)
- 283. M. Rührig, R. Schäfer, A. Hubert, R. Mosler, J. A. Wolf, S. Demokritov, P. Grünberg. Domain observations on Fe-Cr-Fe layered structures Evid. for a biquadratic coupling effect. Phys. Status Solidi A **125**. 635 (1991)
- R. Schäfer, R. Urban, D. Ullmann, H.L. Meyerheim, B. Heinrich, L. Schultz, J. Kirschner, Domain wall induced switching of whisker-based tunnel junctions. Phys. Rev. B 65, 144405 (2002)
- J. McCord, A. Hubert, R. Schäfer, A. Fuss, P. Grünberg, Domain analysis in epitaxial ironaluminium and iron-gold sandwiches with oscillatory exchange. IEEE Trans. Magn. 29, 2735 (1993)
- E. Brüche, Elektronenmikroskopische Abbildung mit lichtelektrischen Elektronen. Z. Phys. 86, 448 (1933)
- J. Pohl, Elektronenoptische Abbildungen mit lichtelektrisch ausgelösten Elektronen. Z. Tech. Phys. 12, 579 (1934)
- 288. R. Fink, M.R. Weiss, E. Umbach, D. Preikszas, H. Rose, R. Spehr, P. Hartel, W. Engel, R. Degenhardt, R. Wichtendahl, H. Kuhlenbeck, W. Erlebach, K. Ihmann, R. Schlögl, H.-J. Freund, A.M. Bradshaw, G. Lilienkamp, T. Schmidt, E. Bauer, G. Benner, SMART: a planned ultrahigh-resolution spectromicroscope for BESSY II. J. Electron Spectrosc. Relat. Phenom. 84, 231 (1997)
- 289. E. Bauer, Low energy electron microscopy. Rep. Prog. Phys. 57, 895 (1994)
- 290. C.M. Schneider, G. Schönhense, Investigating surface magnetism by means of photoexcitation electron emission microscopy. Rep. Prog. Phys. **65**, R1785 (2002)
- 291. J. Stöhr, NEXAFS Spectroscopy (Springer, Berlin, 1995)
- H. Henneken, F. Scholze, G. Ulm, Lack of proportionality of total electron yield and soft x-ray absorption coefficient. J. Appl. Phys. 87, 257 (2000)
- 293. R. Nakajima, J. Stöhr, Y.U. Idzerda, Electron-yield saturation effects in L-edge x-ray magnetic circular dichroism spectra of Fe Co, and Ni. Phys. Rev. B **59**, 6421 (1999)
- H. Henneken, F. Scholze, G. Ulm, Absolute total electron yield of Au(111) and Cu(111) surfaces.
   J. Electron Spectrosc. Relat. Phenom. 101–103, 1019 (1999)
- 295. The x-ray attenuation length  $1/\mu(\hbar\omega)$  can be obtained under http://henke.lbl.gov/optical\_constants/atten2.html
- 296. B. Henke, E. Gullikson, J. Davis, X-Ray Interactions: Photoabsorption, Scattering, Transmission, and Reflection at E = 50–30,000 eV, Z = 1–92. At. Data Nucl. Data Tables **54**, 181 (1993)
- 297. W. Platow, U. Bovensiepen, P. Poulopoulos, M. Farle, K. Baberschke, L. Hammer, S. Walter, S. Müller, K. Heinz, Structure of ultrathin Ni/Cu(001) films as a function of film thickness, temperature, and magnetic order. Phys. Rev. B 59, 12641 (1999)
- J. R. Cerdá, P. L. de Andres, A. Cebollada, R. Miranda, E. Navas, P. Schuster, C. M. Schneider, J. Kirschner. Epitaxial growth of cobalt films on Cu(100): a crystallographic LEED determination. J. Phys. Cond. Matt. 5, 2055 (1993)

 W. Kuch, F. Offi, L.I. Chelaru, M. Kotsugi, K. Fukumoto, J. Kirschner, Magnetic interface coupling in single-crystalline Co/FeMn bilayers. Phys. Rev. B 65, 140408(R) (2002)

- P. Bruno, C. Chappert, Oscillatory coupling between ferromagnetic layers separated by a nonmagnetic metal spacer. Phys. Rev. Lett. 67, 1602 (1991)
- 301. P. Bruno, Theory of interlayer magnetic coupling. Phys. Rev. B 52, 411 (1995)
- J.C. Slonczewski, Fluctuation mechanism for biquadratic exchange coupling in magnetic multilayers. Phys. Rev. Lett. 67, 3172 (1991)
- 303. M.D. Stiles, Interlayer exchange coupling. J. Magn. Magn. Mater. 200, 322 (1999)
- 304. W.L. O'Brien, B.P. Tonner, Transition to the perpendicular easy axis of magnetization in Ni ultrathin films found by x-ray magnetic circular dichroism. Phys. Rev. B **49**, 15370 (1994)
- 305. B. Schulz, K. Baberschke, Crossover from in-plane to perpendicular magnetization in ultrathin Ni/Cu(001) films. Phys. Rev. B **50**, 13467 (1994)
- P. Krams, F. Lauks, R.L. Stamps, B. Hillebrands, G. Güntherodt, Magnetic anisotropies of ultrathin Co(001) films on Cu(001). Phys. Rev. Lett. 69, 3674 (1992)
- M. Kowalewski, C.M. Schneider, B. Heinrich, Thickness and temperature dependence of magnetic anisotropies in ultrathin fcc Co(001) structures. Phys. Rev. B 47, 8748 (1993)
- W. Kuch, J. Gilles, F. Offi, S.S. Kang, S. Imada, S. Suga, J. Kirschner, Imaging microspectroscopy of Ni/Fe/Co/Cu(001) using a photoemission microscope. J. Electron Spectrosc. Relat. Phenom. 109, 249 (2000)
- 309. W. Kuch, X. Gao, J. Kirschner, Competition between in-plane and out-of-plane magnetization in exchange-coupled magnetic films. Phys. Rev. B **65**, 064406 (2002)
- W. Kuch, J. Gilles, S.S. Kang, S. Imada, S. Suga, J. Kirschner, Magnetic-circular-dichroism microspectroscopy at the spin reorientation transition in Ni(001) films. Phys. Rev. B 62, 3824 (2000)
- 311. P. Poulopoulos, P.J. Jensen, A. Ney, J. Lindner, K. Baberschke, Metastable magnetic properties of Co/Cu(001) films below the T<sub>C</sub> jump. Phys. Rev. B **65**, 064431 (2002)
- W. Kuch, J. Gilles, X. Gao, J. Kirschner, Layer-resolved magnetic imaging of spinreorientation transitions in Ni/Cu/Co trilayers. J. Magn. Magn. Mater. 1246, 242–245 (2002)
- 313. P.J. Jensen, K.H. Bennemann, P. Poulopoulos, M. Farle, F. Wilhelm, K. Baberschke, Enhanced induced magnetization in coupled magnetic trilayers in the presence of spin fluctuations. Phys. Rev. B 60, R14994 (1999)
- 314. L. Néel, Magnétisme sur un nouveau mode de couplage entre les animantations de deux couches minces ferromagnetiques. C. R. Hebd. Acad. Sci. **255**, 1676 (1962)
- W. Kuch, L.I. Chelaru, K. Fukumoto, F. Porrati, F. Offi, M. Kotsugi, J. Kirschner, Layer-resolved imaging of magnetic interlayer coupling by domain-wall stray fields. Phys. Rev. B 67, 214403 (2003)
- W. Kuch, Layer-resolved microscopy of magnetic domains in multi-layered systems. Appl. Phys. A 76, 665 (2003)
- 317. J. Kurde, J. Miguel, D. Bayer, J. Sánchez-Barriga, F. Kronast, M. Aeschlimann, H.A. Dürr, W. Kuch, Magnetostatic coupling of 90° domain walls in Fe<sub>19</sub>Ni<sub>81</sub>/Cu/Co trilayers. New J. Phys. 13, 033015 (2011)
- J.A. Borchers, J.A. Dura, J. Unguris, D. Tulchinsky, M.H. Kelley, C.F. Majkrzak, S.Y. Hsu, R. Loloee, J.W.P. Pratt, J. Bass, Observation of antiparallel magnetic order in weakly coupled Co/Cu multilayers. Phys. Rev. Lett. 82, 2796 (1999)
- 319. S. Gider, B.-U. Runge, A.C. Marley, S.S.P. Parkin, The magnetic stability of spin-dependent tunneling devices. Science **281**, 797 (1998)
- L. Thomas, M.G. Samant, S.S.P. Parkin, Domain-wall induced coupling between ferromagnetic layers. Phys. Rev. Lett. 84, 1816 (2000)
- J. Vogel, S. Cherifi, S. Pizzini, F. Romanens, J. Camarero, F. Petroff, S. Heun, A. Locatelli. Layer-resolved imaging of domain wall interactions in magnetic tunnel junction-like trilayers. J. Phys.: Cond. Matt. 19, 476204 (2007)
- 322. J. Vogel, W. Kuch, R. Hertel, J. Camarero, K. Fukumoto, F. Romanens, S. Pizzini, M. Bonfim, F. Petroff, A. Fontaine, J. Kirschner, Influence of domain wall interactions on nanosecond switching in magnetic tunnel junctions. Phys. Rev. B 72, 220402(R) (2005)

323. K. Heinz, S. Müller, P. Bayer, Multilayer reconstruction of ultrathin expitaxial fcc Fe films. Surf. Sci. **337**, 215 (1995)

- 324. A. Biedermann, R. Tscheließnig, M. Schmid, P. Varga, Crystallographic structure of ultrathin Fe films in Cu(100). Phys. Rev. Lett. **87**, 086103 (2001)
- 325. P. Bayer, S. Müller, P. Schmailzl, K. Heinz, Non-pseudomorphic and surface-reconstructed ultrathin epitaxial fcc Fe-films on Cu(100). Phys. Rev. B 48, 17611 (1993)
- 326. D. Li, M. Freitag, J. Pearson, Z.Q. Qiu, S.D. Bader, Magnetic phases of ultrathin Fe grown on Cu(100) as epitaxial wedges. Phys. Rev. Lett. **72**, 3112 (1994)
- 327. M. Straub, R. Vollmer, J. Kirschner, Surface magnetism of ultrathin  $\gamma$ -Fe films investigated by nonlinear magneto-optical Kerr effect. Phys. Rev. Lett. **77**, 743 (1996)
- 328. J. Giergiel, J. Kirschner, J. Landgraf, J. Shen, J. Woltersdorf, Stages of structural transformation in iron thin film growth on copper (100). Surf. Sci. 310, 1 (1994)
- 329. W. Kuch, S.S.P. Parkin, Structural and magnetic phases of Fe in Fe/Ni(001) and Fe/Ni<sub>81</sub>Fe<sub>19</sub>(001) multilayers. J. Magn. Magn. Mater. **184**, 127 (1998)
- E.J. Escorcia-Aparicio, R.K. Kawakami, Z.Q. Qiu, fcc Fe films grown on a ferromagnetic fcc Co(100) substrate. Phys. Rev. B 54, 4155 (1996)
- R.K. Kawakami, E.J. Escorcia-Aparicio, Z.Q. Qiu, Magnetic coupling in Co/face-centeredcubic Fe/Co sandwiches. J. Appl. Phys. 79, 4532 (1996)
- 332. C. Won, Y.Z. Wu, H.W. Zhao, A. Scholl, A. Doran, Z.Q. Qiu, Effect of the interlayer coupling on the Ni spin reorientation in Ni/Fe/Co/Cu(100). Phys. Rev. B 68, 052404 (2003)
- 333. Y.Z. Wu, C. Won, A. Scholl, A. Doran, F. Toyoma, X.F. Jin, N.V. Smith, Z.Q. Qiu, Interfacial magnetism of fcc Fe and the effect of the oscillatory interlayer coupling on the Ni magnetic properties in Ni/Fe/Co/Cu(100). Phys. Rev. B 65, 214417 (2002)
- A. Kirilyuk, J. Giergiel, J. Shen, J. Kirschner, Unusual surfactant effect and the stability of pseudomorphic γ-Fe films. Phys. Rev. B 52, R11672 (1995)
- 335. A. Kirilyuk, J. Giergiel, J. Shen, M. Straub, J. Kirschner, Growth of stabilized  $\gamma$ -Fe films and their magnetic properties. Phys. Rev. B **54**, 1050 (1996)
- 336. C. Won, Y.Z. Wu, A. Scholl, A. Doran, N. Kurahashi, H.W. Zhao, Z.Q. Qiu, Magnetic phase transition in Co/Cu/Ni/Cu(100) and Co/Fe/Ni/Cu(100). Phys. Rev. Lett. 91, 147202 (2003)
- W. Kuch, L.I. Chelaru, F. Offi, J. Wang, M. Kotsugi, J. Kirschner, Three-dimensional noncollinear antiferromagnetic order in single-crystalline FeMn ultrathin films. Phys. Rev. Lett. 92, 017201 (2004)
- 338. W. Kuch, L.I. Chelaru, F. Offi, J. Wang, M. Kotsugi, J. Kirschner, Tuning the magnetic coupling across ultrathin antiferromagnetic films by controlling atomic-scale roughness. Nat. Mater. 5, 128 (2006)
- 339. J.S. Kouvel, J.S. Kasper, Long-range antiferromagnetism in disordered Fe-Ni-Mn alloys, J. Phys. Chem. Solids **24**, 529 (1963)
- 340. H. Umebayashi, Y. Ishikawa, Antiferromagnetism of  $\gamma$  Fe-Mn alloys. J. Phys. Soc. Jpn. 21, 1281 (1966)
- 341. S.J. Kennedy, T.J. Hicks, The magnetic structure of  $\gamma$ -iron-manganese. J. Phys. F: Met. Phys. 17, 1599 (1987)
- S. Maat, K. Takano, S.S.P. Parkin, E.E. Fullerton, Perpendicular exchange bias of Co/Pt multilayers. Phys. Rev. Lett. 87, 087202 (2001)
- 343. C.H. Marrows, Three-dimensional exchange bias in Co/Pd<sub>N</sub>/FeMn. Phys. Rev. B **68**, 012405 (2003)
- 344. F. Offi, W. Kuch, J. Kirschner, Structural and magnetic properties of  $Fe_xMn_{1-x}$  thin films on Cu(001) and on Co/Cu(001). Phys. Rev. B **66**, 064419 (2002)
- 345. H. Ohldag, A. Scholl, F. Nolting, S. Anders, F.U. Hillebrecht, J. Stöhr, Spin reorientation at the antiferromagnetic NiO(001) surface in response to an adjacent ferromagnet. Phys. Rev. Lett. **86**, 2878 (2001)
- H. Ohldag, T.J. Regan, J. Stöhr, F. Nolting, J. Lüning, C. Stamm, S. Anders, R.L. White, Spectroscopic identification and direct imaging of interfacial magnetic spins. Phys. Rev. Lett. 87, 247201 (2001)

- 347. H. Ohldag. Exchange Coupling of Fe and Co on Antiferromagnetic NiO Investigated by Dichroism X-Ray Absorption Spectromicroscopy. Ph.D. thesis, University of Düsseldorf (2003). (http://docserv.uni-duesseldorf.de/servlets/DocumentServlet?id=2637)
- 348. H. Ohldag, A. Scholl, F. Nolting, E. Arenholz, S. Maat, A.T. Young, M. Carey, J. Stöhr, Correlation between exchange bias and pinned interfacial spins. Phys. Rev. Lett. **91**, 017203 (2003)
- N.C. Koon, Calculations of exchange bias in thin films with ferromagnetic/antiferromagnetic interfaces. Phys. Rev. Lett. 78, 4865 (1997)
- J.A. Borchers, M.J. Carey, R.W. Erwin, C.F. Majkrzak, A.E. Berkowitz, Spatially modulated antiferromagnetic order in CoO/NiO superlattices. Phys. Rev. Lett. 70, 1878 (1993)
- 351. J. Lüning, F. Nolting, A. Scholl, H. Ohldag, J.W. Seo, J. Fompeyrine, J.-P. Locquet, J. Stöhr, Determination of the antiferromagnetic spin axis in epitaxial LaFeO<sub>3</sub> films by x-ray magnetic linear dichroism spectroscopy. Phys. Rev. B **67**, 214433 (2003)
- 352. F. Nolting, A. Scholl, J. Stöhr, J.W. Seo, J. Fompeyrine, H. Siegwart, J.-P. Locquet, S. Anders, J. Lüning, E.E. Fullerton, M.F. Toney, M.R. Scheinfein, H.A. Padmore, Direct observation of the alignment of ferromagnetic spins by antiferromagnetic spins. Nature 405, 767 (2000)
- A. Scholl, F. Nolting, J.W. Seo, H. Ohldag, J. Stöhr, S. Raoux, J.-P. Locquet, J. Fompeyrine, Domain-size-dependent exchange bias in Co/LaFeO<sub>3</sub>. Appl. Phys. Lett. 85, 4085 (2004)
- A.P. Malozemoff, Random-field model of exchange anisotropy at rough ferromagneticantiferromagnetic interfaces. Phys. Rev. B 35, 3679 (1987)
- M. Bonfim, G. Ghiringhelli, F. Montaigne, S. Pizzini, N.B. Brookes, F. Petroff, J. Vogel, J. Camarero, A. Fontaine, Element-selective nanosecond magnetization dynamics in magnetic heterostructures. Phys. Rev. Lett. 86, 3646 (2001)
- 356. J. Vogel, W. Kuch, J. Camarero, K. Fukumoto, M. Bonfim, Y. Pennec, S. Pizzini, A. Fontaine, J. Kirschner. Magnetisation dynamics in spin-valves: how fast can a hard disk be read?. In: *BESSY Highlights*, 28–29 (2003)
- 357. J. Vogel, W. Kuch, M. Bonfim, J. Camarero, Y. Pennec, F. Offi, K. Fukumoto, J. Kirschner, A. Fontaine, S. Pizzini, Time-resolved magnetic domain imaging by x-ray photoemission electron microscopy. Appl. Phys. Lett. **82**, 2299 (2003)
- 358. J. Vogel, W. Kuch, J. Camarero, K. Fukumoto, Y. Pennec, M. Bonfim, S. Pizzini, F. Petroff, A. Fontaine, J. Kirschner, Time and layer resolved magnetic domain imaging of FeNi/Cu/Co trilayers using x-ray photoelectron emission microscopy. J. Appl. Phys. 95, 6533 (2004)
- 359. W. Kuch, J. Vogel, J. Camarero, K. Fukumoto, Y. Pennec, S. Pizzini, M. Bonfim, J. Kirschner, Exploring spin valve magnetization reversal dynamics with temporal, spatial and layer resolution: Influence of domain wall energy. Appl. Phys. Lett. **85**, 440 (2004)
- K. Fukumoto, W. Kuch, J. Vogel, F. Romanens, S. Pizzini, J. Camarero, M. Bonfim, J. Kirschner, Dynamics of magnetic domain wall motion after nucleation: Dependence on the wall energy. Phys. Rev. Lett. 96, 097204 (2006)
- J. Miguel, M. Bernien, D. Bayer, J. Sánchez-Barriga, F. Kronast, M. Aeschlimann, H.A. Dürr,
   W. Kuch, A new sample holder for laser-excited pump-probe magnetic measurements on a Focus photoelectron emission microscope. Rev. Sci. Instrum. 79, 033702 (2008)
- 362. C.M. Schneider, A. Kuksov, A. Krasyuk, A. Oelsner, D. Neeb, S.A. Nepijko, G. Schönhense, I. Mönch, R. Kaltofen, J. Morais, C. de Nada, N.B. Brookes, Incoherent magnetization rotation observed in subnanosecond time-resolving x-ray photoemission electron microscopy. Appl. Phys. Lett. 85, 2562 (2004)
- 363. C.M. Schneider, A. Kuksov, A. Krasyuk, A. Oelsner, S.A. Nepijko, G. Schönhense, Time-resolved x-ray photoemission electron microscopy: Imaging magnetodynamics on the 100 ps scale and below. J. Electr. Spectrosc. Relat. Phenom. 144–147, 967 (2005)
- A. Krasyuk, F. Wegelin, S.A. Nepijko, H.J. Elmers, G. Schönhense, M. Bolte, C.M. Schneider, Self-trapping of magnetic oscillation modes in Landau flux-closure structures. Phys. Rev. Lett. 95, 207201 (2005)
- S.-B. Choe, Y. Acreman, A. Scholl, A. Bauer, A. Doran, J. Stöhr, H.A. Padmore, Vortex core-driven magnetization dynamics. Science 304, 420 (2004)

J. Raabe, C. Quitmann, C.H. Back, F. Nolting, S. Johnson, C. Buehler, Quantitative analysis of magnetic excitations in Landau flux-closure structures using synchrotron-radiation microscopy. Phys. Rev. Lett. 94, 217204 (2005)

- X.M. Cheng, K.S. Buchanan, R. Divan, K. Guslienko, D.J. Keavney, Nonlinear vortex dynamics and transient domains in ferromagnetic disks. Phys. Rev. B 79, 172411 (2009)
- C.M. Schneider, A. Kaiser, C. Wiemann, C. Tieg, S. Cramm, Photoemission microscopy study
  of picosecond magnetodynamics in spin-valve-type thin film elements. J. Electron Spectrosc.
  Relat. Phenom. 181, 159 (2010)
- W.D. Doyle, S. Stinnett, C. Dawson, L. He, Magnetization Reversal at High Speed: An Old Problem in a New Context. J. Magn. Soc. Jpn. 22, 91 (1998)
- 370. P. Fischer, D.-H. Kim, W. Chao, J.A. Liddle, E.H. Anderson, D.T. Attwood, Soft X-ray microscopy of nanomagnetism. Mat. Today 9, 26 (2006)
- D. Attwood. Soft X-rays and Extreme Ultraviolet Radiation. (Cambridge University Press, Cambridge)
- 372. G. Schmahl, D. Rudolph, B. Niemann, O. *Christ. Zone-plate X-ray Microscopy*. Quarterly Reviews of Biophysics. *13*(3), 397(1980)
- 373. P. Fischer, T. Eimüller, G. Schütz, G. Denbeaux, A. Pearson, L. Johnson, D. Attwood, S. Tsunashima, M. Kumazawa, N. Takagi, M. Kohler, G. Bayreuther, Element-specific imaging of magnetic domains at 25 nm spatial resolution using soft x-ray microscopy. Rev. Sci. Instrum. 72, 2322 (2001)
- 374. J.R. Groves, R.F. DePaula, L. Stan, R.H. Hammond, B.M. Clemens, Fundamental Aspects of Ion Beam Assisted Deposition of Magnesium Oxide Template Films. IEEE Trans. Appl. Superconductivity 19(3), 3311 (2009)
- F. Kronast, J. Schlichting, F. Radu, S.K. Mishra, T. Noll, H. Dürr, Spin-resolved photoemission microscopy and magnetic imaging in applied magnetic fields. Surf. Interface Anal. 42, 1532 (2010)
- D. Kim, P. Fischer, W. Chao, E. Anderson, M. Im, S. Shin, S. Choe, Magnetic soft x-ray microscopy at 15 nm resolution probing nanoscale local magnetic hysteresis. J. Appl Phys 99, 08H303 (2006)
- 377. J. Turner, X. Huang, O. Krupin, K. Seu, D. Parks, S. Kevan, E. Lima, K. Kisslinger, I. McNulty, R. Gambino, S. Mangin, S. Roy, P. Fischer, X-Ray Diffraction Microscopy of Magnetic Structures. Phys. Rev. Lett. 107, 033904 (2011)
- A. Tripathi, J. Mohanty, S.H. Dietze, O.G. Shpyrko, E. Shipton, E.E. Fullerton, S.S. Kim, I. McNulty, Dichroic coherent diffractive imaging. Proc. Nat. Acad. Soc. 108, 13393 (2011)
- P. Guttmann, C. Bittencourt, S. Rehbein, P. Umek, X. Ke, G. Van Tendeloo, C.P. Ewels, G. Schneider, Nanoscale spectroscopy with polarized X-rays by NEXAFS-TXM. Nat. Photonics 6, 25 (2011)
- 380. G. Schneider, P. Guttmann, S. Heim, S. Rehbein, F. Mueller, K. Nagashima, J.B. Heymann, W.G. Müller, J.G. McNally, Three-dimensional cellular ultrastructure resolved by X-ray microscopy. Nat. Methods 7, 985 (2010)
- 381. J. B. Kortright, S.-K. Kim, H. Ohldag, G. Meigs, A. Warwick. Magnetization imaging using scanning transmission x-ray microscopy. In: W. Meyer-Ilse, T. Warwick, and D. Attwood (Eds.), *X-ray Microscopy, Proceedings of the Sixth International Conference, Berkeley CA*, 2–6 August 1999, vol. 507, 49. American Institute of Physics, Melville, New York (2000)
- 382. A.L.D. Kilcoyne, T. Tyliszczak, W.F. Steele, S. Fakra, P. Hitchcock, K. Franck, E. Anderson, B. Harteneck, E.G. Rightor, G.E. Mitchell, A.P. Hitchcock, L. Yang, T. Warwick, H. Ade, Interferometer-controlled scanning transmission X-ray microscopes at the Advanced Light Source. J. Synch. Radiat. 10, 125 (2003)
- 383. Y. Acremann, J.P. Strachan, V. Chembrolu, S.D. Andrews, T. Tyliszczak, J.A. Katine, M.J. Carey, B.M. Clemens, H.C. Siegmann, J. Stöhr, Time-resolved imaging of spin transfer switching: Beyond the macrospin concept. Phys. Rev. Lett. **96**, 217202 (2006)
- 384. B.V. Waeyenberge, A. Puzic, H. Stoll, K.W. Chou, T. Tyliszczak, R. Hertel, M. Fähnle, H. Brückl, K. Rott, G. Reiss, I. Neudecker, D. Weiss, C.H. Back, G. Schütz, Magnetic vortex core reversal by excitation with short bursts of an alternating field. Nature **444**, 461 (2006)

- M. Bolte, G. Meier, B. Krüger, A. Drews, R. Eiselt, L. Bocklage, S. Bohlens, T. Tyliszczak, A. Vansteenkiste, B. Van Waeyenberge, K.W. Chou, A. Puzic, H. Stoll, Time-Resolved X-Ray Microscopy of Spin-Torque-Induced Magnetic Vortex Gyration. Phys. Rev. Lett. 100, 176601 (2008)
- 386. S. Ladak, D. Read, T. Tyliszczak, W.R. Branford, L.F. Cohen, Monopole defects and magnetic Coulomb blockade. New J. Phys. 13, 023023 (2011)
- S. Wintz, T. Strache, M. Korner, M. Fritzsche, D. Marko, I. Monch, R. Mattheis, J. Raabe, C. Quitmann, J. McCord, A. Erbe, J. Fassbender, Direct observation of antiferromagnetically oriented spin vortex states in magnetic multilayer elements. Appl. Phys. Lett. 98, 232511 (2011)
- 388. J. Raabe, G. Tzvetkov, U. Flechsig, M. Böge, A. Jaggi, B. Sarafimov, M.G.C. Vernooij, T. Huthwelker, H. Ade, D. Kilcoyne, T. Tyliszczak, R.H. Fink, C. Quitmann, PolLux: A new facility for soft x-ray spectromicroscopy at the Swiss Light Source. Rev. Sci. Instrum. 79, 113704 (2008)
- 389. K.P. Lam, A.P. Hitchcock, M. Obst, J.R. Lawrence, G.D. Swerhone, G.G. Leppard, T. Tyliszczak, C. Karunakaran, J. Wang, K. Kaznatcheev, D.A. Bazylinski, U. Lins, Characterizing magnetism of individual magnetosomes by X-ray magnetic circular dichroism in a scanning transmission X-ray microscope. Chemical Geology **270**, 110 (2010)
- 390. A. Vogel, M. Martens, M. Weigand, G. Meier, Signal transfer in a chain of stray-field coupled ferromagnetic squares. Appl. Phys. Lett. **99**, 042506 (2011)
- D. Nolle, M. Weigand, G. Schütz, E. Goering, High Contrast Magnetic and Nonmagnetic Sample Current Microscopy for Bulk and Transparent Samples Using Soft X-Rays. Microscopy and Microanalysis 17, 834 (2011)
- E. Anderson, D. Olynick, B. Harteneck, E. Veklerov, G. Denbeaux, W. Chao, A. Lucero,
   L. Johnson, D. Attwood, Nanofabrication and diffractive optics for high-resolution x-ray applications. J. Vac. Sci. Technol. B 18, 2970 (2000)
- 393. E. Anderson, D. Ha, J. Liddle, Sub-pixel alignment for direct-write electron beam lithography. Microelectron. Eng. **74**, 73–74 (2004)
- W. Chao, E. Anderson, G. Denbeaux, B. Harteneck, A.L. Pearson, D. Olynick, F. Salmassi,
   C. Song, D. Attwood, Demonstration of 20 nm half-pitch spatial resolution with soft x-ray microscopy. J. Vac. Sci. Technol. B 21, 3108 (2003)
- W. Chao, J. Kim, S. Rekawa, P. Fischer, E. Anderson, Demonstration of 12 nm Resolution Fresnel Zone Plate Lens based Soft X-ray Microscopy. Optics Express 17(20), 17669 (2009)
- 396. J. Vila-Comamala, K. Jefimovs, J. Raabe, T. Pilvi, R. Fink, M. Senoner, A. Maaßdorf, M. Ritala, C. David, Advanced thin film technology for ultra high resolution X-ray microscopy. Ultramicroscopy 109, 1360 (2009)
- 397. W. Chao, P. Fischer, T. Tyliszczak, S. Rekawa, E. Anderson, P. Naulleau, Real space soft x-ray imaging at 10 nm spatial resolution. Optics Express **20**, 9777 (2012)
- 398. P. Fischer, T. Eimüller, G. Schütz, P. Guttmann, G. Schmahl, G. Bayreuther. Imaging magnetic structures with a transmission X-ray microscope. In: W. Meyer-Ilse, T. Warwick, and D. Attwood (Eds.), X-ray Microscopy, Proceedings of the Sixth International Conference, Berkeley CA, 2–6 August 1999, vol. 507, 205. (American Institute of Physics, Melville, New York, 2000)
- 399. M. Im, P. Fischer, T. Eimüller, G. Denbeaux, S. Shin, Magnetization reversal study of CoCrPt alloy thin films on a nanogranular-length scale using magnetic transmission soft x-ray microscopy. Appl. Phys. Lett. **83**, 4589 (2003)
- P. Fischer, T. Eimüller, G. Schütz, M. Kohler, G. Bayreuther, G. Denbeaux, D. Attwood, Study of in-plane magnetic domains with magnetic transmission x-ray microscopy. J. Appl. Phys. 89, 7159 (2001)
- M.-Y. Im, P. Fischer, Y. Keisuke, T. Sato, S. Kasai, Y. Nakatani, T. Ono, Symmetry breaking in the formation of magnetic vortex states in a permalloy nanodisk. Nat. Commun. 3, 983 (2012)
- S. Kasai, P. Fischer, M.-Y. Im, K. Yamada, Y. Nakatani, K. Kobayashi, H. Kohno, T. Ono, Probing the spin polarization of current by soft x-ray imaging of current-induced magnetic vortex dynamics. Phys. Rev. Lett. 101, 237203 (2008)

403. H. Jung, Y.-S. Choi, K.-S. Lee, D.-S. Han, Y.-S. Yu, M.-Y. Im, P. Fischer, S.-K. Kim, Logic Operations Based on Magnetic-Vortex-State Networks. ACS Nano 6, 3712 (2012)

- 404. D. Cooke, F. Hellman, J.R. Groves, B.M. Clemens, S. Moyerman, E.E. Fullerton, Calorimetry of epitaxial thin films. Rev. Sci. Instrum. **82**, 023908 (2011)
- D. Denlinger, E.N. Abarra, K. Allen, P.W. Rooney, M.T. Messer, S.K. Watson, F. Hellman, Thin film microcalorimeter for heat capacity measurements from 1.5 to 800 K. Rev. Sci. Instrum. 65, 946 (1994)
- P. Fischer. Magnetic soft X-ray transmission microscopy. Curr. Op. in Solid State Mater. Sci 7, 173 (2003)
- 407. F. Macia, P. Warnicke, D. Bedau, M.-Y. Im, P. Fischer, D.A. Arena, A.D. Kent, Perpendicular magnetic anisotropy in ultrathin Co-Ni multilayer films studied with ferromagnetic resonance and magnetic x-ray microspectroscopy. J. Magn. Mag. Mater. 324, 3629 (2012)
- 408. D. Ralph, M. Stiles, Spin Transfer Torques. J. Magn. Magn. Mater. 320, 1190 (2008)
- 409. P. Fischer, T. Eimüller, G. Schütz, G. Denbeaux, İmaging magnetic domain structures with soft X-ray microscopy. Structural Chemistry 14, 39 (2003)
- 410. P. Fischer, G. Denbeaux, T. Ono, T. Okuno, T. Eimüller, D. Goll, G. Schütz, Study of magnetic domains by magnetic soft x-ray transmission microscopy. J. Phys. D: Appl. Phys. **35**, 2391 (2002)
- H. Kronmüller, R. Hertel, Computational micromagnetism of magnetic structures and magnetisation processes in small particles. J. Magn. Magn. Mater. 215–216, 11 (2000)
- L.J. Heyderman, F. Nolting, C. Quitmann, X-ray photoemission electron microscopy investigation of magnetic thin film antidot arrays. Appl. Phys. Lett. 83, 1797 (2003)
- 413. L.J. Heyderman, H.H. Solak, F. Nolting, C. Quitmann, Fabrication of nanoscale antidot arrays and magnetic observations using x-ray photoemission electron microscopy. J. Appl. Phys. **95**, 6651 (2004)
- L.J. Heyderman, S. Czekaj, F. Nolting, D.-H. Kim, P. Fischer, Cobalt antidot arrays on membranes: Fabrication and investigation with transmission X-ray microscopy. J. Magn. Magn. Mater. 316, 99 (2007)
- L. Torres, L. Lopez-Diaz, J. Iniguez, Micromagnetic tailoring of periodic antidot permalloy arrays for high density storage. Appl. Phys. Lett. 73, 3766 (1998)
- S. Mangin, T. Hauet, P. Fischer, D.H. Kim, J.B. Kortright, K. Chesnel, E. Arenholz, E.E. Fullerton, Influence of interface exchange coupling in perpendicular anisotropy [Pt/Co](50)/TbFe bilayers. Phys. Rev. B 78, 024424 (2008)
- 417. O. Hellwig, A. Berger, E. Fullerton, Domain walls in antiferromagnetically coupled multilayer films. Phys. Rev. Lett. **91**, 197203 (2003)
- O. Hellwig, A. Berger, J.B. Kortright, E. Fullerton, Domain structure and magnetization reversal of antiferromagnetically coupled perpendicular anisotropy films. J. Magn. Magn. Mater. 319, 13 (2007)
- J.B. Kortright, S.-K. Kim, G. Denbeaux, G. Zeltzer, K. Takano, E. Fullerton, Soft-x-ray small-angle scattering as a sensitive probe of magnetic and charge heterogeneity. Phys. Rev. B. 64, 092401 (2001)
- 420. J.B. Kortright, O. Hellwig, K. Chesnel, S. Sun, E.E. Fullerton, Interparticle magnetic correlations in dense Co nanoparticle assemblies. Phys. Rev. B **71**, 012402 (2005)
- 421. M. Gottwald, M. Hehn, D. Lacour, T. Hauet, F. Montaigne, S. Mangin, P. Fischer, M.-Y. Im, A. Berger, Asymmetric magnetization reversal in dipolarly coupled spin valve structures with perpendicular magnetic anisotropy. Phys. Rev. B 85, 064403 (2012)
- 422. T. Hauet, C.M. Guenther, B. Pfau, M.E. Schabes, J.U. Thiele, R.L. Rick, P. Fischer, S. Eisebitt, O. Hellwig, Direct observation of field and temperature induced domain replication in dipolar coupled perpendicular anisotropy films. Phys. Rev. B 77, 184421 (2008)
- 423. H. Stoll, A. Puzic, B. van Waeyenberge, P. Fischer, J. Raabe, M. Buess, T. Haug, R. Hollinger, C. Back, D. Weiss, G. Denbeaux, High-resolution imaging of fast magnetization dynamics in magnetic nanostructures. Appl. Phys. Lett **84**, 3328 (2004)
- 424. K.W. Chou, A. Puzic, H. Stoll, G. Schütz, B. van Waeyenberge, T. Tyliszczak, K. Rott, G. Reiss, H. Brückl, I. Neudecker, D. Weiss, C.H. Back, Vortex dynamics in coupled ferromagnetic multilayer structures. J. Appl. Phys. 99, 08F305 (2006)

A Aberration correction, 141	Magnetic linear birefringence, 20, <b>76</b> , 77–80
Absorption	Bloch line, see Domain walls
Absorption (visible light), 14, <b>23–30</b> , 49, 54–57, 121, 126	Brace-Köhler compensator, see Compensator
Absorption (X rays), 15, 21, 22, 75, <b>86–95</b> , <b>190–191</b>	Buried layers, 142
Absorption coefficient, 30, 75, 92, 94, 144, 147–148, 191–194 Absorption edge (X rays), 7, 16, 22, 86–94 Absorption spectra (visible light), 15, 74–75 Absorption spectra (X rays), 86–95 Airys recursion formula, 114, 125 Antidot array, 208–210 Antiferromagnet, see Materials Antiferromagnetic interlayer coupling, see Oscillatory interlayer coupling Antireflection coating, 72 Atomic scattering factor, 146 Attenuation coefficient, see Absorption coefficient Attenuation of absorption signal, 144, 190 Attenuation of photon intensity, 190, 191	C Canting of magnetization, 156 Cascade numerical projection method, 136 Circular dichroism, see Dichroism Circular polarization, see Polarized light Circularly polarized X rays, see Polarized light Compensator, 40–44, 57, 69, 77–80, 84, 98–100, 117, 118, 127–135 Brace-Köhler compensator, 40, 41, 43, 69 Babinet compensator, 40, 41, 69, 70 Conductivity tensor, 26, 30 Conoscopic image, see Kerr microscopy Continuity conditions (optical), 46, 48, 88, 111 Continuity equation, 25, 28 Cotton-Mouton effect, see Magneto-optical effects
B	
Babinet compensator, see Compensator	D
Backscattering (type II) contrast, 17	_
Biquadratic interlayer coupling, see Oscilla-	Depth-sensitive conventional magneto- optical microscopy, 14, 97–140
tory interlayer coupling Birefringence, <b>36–42</b> , 49, 124	Depth sensitivity of Kerr effect (experimen-
Circular birefringence, 34, 37, 55	tal), 108–109
Magnetic circular birefringence, 20, 54–58, 76–80	Depth sensitivity of Kerr effect (theory), 109–130
© Springer-Verlag Berlin Heidelberg 2015	241

W. Kuch et al., Magnetic Microscopy of Layered Structures,

Springer Series in Surface Sciences 57, DOI 10.1007/978-3-662-44532-7

Cascade numerical projection method, 136  Depth selectivity in magnetic multilayers, 127–130  Depth sensitivity function, 115–127  Depth sensitivity in magnetic films, 119–	360° walls, 109, 110, 133 90° wall, 160, 161, 209 Bloch line, 130, 136 Cross-tie wall, 81, 82 Néel cap, 82, 130 Néel wall, 131, 136, 160, 163
Depth sensitivity in magnetic multilayers, 124–127	Double refraction, 20, 36, 38
Information depth, 13, 14, <b>116</b> , 116–118, 127–130, 137  Matrix method, 109–112  Multiple beam formalism, <b>112–115</b> , 119, 124  Parallel Kerr vector method, 129, 130	E Eigenmodes, 29, 51, 58, 76, 110–112 Electromagnetic field, 24, 25, 26, 119 Electromagnetic light theory, 37, 38, 46, 49–54 Electromagnetic wave, 25, 27, 44
Phase factor, 113, 113–116, 121–123	Electron attenuation length, 143, 145, 147, 148
Projection concept, 128, 129  Depth-selective Kerr microscopy, 14, 101, 127, 130–136  Dichroism, 36, 37, 80  Circular dichroism, 54  Circular magnetic dichroism, 56–58, 73  Linear magnetic dichroism, 77  X ray magnetic circular dichroism, 21, 22, 73, 92–95, 194  X ray magnetic dichroism, 14–16, 21, 86–95	Electron yield, <b>142–150</b> Electronic core levels, <b>15</b> , <b>21</b> , <b>89</b> , <b>93</b> Electrostatic tetrode lens, <b>142</b> Element specificity, <b>12</b> , <b>15</b> , <b>16</b> , <b>21</b> , <b>86</b> Ellipsometry, <b>104</b> Elliptical polarization, <i>see</i> Polarized light Exchange bias, <b>6</b> , <b>8</b> , <b>166</b> , <b>174</b> , <b>175</b> , <b>180</b> , <b>203</b> Exchange splitting, <b>73–74</b> , <b>94</b> Extinction coefficient, <b>29</b>
X ray magnetic linear dichroism, 21, 22, 86–91, 169–180  Dielectric displacement, 26, 28, 30, 38, 46, 80, 83, 84  Dielectric law, 26, 64, 83, 84, 120  Dielectric tensor, 26, 29, 46, 49–50, 63, 73–79, 88, 112, 121  Dielectric media, 23, 26, 30, 39, 47, 72, 110, 114, 124	F Faraday effect, 19–21, 24, 37–39, 54–66, 115, 119–121 Faraday amplitude, 56, 64, 115, 119, 121 Faraday ellipticity, 24, 54–61 Faraday rotation, 24, 39, 54–61, 66, 78 Longitudinal Faraday effect, 64 Polar Faraday effect, 51, 55, 57, 63, 64 Transverse Faraday effect, 64
Difference image, <i>see</i> Kerr Microscopy Dipole selection rules, <i>see</i> Selection rules Dispersion, 25, 26, 49, 54 Domain contrast, <i>see</i> Backscattering (type II) contrast, Gradient contrast, Kerr contrast, Voigt contrast, XMCD con-	Fermi's golden rule, 94, 95 Ferromagnetic interlayer coupling, see Oscillatory coupling Figure of merit, 193 Figure of merit in magneto-optics, 68, 72 Free electron laser, 12, 217, 220
trast Domain patterns Flower state, 209 Landau pattern, 81, 82, 206–209, 219 S state, 209 Stripe domains, 130, 155, 157, 159	Fresnel coefficient, <b>47</b> , 58, 61, 62, 66, 67, 72, 112, 114, 121, 125, 126  Fresnel equations, <b>47</b> , 58, 62, 63, 67, 114, 125, 126  Fresnel zone pate, <i>see</i> Zone plate
V-line, 82–85 Domain wall interaction, 157–163, 185, 213,	G
215 Domain walls, 9, 14, 16, 81–85, 100, 109, 124, 130–140	Giant magnetoresistance (GMR), 2–4, 108, 135 Gradient contrast, <i>see</i> Gradient effect

Gradient effect, 13, 20, 21, <b>81–85</b> , 97, 124, 137	Analyser, 40–42, 44, 45, 57, 66–68, 70–72, 78, 98–102, 106–108
Gradient contrast, 21, 82, 84, 140	Conoscopic image, 99
Gradient microscopy, 97, 137–140	Image processing, 20, 70–72, 80, 100–102
Н	Laser-scanning Kerr microscopy, 10, 97, 103–104
Helical undulator, 15, 91, 92	Lateral resolution, 11, 82, 99, <b>100</b> , 103, 130
	Polarizer, 35, 41, 42, 44, 45, 66, 68, 69,
Ţ	98, 99, 106
Image processing, see Kerr microscopy	Wide-field Kerr microscopy, 10, 40, 41,
Information depth, see Depth sensitivity of	69, 97–102
Kerr effect (theory)	Kerr spectroscopy, 107
Inhomogeneous wave, 48, 51	Kramers-Kronig relation, 75, 95
Interlayer coupling energy, see Magnetic	
interlayer coupling	T
Irradiance, 29, 30, 35	L
	Landau pattern, <i>see</i> Domain patterns Landau-Lifshitz-Gilbert equation, 9, 218
	Laser-scanning Kerr microscopy, see Kerr
J	microscopy
Jones formalism, 34, 43, 77	Linear magnetic dichroism, see Dichroism
Jones matrix, 42–44	Linearly polarized light, see Polarized light
Jones vector, <b>34</b> , 42, 55	Lorentz concept, 19, <b>63</b> , 64, 65, 67, 79, 80, 84, 120
K	
Kerr coefficient, see Kerr effect: Kerr ampli-	M
tude	M-TXM, see Magnetic transmission X-ray
Kerr contrast, see Kerr effect, magneto-	microscopy (M-TXM)
optical	Magnetic circular birefringence, see Bire-
Kerr effect, electro-optical, 40	fringence
Kerr effect, magneto-optical, 13, 14, 54–75	Magnetic circular dichroism, see Dichroism
Kerr amplitude, <b>59</b> , <b>64</b> , 59–72, 99, 106,	Magnetic films, see Materials
114, 116–119, 122, 123, 126–129	Magnetic interlayer coupling, 153, 165
Kerr contrast, 21, 67, <b>68–73</b> , 78, 79, 81,	Magnetic linear birefringence, see Birefrin-
99–102, 104, 116, 127	gence
Kerr ellipticity, 24, 58, <b>61</b> , 67, 105–107,	Magnetic linear dichroism, see Dichroism
112, 128, 129	Magnetic materials, see Materials
Kerr intensity, 66, 69, 70, 107 Kerr phase, <b>60</b> , 128	Magnetic transmission X-ray microscopy
Kerr rotation, 24, 58, <b>60–67</b> , 70, 105–	(M-TXM), 189, 190, 197–204 Magnetization dynamics, 180–188, 217–
107, 112, 114, 128, 129	220
Kerr signal, 68–73, 105, 106, 118, 120,	Magnetization precession, 218
121, 127–129, 133	Magneto-optical amplitude, see Kerr- and
Longitudinal Kerr effect, 19, 21, 65, 66–	Voigt amplitude
68, 99, 108–110	Magneto-optical diffraction analysis, 17, 83,
Microscopic origin, 73–75	124
Polar Kerr effect, 19, 51, 58, 60–63, <b>65</b> ,	Magneto-optical effects, 19-95
68, 73, 99	Conventional magneto-optical effects,
Transverse Kerr effect, 19, <b>66</b> , 88, 99	19–85
Kerr microscopy (technique), 97–104	Cotton-Mouton effect, 20, 39, 40, 77
Köhler illumination technique, 98	Faraday effect, see Faraday effect

Kerr effect, see Kerr effect, magneto-	Gold/Cobalt multilayer, 136
optical	Hematite, 89
Voigt effect, see Voigt effect	Iron (bulk), 19, 84, 93, 117, 127, 130
X-ray magnetic dichroism, see Dichroism	Iron film, 14, 90, 122, 123, 128, 135, 136, 164
X-ray Magneto-optical effects, 86–95	Iron oxid, 86, 90
Magneto-optical gradient effect, see Gradi-	Iron whisker, 135, 137
ent effect	Iron-silicon, 20, 21
Magneto-optical Kerr microscopy, see Kerr	LaFeO <sub>3</sub> , 90
microscopy	Magnesium oxide, 89
Magneto-optical magnetometry (MOKE),	Mica, 37, 41, 42
40, 97, 101, 103, 105–107	MnIr/NiFe bilayer, 203
Magneto-optical microscopy, 97–140	MnZn ferrite, 117, 123
Gradient microscopy, see Gradient effect	Ni <sub>80</sub> Fe <sub>20</sub> /Al <sub>2</sub> O <sub>3</sub> /Co trilayer, 183–186
Kerr microscopy, see Kerr microscopy	Ni/Fe/Co trilayer, 163–166
Voigt microscopy, see Voigt effect	Ni/FeMn/Co trilayer, 166–172
Magneto-optical tensor, 49–50, 63	Nickel oxide, 89, 90
Magneto-optical Voigt effect, see Voigt	NiFe (Permalloy), 40, 109
effect	NiFe microstructure, 206, 217, 218
Materials	NiFe <sub>2</sub> O <sub>4</sub> , 90
(Ga,Mn)As, 90	NiFe/Al <sub>2</sub> O <sub>3</sub> /Co trilayer, 161–163
Antiferromagnets, 8, 16, 89, 90, 92, 108,	NiFe/Co bilayer, 108
135–140, 166, 172–180, 203	NiFe/Cu/Co trilayer, 151–153, 195, 219
Calcite, 36, 37, 40, 41	NiFe/Ru/NiFe trilayer, 110
Cerium, 17, 86	NiO, 172–178
Co/Cu/Co trilayer, 126	Orthoferrite, 20
Co/Cu/Co-NiFe spin valve, 108	PtCo/TbFe multilayer, 211–213
Co/Cu/Fe trilayer, 126	Quartz, 36, 37, 40
Co/Cu/Ni trilayer, 153–161	Rare earth metals, 86
Co/Cu/NiFe trilayer, 131–133	Si <sub>3</sub> N <sub>4</sub> , 202
Co/LaFeO <sub>3</sub> bilayer, 178–180	SrTiO <sub>3</sub> , 178–180
Co/Ni multilayer, 203, 204	TbFe, 211–213
Co/NiO bilayer, 91	Terbium, 86
Co/Pd multilayer, 214–216	Transition metal compounds, 88
Co/Pt multilayer, 211–213	Matrix methods, see Depth sensitivity of
Co/Si/GdCo trilayer, 133–134	Kerr effect (theory)
Cobalt film, 22, 90, 108, 126, 131–134,	Maxwell equations, <b>25</b> , 27, 30, 46, 49, 61,
136, 172–176, 209	63, 79, 109, 120
CoCrPt, 201	Microcoil, 181–183, 186, 217
CoFeSiB/SiO <sub>2</sub> /CoFeSiB trilayer, 109	Micromagnetic simulations, 159, 185, 208,
CoO, 176–178	209, 218
Copper, 123	Microscopic origin of Kerr effect, see Kerr
CoTb/Cu/CoTb trilayer, 213–215	effect, magneto-optical
Dysprosium, 86	MOKE, see Magneto-optical magnetometry
Fe/Al/Fe trilayer, 134, 140	Multiple beam formalism, see Depth sensi-
Fe/Cr/Fe trilayer, 128, 134, 137–140	tivity of Kerr effect (theory)
Fe/MgO/Fe, 136	tivity of Kerr effect (theory)
Fe/V multilayer, 87	
FeCo/Cr/NiFe trilayer, 187–188	
Ferromagnetic-Antiferromagnetic het-	N
erostructures, 8	Néel cap, see Domain walls
Garnet, 13, 20, 23, 61, 86, 124	Néel wall, see Domain walls
GdFe, 200, 201, 204, 205	Numerical aperture, 197

0	Refraction index, 27, 25–30, 36, 48, 53–55,
Optical activity, 26, 36–40, 47, 49, 54	57, 62, 75, 76, 113, 114
Optical anisotropy, 26, 49	Regular amplitude, 59–61, 65–73
Oscillatory interlayer coupling, 165	
Antiferromagnetic interlayer coupling,	
6, 135–140	S
	Scanning transmission X-ray microscope
Biquadratic interlayer coupling, 134–	(STXM), 197
140	Secondary electron conversion factor, 144
Ferromagnetic interlayer coupling, 134–	Selection rules, 73, 74
140	
Overlayer compensation factor, 194, 195	Sign convention, 23, <b>24</b> , 57, 59, 116
	Skin depth, 30
	Snells law, <b>47</b> , 51, 62, 68, 113, 121
P	Spin valve, 3, 108, 109, 161, 213–215
Parallel Kerr vector method, see Depth sen-	Spin-orbit splitting, 73, 74, 86
	Spin-reorientation transition, 86, 167, 168
sitivity of Kerr effect (theory)	Stray-field coupling, see Domain wall inter-
PEEM, see Photoelectron emission	action
microscopy (PEEM)	
Penetration depth, see Skin depth	Strip line, 186, 187
Permeability tensor, 26, 46	Stripe domains, see Domain patterns
Permittivity tensor, see Dielectric displace-	STXM, see Scanning transmission X-ray
ment	microscope (STXM)
Perturbation theory, 26, 112, 115, 119–124	Sum rules, 95
Phase factor, see Depth sensitivity of Kerr	Synchrotron radiation, 11, 16, 86, 91, 92
	, , , , , , , , , , , , , , , , , , , ,
effect (theory)	
Photoconductive switch, 186, 187	T
Photoelasticity, 39	Time-resolved imaging, 10–12, 180–188,
Photoelectron emission microscopy	216–220
(PEEM), 12, 16, 22, 88, 94, <b>141</b> -	
142	Transmission, 44–49
Imaging in magnetic field, 196	Transmission coefficient, 47
Polarized light, 30–36	Transmission of X rays, 191
	Transmission X-ray microscopy (TXM), 12,
Circular polarization, 33–36	16, <b>189–190</b> , 196–204
Circularly polarized X rays, 91	Tunnel magnetoresistance (TMR), 2–4
Elliptical polarization, 31–33	TXM, see Transmission X-ray microscopy
Handedness, 32, 57, 77	(TXM)
Linearly polarized light, 33	(1711)
Precession, see Magnetization precession	
Projection concept, see Depth sensitivity of	U
Kerr effect (theory)	Ultrathin film, 2, 5, 6, 9, 14, 86, 123, 128,
Propagation vector, 27	
Pump–probe experiment, 180–188, 216	129, 135, 136
Tump proof experiment, 100 100, 210	
	V
0	V-line, <i>see</i> Domain patterns
Q	
Quarter-wave plate, 14, 33, 41, 43, 45, 57,	Verdet constant, 39
69	Vibrating sample magnetometry (VSM),
	213, 214
	Voigt amplitude, see Voigt constant (parame-
R	ter)
Rayleigh criterion, 100, 198	Voigt constant (parameter), 50, 51–54, 57–
Reflection, 44–49	68, 72, 75, 76, 79, 117, 119–122, 125,
Reflection coefficient, 47	126
Reflectivity, 25, 72, 76, 77, 87, 88	Voigt contrast, see Voigt effect

Voigt effect, 13, 20, 21, 37, 39, 40, 50, 53, 59, 66, 68, 69, <b>75–81</b> , 137–140 Gyrotropic Voigt effect, 54, 76, 79, 80 Intrinsic Voigt effect, 53, 75–79 Voigt contrast, 21, 68, 78, 80–82, 137–140 Voigt microscopy, 21, 137–140 VSM, <i>see</i> Vibrating sample magnetometry  W Wave equation, 23–30, 37, 49–51, 53, 58, 111, 119	X X-ray absorption, see Absorption X-ray magnetic circular dichroism, see Dichroism X-ray magnetic dichroism, see Dichroism X-ray magnetic linear dichroism, see Dichroism X-ray penetration depth, 202 X-ray resonant magnetic scattering (XRMS), 211, 212 XMCD contrast, see X-ray magnetic circular dichroism XRMS, see X-ray resonant magnetic scattering
Wave vector, <i>see</i> Propagation vector Wide-field Kerr microscopy, <i>see</i> Kerr	<b>Z</b> Zeeman effect, 19

microscopy

Zone plate, 197-199